Mathematical models of biological invasion

Maud El-Hachem
B.Eng., M.Eng. (Computer Engineering)

2022

Statement of original authorship

The work contained in this thesis has not been previously submitted to meet requirements for an award at this or any other higher education institution. To the best of my knowledge and belief, the thesis contains no material previously published or written by another person except where due reference is made.

Maud El-Hachem

27/05/2022

Acknowledgements

I would like to express my immense gratitude to my supervisors, Prof. Matthew Simpson and Prof. Scott McCue. Matthew, thank you for giving me this wonderful opportunity to study in applied mathematics, for encouraging me to always do better, for guiding me thorough this "PhD journey". Scott, thank you for being involved in all the research I have done in this thesis, thank you for sharing your expertise, for guiding and supporting me.

I would like thank Dr Wang Jin for his precious help in the first year and half of my PhD studies. I would like to thank Prof. Yihong Du whose work inspired the first steps of this whole journey.

I would like to thank the Australian Research Council and Matthew Simpson for their financial support, as well as QUT Postgraduate Research Award for the scholarship. I am grateful to the QUT School of Mathematical Sciences for the funding that gave me the opportunity to participate to ANZIAM conferences. I am also grateful to the Australian Mathematical Society for their support and recognition.

Thank you my family and friends. Josephine, Maguy, Maria, Tania, your unconditional love, travelling thousands of miles by text messages, videos and phone calls, kept me strong and focussed.

Abstract

The Fisher-Kolmogorov equation supports travelling wave solutions that are successfully used to model numerous invasive phenomena with applications in biology and ecology. The Fisher-Kolmogorov equation assumes that individuals, or cells, in the population proliferate logistically and move according to a linear diffusion mechanism. The long-term solution of the Fisher-Kolmogorov equation is a travelling wave solution with a smooth front that captures important features of invasion, however the solution fails to represent a population on a well-defined domain. Another limitation of the Fisher-KPP equation is that the solution always evolves to an invading front and therefore the solution is unable to mimic the extinction of invasive populations. We modify the Fisher-Kolmogorov equation to include a moving boundary whose evolution is governed by a Stefan condition. The novel Fisher-Stefan model gives rise to the spreading-extinction dichotomy. We aim to extend further the model by considering two cell populations, such as a population of cancer cells invading into a population of skin cells. Both populations of cells in the two-phase moving boundary model undergo linear diffusion and proliferate logistically. The interface between the two populations moves according to a two-phase Stefan condition.

List of publications

1. El-Hachem M, McCue SW, Jin W, Du Y, Simpson MJ (2019) Revisiting the Fisher-Kolmogorov-Petrovsky-Piskunov equation to interpret the spreading-extinction dichotomy. *Proceedings of the Royal Society A* **475**, 20190378. (10.1098/rspa.2019.0378).

2. El-Hachem M, McCue SW, Simpson MJ (2021) Invading and receding sharp-fronted travelling waves. *Bulletin of Mathematical Biology* **83**, 35. (doi:10.1007/s11538-021-00862-y).

3. El-Hachem M, McCue SW, Simpson MJ (2021) Non-vanishing sharp-fronted travelling wave solutions of the Fisher-Kolmogorov model. Accepted for publication in *Mathematical Medecine and Biology.* (arXiv: 2107.05210).

4. El-Hachem M, McCue SW, Simpson MJ (2020) A sharp-front moving boundary model for malignant invasion. *Physica D: Nonlinear Phenomena* **412**, 132639. (doi:10.1016/j.physd.2020.132639).

5. El-Hachem M, McCue SW, Simpson MJ (2021) Travelling wave analysis of cellular invasion into surrounding tissues. *Physica D: Nonlinear Phenomena* **428**, 133026. (10.1016/j.physd.2020.132639)

6. El-Hachem M, McCue SW, Simpson MJ (2022) A continuum mathematical model of substrate-mediated tissue growth. *Bulletin of Mathematical Biology* **84**, 49. (doi: 10.1007/s11538-022-01005-7).

Contents

Chapter 1

Introduction

1.1 Background

Biological invasion occurs when populations of motile and proliferative individuals or cells evolve to moving fronts that invade vacant regions. Wound healing is a common example of biological invasion [Sherratt and Murray 1990, Maini et al. 2004a, Cai et al. 2007, Simpson et al. 2013], where the population of epidermal cells diffuses and proliferates to close the open wound. Tumour invasion is another example of biological invasion where cancerous cells invade the tissues of an organ or metastasise throughout the body [Swanson et al. 2003, Pérez-Beteta et al. 2018]. Embryonic development is an example of non pathological invasion, when cells derived from the neural crest colonises the gastrointestinal tract to form the enteric nervous system [Simpson et al. 2007]. Biological invasion has many applications in ecology [Skellam 1951, Shigesada et al. 1951, Steel et al. 1998] where the models used include interactions between the populations such as mating, mutualism, competition and predation [Kot 2003].

Mathematical models of invasion are useful to study the factors that influence the evolution of a population. For example, a mathematical model of invasion can help to determine how to preserve an endangered species [Griffith et al. 1989], how to predict the survival rate of a patient in cancer therapy [Swanson et al. 2003, Swanson et al. 2008], how to ensure the success of an implant in tissue reconstruction [Buenzli et al. 2020].

Biological invasions are studied using partial differential equation (PDE) models based upon the classical Fisher-Kolmogorov-Petrovsky-Piskunov (Fisher-

KPP) equation [Fisher 1937, Kolmogorov et al. 1937]. The Fisher-KPP equation is a one-dimensional reaction–diffusion equation that assumes that individuals, or cells, in the population proliferate logistically and move according to a linear diffusion mechanism, such as

$$\frac{\partial u}{\partial t} = D\frac{\partial^2 u}{\partial x^2} + \lambda u \left(1 - \frac{u}{K}\right) \tag{1.1}$$

where the cell density $u(x,t)$ of the population is a function of position $-\infty < x < \infty$ and time $t > 0$, the diffusion coefficient or the diffusivity is $D > 0$, the proliferation rate is $\lambda > 0$ and the carrying capacity is $K > 0$.
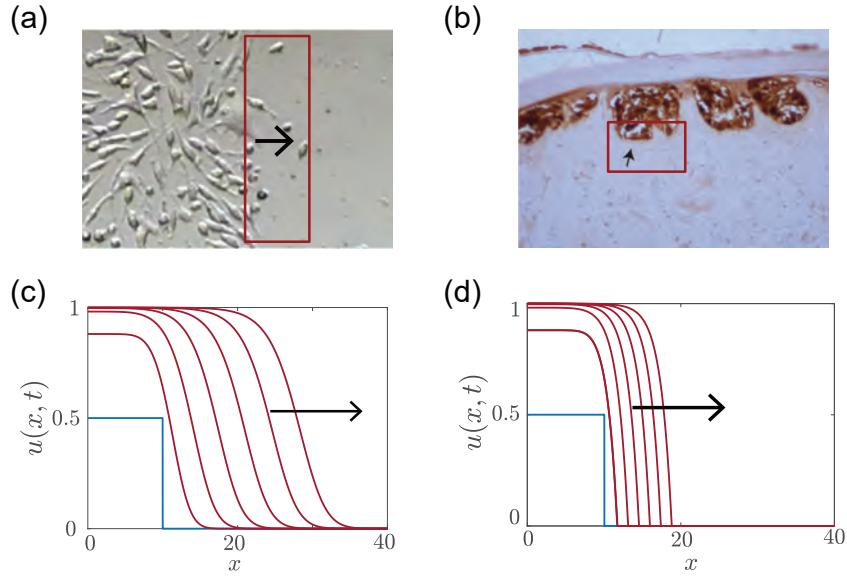
Figure 1.1: Biological invasion and moving front. (a) Picture of scratch wound healing assay experiment of sarcoma cells. The original picture is from Dihaf Zeki, obtained under Creative Common Licence CC BY-SA 4.0 [Wikipedia 2016]. The modified picture shows one side of the scratch. (b) Cross-section of clusters of cultured melanoma cells invading surrounding tissues (Figure 1 from Chapter 5). The red box in (a) and (b) highlights the invading front. (c) Time-dependent solutions of Fisher-KPP equation (1.1) with $D = 1$ and $\lambda = 1$ evolving to a smooth-fronted travelling wave solution. (d) Time-dependent solutions of Porous-Fisher equation (1.2) with $\lambda = 1$ evolving to a sharp-fronted travelling wave solution. In (c) and (d) the density profiles are shown at $t = 2, 4, 6, 8, 10$ and 12. The initial conditions on compact support are shown in blue. Homogeneous Neumann boundary conditions are used at $x = 0$ and $x = 40$. The black arrow in (a), (c) and (d) indicates the direction of the moving front. The black arrow in (b) indicates the position of the invading front.

The long term solution of Fisher-KPP equation with appropriate boundary conditions, such as no-flux at the boundaries, is a travelling wave with a speed that depends on the initial conditions. A travelling wave solution is a function that moves with a constant speed while keeping its shape. The travelling wave solution of Fisher-KPP equation has a minimum speed $c_{\min} = 2\sqrt{D\lambda}$. Figure

1.1(c) shows the density profiles obtained by solving numerically the Fisher-KPP equation (1.1) for an interval of time sufficiently long so the solution evolves to a travelling wave. The parameters used in Figure 1.1(c) are $D = 1$ and $\lambda = 1$ such as the travelling wave speed is $c = 2$. We can identify two steady states in the travelling wave solution: behind the invading front, where $u(x, t) \to 1$ and $\partial u / \partial x \to 0$, where the population has reached a density corresponding to the maximum carrying capacity, and ahead of the moving front, where $u(x, t) \to 0$ and $\partial u / \partial x \to 0$, where the population vanishes.

Figure 1.1(a) shows a picture of a scratch assay experiment, that can be characterised by a diffusion coefficient and a proliferation rate of cells. A scratch assay involves creating a laceration into a monolayer of homogenous cells and monitoring the migration of cells at the leading edge of the scratch. Many scratch assay experiments [Maini et al. 2004a, Jin et al. 2016, Johnston et al. 2015, Warne et al. 2019] have successfully validated the relationship that defines the wave speed as a function of the proliferation rate and the diffusivity, as in Fisher-KPP equation, such as $c = 2\sqrt{D\lambda}$. Two-dimensional extensions of the Fisher-KPP equation have also been studied [Sherratt and Murray 1990, Simpson et al. 2013, Swanson et al. 2003].

The solution of the Fisher-KPP equation misses an important feature of biological invasion: a well defined position of the moving front. In the experiment of Figure 1.1(a) the population occupies a well-defined domain where $u(x, t) > 0$, and the population vanishes outside the domain, where $u(x, t) = 0$. Figure 1.1(b) shows a cross-section of an experiment of cultured melanoma cells invading into the surrounding skin cells. Again, as highlighted in the red box in Figure 1.1(b), the moving front of the cluster of melanoma cells is well defined. In Figure 1.1(c) we cannot define a position where $u(x, t) = 0$, as the solution in Fisher-KPP model does not have compact support. A well-known extension of the Fisher-KPP equation is the Porous-Fisher equation that supports a travelling wave solution with a sharp-front (Figure 1.1(d)).

The Porous-Fisher equation [Murray 2002, Sánchez-Garduño and Maini 1994, Sánchez Garduño and Maini 1994] includes a non-linear diffusion term and is defined by

$$\frac{\partial u}{\partial t} = D \frac{\partial}{\partial x} \left[u \frac{\partial u}{\partial x} \right] + \lambda u \left(1 - \frac{u}{K} \right),$$ (1.2)

where the solution $u(x,t)$ is a density function of position $-\infty < x < \infty$ and time $t > 0$, the constant diffusivity is $D > 0$, the proliferation rate is $\lambda > 0$ and the carrying capacity is $K > 0$. Experiments show that the velocity of cell population is affected by contact inhibition [Tremel et al. 2009, Warne et al. 2019] and that a density-dependant diffusion makes the model more easily reproduced in experiments [Jin et al. 2016, McCue et al. 2019]. As in the Fisher-KPP equation, the travelling wave solution of the Porous-Fisher equation depends on the initial conditions. Minimal speed $c_{\min} = \sqrt{D\lambda/2}$ is achieved from initial condition with compact support. The difference with Fisher-KPP equation is that the solution of Porous-Fisher equation with minimum speed has a compact support and a sharp front such as $u(x,t) = 0$ at the position of the moving front.

Another limitation of the solution of the Fisher-KPP equation is that the solution always evolves to a travelling wave with a positive speed, from initial condition with compact support. It means that the solution cannot represent the stalling, the recession or the extinction of biological populations. It is also a missing feature in the Porous-Fisher equation. We know, for example, that the success of a translocation in species conservation depends on many factors, as the population goes extinct in some areas [Griffith et al. 1989] and do not always invade the new geographic region. Another example of a biological population that could not be represented by the Fisher-KPP equation is a population that could recede, like a tumour that is shrinking.
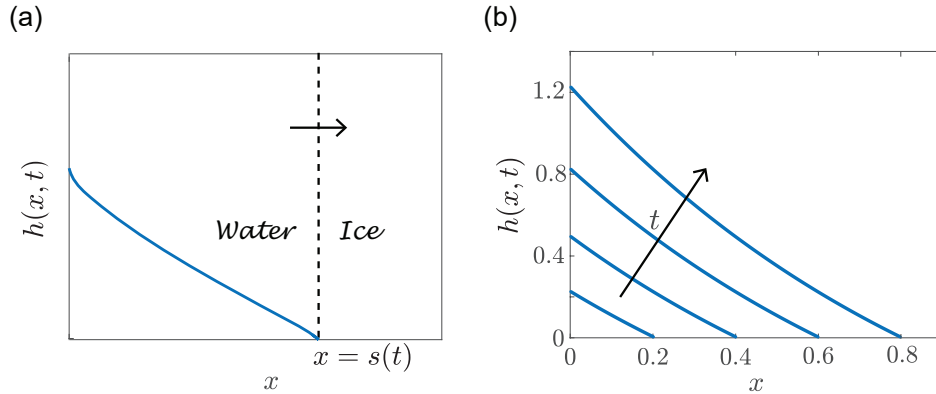
Figure 1.2: **One-phase Stefan problem of melting ice.** (a) The temperature $h(x,t)$ is shown in blue on the domain of the water $0 < x < s(t)$. The ice occupies the domain $s(t) < x < \infty$. The black arrow indicates the direction of the moving boundary when the ice is melting. (b) The solution $h(x,t)$ of the classic Stefan problem (1.3)–(1.5) is shown when $\kappa = 1$, $f(t) = -\exp(t)$ at $t = 0.2, 0.4, 0.6$ and 0.8, for initial conditions $u(x,0) = 0$. The black arrow indicates the direction of increasing time t.

We reformulate the Fisher-KPP equation to include a moving boundary such as the domain of the population is defined on $0 < x < s(t)$, where $s(t)$ is the position of the moving boundary. We use the Stefan condition from the classic Stefan problem [Crank 1987]. The classic Stefan problem is a boundary value problem that describes the evolution of the boundary between two phases during a change of phase at a constant temperature. We pose the Stefan problem as

$$\frac{\partial h}{\partial t} = \alpha \frac{\partial^2 h}{\partial x^2}, \tag{1.3}$$

$$\frac{\partial h(0,t)}{\partial x} = f(t), \quad h(s(t),t) = 0, \tag{1.4}$$

$$\frac{\mathrm{d}s(t)}{\mathrm{d}t} = -\kappa \frac{\partial h(s(t),t)}{\partial x}, \tag{1.5}$$

where $h(x,t)$ is the temperature function of position $0 < x < s(t)$ and time $t > 0$. The parameter $\alpha > 0$ is the thermal diffusivity in the heat equation (1.3). The condition $h(s(t),t) = 0$ at the interface represents the temperature of solidification or the temperature of fusion. The parameter in the Stefan condition (1.5) represents the quotient $K/(\rho l)$ where K is the thermal conductivity of the liquid, ρ is the density and l is the latent heat [Crank 1987]. The latent heat is the energy absorbed during the fusion of a solid or the energy released during the solidification of a liquid. We assume that $\kappa > 0$ if the latent heat is positive, as when ice is melting (Figure 1.2(a)). The Stefan condition (1.5) describes the heat balance at the interface of the liquid and the solid. The velocity of the moving boundary $s(t)$ is limited by the diffusion of heat in the liquid as the liquid supplies the energy to melt the solid. The solution of the problem depends on the function $f(t)$. Figure 1.2(a) shows the domain of the water and the direction of the moving boundary when the ice is melting. The initial condition used is $u(x,0) = 0$, corresponding to $s(0) = 0$. The flux of heat at $x = 0$ corresponds to $f(t) = -\exp(t)$, as used in (1.4) [Kutluay 1997]. Figure 1.2(b) shows how the temperature and the length of the domain of the liquid are evolving with time t increasing.

We aim to apply the idea behind the classic Stefan problem to the Fisher-KPP equation [Du and Lin 2010, Du and Guo 2011, Du and Guo 2012, Du et al. 2014a, Du et al. 2014b, Du and Lou 2015]. We define the dimensionless

boundary value problem as

$$\frac{\partial u}{\partial t} = \frac{\partial^2 u}{\partial x^2} + u(1-u), \tag{1.6}$$

$$\frac{\partial u(0,t)}{\partial x} = 0, \quad u(s(t),t) = u_{\mathrm{f}}, \tag{1.7}$$

$$\frac{\mathrm{d}s(t)}{\mathrm{d}t} = -\kappa \frac{\partial u(s(t),t)}{\partial x}, \tag{1.8}$$

where $u(x,t)$ is the density function of position $0 < x < s(t)$ and time $t > 0$, the parameter in the Stefan condition is κ, and the density at the position of the moving boundary is set to a constant $u_{\mathrm{f}} \in [0,1)$. As the model defined by equations (1.6)–(1.8) describes the evolution of the density for one population, we are also looking to define the model for two populations of cells, separated at their interface by a moving boundary.

The boundary value problem is represented in (1.6)–(1.8) with nondimensional variables. A parameter κ remains in the Stefan condition (1.8), originally applied to heat transfer problems. The novel use of this parameter in the context of biological applications implies some challenges. First, the role of the parameter κ in the resulting mathematical solution is yet to be fully understood. Second, the parameter κ has to be quantified experimentally. Many questions arise while defining κ in the boundary value problem (1.6)–(1.8). For example, is the parameter κ strictly positive? Usually, biological quantities, such as density, diffusivity and proliferation rate, are expected to be positive. We may consider first $\kappa > 0$. We may also examine the Stefan condition where the flux of density at the boundary multiplied by κ is proportionnal to the speed. The flux of density and the speed could be positive or negative. Consequently, could we consider κ to not be strictly positive? Do we have to apply limitations on the parameter κ to yield a solution where $u(x,t)$ is positive, so that the density has a biological meaning? We expect this work to build gradually solid mathematicals results in order to open the door to experimental estimations of the parameter κ.

Single-species invasion equations such as the Fisher-KPP equation and Porous-Fisher equations do not describe explicitly the interactions between the invading populations and their environment [Painter and Sherratt 2003]. We know, for example, that tumour cells induce a change in the pH of the micro-environment of the host tissue [Gatenby and Gawlinski 1996, Astanin

and Preziosi 2009]. Gatenby and Gatwinski proposed a complex model of three differential equations that describes the dynamics between acid, tumour and host populations [Gatenby and Gawlinski 1996]. The model shows how the production of acid by tumour cells is detrimental to the skin and promotes cancer invasion. Another type of interaction between populations describes the production of an extracellular matrix that benefits the growth of a tissue [Browning et al. 2021]. We aim to include the analysis of a novel model of acid-mediated invasion [Browning et al. 2019], and a model of substrate-mediated invasion [Browning et al. 2021] to this study.

When studying a mathematical model of biological invasion, we look for the travelling wave solution. However, it is not always possible to determine the exact solution of a differential equation or a system of differential equations. For example, the travelling wave solution of the Fisher-KPP equation has known exact solutions for $c = 0$ and for $c = \pm 5/\sqrt{6}$ [Murray 2002, McCue et al. 2021a]. There is many numerical schemes that we can use to solve differential equations. The Newton-Raphson method is a numerical method that we use to solve the nonlinear partial differential equation, such as the Fisher-KPP equation. A combination of phase plane and perturbation analysis can also be used to explore the solutions of the governing equations that we are studying. As the phase plane analysis has a pivotal role in this thesis, we give a summary of some results obtained from the phase plane analysis of the Fisher-KPP equation and the Porous-Fisher equation [Murray 2002].

The phase plane dynamical system of the Fisher-KPP equation is obtained after expressing the dimensionless equation with respect to the travelling wave coordinate $z = x - ct$, such as

$$\frac{\mathrm{d}U}{\mathrm{d}z} = V, \quad \frac{\mathrm{d}V}{\mathrm{d}z} = -cV - U(1 - U). \tag{1.9}$$

The linearisation around equilibrium points $(U, V) = (1, 0)$ and $(U, V) = (0, 0)$ indicates that equilibrium point $(1, 0)$ is a saddle and that equilibrium point $(0, 0)$ is a stable node, if $c > c_{\min}$ and a stable spiral, if $c < c_{\min}$, where the dimensionless wave speed $c_{\min} = 2$. Figure 1.3 shows the phase portrait of dynamical system of equations (1.9). The travelling wave solution is an heteroclinic orbit leaving the saddle $(1, 0)$ and entering the stable node $(0, 0)$ when $c \geq c_{\min}$, as in Figure 1.3(a)–(b). We also show the heteroclinic orbit

Figure 1.3: Phase plane of Fisher-KPP system (1.9). (a) Heteroclinic orbit in solid green, where $c > c_{\min}$. (b) Heteroclinic orbit in solid green, where $c = c_{\min}$. (b) Heteroclinic orbit in dashed green, where $c < c_{\min}$. The minimum speed is $c_{\min} = 2$. The black disks represent equilibrium points $(1,0)$ and $(0,0)$.

leaving the saddle $(1,0)$ and spiralling around equilibrium point $(0,0)$ when $c < c_{\min}$ in dashed green in Figure 1.3(c), that is usually completely discarded as a part of trajectory goes into quadrants where $U(z) < 0$.

The phase plane system of Porous-Fisher equation is usually studied after removing the singularity at $U = 0$ by rescaling the travelling wave coordinate, using $\zeta(z) = \int_0^z \mathrm{d}y/U(y)$ [Murray 2002], such as

$$\frac{\mathrm{d}U}{\mathrm{d}\zeta} = UV \quad \frac{\mathrm{d}V}{\mathrm{d}\zeta} = -cV - V^2 - U(1-U). \tag{1.10}$$

By looking at the linearisation around equilibrium points $(U,V) = (0,0)$, $(U,V) = (1,0)$ and $(U,V) = (0,-c)$, from the desingularised system (1.10), one solution is an heteroclinic orbit leaving the saddle $(1,0)$ and entering the stable node $(0,0)$, as shown in Figure 1.4(a). An exact solution can be found by taking the trajectory that is a straight line between the equilibrium point $(1,0)$ and the saddle $(0,-c)$, as shown in Figure 1.4(b). We can write the line equation $V = -c_{\min}(1 - U)$ that we substitute in $\mathrm{d}V/\mathrm{d}U = [-cV - V^2 - U(1-U)]/(UV)$ to determine the minimum speed $c_{\min} = 1/\sqrt{2}$. Solving $\mathrm{d}U/\mathrm{d}z = -[1 - U(z)]/\sqrt{2}$, we obtain the exact solution

$$U(z) = \begin{cases} 1 - \exp\left(\dfrac{z - z_c}{\sqrt{2}}\right) & z < z_c, \\ 0 & z > z_c, \end{cases} \tag{1.11}$$

where the z_c is the chosen position of the front of the sharp travelling wave solution. When $c < c_{\min}$, no heteroclinic orbit can be found leaving the saddle $(1,0)$. As shown in Figure 1.4(c), the trajectory leaving the saddle $(1,0)$ goes to $U(\zeta) \to -\infty$.
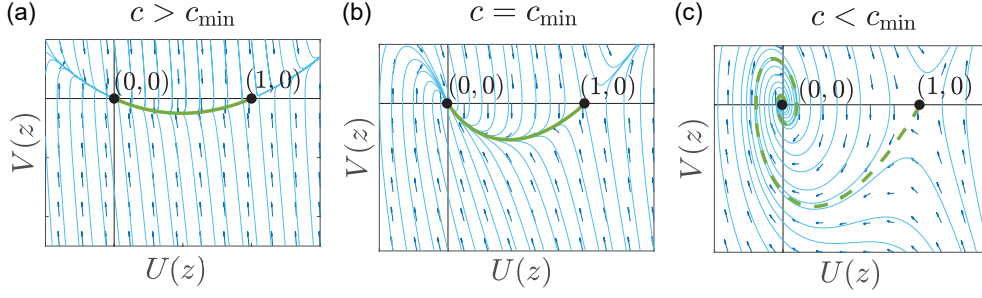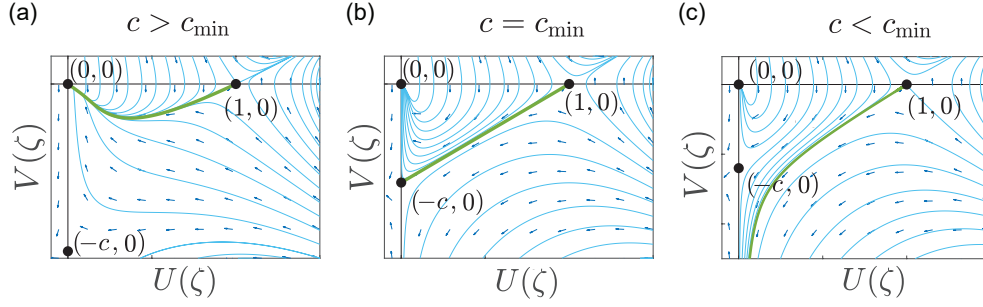
Figure 1.4: Phase plane of Porous-Fisher system (1.10). (a) Heteroclinic orbit in solid green, when $c > c_{\min}$. (b) Heteroclinic orbit in solid green, when $c = c_{\min}$. (b) Phase portrait when $c < c_{\min}$, no heteroclinic orbit between equilibrium points. The minimum speed is $c_{\min} = 1/\sqrt{2}$. The black disks represent equilibrium points $(1, 0)$, $(0, -c)$ and $(0, 0)$.

1.2 Research questions

1. **What features of biological invasion are enabled in the travelling solution of the Fisher-KPP model reformulated with a moving boundary?**

   The Fisher-KPP model supports a travelling wave solution that represent some features of biological invasion: the moving front has a speed proportional to the diffusivity and to the proliferation rate, such as $c_{\min} = 2\sqrt{\lambda D}$. The Fisher-KPP model fails to represent a moving front where the population occupies a well defined domain and where the density falls at zero at the moving front ($u_{\mathrm{f}} = 0$). Moreover, the model cannot represent the stalling or the extinction of a population.

   We reformulate the Fisher-KPP model with a moving boundary. A Stefan condition relates the speed of the moving front to a proportion ($\kappa > 0$) of the loss of population at the boundary. We suppose that the reformulated model, that we call the Fisher-Stefan model, gives rise to a travelling solution with compact support, and we want to understand the relationship between the wave speed and the condition at the moving boundary. We also want to understand what conditions in the model lead to extinction.

2. **How does the parameter κ in the Stefan condition modify the type of travelling wave solution in the Fisher-Stefan model?**

   The Fisher-Stefan model admits a travelling wave solution with a sharp front where the wave speed depends on the parameter κ. In the first

research question, we set $\kappa > 0$ to obtain a positive travelling wave speed. A receding biological population, that is leaving a domain previously occupied, is represented by a travelling wave solution with speed $c < 0$. We expect the Fisher-Stefan model to give rise to a travelling wave solution with speed $c < 0$ when $\kappa < 0$. The model could represent both biological invasion and recession. We aim to determine the role and the limits of the parameter κ .

3. **How does the density u_{f} in the Stefan condition modify the speed and the shape of the travelling wave solution in the Fisher-Stefan model?**

   The Stefan condition relates the speed of the moving front to a proportion (κ) of the loss of population at the boundary. By default, in the two previous research questions, we set the density to fall at zero at the moving boundary. The travelling solution obtained in the two previous research questions represents either the invasion or the recession of the population. In this question, we explore the effect of setting the density of population at the moving boundary to a positive value, such as $u_{\mathrm{f}} \in [0, 1)$. This condition can be seen as if the moving front is invading a domain where there is a pre-existent density of population or as if the moving front is receding and leaving a remaining population in the previously fully occupied domain. We want to determine the relationship between the wave speed c, the parameter κ and the density of population u_{f} at the moving front.

4. **What features of biological invasion are enabled in a model of two populations, where the dynamics of each population is described by Fisher-KPP equation, and where the two populations are separated by a moving boundary?**

Real biological population of cells invade a domain occupied by another population, as when cancer cells invade a host tissue. We propose a novel mathematical model of malignant invasion consisting of a two-phase moving boundary problem where the cells in each population undergo diffusive migration and logistic proliferation. The populations are separated by an interface that moves according to a two-phase Stefan condition. We expect the solution of the moving boundary model to describe a sharp moving front between the cancer and surrounding tissues. We aim to understand the relationship between the travelling wave solution, and the parameters of the model: the relative diffusivity, the relative proliferation rate and the parameters in the Stefan condition.

5. **How does the travelling wave solution that represents acid-mediated cancer invasion into skin is influenced by the degradation rate of the skin and the far field density of the skin?**

Single-species models, like the Fisher-KPP model and the one-phase Fisher-Stefan model, support travelling wave solutions but do not explicitly describe interactions between the invading population and the surrounding environment. We study a model of two coupled differential equations to represent the acid-mediated cancer invasion into surrounding tissues. The first equation relates the rate of change of density of cancer population to the nonlinear diffusion and the proliferation of the cancer cells. The second equation relates the rate of change of density of skin population to the degradation of the skin by cancer cells. We aim to understand how the characteristics of the travelling wave solution representing invasion depend on two factors: the degradation rate γ of the skin by cancer cells and the far-field density $\mathcal{V}$ of the skin density of population ahead of the moving front.

6. **How does the travelling wave solution that represents substrate-mediated cellular invasion is influenced by the rates of production and decay of substrate?**

The migration and proliferation of healthy cells into a surrounding environment can be associated to the production of a substrate. The phenomenon is observed in tissue engineering when osteoblast precursor cells are transplanted on bioscaffolds. The cells invade the structure of the bioscaffold and bridge the pore within the scaffold. A single-species model able to represent the substrate-mediated invasion is the modified Fisher-KPP model that includes a degenerate diffusivity. The exponent in the power law function of the degenerate diffusivity is still to be determined, which can makes the model complicated to apply. An other limitation of the single-species model is the inadequacy to describe explicitly the interactions between the tissue and the substrate.

We study two coupled differential equations that describe the dynamics of substrated-mediated tissue invasion. The first equation relates the rate of change of tissue density to the density-dependant diffusion of the cells and to the growth of the tissue. The second equation relates the rate of change of the substrate density to the production of substrate by the tissue cells and to the decay of the substrate. We aim to understand how the characteristics of the travelling wave solution depend on two factors: the rate of production r_1 of substrate by tissue cells and the degradation rate r_2 of the substrate.

1.3   Objectives and outcome

We divide the research investigation into six objectives, listed as follows:

- Objective 1: Determine the relationship between Fisher-KPP and Fisher-Stefan models using numerical computation, phase plane analysis, perturbation analysis, focussing on travelling wave solutions.

- Objective 2: Build upon Objective 1 to develop and analyse a Fisher-Stefan model to represent the invasion and the recession of one population of cells.

- Objective 3: Build upon Objective 1 and 2 to develop and analyse a generalised Fisher-Stefan model to represent the invasion and the recession of one population of cells with any value of wave speed.

- Objective 4: Extend Objective 1 to develop and analyse a Fisher-Stefan model for two different populations of cell, separated by a moving boundary.

- Objective 5: Determine the features of travelling wave solutions of acid-mediated cancer-skin model of invasion and the relationship to Fisher-KPP model using a combination of numerical simulation, phase plane analysis and perturbation techniques.

- Objective 6: Determine the features of travelling wave solutions of substrate-mediated model of invasion and the relationship to Porous-Fisher model using a combination of numerical simulation, phase plane analysis and perturbation techniques.

The outcome of this thesis by publication consists of four published articles in different peer-reviewed journals and two manuscripts submitted for publication. The journals selected are ranked Q1 or Q2. We present the list of articles by order of appearance in the document. Items in the list of publications numbered from 1 to 6 correspond respectively to chapters numbered from 2 to 7.

1. El-Hachem M, McCue SW, Jin W, Du Y, Simpson MJ (2019) Revisiting the Fisher-Kolmogorov-Petrovsky-Piskunov equation to interpret the spreading-extinction dichotomy. *Proceedings of the Royal Society A* **475**, 20190378. (10.1098/rspa.2019.0378).

Abstract The Fisher-Kolmogorov-Petrovsky-Piskunov model, also known as the Fisher-KPP model, supports travelling wave solutions that are successfully used to model numerous invasive phenomena with applications in biology, ecology, and combustion theory. However, there are certain phenomena that the Fisher-KPP model cannot replicate, such as the extinction of invasive populations. The Fisher-Stefan model is an adaptation of the Fisher-KPP model to include a moving boundary whose evolution is governed by a Stefan condition. The Fisher-Stefan model also supports travelling wave solutions; however, a key

additional feature of the Fisher-Stefan model is that it is able to simulate population extinction, giving rise to a *spreading-extinction dichotomy*. In this work, we revisit travelling wave solutions of the Fisher-KPP model and show that these results provide new insight into travelling wave solutions of the Fisher-Stefan model and the spreading-extinction dichotomy. Using a combination of phase plane analysis, perturbation analysis and linearisation, we establish a concrete relationship between travelling wave solutions of the Fisher-Stefan model and often-neglected travelling wave solutions of the Fisher-KPP model. Furthermore, we give closed-form approximate expressions for the shape of the travelling wave solutions of the Fisher-Stefan model in the limit of slow travelling wave speeds, $c \ll 1$

2. El-Hachem M, McCue SW, Simpson MJ (2021) Invading and receding sharp-fronted travelling waves. *Bulletin of Mathematical Biology* **83**, 35. (doi:10.1007/s11538-021-00862-y).

Abstract Biological invasion, whereby populations of motile and proliferative individuals lead to moving fronts that invade vacant regions, are routinely studied using partial differential equation (PDE) models based upon the classical Fisher-KPP equation. While the Fisher-KPP model and extensions have been successfully used to model a range of invasive phenomena, including ecological and cellular invasion, an often-overlooked limitation of the Fisher-KPP model is that it cannot be used to model biological recession where the spatial extent of the population decreases with time. In this work we study the *Fisher-Stefan* model, which is a generalisation of the Fisher-KPP model obtained by reformulating the Fisher-KPP model as a moving boundary problem. The nondimensional Fisher-Stefan model involves just one parameter, κ, which relates the shape of the density front at the moving boundary to the speed of the associated travelling wave, c. Using numerical simulation, phase plane and perturbation analysis, we construct approximate solutions of the Fisher-Stefan model for both slowly invading and receding travelling waves, as well as for rapidly receding travelling waves. These approximations allow us to determine the relationship between c and κ so that commonly-reported experimental estimates of c can be used to provide estimates of the unknown parameter κ. Interestingly, when we reinterpret the Fisher-KPP model as a moving boundary problem, many disregarded features of the classical Fisher-KPP phase plane

take on a new interpretation since travelling waves solutions with $c < 2$ are normally disregarded. This means that our analysis of the Fisher-Stefan model has both practical value and an inherent mathematical value.

3. El-Hachem M, McCue SW, Simpson MJ (2021) Non-vanishing sharp-fronted travelling wave solutions of the Fisher-Kolmogorov model. Accepted for publication in *Mathematical Medecine and Biology*. (arXiv: 2107.05210).

Abstract The Fisher-KPP model, and generalisations thereof, involve simple reaction-diffusion equations for biological invasion that assume individuals in the population undergo linear diffusion with diffusivity D, and logistic proliferation with rate λ. For the Fisher-KPP model, biologically-relevant initial conditions lead to long-time travelling wave solutions that move with speed $c = 2\sqrt{\lambda D}$. Despite these attractive features, there are several biological limitations of travelling wave solutions of the Fisher-KPP model. First, these travelling wave solutions do not predict a well-defined invasion front. Second, biologically-relevant initial conditions lead to travelling waves that move with speed $c = 2\sqrt{\lambda D} > 0$. This means that, for biologically-relevant initial data, the Fisher-KPP model can not be used to study invasion with $c \neq 2\sqrt{\lambda D}$, or retreating travelling waves with $c < 0$. Here, we reformulate the Fisher-KPP model as a moving boundary problem and show that this reformulated model alleviates the key limitations of the Fisher-KPP model. Travelling wave solutions of the moving boundary problem predict a well-defined front that can propagate with *any* wave speed, $-\infty < c < \infty$. Here, we establish these results using a combination of high-accuracy numerical simulations of the time-dependent partial differential equation, phase plane analysis and perturbation methods. All software required to replicate this work is available on GitHub.

4. El-Hachem M, McCue SW, Simpson MJ (2020) A sharp-front moving boundary model for malignant invasion. *Physica D: Nonlinear Phenomena* **412**, 132639. (doi:10.1016/j.physd.2020.132639).

Abstract We analyse a novel mathematical model of malignant invasion which takes the form of a two-phase moving boundary problem describing the invasion of a population of malignant cells into a population of background tissue, such as skin. Cells in both populations undergo diffusive migration and

logistic proliferation. The interface between the two populations moves according to a two-phase Stefan condition. Unlike many reaction-diffusion models of malignant invasion, the moving boundary model explicitly describes the motion of the sharp front between the cancer and surrounding tissues without needing to introduce degenerate nonlinear diffusion. Numerical simulations suggest the model gives rise to very interesting travelling wave solutions that move with speed c, and the model supports both malignant invasion and malignant retreat, where the travelling wave can move in either the positive or negative x-directions. Unlike the well-studied Fisher-Kolmogorov and Porous-Fisher models where travelling waves move with a minimum wave speed $c \geq c^* > 0$, the moving boundary model leads to travelling wave solutions with $|c| < c^{**}$. We interpret these travelling wave solutions in the phase plane and show that they are associated with several features of the classical Fisher-Kolmogorov phase plane that are often disregarded as being nonphysical. We show, numerically, that the phase plane analysis compares well with long time solutions from the full partial differential equation model as well as providing accurate perturbation approximations for the shape of the travelling waves.

5. El-Hachem M, McCue SW, Simpson MJ (2021) Travelling wave analysis of cellular invasion into surrounding tissues. *Physica D: Nonlinear Phenomena* **428**, 133026. (doi:10.1016/j.physd.2021.133026).

Abstract Single-species reaction-diffusion equations, such as the Fisher-KPP and Porous-Fisher equations, support travelling wave solutions that are often interpreted as simple mathematical models of biological invasion. Such travelling wave solutions are thought to play a role in various applications including development, wound healing and malignant invasion. One criticism of these single-species equations is that they do not explicitly describe interactions between the invading population and the surrounding environment. In this work we study a reaction-diffusion equation that describes malignant invasion which has been used to interpret experimental measurements describing the invasion of malignant melanoma cells into surrounding human skin tissues [Browning et al. 2019]. This model explicitly describes how the population of cancer cells degrade the surrounding tissues, thereby creating free space into which the cancer cells migrate and proliferate to form an invasion wave of malignant tissue that is coupled to a retreating wave of skin tissue. We analyse travel-

ling wave solutions of this model using a combination of numerical simulation, phase plane analysis and perturbation techniques. Our analysis shows that the travelling wave solutions involve a range of very interesting properties that resemble certain well-established features of both the Fisher-KPP and Porous-Fisher equations, as well as a range of novel properties that can be thought of as extensions of these well-studied single-species equations.

6. El-Hachem M, McCue SW, Simpson MJ (2022) A continuum mathematical model of substrate-mediated tissue growth. *Bulletin of Mathematical Biology* **84**, 49. (doi: 10.1007/s11538-022-01005-7).

Abstract We consider a continuum mathematical model of biological tissue formation inspired by recent experiments describing thin tissue growth in 3D–printed bioscaffolds. The continuum model involves a partial differential equation describing the density of tissue, $\hat{u}(\hat{\mathbf{x}}, \hat{t})$, that is coupled to the concentration of an immobile extracellular substrate, $\hat{s}(\hat{\mathbf{x}}, \hat{t})$. Cell migration is modelled with a nonlinear diffusion term, where the diffusive flux is proportional to $\hat{s}$, while a logistic growth term models cell proliferation. The extracellular substrate $\hat{s}$ is produced by cells, and undergoes linear decay. Preliminary numerical simulations show that this mathematical model, which we call the *substrate model*, is able to recapitulate key features of recent tissue growth experiments, including the formation of sharp fronts. To provide a deeper understanding of the model we then analyse travelling wave solutions of the substrate model, showing that the model supports both sharp-fronted travelling wave solutions that move with a minimum wave speed, $c = c_{\min}$, as well as smooth-fronted travelling wave solutions that move with a faster travelling wave speed, $c > c_{\min}$. We provide a geometric interpretation that explains the difference between smooth- and sharp-fronted travelling wave solutions that is based on a slow manifold reduction of the desingularised three-dimensional phase space. In addition to exploring the nature of the smooth- and sharp-fronted travelling waves, we also develop and test a series of useful approximations that describe the shape of the travelling wave solutions in various limits. These approximations apply to both the sharp–fronted travelling wave solutions, and the smooth-fronted travelling wave solutions.

1.4 Structure of the thesis

Each chapter following the introduction corresponds to one publication or one manuscript submitted for publication. As each publication presented is independent of the others, the chapters may overlap each other when presenting the equations or the methods.

Chapter 2 addresses the first research question that corresponds to objective 1. The literature review is about biological invasion and the classic one-phase Stefan problem. The Fisher-Stefan model is described with a density $u_{\mathrm{f}} = 0$ at the moving boundary. Time-dependant numerical solutions of the model are shown. A phase plane analysis of both Fisher-KPP and Fisher-Stefan models is given to compare the features of their solutions. An important result is derived: the relationship between the wave speed c and the parameter κ of the Stefan condition. The spreading-extinction dichotomy is demonstrated. Additional material gives the details about the numerical methods used, including the numerical method to solve a moving boundary problem.

Chapter 3 addresses the second research question that corresponds to objective 2. A literature review is presented on the Fisher-Stefan model and on biological recession. The previous Fisher-Stefan model from chapter 2 is modified to include $\kappa < 0$. Both receding and invading travelling waves solutions are obtained from the model. A phase plane and perturbation analysis give the solutions in some interesting limits. The numerical methods are given in the last section. The PDE solver used is the same as in Chapter 2.

Chapter 4 addresses the third research question that corresponds to objective 3. A literature review is presented on the limitation of Fisher-KPP and Porous-Fisher models. The Fisher-Stefan model is generalised to include a density $u_{\mathrm{f}} \in [0, 1)$ at the moving boundary. Slow and fast, receding and invading travelling waves solutions are obtained from the model. Phase plane and perturbation analysis give an accurate relationship between the wave speed c and κ in some important limits. The numerical method for solving the PDE on a non uniform mesh is given in the last section, that includes additional results.

Chapter 5 addresses the fourth research question that corresponds to objective 4. A literature review is presented on skin-cancer invasion and the

Fisher-Stefan problem. The two-phase moving boundary model is posed. Numerical solutions of the model are presented in either the positive or the negative direction. The solutions are also studied in the phase plane. The last section gives the numerical methods to solve the two-phase moving boundary problem. The last section also gives additional results in the phase plane.

Chapter 6 addresses the fifth research question that corresponds to objective 5. A literature review is presented on models of acid-mediated cancer invasion. The model is presented with time-dependant solutions that evolve to travelling waves. A phase plane analysis compares the features of travelling wave solution of the model with the Fisher-KPP model. The relationship of the minimal speed with the density of the skin in the far field, $\mathcal{V}$ is obtained numerically. Some interesting limits, such as when the decay rate of the skin $\gamma \gg 1$, are studied with perturbation analysis. A dispersion relationship is derived and validated. The last section gives the numerical methods to solve the system of coupled partial differential equations.

Chapter 7 addresses the fifth research question that corresponds to objective 6. A literature review is presented on tissue growth in printed bioscaffolds and different models describing the interaction between populations. Smooth and sharp fronted travelling wave solutions are presented in the physical plane. The relationship between the minimum wave speed and the production and decay rates of the substrate, r_1 and r_2, is obtained numerically. An exhaustive phase plane/space analysis demonstrates the existence of the minimum speed. A comparison is made with Porous-Fisher equation when $r_1 \gg 1$ and when $r_2 \gg 1$. A perturbation solution is given for fast smooth-fronted travelling wave solutions.

We conclude the thesis in Chapter 8 that gives a summary of the research and describes the future work to be done. At the end of the document, the bibliography lists all the references by alphabetical order of first author.

1.5 Statement of joint authorship

This thesis consists of four published articles in different peer-reviewed journals and of two manuscripts submitted for publication. The PhD candidate has contributed substantively to all six manuscripts. We present a summary of the contribution of the PhD candidate and the co-authors for each manuscript, in

this section. The listed description of the contributions has been approved by all co-authors.

Chapter 2: Revisiting the Fisher-Kolmogorov-Petrovsky-Piskunov equation to interpret the spreading-extinction dichotomy

The corresponding article is:

El-Hachem M, McCue SW, Jin W, Du Y, Simpson MJ (2019) Revisiting the Fisher-Kolmogorov-Petrovsky-Piskunov equation to interpret the spreading-extinction dichotomy. *Proceedings of the Royal Society A* **475**, 20190378. (10.1098/rspa.2019.0378).

Statement of joint authorship:

- Maud El-Hachem conceived and designed the study, performed all numerical and symbolic calculations, drafted the article, and gave final approval for publication.

- Scott W McCue conceived and designed the study, gave final approval for publication.

- Jin Wang conceived and designed the study, gave final approval for publication.

- Yihong Du conceived and designed the study, gave final approval for publication.

- Matthew J Simpson conceived and designed the study, gave final approval for publication.

Chapter 3: Invading and receding sharp-fronted travelling waves

The corresponding article is:

El-Hachem M, McCue SW, Simpson MJ (2021) Invading and receding sharp-fronted travelling waves. *Bulletin of Mathematical Biology* **83**, 35. (doi:10.1007/s11538-021-00862-y).

Statement of joint authorship:

- Maud El-Hachem conceived and designed the study, performed all numerical and symbolic calculations, drafted the article, and gave final approval for publication.

- Scott W McCue conceived and designed the study, gave final approval for publication.

- Matthew J Simpson conceived and designed the study, gave final approval for publication.

Chapter 4: Non-vanishing sharp-fronted travelling wave solutions of the Fisher-Kolmogorov model.

The corresponding article is:

El-Hachem M, McCue SW, Simpson MJ (2021) Non-vanishing sharp-fronted travelling wave solutions of the Fisher-Kolmogorov model. Accepted for publication in *Mathematical Medecine and Biology*. (arXiv: 2107.05210).

Statement of joint authorship:

- Maud El-Hachem conceived and designed the study, performed all numerical and symbolic calculations, drafted the article, and gave final approval for publication.

- Scott W McCue conceived and designed the study, gave final approval for publication.

- Matthew J Simpson conceived and designed the study, gave final approval for publication.

Chapter 5: A sharp-front moving boundary model for malignant invasion

The corresponding article is:

El-Hachem M, McCue SW, Simpson MJ (2020). A sharp-front moving boundary model for malignant invasion. *Physica D: Nonlinear Phenomena* **412**, 132639. (doi:10.1016/j.physd.2020.132639)

- Maud El-Hachem conceived and designed the study, performed all numerical and symbolic calculations, drafted the article, and gave final approval for publication.

- Scott W McCue conceived and designed the study, gave final approval for publication.

- Matthew J Simpson conceived and designed the study, gave final approval for publication.

Chapter 6: Travelling wave analysis of cellular invasion into surrounding tissues

The corresponding article is:

El-Hachem M, McCue SW, Simpson MJ (2021) Travelling wave analysis of cellular invasion into surrounding tissues. *Physica D: Nonlinear Phenomena* **428**, 133026. (10.1016/j.physd.2020.132639)

Statement of joint authorship:

- Maud El-Hachem conceived and designed the study, performed all numerical and symbolic calculations, drafted the article, and gave final approval for publication.

- Scott W McCue conceived and designed the study, gave final approval for publication.

- Matthew J Simpson conceived and designed the study, gave final approval for publication.

Chapter 7: A continuum mathematical model of substrate-mediated tissue growth

The corresponding article is: El-Hachem M, McCue SW, Simpson MJ (2022) A continuum mathematical model of substrate-mediated tissue growth. *Bulletin of Mathematical Biology* **84**, 49. (doi: 10.1007/s11538-022-01005-7).

Statement of joint authorship:

- Maud El-Hachem conceived and designed the study, performed all numerical and symbolic calculations except for the 2D model, drafted the article, and gave final approval for publication.

- Scott W McCue conceived and designed the study, performed the mathematical analysis, drafted the article, and gave final approval for publication.

- Matthew J Simpson conceived and designed the study, performed the mathematical analysis and numerical calculations for the 2D model, drafted the article and gave final approval for publication.

Chapter 2

Revisiting the Fisher-KPP equation to interpret the spreading-extinction dichotomy

Statement of Contribution of Co-Authors for
Thesis by Published Paper

The following is the suggested format for the required declaration provided at the start of any thesis chapter which includes a co-authored publication.

The authors listed below have certified that:

1. they meet the criteria for authorship and that they have participated in the conception, execution, or interpretation, of at least that part of the publication in their field of expertise;
2. they take public responsibility for their part of the publication, except for the responsible author who accepts overall responsibility for the publication;
3. there are no other authors of the publication according to these criteria;
4. potential conflicts of interest have been disclosed to (a) granting bodies, (b) the editor or publisher of journals or other publications, and (c) the head of the responsible academic unit, and
5. they agree to the use of the publication in the student's thesis and its publication on the QUT's ePrints site consistent with any limitations set by publisher requirements.

In the case of this chapter 2:

Please state the publication title and date of publication or status:
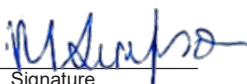
El-Hachem M, McCue SW, Jin W, Du Y, Simpson MJ, 2019. Revisiting the Fisher-Kolmogorov-Petrovsky-Piskunov equation to interpret the spreading-extinction dichotomy. *Proceedings of the Royal Society A* **475**, 20190378. Published on 4 September 2019.

Contributor	Statement of contribution*
Maud El-Hachem *Maud El-Hachem* 15/11/2021	Conceived and designed the study, performed all numerical and symbolic calculations, drafted the article and gave final approval for publication.
Scott W McCue	Conceived and designed the study, gave final approval for publication.
Wang Jin	Conceived and designed the study, gave final approval for publication.
Yihong Du	Conceived and designed the study, gave final approval for publication.
Matthew J Simpson	Conceived and designed the study, gave final approval for publication.

Principal Supervisor Confirmation

I have sighted email or other correspondence from all Co-authors confirming their certifying authorship. (If the Co-authors are not able to sign the form please forward their email or other correspondence confirming the certifying authorship to the GRC).

Professor Matthew Simpson   *[signature]*   16/11/2021
Name   Signature   Date

2.1 Abstract

The Fisher–Kolmogorov–Petrovsky–Piskunov model, also known as the Fisher-KPP model, supports travelling wave solutions that are successfully used to model numerous invasive phenomena with applications in biology, ecology, and combustion theory. However, there are certain phenomena that the Fisher-KPP model cannot replicate, such as the extinction of invasive populations. The Fisher-Stefan model is an adaptation of the Fisher-KPP model to include a moving boundary whose evolution is governed by a Stefan condition. The Fisher-Stefan model also supports travelling wave solutions; however, a key additional feature of the Fisher-Stefan model is that it is able to simulate population extinction, giving rise to a *spreading-extinction dichotomy*. In this work, we revisit travelling wave solutions of the Fisher-KPP model and show that these results provide new insight into travelling wave solutions of the Fisher-Stefan model and the spreading-extinction dichotomy. Using a combination of phase plane analysis, perturbation analysis and linearisation, we establish a concrete relationship between travelling wave solutions of the Fisher-Stefan model and often-neglected travelling wave solutions of the Fisher-KPP model. Furthermore, we give closed-form approximate expressions for the shape of the travelling wave solutions of the Fisher-Stefan model in the limit of slow travelling wave speeds, $c \ll 1$.

2.2 Introduction

The Fisher-KPP model [Aronson and Weinberg 1978, Fisher 1937, Kolmogorov et al. 1937, Canosa 1973, Murray 2002, Grindrod 2007] is a one-dimensional reaction-diffusion equation combining linear diffusion with a nonlinear logistic source term,

$$\frac{\partial \tilde{u}}{\partial \tilde{t}} = \tilde{D}\frac{\partial^2 \tilde{u}}{\partial \tilde{x}^2} + \tilde{\lambda}\tilde{u}\left(1 - \frac{\tilde{u}}{\tilde{K}}\right), \tag{2.1}$$

where $\tilde{u}(\tilde{x}, \tilde{t}) \geq 0$ is the population density that depends on position $\tilde{x} \geq 0$, and time $\tilde{t} > 0$. The dimensional parameters in Fisher-KPP model are the diffusivity $\tilde{D} > 0$, the proliferation rate $\tilde{\lambda} > 0$ and the carrying capacity density $\tilde{K} > 0$. Solutions of the Fisher-KPP model on a semi-infinite domain that evolve from initial conditions with compact support asymptote to a travelling wave with a minimum wave speed, $\tilde{c}_{\min} = 2\sqrt{\tilde{\lambda}\tilde{D}}$ in the long time limit, $\tilde{t} \to$

25

∞ [Aronson and Weinberg 1978, Fisher 1937, Kolmogorov et al. 1937, Canosa 1973, Murray 2002, Grindrod 2007]. The Fisher-KPP model also gives rise to travelling wave solutions with $\tilde{c} > \tilde{c}_{\min}$ for initial conditions that decay sufficiently slowly as $\tilde{x} \rightarrow \infty$ [Aronson and Weinberg 1978, Fisher 1937, Kolmogorov et al. 1937, Canosa 1973, Murray 2002, Grindrod 2007], although for most practical applications we are interested in travelling wave solutions that move with the minimum wave speed since initial conditions with compact support are more often relevant [Maini et al. 2004a, Maini et al. 2004b, Simpson et al. 2013, Sherratt and Murray 1990].

The Fisher-KPP model and its extensions have been used successfully in a wide range of applications including the study of spatial spreading of invasive species in ecology [Skellam 1951, Shigesada et al. 1951, Steel et al. 1998, Levin et al. 2003]. In cell biology, the spatial spreading of invasive cell populations has been modelled using the Fisher-KPP model and its extensions for a range of applications including *in vitro* cell biology experiments [Cai et al. 2007, Sengers et al. 2007, Tremel et al. 2009, Nardini et al. , Warne et al. 2019, Vo et al. 2015] and *in vivo* malignant spreading [Swanson et al. 2003, Swanson et al. 2008, Pérez-Beteta et al. 2018]. Other areas of application include combustion theory [Mercer and Weber 1995, Tang et al. 1993] and bushfire invasion [Forbes 1997]. Some of the extensions of the Fisher-KPP model involve working with different geometries [Simpson et al. 2013, Sengers et al. 2007], such as inward and outward spreading in geometries with [Treloar et al. 2014] and without [Jin et al. 2018] radial symmetry. Other variations include: (i) considering models with nonlinear diffusivity [King and McCabe 2003, Sánchez-Garduño and Maini 1994, McCue et al. 2019, Simpson et al. 2006, Witelski 1995, Sherratt and Marchant 1996]; (ii) incorporating different nonlinear transport mechanisms [Perumpanani et al. 1999, Marchant et al. 2001, Landman et al. 2005]; (iii) models of multiple invading subpopulations [Simpson et al. 2006, Painter and Sherratt 2003]; and (iv) multi-dimensional models incorporating anisotropy [Painter and Hillen 2013]. The Fisher-KPP model gives rise to travelling wave-like solutions that do not allow the solution to go extinct. A cartoon of this kind of behaviour is shown schematically in Figure 2.1(a)-(c) where an invading cell population will propagate indefinitely on a semi-infinite domain. In contrast, the schematic in Figure 2.1(d)-(f) shows a

different outcome where the same initial condition evolves in such a way that the population eventually becomes extinct.
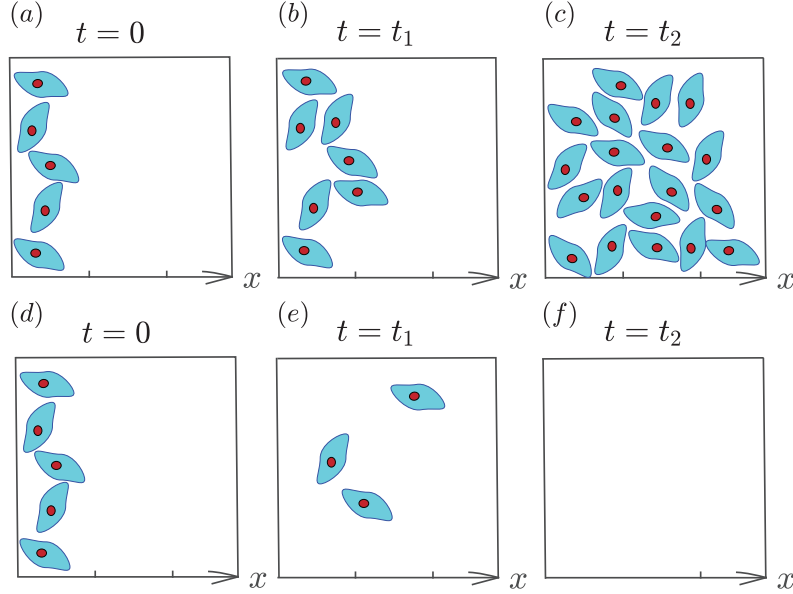
Figure 2.1: Schematic showing the evolution of a cell population. *(a)-(c)* The evolution of an invading cell population at $t = 0$, t_1, and t_2, with $t_2 > t_1 > 0$. In this case the population invades in the positive x direction indefinitely, provided that the domain is infinite. *(d)-(f)* The evolution of a cell population at $t = 0$, t_1, and t_2, with $t_2 > t_1 > 0$. In this case the population tends to extinction. Note that we have deliberately made the initial distribution of cells in *(a)* and *(d)* identical.

We are concerned here with the Fisher-Stefan model [Du and Lin 2010, Du and Guo 2011, Bunting et al. 2012, Du and Guo 2012, Du et al. 2014a, Du et al. 2014b, Du and Lou 2015]

$$\frac{\partial \tilde{u}}{\partial \tilde{t}} = \tilde{D}\frac{\partial^2 \tilde{u}}{\partial \tilde{x}^2} + \tilde{\lambda}\tilde{u}\left(1 - \frac{\tilde{u}}{\tilde{K}}\right), \tag{2.2}$$

$$\frac{\partial \tilde{u}}{\partial \tilde{x}} = 0 \quad \text{at} \quad \tilde{x} = 0, \tag{2.3}$$

$$\tilde{u}(\tilde{L}(\tilde{t}), \tilde{t}) = 0 \tag{2.4}$$

$$\frac{\mathrm{d}\tilde{L}(\tilde{t})}{\mathrm{d}\tilde{t}} = -\tilde{\kappa}\frac{\partial \tilde{u}}{\partial \tilde{x}} \quad \text{at} \quad \tilde{x} = \tilde{L}(\tilde{t}), \tag{2.5}$$

where $\tilde{u}(\tilde{x}, \tilde{t}) \geq 0$ is the population density that depends on position $0 \leq \tilde{x} \leq L(t)$ and time $\tilde{t} > 0$. In this model the length of the domain, $L(t)$, is determined as part of the solution. The parameters in the Fisher-Stefan model are the same as in the Fisher-KPP model, as well as the Stefan parameter $\tilde{\kappa} > 0$, which relates the time rate of change of $\tilde{L}(\tilde{t})$ with the spatial gradient of the density, $\partial \tilde{u}/\partial \tilde{x}$, at the moving boundary $\tilde{x} = \tilde{L}(\tilde{t})$. One way of interpreting (2.3) is that we have zero net flux at $\tilde{x} = 0$. Another way of interpreting (2.3)

is that we have a symmetry condition at $\tilde{x} = 0$, and in this case the behaviour of the solution where $\tilde{x} > 0$ is reflected about the point $\tilde{x} = 0$. In this work we focus on the solution where $\tilde{x} > 0$, with $\tilde{t} > 0$, with a zero flux boundary condition at $\tilde{x} = 0$.

As with the Fisher-KPP model, solutions of the Fisher-Stefan model, (2.2)-(2.5), can also lead to constant speed, constant shape travelling waves in the long time limit, as $\tilde{t} \to \infty$ [Du and Lin 2010, Du and Guo 2011, Bunting et al. 2012, Du and Guo 2012, Du et al. 2014a, Du et al. 2014b, Du and Lou 2015]. Interestingly, for the same initial condition but different choice of parameter $\tilde{\kappa}$, the Fisher-Stefan model can also give rise to a very different outcome whereby the population tends to extinction, $\tilde{u}(\tilde{x}, \tilde{t}) \to 0$ on $0 < \tilde{x} < \tilde{L}_e$ as $\tilde{t} \to \infty$ [Du and Lin 2010, Du and Guo 2011, Bunting et al. 2012, Du and Guo 2012, Du et al. 2014a, Du et al. 2014b, Du and Lou 2015]. This major difference between the Fisher-KPP model and Fisher-Stefan model is of great interest because the Fisher-KPP model never leads to extinction, regardless of the choice of parameters. One way of interpreting this difference is that the Fisher-Stefan model is able to capture and predict additional details that are of practical interest because it is well known that many initially small translocated populations will become extinct [Griffith et al. 1989]. This is one of the shortcomings of the Fisher-KPP model since this model implies that every small initial population always leads to successful invasion.

The Fisher-Stefan model is an adaptation of the Fisher-KPP model that includes a moving boundary, $x = L(t)$, inspired by the classical Stefan problem [Crank 1987, Gupta 2017]. The classical Stefan problem is a one-dimensional model of heat conduction that includes a phase change, such as the conduction of heat associated with the melting of ice into water [Crank 1987, Gupta 2017]. An interesting mathematical and physical feature of the classical Stefan problem is that the interface between the two phases can move with time, giving rise to the notion of a *moving boundary problem* [Crank 1987, Gupta 2017]. Unlike classical models of heat conduction without any phase change [Cranck 1979], the solution of the Stefan problem requires the specification of two boundary conditions at the moving interface [Crank 1987, Gupta 2017]. First, the temperature at which the phase change occurs is specified at the moving boundary. This is analogous to Equation (2.3) in the Fisher-Stefan model.

Second, the Stefan condition specifies a balance of latent heat energy to specific heat energy at the moving boundary, relating the time rate of change of position of the moving boundary to the flux of heat at the boundary [Crank 1987, Gupta 2017]. This is analogous to Equation (2.5) in the Fisher-Stefan model.

The moving boundary problem (2.2)-(2.5) with $\tilde{\lambda} = 0$ represents a one-phase Stefan problem which has an initial domain of solid, $0 < \tilde{x} < \tilde{L}(0)$, at some initial temperature $\tilde{u}(\tilde{x}, 0)$, insulated at $\tilde{x} = 0$. The interval $\tilde{x} > \tilde{L}(0)$ is initially occupied by liquid assumed to already be at the fusion temperature. For this particular problem formulation, the interface $\tilde{L}(\tilde{t})$ propagates into the liquid region as the heat energy contained within the solid is continually used as latest energy to convert the liquid to solid. The process continues until $\tilde{u}(\tilde{x}, \tilde{t}) \to 0$ and $\tilde{L}(\tilde{t}) \to \tilde{L}_{e}$ as $\tilde{t} \to \infty$, where a simple energy balance shows that

$$\tilde{L}_{e} = \tilde{L}(0) + \frac{\tilde{\kappa}}{\tilde{D}} \int_{0}^{\tilde{L}(0)} \tilde{u}(\tilde{x}, 0) \, d\tilde{x}. \tag{2.6}$$

We shall return to this result later. A more general two-phase Stefan problem involves heat conduction in both phases, again separated by a moving boundary [Crank 1987, Gupta 2017]. Just like the Fisher-KPP model, there are many extensions of the classical Stefan problem such as dealing with higher-dimensions [King et al. 1999, McCue et al. 2003, McCue et al. 2005, McCue et al. 2008] as well as modifying the moving boundary condition [King and Riley 2000].

2.3   Results and discussion

2.3.1   Nondimensionalisation

We introduce the dimensionless variables, $x = \tilde{x}\sqrt{\tilde{\lambda}/\tilde{D}}$, $t = \tilde{\lambda}\tilde{t}$ and $u = \tilde{u}/\tilde{K}$, to rescale the Fisher-KPP equation as

$$\frac{\partial u}{\partial t} = \frac{\partial^2 u}{\partial x^2} + u(1 - u), \tag{2.7}$$

on $x \geq 0$ and $t > 0$. It is useful to note that Equation (2.7) involves no free parameters, and that all solutions of Equation (2.7) with compactly supported initial conditions will eventually lead to travelling waves that move with speed

$c_{\min} = 2$. In this work we always specify the boundary conditions for the Fisher-KPP model to be

$$\frac{\partial u}{\partial x} = 0 \quad \text{at} \quad x = 0, \tag{2.8}$$

$$\frac{\partial u}{\partial x} = 0 \quad \text{at} \quad x = x_\infty, \tag{2.9}$$

and the initial condition to be

$$u(x, 0) = \alpha \left[1 - H(x - \beta) \right], \tag{2.10}$$

where $H(x)$ is the usual Heaviside function, and α and β are positive constants so that we have $u(x, 0) = \alpha$ for $x < \beta$ and $u(x, 0) = 0$ for $x > \beta$. Here x_∞ is chosen to be sufficiently large so that we can numerically approximate the infinite domain problem on $0 \leq x < \infty$ by the finite domain problem $0 \leq x \leq x_\infty$ [Simpson and Landman 2006]. Full details of the numerical method used to solve Equation (2.7), together with benchmark test cases to confirm the accuracy of our numerical solutions are given in the Additional Material.

To nondimensionalise the Fisher-Stefan model we employ the same dimensionless variables as in the Fisher-KPP model with $L(t) = \tilde{L}(\tilde{t})\sqrt{\tilde{\lambda}/\tilde{D}}$ and $\kappa = \tilde{\kappa}/\tilde{D}$ so that we have

$$\frac{\partial u}{\partial t} = \frac{\partial^2 u}{\partial x^2} + u(1 - u), \tag{2.11}$$

$$\frac{\partial u}{\partial x} = 0 \quad \text{at} \quad x = 0, \tag{2.12}$$

$$u(L(t), t) = 0, \tag{2.13}$$

$$\frac{\mathrm{d}L(t)}{\mathrm{d}t} = -\kappa \frac{\partial u}{\partial x} \quad \text{at} \quad x = L(t). \tag{2.14}$$

It is relevant to note that the nondimensional Fisher-Stefan model involves one parameter, $\kappa > 0$. For all numerical solutions of Equations (2.11)-(2.14) in this work we always apply the initial condition (2.10) such that $L(0) = \beta$. Full details of the numerical method used to solve Equations (2.11)-(2.14), together with benchmark test cases to confirm the accuracy of our numerical solutions, are given in the Additional Material.

To illustrate key features of the Fisher-KPP and Fisher-Stefan models we

present numerical solutions of both models in Figure 2.2. Results in Figure 2.2(a) show the time evolution of the solution of the Fisher-KPP model from an initial condition with compact support. Plotting solutions at equally spaced values of time suggests that the solution approaches a travelling wave that moves in the positive x direction with constant speed and constant shape. Our numerical solutions confirm that the speed of propagation is $c = 2$, as expected. Results in Figure 2.2(b) show the time evolution of the solution of the Fisher-Stefan model (2.11)-(2.14) for the same initial condition used in Figure 2.2(a) together with a particular choice of κ. Again, plotting solutions at equally spaced values of time suggests that the solution approaches a travelling wave that moves in the positive x direction with constant speed and constant shape. In this case, for our choice of κ, our numerical solution suggests that $c = 1.2$, which is slower than the minimum wave speed for the Fisher-KPP model. Another important difference between the travelling wave solutions in Figure 2.2(a)-(b) is that the travelling wave solution of the Fisher-KPP model does not have compact support since $u(x,t) > 0$ for all $x \geq 0$ and $t > 0$. This feature of the Fisher-KPP model has been previously criticised as being biologically implausible [Maini et al. 2004a, Maini et al. 2004b, McCue et al. 2019] (and this observation has motivated extensions of the Fisher-KPP model to include various nonlinear diffusion terms so that the resulting travelling waves have compact support [Maini et al. 2004a, Maini et al. 2004b, McCue et al. 2019]). In contrast, owing to the boundary conditions at $x = L(t)$, the travelling wave solution of the Fisher-Stefan has compact support since we have $u(L(t),t) = 0$ for $t > 0$. Therefore, we have identified two features of the Fisher-Stefan model that are appealing when compared to the Fisher-KPP model: (i) the Fisher-Stefan model permits population extinction whereas the Fisher-KPP model implies that all initial populations successfully invade; and (ii) travelling wave solutions of the Fisher-Stefan model have compact support whereas travelling wave solutions of the Fisher-KPP model do not.
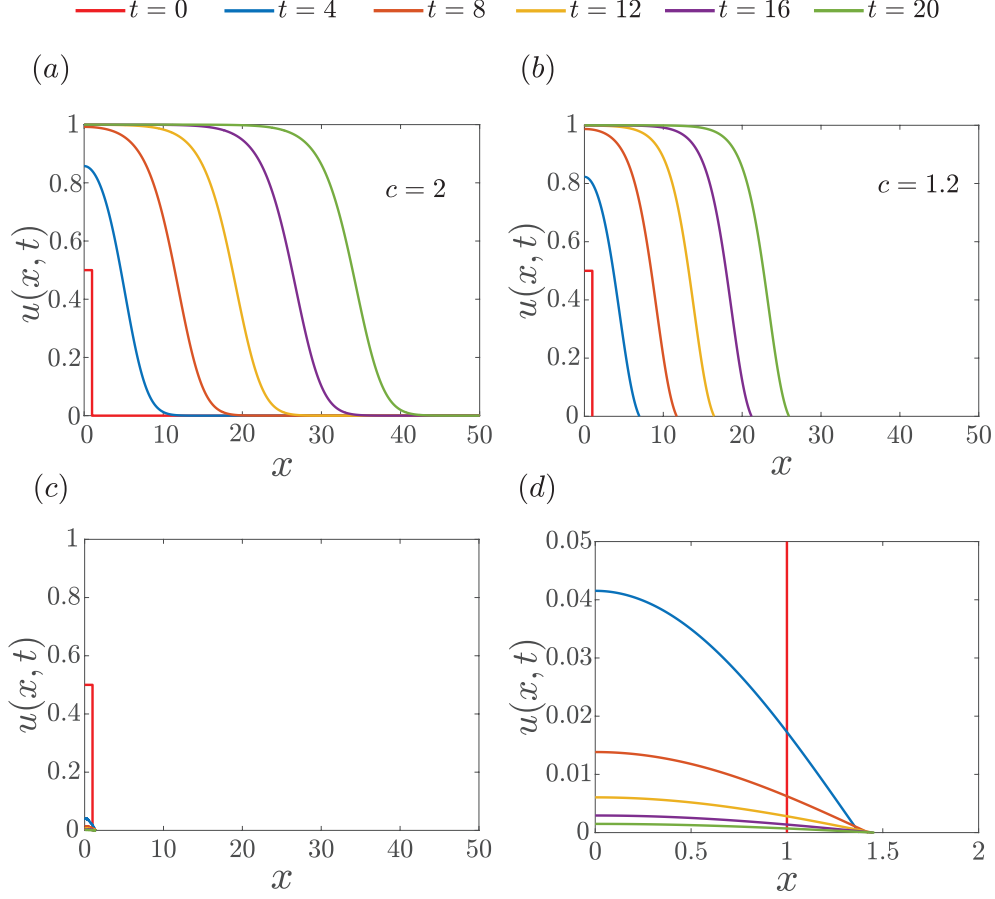
Figure 2.2: Numerical solutions of the Fisher-KPP and the Fisher-Stefan models. *(a)* Numerical solutions of the Fisher-KPP equation evolving into a travelling wave solution with the minimum wave speed, $c = 2$. *(b)* Numerical solutions of Fisher-Stefan model evolving into a travelling wave solution with $c = 1.2$. *(c)* Numerical solutions of the Fisher-Stefan model leading to extinction. *(d)* Magnified region of the solution in *(c)*, for $0 \leq x \leq 2$, to clearly show the dynamics of the extinction behaviour. For the Fisher-Stefan model we set $\kappa = 20$ in *(b)* and $\kappa = 0.45$ in *(c)*. Numerical solutions of the Fisher-Stefan model are obtained with $\Delta\xi = 1 \times 10^{-4}$, whereas numerical solutions of the Fisher-KPP model are obtained with $\Delta x = 1 \times 10^{-4}$. For both the Fisher-KPP and Fisher-Stefan models we set $\Delta t = 1 \times 10^{-3}$ and $\epsilon = 1 \times 10^{-8}$. For all results presented here the initial condition is Equation (2.10) with $\alpha = 0.5$ and $\beta = 1$.

Results in Figure 2.2(c) show the time evolution of the solution of the Fisher-Stefan model for the same initial condition used in Figure 2.2(a)-(b), but this time we choose a slightly smaller value of κ. In this instance, plotting the solutions at the same intervals of time as in Figures 2.2(a)-(b) indicates that the solution does not tend towards a travelling wave, and instead appears to go extinct. Figure 2.2(d) shows a magnified view of the solution in Figure 2.2(c) so that we can see additional details as the population tends to extinction. From these magnified solutions we see that $L(0) = 1$. By $t = 20$ we have $L(20) \approx 1.4$, and after this time the solution rapidly tends to zero. Together,

the results in Figure 2.2(b)-(d) illustrate the spreading-extinction dichotomy since for certain choices of κ we observe spreading as a travelling wave in Figure 2.2(b), whereas keeping everything else identical except for choosing a smaller value of κ we observe the population going extinct in Figure 2.2(c)-(d). These initial comparisons in Figure 2.2 indicate that the solutions of the Fisher-KPP and Fisher-Stefan models can be very different. As we will show, it is the difference in boundary conditions in the two models that drives these differences in the time dependent solutions of the partial differential equation models. Since both the Fisher-KPP and Fisher-Stefan models support travelling wave solutions we will now explore these models in the phase plane.

2.3.2 Phase plane analysis

Numerical solutions of the Fisher-KPP model in Figure 2.2(a) suggest that we seek travelling wave solutions with travelling wave coordinate $z = x - ct$, where $c > 0$ is the constant speed of propagation in the positive x direction. In the travelling wave coordinate, Equation (2.7) simplifies to a second order nonlinear ordinary differential equation

$$\frac{\mathrm{d}^2 U}{\mathrm{d}z^2} + c \frac{\mathrm{d}U}{\mathrm{d}z} + U(1 - U) = 0, \tag{2.15}$$

where $-\infty < z < \infty$, with $U(-\infty) = 1$ and $U(\infty) = 0$.

Our treatment of the analysis of travelling wave solutions of the Fisher-Stefan model is very similar except that we must first assume that our choice of initial condition and κ in Equation (2.11)-(2.14) is such that a travelling wave solution forms, as in Figure 2.2(b). In this case, writing Equation (2.11) in the travelling wave coordinate gives rise to the same second order nonlinear ordinary differential equation, Equation (2.15) with $U(-\infty) = 1$. The other boundary condition is treated differently and to see this difference we express the Stefan condition (2.14) in terms of z, giving

$$\frac{\mathrm{d}L(t)}{\mathrm{d}t} = -\kappa \frac{\mathrm{d}U}{\mathrm{d}z}, \tag{2.16}$$

at $z = L(t) - ct$. For a travelling wave solution we have $\mathrm{d}L(t)/\mathrm{d}t = c$, so that the differential equation (2.15) holds on $-\infty < z < 0$. The boundary

33

conditions are given by $U(-\infty) = 1$, and

$$-\kappa \frac{\mathrm{d}U}{\mathrm{d}z} = c, \tag{2.17}$$

at $z = 0$. Therefore, while the Fisher-KPP and Fisher-Stefan models presented as partial differential equations appear to be very different, when we seek travelling wave solutions of these models in the travelling wave coordinate we find that the equations governing the phase planes for the two models are the same, with differences only at one boundary condition.

We first examine travelling wave solutions of the Fisher-KPP model by re-writing Equation (2.15) as a first order dynamical system

$$\frac{\mathrm{d}U}{\mathrm{d}z} = V, \tag{2.18}$$

$$\frac{\mathrm{d}V}{\mathrm{d}z} = -cV - U(1 - U), \tag{2.19}$$

for $-\infty < z < \infty$. This dynamical system has two equilibrium points: $(1, 0)$ and $(0, 0)$. A travelling wave solution corresponds to a heteroclinic trajectory between these two equilibrium points. Linear analysis shows that the eigenvalues at $(1, 0)$ are $\left(-c \pm \sqrt{c^2 + 4}\right)/2$ so that the local behaviour at $(1, 0)$ is a saddle point [Murray 2002]. The eigenvalues at $(0, 0)$ are $\left(-c \pm \sqrt{c^2 - 4}\right)/2$, meaning that the local behaviour at $(0, 0)$ is a stable spiral for $c < 2$ and a stable node if $c \geq 2$ [Murray 2002]. Therefore, to avoid nonphysical negative solutions near $(0, 0)$ we require $c \geq 2$, giving rise to the well known minimum wave speed for the Fisher-KPP model [Murray 2002, Harley et al. 2015].

The shape of the heteroclinic orbit between $(0, 0)$ and $(1, 0)$ is given by the solution of

$$\frac{\mathrm{d}V}{\mathrm{d}U} = \frac{-cV - U(1 - U)}{V}. \tag{2.20}$$

Neither the system (2.18)–(2.19) or Equation (2.20) have exact solutions for an arbitrary choice of $c > 0$. Therefore, we will consider numerical solutions of these ordinary differential equations when we present and visualise the phase planes in this work, with details of the numerical methods given in the Additional Material. The solution of Equation (2.20) gives $V(U)$, while the solution of the system (2.18)–(2.19) gives $U(z)$ and $V(z)$, and we will use both approaches where relevant. All phase planes presented in this work are gen-

erated using a combination of exact and numerical methods that are outlined in the Additional Material.
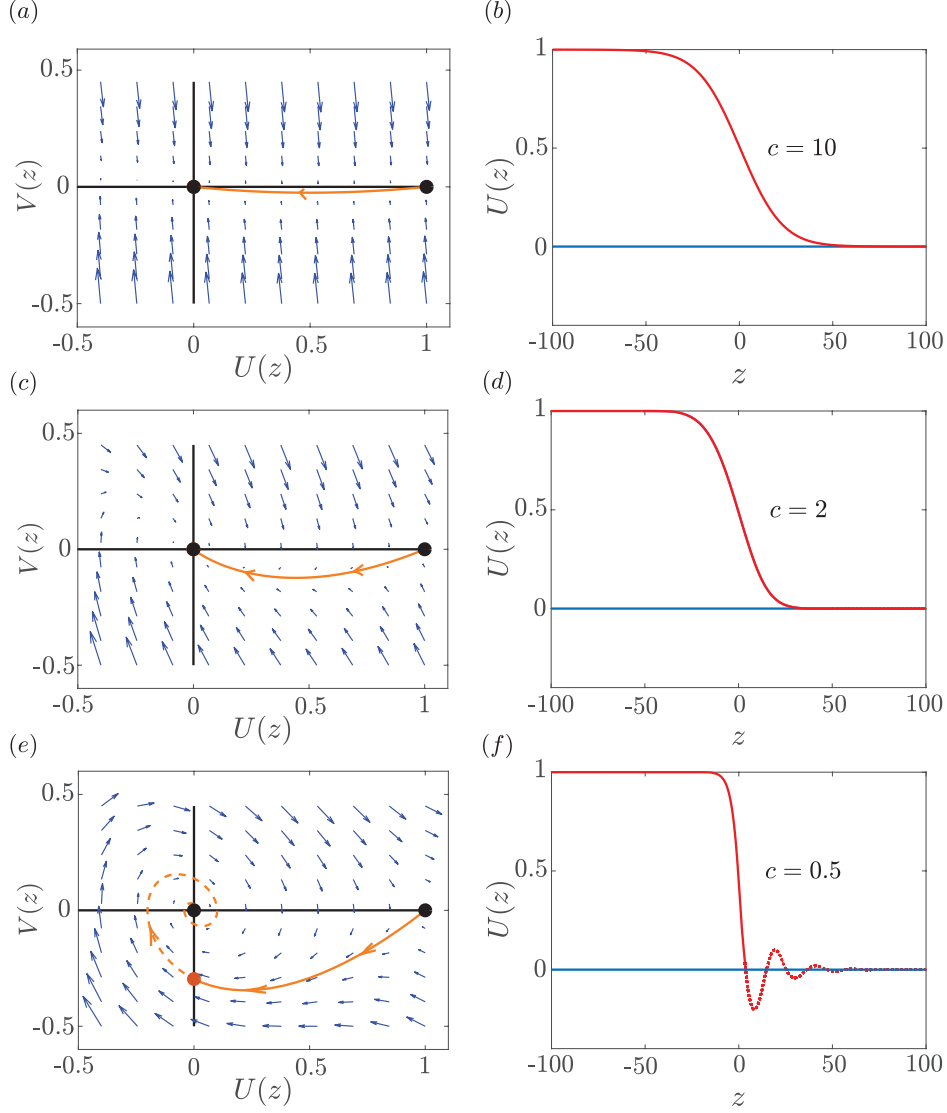
Figure 2.3: Phase planes and density profiles for the Fisher-KPP equation with various choices of c. *(a)* Phase plane and heteroclinic trajectory for $c = 10$. *(b)* The corresponding density profile for the heteroclinic trajectory in *(a)*. *(c)* Phase plane and heteroclinic trajectory for $c = 2$. *(d)* The corresponding density profile for the heteroclinic trajectory in *(c)*. *(e)* Phase plane and heteroclinic trajectory for $c = 0.5$. *(f)* The corresponding density profile for the heteroclinic trajectory in *(e)*. Equilibrium points at $(1, 0)$ and $(0, 0)$ are shown with black discs. The blue arrows show the flow associated with the dynamical system, and the solid orange line shows the heteroclinic trajectory that runs between $(0, 0)$ and $(1, 0)$. The orange disc in (c) shows the location where the heteroclinic trajectory intersects with the $U(z) = 0$ axis where $V(z) < 0$.

Results in Figure 2.3 show a suite of phase planes for the Fisher-KPP model for a range of c. The phase plane in Figure 2.3(a) shows the flow, the location of the equilibrium points and the heteroclinic orbit for $c = 10$, which approaches $(0, 0)$ without spiralling. When we plot the solution in terms of the

density, $U = U(z)$, in Figure 2.3(b), we see that this solution is positive and monotonically decreasing. Similar results are presented in Figure 2.3(c)-(d) for $c = 2$. In contrast, Figure 2.3(e) shows the phase plane for $c = 0.5$ where we see that the heteroclinic orbit approaches $(0,0)$ as a spiral, indicating that $U(z) < 0$ in certain regions. This oscillatory behaviour is often invoked to justify the condition that $c \geq c_{\min} = 2$ for the Fisher-KPP model and the possibility of travelling waves with $c < 2$ is typically ignored [Murray 2002].

Since travelling wave solutions of the Fisher-KPP and Fisher-Stefan models are governed by the same phase planes, it is worthwhile to examine how the phase planes in Figure 2.3 relate to the travelling wave solutions of the Fisher-Stefan model. As previously stated, travelling wave solutions of the Fisher-Stefan model satisfy a different boundary condition, (2.17). The trajectory in the phase plane must intersect with, and terminate at, $(0, -c/\kappa)$. The phase planes and heteroclinic orbits for the Fisher-KPP model in Figure 2.3(a)-(b) and Figure 2.3(c)-(d) show that such an intersection is impossible for these choices of $c \geq 2$. In particular, the linearisation about $(0,0)$ means that whenever $c \geq 2$, the stable node at $(0,0)$ precludes the possibility of such an intersection, illustrating that there is no travelling wave solution for the Fisher-Stefan model with $c \geq 2$. In contrast, for $c < 2$, the trajectory intersects the V-axis at some point, $(0, -c/\kappa)$, as indicated by the orange disc in Figure 2.3(e). Therefore, this additional boundary condition for the Fisher-Stefan model together with the linearisation about $(0,0)$ indicates that travelling wave solutions for the Fisher-Stefan model require $c < 2$. Under these conditions, the trajectory in the phase plane corresponding to the travelling wave solutions runs between $(1,0)$ and $(0, -c/\kappa)$, and since this trajectory never leaves the fourth quadrant we avoid the issue of negative densities. This is a very interesting result because the standard phase plane analysis of travelling wave solutions of the Fisher-KPP model typically discard any solutions for which $c < 2$ based on physical grounds [Murray 2002, Canosa 1973]. In this work we show that it is precisely these normally-discarded solutions that actually form the basis of the travelling wave solutions of the Fisher-Stefan model provided that we only consider that part of the trajectory between $(1,0)$ and $(0, -c/\kappa)$, where $U(z) \geq 0$. Therefore, by revisiting the travelling wave solutions of the Fisher-KPP model we are providing insight into the properties of

travelling wave solutions of the Fisher-Stefan model.
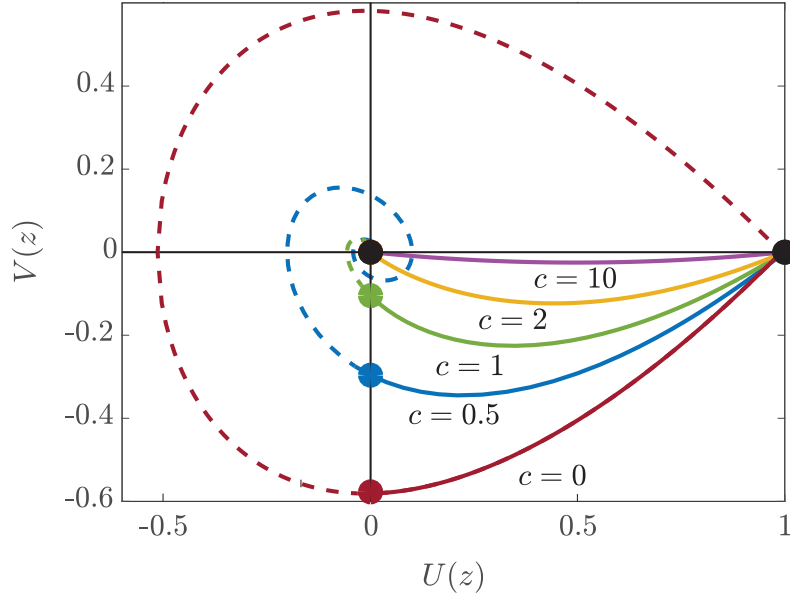
Figure 2.4: Family of trajectories in the phase plane for various choices of
c. Heteroclinic trajectories running between $(1,0)$ to $(0,0)$ for $c = 10, 2, 1$ and 0.5,
as indicated. An additional trajectory with $c = 0$ forms a homoclinic trajectory to
$(1,0)$. Equilibrium points at $(1,0)$ and $(0,0)$ are shown with black discs. For the
trajectories with $0 < c < 2$ the intersection with the $U(z) = 0$ axis is shown with an
appropriately coloured disc: green for $c = 1$; blue for $c = 0.5$; and red for $c = 0$.

We now provide additional results in Figure 2.4 comparing trajectories
in the phase plane for a wider range of c. The trajectories for $c = 10$ and
$c = 2$ show a heteroclinic orbit that runs between $(1,0)$ and $(0,0)$ without
spiralling around the origin. These trajectories are associated with travelling
wave solutions of the Fisher-KPP model for these choices of c. Additional
results for $c = 1$ and $c = 0.5$ are also shown, and these trajectories clearly
spiral near to the origin. However, both of these trajectories cross the V-
axis at some point, shown with an appropriately coloured disc in Figure 2.4,
where $U(z) = 0$ and $V(z) < 0$, which satisfies the Fisher-Stefan boundary
condition. Therefore, the trajectories in Figure 2.4 with $c < 2$ are shown
as a combination of solid and dashed lines. Those parts of the trajectories
shown in solid correspond to the travelling wave solution of the Fisher-Stefan
model, whereas the dashed parts of the trajectories are not associated with
the travelling wave solution. Finally, we also include a trajectory in Figure
2.4 for $c = 0$. In this case the trajectory forms a homoclinic orbit with $(1,0)$.
Although this trajectory does not correspond to any travelling waves with
$c > 0$, later we will show it is important when constructing approximate

perturbation solutions for $c \ll 1$.

2.3.3 Relationship between κ and c
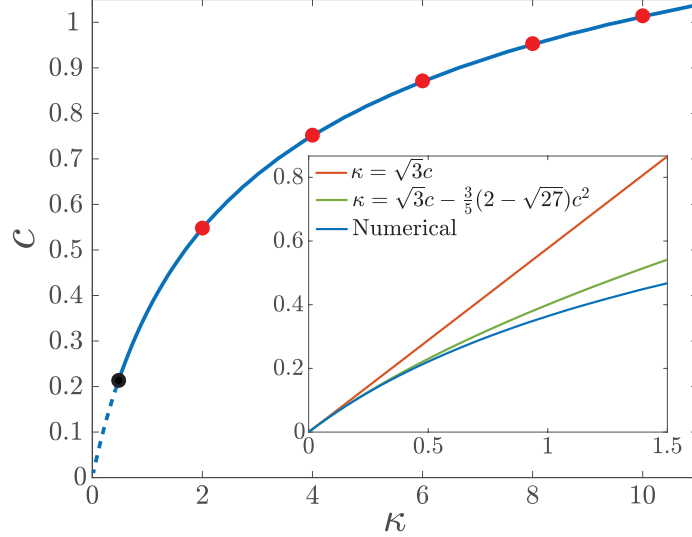
Figure 2.5: Relationship between c and κ for the Fisher-Stefan model. The blue curve is obtained by solving Equation (2.20) and calculating the value of κ corresponding to the intersection of $(0, -c/\kappa)$. The red circles are obtained by solving Equations (2.2-2.4) and using the full time dependent solutions to estimate the eventual long time travelling wave speed, c. The black circle denotes the approximate critical value of κ_{crit}. The Fisher-Stefan model is solved with $\Delta \xi = 1 \times 10^{-4}$, $\Delta t = 1 \times 10^{-3}$, $\epsilon = 1 \times 10^{-8}$ and the initial condition given by Equation (2.10), where $\alpha = 0.5$ and $\beta = 1$. The inset shows the comparison of the numerical solution the perturbation solutions. The red line is the $\mathcal{O}(1)$ perturbation solution, the green curve is the $\mathcal{O}(c)$ perturbation solution and the blue curve is the full numerical result.

It is interesting to recall that all solutions of the Fisher-KPP model evolving from initial conditions with compact support always eventually form a travelling wave with the minimum wave speed, $c_{\min} = 2$. In contrast, the question of whether travelling wave solutions will form for the Fisher-Stefan model depends upon the choice of initial condition. Furthermore, if a travelling wave solution for the Fisher-Stefan model does form, the speed of that travelling wave will depend on the choice of κ. To explore the relationship between the speed of the travelling wave and κ, we use a combination of phase plane analysis and numerical solutions of the Fisher-Stefan model (2.11)-(2.14). By repeatedly solving the phase plane equations, (2.18) for different values of $c < 2$, we are able to estimate the point at which the trajectory leaving $(1, 0)$ first intersects the V-axis and then use the boundary condition, $V = -c/\kappa$ at $U = 0$, to calculate the corresponding values of κ. The solid blue curve in Figure 2.5 shows this relationship. The results in the inset of Figure 2.5 will

be discussed in section 2.3.5. We find that as we examine increasing values of c towards the threshold value of $c = 2$, κ appears to grow without bound. This numerical result suggests that $\kappa \to \infty$ as $c \to 2^-$.

In addition to exploring the relationship between κ and c in the phase plane, we also solve the Fisher-Stefan model (2.11)-(2.14) numerically with a particular choice of initial condition given by Equation (2.10) with $\beta = 1$ and $\alpha = 0.5$. We allow such numerical solutions to evolve for a sufficient duration of time that the resulting solution appears to settle into a travelling wave, from which we can estimate the speed, c. Repeating this procedure for various values of κ enables us to estimate how our choice of κ influences c. Additional results, shown as red discs in Figure 2.5, confirm that long time travelling wave solutions from the partial differential equation description compare very well with the relationship implied by the phase plane analysis.

As we stated in Section 2.3.2, whenever we are working in the phase plane we make the implicit assumption that a travelling wave solution has been generated. Yet, when we compare results in Figure 2.2(b)-(c) we know that long time travelling wave solutions do not always form, since this outcome depends upon the choice of κ. We explore this in Figure 2.5 by holding the initial condition constant in the numerical solution of Equations (2.11)-(2.14) and choosing a sequence of increasingly small values of κ. The numerical solutions suggest that for this initial condition there is a threshold value, $\kappa_{\text{crit}} \approx 0.48$. If $\kappa > \kappa_{\text{crit}}$ we observe long time travelling wave solutions and for $\kappa < \kappa_{\text{crit}}$ the population eventually becomes extinct. This approximate threshold value is shown in Figure 2.5 as a black disc, and the relationship between κ and c obtained in the phase plane is shown as a solid line for $\kappa > \kappa_{\text{crit}}$ and as a dashed line for $\kappa < \kappa_{\text{crit}}$.

2.3.4 Critical length and the spreading-extinction dichotomy

We will now provide insight into the spreading-extinction dichotomy by examining time-dependent numerical solutions of Equations (2.11)-(2.14) in Figure 2.6. Figure 2.6(a) shows numerical solutions for a particular choice of κ where we see some very interesting behaviour. At $t = 30$ the solution appears to be decreasing, almost to extinction, whereas by $t = 60$ and $t = 90$ the solution recovers from the initial decline to eventually form a travelling wave. Results

in Figure 2.6(b) show details at intermediate values of t to clearly highlight this initial decline followed by the recovery. Figure 2.6(c) shows estimates of $L(t)$ as a function of t, where we see that $L(t)$ increases slowly at early time before eventually increasing at a constant rate, corresponding to a travelling wave solution. In contrast, Figure 2.6(d) shows the solution of Equations (2.11)-(2.14) for the same initial condition as in Figure 2.6(a) with the only difference being that κ is reduced. Figure 2.6(d) indicates that the population appears to be almost extinct at $t = 90$, and additional results magnified in Figure 2.6(e) show that the population never recovers, and instead goes extinct as t increases. Figure 2.6(f) shows $L(t)$ as a function of t, where we see that the spreading population initially increases its domain before eventually stalling.
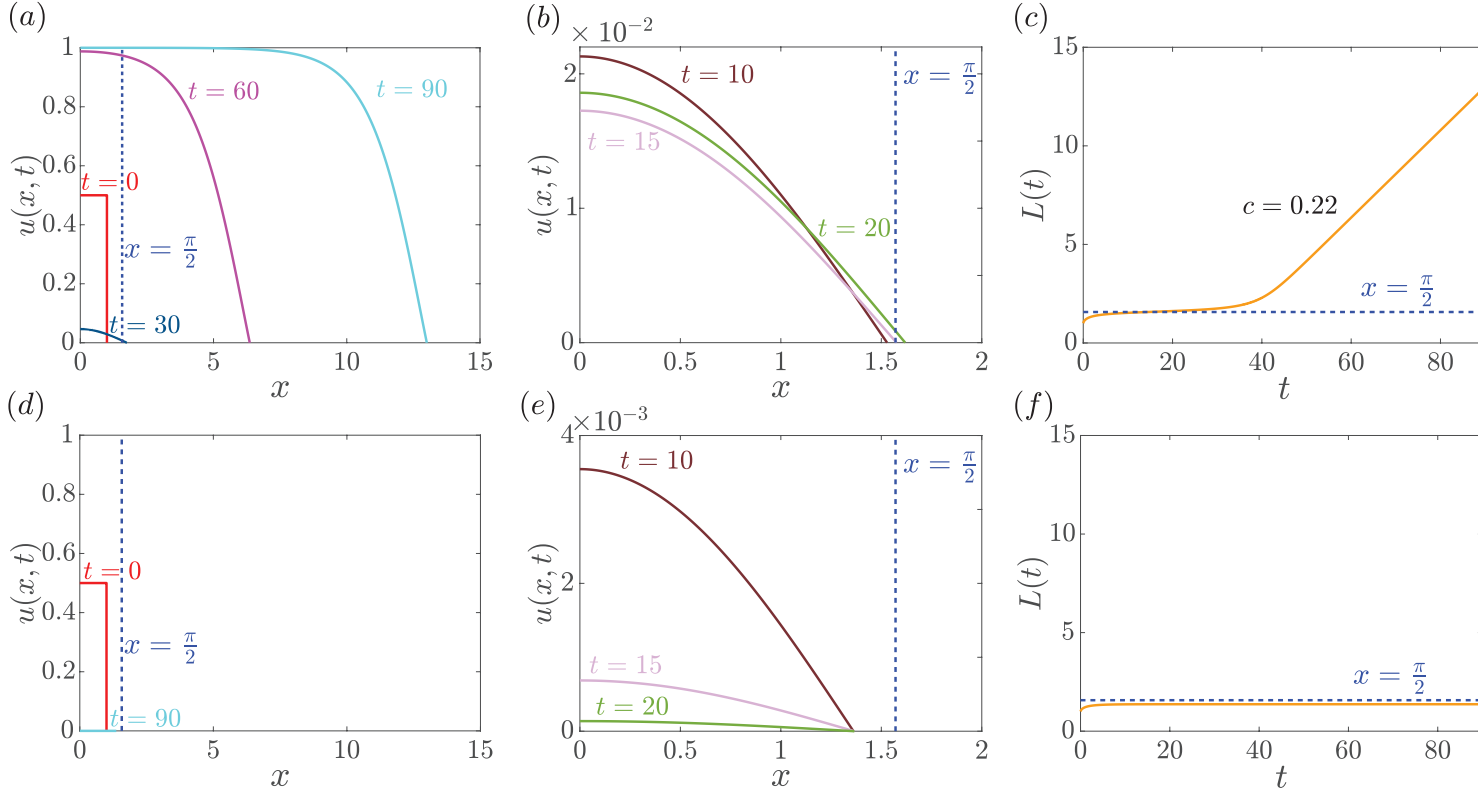
Figure 2.6: Numerical solutions of the Fisher-Stefan model showing both travelling wave and extinction phenomena. The first row represents the invasion phenomenon, and the second row represents the extinction. *(a)* Time evolution of the density profiles for invading cell population. *(b)* Magnified density profiles in *(a)* from $x = 0$ to 2 at intermediate times. *(c)* Progression of $L(t)$ superimposed with the critical length of $\pi/2$. *(d)* Time evolution of the density profiles for extinction. *(e)* Magnified density profiles in *(d)* from $x = 0$ to 2 at intermediate times. *(f)* Progression of $L(t)$ superimposed with the critical length of $\pi/2$. For both simulations, $\Delta\xi = 1 \times 10^{-4}$, $\Delta t = 1 \times 10^{-3}$, $\epsilon = 1 \times 10^{-8}$, and the initial condition given by Equation (2.10), where $\alpha = 0.5$ and $\beta = 1$. Results in *(a)-(c)* correspond to $\kappa = 0.5$, while results in *(d)-(f)* correspond to $\kappa = 0.4$.

Du and colleagues [Du and Lin 2010] provide a formal proof of the existence of a critical length, $L_{\mathrm{crit}} = \pi/2$, such that if ever $L(t) > L_{\mathrm{crit}}$ the population will evolve to a travelling wave, whereas if $L(t)$ never exceeds this critical length then the population will eventually become extinct. Here we provide some simple physical and mathematical arguments to confirm this result. Visual inspection of the time dependent solutions of Equations (2.11)-(2.14) in Figure 2.6(b) and (e) confirm that we have $u(x,t) \ll 1$ close to the time when population recovers (Figure 2.6(b)) or fails to recover from the initial decline (Figure 2.6(e)). This observation suggests that we can study the spreading-extinction dichotomy using an approximate linearised model where $\mathcal{U}(x,t) \ll 1$. Under these conditions we can approximate the Fisher-Stefan model with

$$\frac{\partial \mathcal{U}}{\partial t} = \frac{\partial^2 \mathcal{U}}{\partial x^2} + \mathcal{U}, \tag{2.21}$$

for $0 < x \le L$, with $\partial \mathcal{U}/\partial x = 0$ at $x = 0$ and $\mathcal{U} = 0$ at $x = L$. In this approximate analysis we treat the domain length as a fixed quantity and this allows us to write down the exact solution of the linear equation (2.21) as

$$\mathcal{U}(x,t) = \sum_{n=1}^{\infty} A_n \cos(\gamma_n x) \mathrm{e}^{t\left(1-\gamma_n^2\right)}, \tag{2.22}$$

where $\gamma_n = \pi(2n-1)/(2L)$, $n = 1, 2, 3, \ldots$ and A_n are constants chosen so that the solution matches the initial condition, $\mathcal{U}(x,0)$. The solution of the linearised model (2.22) can be further simplified by assuming that the dynamics near the time of population recovery, or decline, can be approximated by taking a leading eigenvalue approximation so that

$$\hat{\mathcal{U}}(x,t) \sim A_1 \cos\left(\frac{\pi x}{2L}\right) \mathrm{e}^{t\left(1-\pi^2/[4L^2]\right)}. \tag{2.23}$$

With this approximate solution we formulate a conservation statement describing the time rate of change of the total population within the domain,

$$\frac{\mathrm{d}n}{\mathrm{d}t} = \int_0^L \hat{\mathcal{U}}(x,t)\,\mathrm{d}x + \frac{\partial \hat{\mathcal{U}}(L,t)}{\partial x}, \tag{2.24}$$

where $n(t) = \int_0^L \hat{\mathcal{U}}(x,t)\,\mathrm{d}x$ is the total population within the domain. The first term on the right of Equation (2.24) is the rate of increase of the total population owing to the source term and the second term on the right of

Equation (2.24) is the rate of decrease of the total population owing to diffusive loss at the boundary at $x = L$. Setting $\mathrm{d}n/\mathrm{d}t = 0$, and substituting Equation (2.23) into (2.24) gives $L = L_{\mathrm{crit}} = \pi/2$, corroborating the results of Du and colleagues [Du and Lin 2010]. We interpret this as follows. Once a time-dependent solution of Equations (2.11)-(2.14) evolves such that $L(t) > \pi/2$, the net positive accumulation of mass in the system means that a travelling wave solution will eventually form, as in Figure 2.6(a)-(c). Alternatively, if the time dependent solution of Equations (2.11)-(2.14) evolves such that $L(t)$ never exceeds $\pi/2$, the net loss of mass in the system means that the population will always go extinct, as in Figure 2.6(d)-(f). It is also worthwhile to note that since the result that $L_{\mathrm{crit}} = \pi/2$ is governed by a linearised model (2.21), this outcome will hold for any generalisation of the Fisher-Stefan model that can be linearised to give Equation (2.21). For example, if we extended the Fisher-Stefan model to consider a generalised logistic source term, $u(1 - u)^m$, where $m > 0$ is some exponent [Simpson et al. 2010, Tsoularis and Wallace 2002, Broadbridge et al. 2002, Bradshaw-Hajek and Broadbridge 2004], then the same $L_{\mathrm{crit}} = \pi/2$ would apply.

2.3.5 Perturbation solution when $c \ll 1$

Now that we have used phase plane analysis and linearisation to establish conditions for travelling wave solutions of the Fisher-Stefan model to form, we turn our attention to whether it is possible to provide additional mathematical insight into the details of the shape of the travelling wave solutions. It is well known that travelling wave solutions of the Fisher-KPP model travel with speed $c \geq c_{\mathrm{min}} = 2$, and that it is possible to obtain approximate perturbation solutions to describe the shape of the travelling wave solutions in large c limit [Canosa 1973, Murray 2002, Simpson et al. 2006]. We now attempt to follow a similar analysis to describe the shape of the travelling wave solution of the Fisher-Stefan model for which $c < 2$, suggesting that we attempt to find a perturbation solution for small c:

$$V(U) = V_0(U) + cV_1(U) + \mathcal{O}(c^2). \tag{2.25}$$

Substituting this expansion into Equation (2.20) we obtain ordinary differential equations governing $V_0(U)$ and $V_1(U)$ which can be integrated exactly.

Ensuring that $U(1) = 0$ we obtain

$$V_0(U) = \pm\sqrt{-U^2 + \frac{2U^3}{3} + \frac{1}{3}}, \tag{2.26}$$

$$V_1(U) = \frac{-(U-2)(1+2U)^{3/2} - \sqrt{27}}{5(U-1)\sqrt{1+2U}}. \tag{2.27}$$

Since we solve for both $V_0(U)$ and $V_1(U)$ we can construct both an $\mathcal{O}(1)$ perturbation solution given by $V(U) = V_0(U) + \mathcal{O}(c)$, as well as an $\mathcal{O}(c)$ perturbation solution given by $V(U) = V_0(U) + cV_1(U) + \mathcal{O}(c^2)$. To compare the accuracy of these perturbation solutions for the shape of the $V(U)$ curve in the phase plane we generate a series of numerical phase planes for $c = 0.05, 0.1, 0.2$ and 0.5 in Figure 2.7. The numerical trajectories, shown in blue, run between the equilibrium points $(1, 0)$ and $(0, 0)$, and pass through the point $(0, -c/\kappa)$. In the numerical solutions we highlight $(0, -c/\kappa)$ with a blue disc. In each subfigure of Figure 2.7, we compare the numerical trajectory with the $\mathcal{O}(1)$ perturbation solution in red. In each case the $\mathcal{O}(1)$ perturbation solution runs between $(1, 0)$ and first intersects the V-axis at $(0, -1/\sqrt{3})$. We show this point with a red disc. Comparing the red and blue trajectories in the fourth quadrant clearly shows a discrepancy that increases with c, as expected. Similarly, in each subfigure of Figure 2.7 we also compare the numerical trajectory with the $\mathcal{O}(c)$ perturbation solution shown in green. In each case the $\mathcal{O}(c)$ perturbation solution runs between $(1, 0)$ and first intersects the V-axis at $(0, -1/\sqrt{3} + c(\sqrt{27} - 2)/5)$, and we show this point with a green disc. Comparing the green and blue trajectories in the fourth quadrant shows that we have an excellent match between the numerical and perturbation solutions. This comparison indicates that the $\mathcal{O}(c)$ perturbation solution can be used to provide a highly-accurate approximation of the shape of the travelling wave solutions of the Fisher-Stefan model for $c < 0.5$.
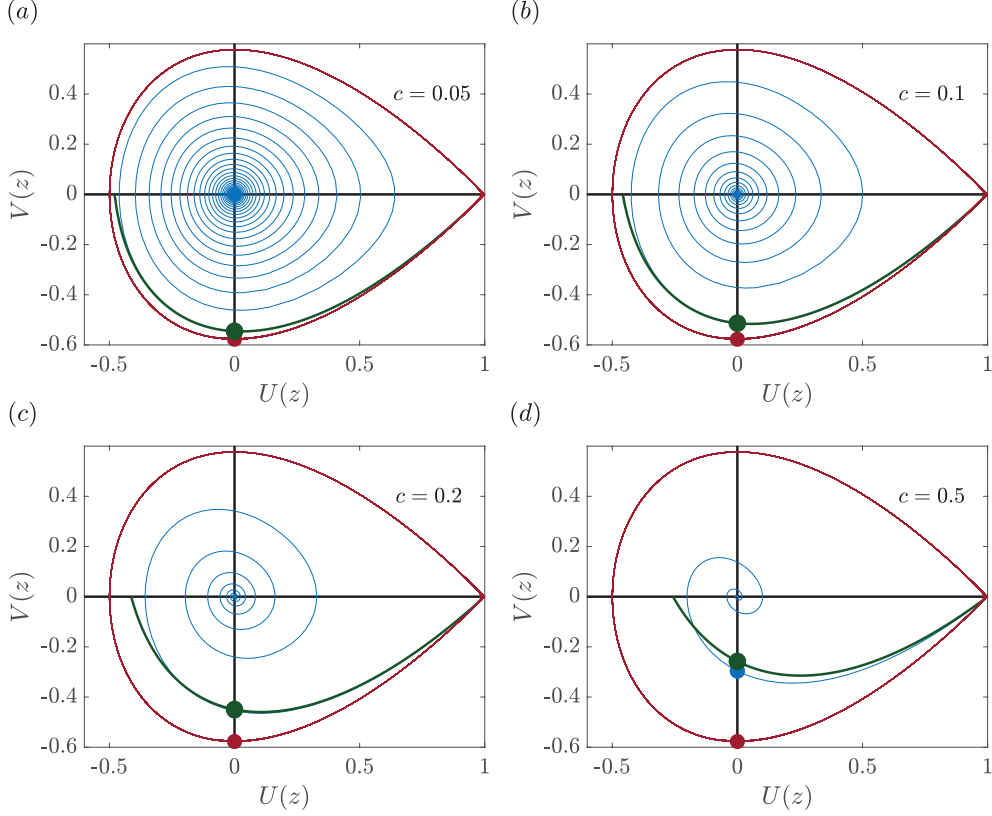
Figure 2.7: Comparison of numerical trajectories in the phase plane and perturbation solutions for various choices of c. The blue lines are the numerical trajectories for $c = 0.05, 0.1, 0.2$ and 0.5 in *(a)-(d)*, respectively. The red curves are the $\mathcal{O}(1)$ perturbation solution. The green curves are the $\mathcal{O}(c)$ perturbation solution. The red, blue and green discs indicate the intersection points of the trajectories with $U(z) = 0$.

Using Equations (2.25)-(2.27) we can obtain additional analytical insight into the relationship between c and κ that we previously explored numerically in Figure 2.5. Since the ordinate of the intersection point is $V = -\kappa/c$, we can develop approximate closed-form relationships between c and κ. These relationships are plotted in the inset of Figure 2.5 for $\kappa < 2$ and $c < 1$. Comparing the numerically deduced relationship between c and κ with the perturbation solutions shows a good match, with the expected result that the $\mathcal{O}(c)$ perturbation solution leads to a particularly accurate approximation.

Since our perturbation solutions provide good approximations to the $V(U)$ curve in the fourth quadrant of the phase plane, shown in Figure 2.7, we now compare the accuracy of the perturbation solutions in the travelling wave coordinate system. For the $\mathcal{O}(1)$ perturbation solution we have

$$\frac{\mathrm{d}U}{\mathrm{d}z} = -\sqrt{-U^2 + \frac{2U^3}{3} + \frac{1}{3}}. \tag{2.28}$$

Integrating Equation (2.28) with $U = 0$ at $z = 0$ gives an implicit solution

$$\frac{2(U-1)\sqrt{1+2U}\operatorname{arctanh}\sqrt{\frac{1+2U}{3}}}{\sqrt{3}(U-1)\sqrt{1+2U}} = \frac{z}{\sqrt{3}} + 2\operatorname{arctanh}\sqrt{\frac{1}{3}}. \qquad (2.29)$$

For the $\mathcal{O}(c)$ perturbation solution we have

$$\frac{\mathrm{d}U}{\mathrm{d}z} = -\sqrt{-U^2 + \frac{2U^3}{3} + \frac{1}{3}} + c\frac{-(U-2)(1+2U)^{3/2} - \sqrt{27}}{5(U-1)\sqrt{1+2U}}, \qquad (2.30)$$

for which we cannot find an exact solution. Nonetheless, Equation (2.30) can be integrated numerically to give a numerical approximation of $U(z)$.
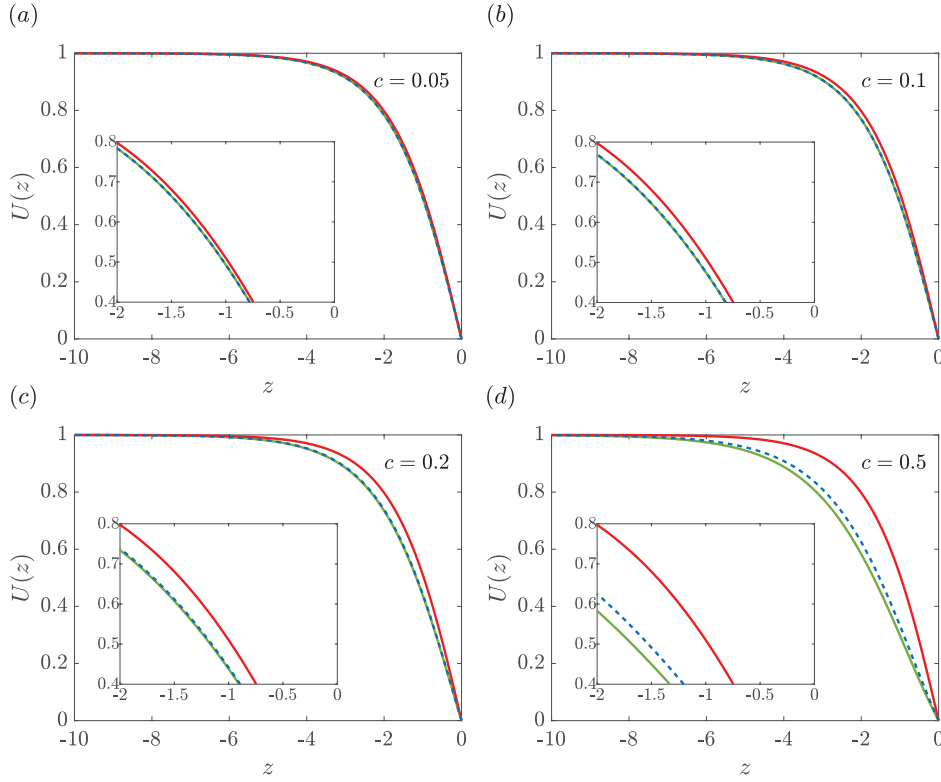
Figure 2.8: **Density profiles comparing the numerical solution of the Fisher-Stefan equation with the perturbation solution for $c \ll 1$.** *(a)* c = 0.05. *(b)* c = 0.1. *(c)* c = 0.2. *(d)* c = 0.5. The solid blue line represents the travelling wave solution obtained from the time-dependent Fisher-Stefan model, (2.2) and shifting the resulting travelling wave profile so that $U(0) = 0$. The red solid line represents the travelling wave profile obtained from the $\mathcal{O}(1)$ perturbation solution and the dashed green line represents the travelling wave profile obtained from the $\mathcal{O}(c)$ perturbation solution. In each subfigure we show an inset magnifying the travelling wave profiles so that the differences between the numerical and perturbation solutions are visually distinct.

Figure 2.8 shows a suite of travelling wave solutions obtained by solving Equations (2.11)-(2.14) (in dashed blue) presented for $c = 0.05, 0.1, 0.2$ and 0.5. In each case the solutions are obtained for a sufficiently long time that

the full time dependent numerical solutions have settled into a travelling wave. These travelling waves are then shifted so that $u(x, t) = 0$ at $z = 0$, where $z = x - ct$. For each value of c, we superimpose plots of the $\mathcal{O}(1)$ solution, given by Equation (2.29) (in solid red). The results show that the $\mathcal{O}(1)$ solution provides an excellent match to the shape of the full numerical solutions of Equations (2.11)-(2.14) for $c = 0.05$. For larger c, however, the $\mathcal{O}(1)$ solution provides a relatively poor approximation. Similarly, for each value of c we also plot the $\mathcal{O}(c)$ solution (in solid green). Here we see that the $\mathcal{O}(c)$ perturbation solution provides an excellent match, being indistinguishable from the full numerical solutions of Equations (2.11)-(2.14) for $c < 0.1$. In each subfigure of Figure 2.8 we also provide an inset showing a magnified region just behind the leading edge of the wavefront to make the comparison between the numerical solution of the partial differential equation and the two perturbation solutions clearer.

2.4 Conclusion

In this work we directly compare features of the travelling wave solutions of the well-known Fisher-KPP model and solutions to the Fisher-Stefan model. A key feature of the Fisher-KPP model is that any positive initial condition with compact support will always evolve into a travelling wave that moves with the minimum wave speed, $c_{\min} = 2$. Therefore, according to the Fisher-KPP model, any initial population will lead to successful invasion. This feature is a potential weakness of the Fisher-KPP model since it is well known that small translocated populations do not always invade, and can become extinct [Griffith et al. 1989]. In contrast, the Fisher-Stefan model is an adaptation of the Fisher-KPP model with a moving boundary, $x = L(t)$. In the Fisher-Stefan model, the evolution of the moving boundary is governed by a one-phase Stefan condition [Du and Lin 2010, Du and Guo 2011, Bunting et al. 2012, Du and Guo 2012, Du et al. 2014a, Du et al. 2014b, Du and Lou 2015]. The Fisher-Stefan model can support travelling wave solutions with speed $c < 2$. Since both the Fisher-KPP and the Fisher-Stefan model support travelling wave solutions, both of these models can be used to simulate invasion processes. However, unlike the Fisher-KPP model, the Fisher-Stefan model also predicts the extinction of certain initial populations, giving rise to the spreading-extinction

dichotomy [Du and Lin 2010, Du and Guo 2011, Bunting et al. 2012, Du and Guo 2012, Du et al. 2014a, Du et al. 2014b, Du and Lou 2015]. The key difference between these two models is the difference in boundary conditions.

The spreading-extinction dichotomy associated with the Fisher-Stefan model has been studied, mainly using rigorous mathematical approaches, leading to many important existence results [Du and Lin 2010, Du and Guo 2011, Bunting et al. 2012, Du and Guo 2012, Du et al. 2014a, Du et al. 2014b, Du and Lou 2015]. One of the aims of this work is to provide a more practical comparison of the Fisher-KPP and Fisher-Stefan models using standard tools of applied mathematics and engineering to provide insight into the similarities and differences between these two models of invasion. It is interesting to note that the partial differential equation descriptions of the Fisher-KPP and Fisher-Stefan models are very different, since the Fisher-KPP model is associated with a fixed domain and the Fisher-Stefan model is a moving boundary problem. In contrast, when we analyse the travelling wave solutions of both models we find that the equations governing the trajectories in the phase plane are the same. Interestingly, standard phase plane arguments for the Fisher-KPP model lead us to conclude that travelling wave solutions with $c < c_{\min} = 2$ are not possible since these solutions would involve negative densities and are therefore not normally recorded or discussed. In this work we show that the travelling wave solutions of the Fisher-Stefan model require that $c < 2$, and it turns out that it is precisely these normally-discarded solutions for the Fisher-KPP model that are relevant for the Fisher-Stefan model.

In the non-dimensional Fisher-Stefan model there is one free parameter, $\kappa > 0$, that relates the dynamics of the moving boundary, $x = L(t)$, and the spatial gradient of the density function at the moving boundary. By analysing trajectories in the phase plane associated with travelling wave solutions of the Fisher-Stefan model we are able to arrive at a relationship between κ and c, confirming that $c \to 2^-$ as $\kappa \to \infty$. However, all phase plane analysis of the Fisher-Stefan model implicitly assumes that a travelling wave solution has formed, whereas numerical solutions of the full partial differential equation description of the Fisher-Stefan model shows that for a fixed initial condition there is a critical value κ_{crit}: for $\kappa > \kappa_{\mathrm{crit}}$ the solution eventually evolves to a travelling wave, whereas for $\kappa < \kappa_{\mathrm{crit}}$ the solution eventually goes extinct.

The time-dependent solutions of the partial differential equation model suggest that near this transition between eventual extinction and eventual travelling wave formation, we have $u(x,t) \ll 1$, suggesting that we can obtain insight using a linearised model. Working in a linearised framework we obtain an approximate solution from which we form a conservation statement describing the net accumulation of total population numbers in the domain. In the critical case where there is zero net accumulation of mass in the domain, we find that there is a critical length, $L_{\mathrm{crit}} = \pi/2$, and whenever $L(t)$ exceeds $\pi/2$ the solution will always evolve to a travelling wave while if $L(t)$ never exceeds $\pi/2$ the density will always eventually go extinct. Using a comparison with the Stefan problem, Equations (2.11)–(2.14) with $\tilde{\lambda} = 0$, we can strengthen these results to be that if $L(t)$ exceeds

$$\frac{\pi}{2} - \kappa \int_0^{L(t)} u(x,t)\, \mathrm{d}x,$$

then a travelling wave will form. Or, if the population goes extinct with $L(t) \to L_{\mathrm{e}}$ as $t \to \infty$, then

$$L(0) + \kappa \int_0^{L(0)} u(x,t)\, \mathrm{d}x < L_{\mathrm{e}} < \frac{\pi}{2}.$$

While it is well-known that there are no closed-form exact solutions describing travelling wave solutions of the Fisher-KPP equation for arbitrary c, it is possible to obtain approximate perturbation solutions for $c \gg 1$ [Canosa 1973, Murray 2002]. Since travelling wave solutions for the Fisher-Stefan model move with speed $c < 2$, we construct a perturbation solution for $c \ll 1$, leading to approximate closed form solutions for the shape of the trajectory in the phase plane which can be used to estimate the shape of the travelling wave. We find that the $\mathcal{O}(c)$ perturbation solutions provide an excellent match to our full numerical solutions for $c < 0.5$, thereby providing analytical insight into the relationship between the speed and shape of the travelling wave solutions of the Fisher-Stefan model.

There are many ways that our work could be extended. For example, all our results involve a thorough comparison between full time-dependent solutions of partial differential equation models and the phase portrait in the case where a travelling wave solution forms. While such comparisons strongly

suggest that the travelling wave solutions are stable, we have not attempted any formal proof of stability. We leave this question for future consideration. Furthermore, this work focuses almost entirely upon travelling wave solutions of the full time dependent partial differential equation models and we do not consider any other kind of time dependent solution in any detail.

The purpose of this work is to compare the Fisher-Stefan and Fisher-KPP models of invasion. Although we begin our work by pointing out that Fisher-Stefan model enables us to simulate population extinction, whereas Fisher-KPP does not, there are also limitations of the Fisher-Stefan model that warrant acknowledgement and discussion. For example, time-dependent solutions of the Fisher-Stefan model that move in the positive x-direction, including travelling wave solutions, involve a loss of the population at the free boundary, $x = L(t)$, since $\partial u / \partial x < 0$ at $x = L(t)$. It could be difficult to justify this loss at the moving boundary based on biological, ecological or physical grounds and/or to calibrate the model to estimate a relevant value of κ. To address this point, it is worthwhile recalling that the Fisher-Stefan model makes use of a one-phase Stefan boundary condition which is a simplification of a more realistic two-phase Stefan boundary condition [Crank 1987, Gupta 2017]. In more realistic applications of invasion, such as malignant cellular invasion into surrounding tissues, there will be a conversion of consumed tissue into malignant cells at the interface [Perumpanani et al. 1999, Gatenby and Gawlinski 1996, Haridas 2017, Browning et al. 2019]. One way of interpreting this conversion from tissues to cells is that there is a loss of one species, in this case the surrounding tissue, that is converted into another species, in this case invasive cells. Therefore, while we appreciate that the practical interpretation of loss at the moving boundary in the one phase Fisher-Stefan model is difficult to justify, we anticipate that this loss at a moving boundary would be very natural in an extended framework where the Fisher-Stefan model is re-cast as a two-phase problem.

This article has no additional data. Key algorithms used to generate results are available on Github at GitHub.

2.5 Additional material

2.5.1 Numerical methods

2.5.1.1 Fisher-KPP model

We solve the Fisher-KPP equation

$$\frac{\partial u}{\partial t} = \frac{\partial^2 u}{\partial x^2} + u(1-u), \tag{2.31}$$

on $0 \leq x \leq x_\infty$, with x_∞ chosen to be sufficiently large. We discretise the domain with a uniform finite difference mesh, with spacing Δx. We approximate the spatial derivatives in Equation (2.31) using a central finite difference approximation, and we integrate Equation (2.31) using an implicit Euler approximation, giving rise to

$$\frac{u_i^{j+1} - u_i^j}{\Delta t} = \left(\frac{u_{i-1}^{j+1} - 2u_i^{j+1} + u_{i+1}^{j+1}}{\Delta x^2}\right) + u_i^{j+1}(1 - u_i^{j+1}), \tag{2.32}$$

for $i = 2, \ldots, m-1$, where $m = x_\infty/\Delta x + 1$ is the total number of spatial nodes on the finite difference mesh, and the index j represents the time index so that we approximate $u(x,t)$ by u_i^j, where $x = (i-1)\Delta x$ and $t = j\Delta t$.

For all numerical solutions of Equation (2.31) we enforce no-flux boundary conditions at $x = 0$ and $x = x_\infty$

$$u_2^{j+1} - u_1^{j+1} = 0, \tag{2.33}$$

$$u_m^{j+1} - u_{m-1}^{j+1} = 0. \tag{2.34}$$

Together, Equations (2.32)–(2.34) form a nonlinear system of algebraic equations that describe how to approximate u_i^{j+1} from u_i^j for $i = 1, \ldots, m$.

We use Newton-Raphson iteration to solve this non-linear system and we continue with the iterations until the infinity norm of the difference between successive estimates of u_i^{j+1} falls below some small tolerance, ϵ. For all results presented we are always careful to choose Δx, Δt and ϵ so that the numerical algorithm produces grid-independent results. To illustrate the accuracy of our algorithm we present results in Figure 2.9 showing the evolution of the solution of Equation (2.31) evolving from an initial condition with compact support. Here we see that the solution rapidly approaches a constant shape, constant

speed travelling wave what moves with the minimum wave speed, $c = 2$, as expected [Murray 2002].
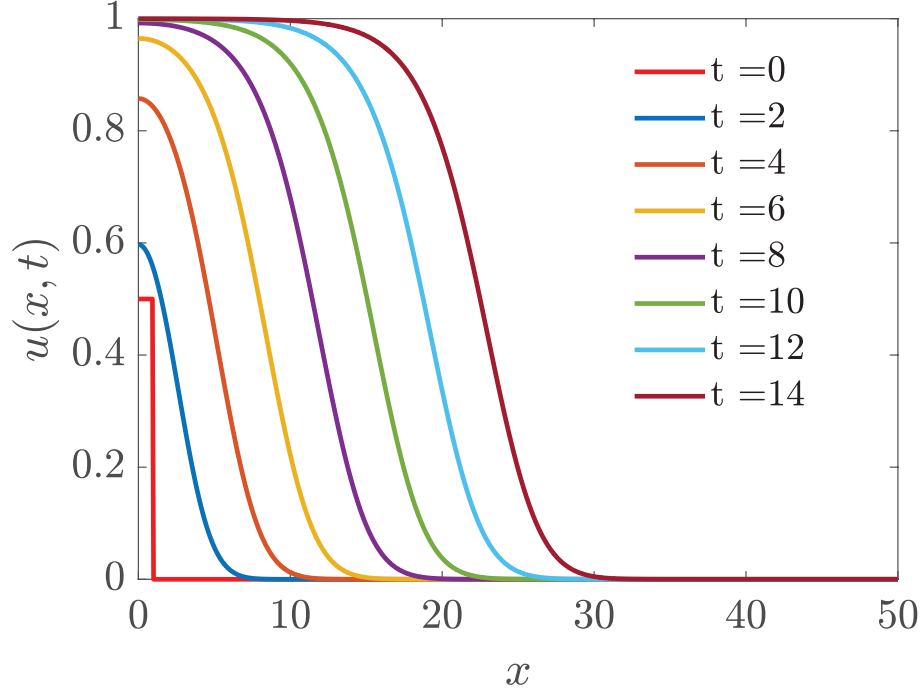
Figure 2.9: Numerical solutions of Equation (2.31) with $\Delta x = 1 \times 10^{-4}$, $\Delta t = 1 \times 10^{-3}$, $x_\infty = 50$ and $\epsilon = 1 \times 10^{-8}$. For this example the initial condition is $u(x, 0) = 0.5$ for $x \leq 1$ and $u(x, 0) = 0$ for $x > 1$.

We have confidence in our numerical results in Figure 2.9 since we find that the results are grid-independent. Furthermore, if we change the initial condition so that $u(x, 0) \sim e^{-ax}$, as $x \to \infty$, we find that $c = 1/a + a$, for $a > 1$, as expected [Murray 2002].

2.5.1.2 Fisher-Stefan equation

To obtain numerical solutions of the Fisher-Stefan problem,

$$\frac{\partial u}{\partial t} = \frac{\partial^2 u}{\partial x^2} + u(1-u), \tag{2.35}$$

for $0 < x < L(t)$ and $t > 0$, we first use a boundary fixing transformation $\xi = x/L(t)$ [Simpson 2015] so that we have

$$\frac{\partial u}{\partial t} = \frac{1}{L^2(t)}\frac{\partial^2 u}{\partial \xi^2} + \frac{\xi}{L(t)}\frac{\mathrm{d}L(t)}{\mathrm{d}t}\frac{\partial u}{\partial \xi} + u(1-u), \tag{2.36}$$

on the fixed domain $0 < \xi < 1$ and $t > 0$. Here $L(t)$ is the length of the domain that we will discuss later. To close the problem we must also transform the appropriate boundary conditions giving

$$\frac{\partial u}{\partial \xi} = 0 \quad \text{at} \quad \xi = 0, \tag{2.37}$$

$$u = 0 \quad \text{at} \quad \xi = 1. \tag{2.38}$$

We spatially discretise Equations (2.36)-(2.38) with a uniform finite difference mesh, with spacing $\Delta\xi$, approximating the spatial derivatives using a central finite difference approximation, giving

$$\frac{u_i^{j+1} - u_i^j}{\Delta t} = \frac{1}{(L^j)^2}\left(\frac{u_{i-1}^{j+1} - 2u_i^{j+1} + u_{i+1}^{j+1}}{\Delta\xi^2}\right)$$
$$+ \frac{\xi}{L^j}\left(\frac{L^{j+1} - L^j}{\Delta t}\right)\left(\frac{u_{i+1}^{j+1} - u_{i-1}^{j+1}}{2\Delta\xi}\right) + u_i^{j+1}(1 - u_i^{j+1}), \tag{2.39}$$

for $i = 2,\dots,m-1$, where $m = 1/\Delta\xi + 1$ is the total number of spatial nodes on the finite difference mesh, and the index j represents the time index so that $u_i^j \approx u(\xi, t)$, where $\xi = (i-1)\Delta\xi$ and $t = j\Delta t$.

Discretising Equations (2.37)-(2.38) leads to

$$u_2^{j+1} - u_1^{j+1} = 0, \tag{2.40}$$

$$u_m^{j+1} = 0. \tag{2.41}$$

We use Newton-Raphson iteration to solve the non-linear system defined by Equations (2.39)-(2.41) and we continue with the iterations until the infinity

norm of the difference between successive estimates of u_i^{j+1} falls below some small tolerance, ϵ. As the Newton-Raphson iterates converge we also update the $L(t)$ by considering the Stefan boundary condition

$$\frac{\mathrm{d}L(t)}{\mathrm{d}t} = -\kappa \frac{\partial u}{\partial x}, \quad \text{at} \quad x = L(t). \tag{2.42}$$

To incorporate the Stefan boundary condition into our numerical method we must transform the boundary condition to the fixed domain,

$$\frac{\mathrm{d}L(t)}{\mathrm{d}t} = -\frac{\kappa}{L(t)} \frac{\partial u}{\partial \xi}, \quad \text{at} \quad \xi = 1, \tag{2.43}$$

and we then discretise Equation (2.43) allowing us to update $L(t + \Delta t)$ as the Newton-Raphson iterates converge

$$L^{j+1} = L^j - \frac{\Delta t \kappa}{L^j} \left(\frac{u_m^{j+1} - u_{m-1}^{j+1}}{\Delta \xi} \right). \tag{2.44}$$

To demonstrate the accuracy of our numerical method to solve the Fisher-Stefan problem we consider a closely related, but simplified problem, that has an exact solution [Kutluay 1997]. We consider

$$\frac{\partial u}{\partial t} = \frac{\partial^2 u}{\partial x^2}, \tag{2.45}$$

on $0 < x < L(t)$ for $t > 0$, with a moving boundary at $L(t)$. The boundary conditions are given by

$$\frac{\partial u}{\partial x} = -\mathrm{e}^t \quad \text{at} \quad x = 0, \tag{2.46}$$

$$u = 0 \quad \text{at} \quad x = L(t), \tag{2.47}$$

with the Stefan condition is

$$\frac{\mathrm{d}L(t)}{\mathrm{d}t} = -\frac{\partial u}{\partial x} \quad \text{at} \quad x = L(t), \tag{2.48}$$

With $L(0) = 0$, the exact solution to this moving boundary problem is

$$u(x, t) = -\mathrm{e}^{(t-x)} - 1, \tag{2.49}$$

on $0 < x < t$, for $0 < t < 1$. Therefore, by setting $\tilde{\lambda} = 0$, $\kappa = 1$ and

54

changing the boundary condition from $\partial u/\partial x = 0$ at $x = 0$ to $\partial u/\partial x = -\mathrm{e}^t$ at $x = 0$, our numerical scheme ought to approximate the exact solution, Equation (2.49). Since the initial condition for the exact solution has $L(0) = 0$, we make progress by evaluating the exact solution at $t = \tau < 1$ and we use this solution as the initial condition from which the numerical solution can be evaluated for $t > \tau$. Results in Figure 2.10 compare numerical solutions and this exact solution with $\tau = 0.2$. This exercise gives us confidence in our numerical solution of the moving boundary problem since the numerical and exact solutions in Figure 2.10 are indistinguishable at this scale.
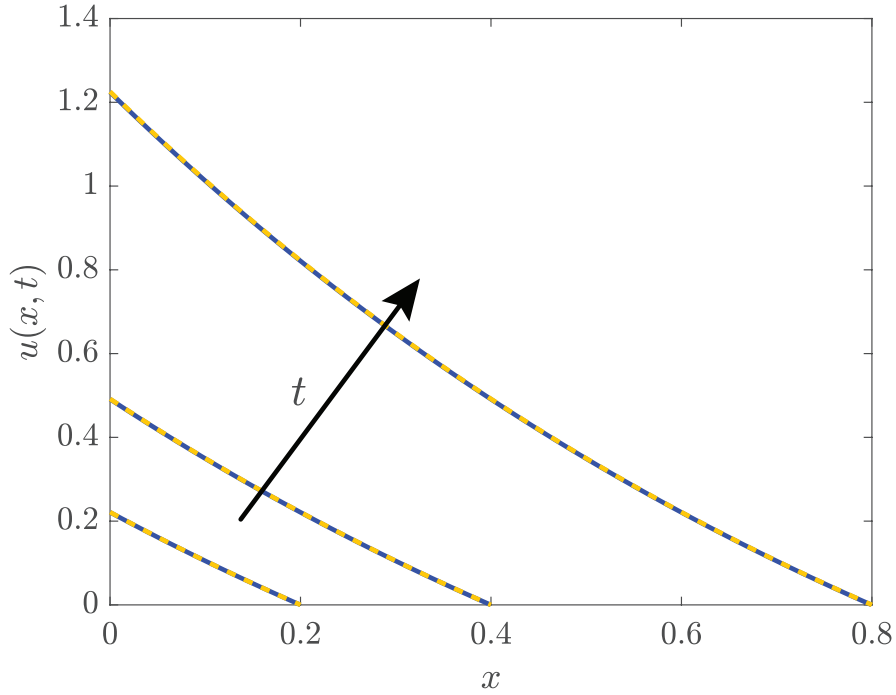
Figure 2.10: Comparison of numerical and exact solutions for the simplified moving boundary problem. Numerical solutions are obtained with $\Delta\xi = 1 \times 10^{-4}$, $\Delta t = 1 \times 10^{-3}$ and $\epsilon = 1 \times 10^{-8}$. The numerical solutions (blue solid) are superimposed on the exact solutions (yellow dashed) and solutions are shown at $t = 0.2, 0.4$ and 0.8, with the arrow showing the direction of increasing t.

2.5.1.3 Numerical estimate of c

In this work we solve both the Fisher-KPP and the Fisher-Stefan models and use the time-dependent solutions to provide an estimate of the travelling wave speed, c. To obtain this estimate we specify a contour value, $u(x, t) = u^*$. At the end of each time step in we use linear interpolation to estimate x^* such that $u(x^*, t) = u^*$. Therefore, at the end of each time step we have estimates of both $x^*(t + \Delta t)$ and $x^*(t)$, allowing us to estimate the speed at which the

contour moves

$$c = \frac{x^*(t + \Delta t) - x^*(t)}{\Delta t}. \qquad (2.50)$$

We find that evaluating Equation (2.50) at each time step leads to a time series of estimates of c, and we find that these estimates asymptote to some positive constant value as $t \to \infty$ for those problems that support a travelling wave solution. For all results presented we set $u^* = 0.5$, but we find that our estimates of c obtained using this approach are not particularly sensitive to our choice of u^* [Landman et al. 2005].

2.5.1.4 Construction of the phase planes

The dynamical system that defines the phase plane for travelling wave solutions of the Fisher-KPP and Fisher-Stefan models is given by

$$\frac{dU}{dz} = V, \qquad (2.51)$$

$$\frac{dV}{dz} = -cV - U(1 - U). \qquad (2.52)$$

Using the chain rule, Equations (2.51)-(2.52) can be written equivalently as

$$\frac{dV}{dU} = \frac{-cV - U(1 - U)}{dV}, \qquad (2.53)$$

where $V = V(U)$.

When we construct phase planes in the main document we use a combination of exact and computational techniques. The locations of equilibrium points and boundary conditions are plotted on the phase plane using exact mathematical expressions for their location. The flow, defined exactly by Equations (2.51)-(2.52), is plotted using the `quiver` function in MATLAB [Mathworks 2021]. To estimate the trajectories in the phase plane we integrate Equations (2.51)-(2.52) numerically using the `ODE45` function in MATLAB [Mathworks 2021]. When we compute the phase plane trajectories we set the tolerance to 1×10^{-4} in `ODE45` and we choose the initial condition using information from the linear analysis nearby the $(1, 0)$ equilibrium point to ensure that the initial condition is close to the heteroclinic orbit.

Chapter 3

Invading and receding sharp–fronted travelling waves

Statement of Contribution of Co-Authors for Thesis by Published Paper

The following is the suggested format for the required declaration provided at the start of any thesis chapter which includes a co-authored publication.
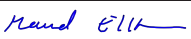
The authors listed below have certified that:

1. they meet the criteria for authorship and that they have participated in the conception, execution, or interpretation, of at least that part of the publication in their field of expertise;
2. they take public responsibility for their part of the publication, except for the responsible author who accepts overall responsibility for the publication;
3. there are no other authors of the publication according to these criteria;
4. potential conflicts of interest have been disclosed to (a) granting bodies, (b) the editor or publisher of journals or other publications, and (c) the head of the responsible academic unit, and
5. they agree to the use of the publication in the student's thesis and its publication on the QUT's ePrints site consistent with any limitations set by publisher requirements.

In the case of this chapter 3:

Please state the publication title and date of publication or status:

El-Hachem M, McCue SW, Simpson MJ, 2021. Invading and receding sharp-fronted travelling waves. *Bulletin of Mathematical Biology* **83**, 35. Published on 21 February 2021

Contributor	Statement of contribution*
Maud El-Hachem *Maud Ell[signature]* 15/11/2021	Conceived and designed the study, performed all numerical and symbolic calculations, drafted the article, and gave final approval for publication.
Scott W McCue	Conceived and designed the study, gave final approval for publication.
Matthew J Simpson	Conceived and designed the study, gave final approval for publication.

Principal Supervisor Confirmation

I have sighted email or other correspondence from all Co-authors confirming their certifying authorship.
(If the Co-authors are not able to sign the form please forward their email or other correspondence confirming the certifying authorship to the GRC).

Professor Matthew Simpson   *[signature]*   16/11/2021
Name   Signature   Date

3.1 Abstract

Biological invasion, whereby populations of motile and proliferative individuals lead to moving fronts that invade vacant regions, are routinely studied using partial differential equation (PDE) models based upon the classical Fisher–KPP equation. While the Fisher–KPP model and extensions have been successfully used to model a range of invasive phenomena, including ecological and cellular invasion, an often–overlooked limitation of the Fisher–KPP model is that it cannot be used to model biological recession where the spatial extent of the population decreases with time. In this work we study the *Fisher–Stefan* model, which is a generalisation of the Fisher–KPP model obtained by reformulating the Fisher–KPP model as a moving boundary problem. The nondimensional Fisher–Stefan model involves just one parameter, κ, which relates the shape of the density front at the moving boundary to the speed of the associated travelling wave, c. Using numerical simulation, phase plane and perturbation analysis, we construct approximate solutions of the Fisher–Stefan model for both slowly invading and receding travelling waves, as well as for rapidly receding travelling waves. These approximations allow us to determine the relationship between c and κ so that commonly–reported experimental estimates of c can be used to provide estimates of the unknown parameter κ. Interestingly, when we reinterpret the Fisher–KPP model as a moving boundary problem, many disregarded features of the classical Fisher–KPP phase plane take on a new interpretation since travelling waves solutions with $c < 2$ are normally disregarded. This means that our analysis of the Fisher–Stefan model has both practical value and an inherent mathematical value.

3.2 Introduction

Biological invasion is normally associated with situations where individuals within a population undergo both movement and proliferation events [Edelstein-Keshet 2005, Kot 2003, Murray 2002]. Such proliferation and movement, combined, can give rise to an *invading front*. An invading front involves a population moving into a previously unoccupied space. Ecologists are particularly interested in biological invasion. For example, Skellam's [Skellam 1951]

59

work studies the invasion of muskrats in Europe; similarly, Otto and coworkers [Otto et al. 2018] study the spatial spreading of insects, whereas Bate and Hilker [Bate and Hilker 2019] study the invasion of predators in a predator–prey system. As with many other similar examples, these three studies all make use of partial differential equation (PDE) models of invasion.

Another common application of biological invasion is the study of cell invasion, including wound healing and malignant spreading. Mathematical models of wound healing often consider the closure of a wound space by populations of cells that are both migratory and proliferative [Flegg et al. 2020, Jin et al. 2016, Jin et al. 2017, Maini et al. 2004a, Sherratt and Murray 1990]. Malignant invasion involves combined migration and proliferation of tumour cells, which leads to tumour invasion into surrounding tissues [Byrne 2010, Curtin et al. 2020, Strobl et al. 2020, Swanson et al. 2003], as illustrated in Figure 3.1(a)–(b), which shows the invasion of malignant melanoma cells. Regardless of the application, many mathematical models of biological invasion involve the study of moving fronts, shown schematically in Figure 3.1(c), using PDE models [Browning et al. 2019, Sengers et al. 2007, Warne et al. 2019]. We interpret the schematic in Figure 3.1(c) by thinking of the population as being composed of individuals that undergo diffusive migration with diffusivity $D > 0$, and logistic proliferation, with proliferation rate $\lambda > 0$. As indicated, these two processes can lead to the spatial expansion as the population density profile moves in the positive x–direction.

The Fisher–KPP model [Canosa 1973, Fisher 1937, Kolmogorov et al. 1937, Edelstein-Keshet 2005, Murray 2002] is probably the most commonly used reaction–diffusion equation to describe biological invasion in a single homogeneous population. The Fisher–KPP model assumes that individuals in the population proliferate logistically and move according to a linear diffusion mechanism [Fisher 1937, Kolmogorov et al. 1937]. Travelling wave solutions of the Fisher–KPP model are often used to mimic biological invasion [Maini et al. 2004a, Maini et al. 2004b, Simpson et al. 2013]. Long time solutions of the Fisher–KPP model that evolve from initial conditions with compact support eventually form smooth travelling waves without compact support such that $u(x, t) \to 0$ as $x \to \infty$. These travelling wave solutions of the Fisher-KPP model move with speed $c = 2\sqrt{\lambda D}$ [Edelstein-Keshet 2005, Murray 2002].
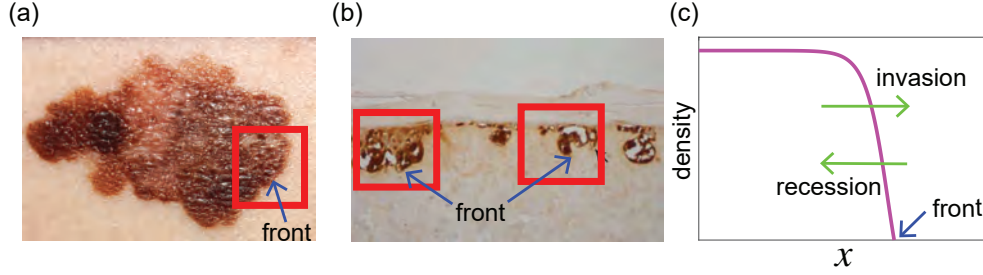
Figure 3.1: Biological motivation. (a) Malignant melanoma (dark) spreading superficially across the skin surface [NCI 1985] (reproduced with permission). (b) Vertical cross section through a human skin equivalent experiment showing the inward invasion of a population of melanoma cells (dark) [Haridas 2017, Haridas et al. 2018] (reproduced with permission). In (a)–(b) the region containing the leading edge of the invading population is highlighted in a red rectangle and the location of the sharp front is highlighted with blue arrows. (c) Schematic solution of a mathematical model showing a sharp–fronted density profile that could either invade or recede, by moving in the positive or negative x–direction, respectively. In the schematic the location of the sharp front is also highlighted with a blue arrow.

There are many other popular choices of single–species mathematical models of biological invasion; for example, the *Porous–Fisher* model [McCue et al. 2019, Sánchez Garduno and Maini 1995, Sherratt and Marchant 1996, Witelski 1995] is a generalisation of the Fisher–KPP model with a degenerate nonlinear diffusion term which results in sharp–fronted travelling wave solutions. Long time solutions of the Porous–Fisher model that evolve from initial conditions with compact support lead to invasion waves that move with speed $c = \sqrt{(\lambda D)/2}$ [Murray 2002]. Another generalisation of the Fisher–KPP model is the *Fisher–Stefan* model [Du and Lin 2010, Du et al. 2014a, Du et al. 2014b, Du and Lou 2015]. This approach involves reformulating the Fisher–KPP model as a moving boundary problem on $0 < x < L(t)$. Setting the density to zero at the moving front, $x = L(t)$, means that the Fisher–Stefan model also gives rise to sharp–fronted solutions like the Porous–Fisher model [El-Hachem et al. 2019]. The motion of $L(t)$ in the Fisher–Stefan model is controlled by a one–phase Stefan condition [Crank 1987, Dalwadi et al. 2020, Hill 1987, Mitchell and O'Brien 2014] with parameter κ.

Populations of motile and proliferative individuals do not always invade new territory; in fact, sometimes motile and proliferative populations recede or retreat. The spatial recession of biological populations are often described in ecology. For example, populations of desert locusts [Ibrahim et al. 2000],

61

plants in grazed prairies [Sinkins and Otfinowski 2012], Arctic foxes [Killengreen et al. 2007] and dung beetles [Horgan 2009] have all been observed to undergo both invasion and recession in different circumstances. While some previous mathematical models of biological invasion and recession have been described [Chaplain et al. 2020, El-Hachem et al. 2020, Painter and Sherratt 2003], these previous models often focus on describing interactions between multiple subpopulations in a heterogeneous community rather than classical single species models, such as the Fisher–KPP model. In fact, none of the three commonly–used single species models described here, the Fisher–KPP, Porous–Fisher or Fisher–Stefan models, have been used to study biological recession. This is probably because neither the classical Fisher–KPP or Porous–Fisher models ever give rise to receding populations. Given that the recession of population fronts is often observed, this limitation of the commonly–used Fisher–KPP and Porous–Fisher models is important and often overlooked.

The ability of these three single–species models to support invading or receding travelling wave solutions is illustrated schematically in Figure 3.2. At this point it useful to provide a physical interpretation of what we mean by the *invading* travelling wave. If we consider a fixed position, $x = X$, a monotone invading travelling wave means that the density at that point, $u(X, t)$, increases with time, $\partial u(X, t)/\partial t > 0$. In contrast, a monotone *receding* travelling wave leads to the opposite behaviour where $\partial u(X, t)/\partial t < 0$ at a fixed position $x = X$. This simple interpretation is useful because it holds regardless of the spatial orientation of the travelling wave. For example, in this work we always consider moving fronts with the spatial orientation shown in Figure 3.1(c). Here, invasion is associated with movement in the positive x–direction and recession is associated with movement in the negative x–direction. All results and definitions in this work hold when we consider fronts with the opposite spatial orientation, where invasion is associated with movement in the negative x–direction, and recession is associated with movement in the positive x–direction. For convenience we adopt the usual convention shown in Figure 3.1(c), but it is useful to remember that all results hold for the travelling waves with the opposite spatial orientation.

In this work, we focus on the Fisher–Stefan model to study biological invasion *and* recession. As just mentioned, unlike the classical Fisher–KPP and
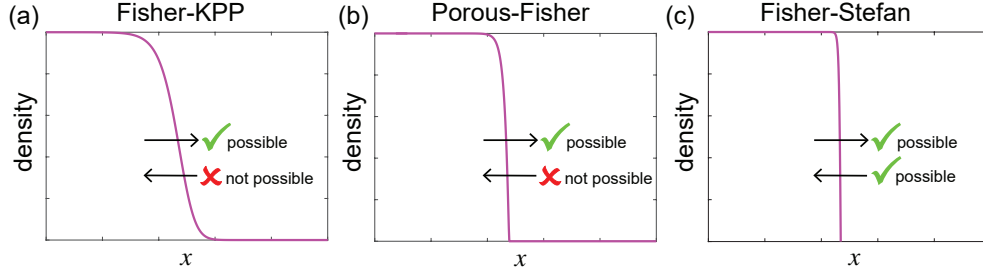
Figure 3.2: Travelling wave schematic. (a) Travelling wave solution of the Fisher-KPP model supports invasion but not recession. (b) Travelling wave solution of the Porous–Fisher model supports invasion but not recession. (c) Travelling wave solution of the Fisher–Stefan model supports invasion and recession.

Porous–Fisher models, the Fisher–Stefan model can be used to simulate both biological invasion and recession. One way of interpreting this difference is that the Fisher–Stefan model could be thought of as being more versatile than the more commonly–used Fisher–KPP or Porous–Fisher models. As we will show, travelling wave solutions of the Fisher–Stefan model can be used to represent biological invasion with a positive travelling wave speed, $c > 0$, as well as being able to model biological recession with a negative travelling wave speed, $c < 0$. We explore these travelling wave solutions using full time–dependent numerical solutions of the governing PDE, phase plane analysis, and perturbation approximations. A regular perturbation approximation around $c = 0$ provides insight into both slowly invading and receding travelling waves, whereas a matched asymptotic expansion in the limit as $c \to -\infty$ provides insight into rapidly receding waves. These perturbation solutions provide simple relationships between κ and c. For example, we show that slowly invading or receding travelling wave solutions of the Fisher-Stefan model move with speed $c \sim \kappa/\sqrt{3}$ as $\kappa \to 0$, whereas rapidly receding travelling wave solutions of the Fisher-Stefan model move with speed $c \sim 2^{-1}(\kappa + 1)^{-1/2}$ as $\kappa \to -1^+$. Such relationships are useful because estimates of κ are not available in the literature, whereas experimental measurements of c are relatively straightforward to obtain [Maini et al. 2004a, Maini et al. 2004b, Simpson et al. 2007].

3.3 Mathematical model

In this work all dimensional variables and parameters are denoted with a circumflex and nondimensional quantities are denoted using regular symbols. The Fisher–Stefan model is a reformulation of the classical Fisher–KPP equation to include a moving boundary,

$$\frac{\partial \hat{u}}{\partial \hat{t}} = \hat{D}\frac{\partial^2 \hat{u}}{\partial \hat{x}^2} + \hat{\lambda}\hat{u}\left(1 - \frac{\hat{u}}{\hat{K}}\right), \quad 0 < \hat{x} < \hat{L}(\hat{t}), \tag{3.1}$$

where $\hat{u}(\hat{x}, \hat{t}) \geq 0$ is the population density that depends upon position, $\hat{x}$, and time, $\hat{t} > 0$. Individuals in the population move according to a linear diffusion mechanism with diffusivity $\hat{D} > 0$, the proliferation rate is $\hat{\lambda} > 0$ and the carrying capacity density is $\hat{K} > 0$.

We consider the Fisher–Stefan model on $0 < \hat{x} < \hat{L}(\hat{t})$, with a zero flux condition at the origin. The sharp front is modelled by setting the density to be zero at the leading edge, giving

$$\frac{\partial \hat{u}(0, \hat{t})}{\partial \hat{x}} = 0, \qquad \hat{u}(\hat{L}(\hat{t}), \hat{t}) = 0. \tag{3.2}$$

The evolution of the domain is controlled by a classical one–phase Stefan condition that relates the speed of the moving front to the spatial gradient of the density profile at the moving boundary,

$$\frac{\mathrm{d}\hat{L}(\hat{t})}{\mathrm{d}\hat{t}} = -\hat{\kappa}\frac{\partial \hat{u}}{\partial \hat{x}}\bigg|_{\hat{x}=\hat{L}(\hat{t})}, \tag{3.3}$$

where $\hat{\kappa}$ is a constant to be specified [Crank 1987, Dalwadi et al. 2020, Hill 1987, Mitchell and O'Brien 2014]. While it is possible to consider different, potentially more complicated conditions at the moving boundary [Crank 1987, El-Hachem et al. 2020, Gaffney and Maini 1999, Hill 1987], here we restrict our attention to the classical one–phase Stefan condition.

In the context of cell invasion, typical values of $\hat{D}$ are approximately 100–3000 μm^2/h [Johnston et al. 2015, Johnston et al. 2016, Jin et al. 2016]; typical values $\hat{\lambda}$ are approximately 0.04–0.06 /h [Johnston et al. 2015, Jin et al. 2016]; and typical values of the carrying capacity density are 0.001–0.003 cells/μm^2 [Johnston et al. 2015, Jin et al. 2016]. To simplify our analysis we will now nondimensionalise the Fisher–Stefan model.

3.3.1 Nondimensional model

Introducing dimensionless variables, $x = \hat{x}\sqrt{\hat{\lambda}/\hat{D}}$, $t = \hat{\lambda}\hat{t}$, $u = \hat{u}/\hat{K}$, $L(t) = \hat{L}(\hat{t})\sqrt{\hat{\lambda}/\hat{D}}$ and $\kappa = \hat{\kappa}/\hat{D}$, the Fisher–Stefan model can be simplified to give

$$\frac{\partial u}{\partial t} = \frac{\partial^2 u}{\partial x^2} + u\,(1 - u)\,, \quad 0 < x < L(t), \tag{3.4}$$

$$\frac{\partial u(0,t)}{\partial x} = 0, \qquad u(L(t), t) = 0, \tag{3.5}$$

$$\frac{\mathrm{d}L(t)}{\mathrm{d}t} = -\kappa \frac{\partial u(L(t), t)}{\partial x}, \tag{3.6}$$

so that we only need to specify one parameter, κ together with initial conditions for u and L. As mentioned previously, estimates of diffusivity, proliferation rate and carrying capacity in the context of cell invasion are available in the literature [Jin et al. 2016, Maini et al. 2004a]. In contrast, estimates of κ are not. Therefore, one of the aims of this work is to provide mathematical insight into how estimates of κ can be obtained, and we will provide more discussion on this point later.

In all cases where we consider time–dependent solutions of Equations (3.4)–(3.6) we always choose the initial condition to be

$$u(x, 0) = \alpha \left(1 - \mathrm{H}[x - L(0)]\right), \tag{3.7}$$

where $\alpha > 0$ is a positive constant and $\mathrm{H}[\cdot]$ is the Heaviside function, so that $u(x, 0) = \alpha$ for $x < L(0)$ and $u(x, L(0)) = 0$.

To solve Equations (3.4)–(3.7) numerically, we transform the governing equations from an evolving domain, $0 < x < L(t)$ to a fixed domain, $0 < \xi < 1$ by setting $\xi = x/L(t)$. The transformed equations on the fixed domain are spatially discretised using a uniform finite difference mesh and standard central finite difference approximations. The resulting system of nonlinear ordinary differential equations (ODE) is integrated through time using an implicit Euler approximation. Newton–Raphson iteration and the Thomas algorithm are used to solve the resulting system of nonlinear algebraic equations [Simpson et al. 2005]. Full details of the numerical method are given in the Supplementary Material; MATLAB implementation of the algorithm is available on GitHub.

3.4   Results and Discussion

We begin our analysis of the Fisher–Stefan model by presenting some time–dependent solutions of Equations (3.4)–(3.7) before analysing these solutions using the phase plane and perturbation techniques.

3.4.1   Time–dependent partial differential equation solutions

Results in Figure 3.3 show a suite of numerical solutions of Equations (3.4)–(3.7) plotted at regular time intervals. Similar to our previous work [El-Hachem et al. 2019], the results in Figure 3.2(a)–(d) suggest that the initial condition evolves into invading travelling waves for $\kappa > 0$. However, unlike our previous work, the results in Figure 3.2(e)–(h) show that we obtain receding travelling waves for $\kappa < 0$. To obtain these solutions we specify a value of κ, as indicated in each subfigure, and then measure the eventual speed of the travelling wave, c, by estimating $\mathrm{d}L(t)/\mathrm{d}t$ using the numerical solution of the PDE as described in the Supplementary Material. Therefore, in this approach to studying the travelling wave solutions, we treat κ as an input to the numerical algorithm, and c is an output. In fact, in generating results in Figure 3.2 we took great care to choose κ so that our resulting estimates of c are clean values, such as $c = 0.25, 0.50, 0.75$ and 1.00. We will explain how to make this choice later, in Section 3.4.2.

All results in Figure 3.3 correspond to the initial condition (3.7) with $\alpha = 0.5$. Additional results in the Supplementary Material show similar results for different initial conditions by varying the choice of $\alpha = 0.25, 0.75$ and 1.00. These additional results strongly suggest that the time-dependent solutions of Equations (3.4)–(3.7) always approaches the same travelling wave solution with the same speed, c, regardless of the choice of α.
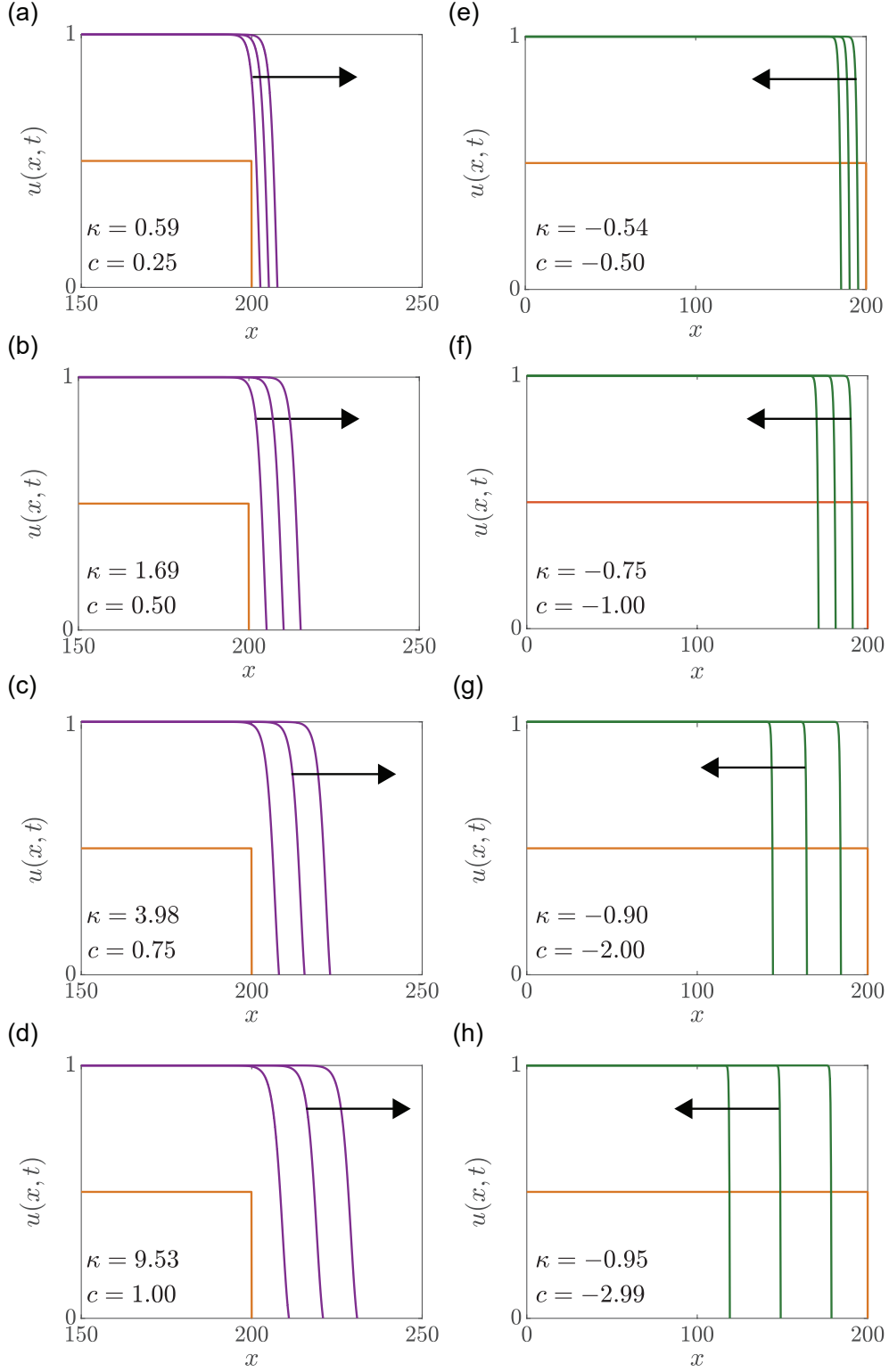
Figure 3.3: Late-time numerical solutions of the Fisher–Stefan model.
Numerical solutions of Equations (3.4)–(3.7) are given at $t = 0, 10, 20$ and 30. The initial condition is given by Equation (3.7) with $\alpha = 0.5$ and $L(0) = 200$. Results in (a)–(d) lead to invading travelling waves with $c = 0.25, 0.50, 0.75$ and 1.00, respectively. These travelling waves are obtained by choosing $\kappa = 0.5859, 1.6879, 3.9823$ and 9.5315, respectively. Results in (e)–(h) lead to receding travelling waves with $c = -0.50, -1.00, -2.00$ and -2.99, respectively. These receding travelling waves are obtained by choosing $\kappa = -0.5387, -0.7529, -0.9036$ and -0.9510, respectively. Our estimates of c correspond are obtained at late time, here $t = 30$. Note that estimates of κ are reported in the caption to four decimal places, whereas the estimates given in the subfigures are reported to two decimal places to keep the figure neat.

Results in Figure 3.3 show that c is an increasing function of κ. The density profile at the leading edge is sharp in all cases and indeed the slope of u at $x = L(t)$ decreases as κ decreases. The shape of the density profile differs depending on whether we consider an invading or receding travelling wave, since the receding travelling waves are much steeper than the invading travelling waves. These numerical results in Figure 3.2 are interesting since neither the Fisher–KPP nor the Porous–Fisher can be used to simulate this range of behaviours. The feature of the Fisher–Stefan model which enables us to simulate both invasion and retreat is the choice of κ. We will now explore the relationship between c and κ by studying the travelling wave solutions in the phase plane.

Interpreting the Stefan condition, Equation (3.6), in terms of the underlying biology is an open question that is very interesting. In essence, the Stefan condition states that the time rate of change of the right-most position of the boundary is proportional to the spatial gradient of the density at that point, $\mathrm{d}L(t)/\mathrm{d}t \propto \partial u(L(t), t)/\partial x$. There are many ways to interpret this widely–used boundary condition. In the usual geometry, shown in Figure 3.1(a), we have $\partial u(L(t), t)/\partial x < 0$, and setting the coefficient of proportionality to be negative leads to the standard case where $L(t)$ increases. One way of interpreting this is that the position of the boundary evolves so that $L(t)$ moves down the spatial gradient of $u(x, t)$ at $x = L(t)$. In the same situation as in Figure 3.1(a), where $\partial u(L(t), t)/\partial x < 0$, setting the coefficient of proportionality to be positive leads to $L(t)$ decreasing. One way of interpreting this is that the position of the boundary evolves so that $L(t)$ moves up the spatial gradient of $u(x, t)$ at $x = L(t)$. Of course, this theoretical interpretation is not tested or confirmed biologically, but this distinction between invasion and recession, dictated by the sign of the proportionality coefficient in the Stefan condition, is analogous to the distinction between *chemoattraction* and *chemorepulsion* in bacterial and cellular chemotaxis [Edelstein-Keshet 2005, Keller and Segal 1971, Murray 2002]. In practical terms we provide a description of how κ could be estimated using simple experiments in the Discussion section.

3.4.2   Phase plane analysis

To analyse travelling wave solutions of the Fisher–Stefan model in the phase plane we consider Equation (3.4) in terms of the travelling wave coordinate, $z = x - ct$ and we seek solutions of the form $u(x, t) = U(z)$ which leads to the following ODE,

$$\frac{\mathrm{d}^2 U}{\mathrm{d}z^2} + c\frac{\mathrm{d}U}{\mathrm{d}z} + U(1 - U) = 0, \quad -\infty < z < 0, \tag{3.8}$$

with boundary conditions

$$U(-\infty) = 1, \quad U(0) = 0, \tag{3.9}$$

$$c = -\kappa\frac{\mathrm{d}U(0)}{\mathrm{d}z}, \tag{3.10}$$

where we choose $z = 0$ to correspond to the moving boundary.

To study Equation (3.8) in the phase plane we rewrite this second order ODE as a first order dynamical system

$$\frac{\mathrm{d}U}{\mathrm{d}z} = V, \tag{3.11}$$

$$\frac{\mathrm{d}V}{\mathrm{d}z} = -cV - U(1 - U), \tag{3.12}$$

with the equilibrium points $(0, 0)$ and $(1, 0)$. Equations (3.11)–(3.12) are the well–known dynamical system associated with travelling wave solutions of the classical Fisher–KPP model [Canosa 1973, Edelstein-Keshet 2005, Murray 2002]. Therefore, many previous results for this system also apply here to the Fisher–Stefan model. For example, linear stability analysis shows that $(1, 0)$ is a saddle point for all values of c, whereas $(0, 0)$ is a stable node if $c \geq 2$; a stable spiral if $0 < c < 2$; a centre if $c = 0$; an unstable spiral if $-2 < c < 0$; and, an unstable node if $c \leq -2$. Typically, in the regular analysis of the Fisher–KPP model the possibility of travelling wave solutions with $c < 0$ (and $\partial u/\partial x < 0$) is never considered because time–dependent numerical solutions of the Fisher–KPP model only ever evolve into invading travelling waves with positive wave speed. Further, in the regular analysis of the Fisher–KPP model, the possibility of travelling waves with $c < 2$ is disregarded because linear stability analysis shows that $(0, 0)$ is a stable spiral, implying that $U(z) < 0$ for various intervals in z [Murray 2002]. Our previous

work has shown that this caution is not required for the Fisher–Stefan model as these often–neglected trajectories in the phase plane are, in fact, associated with physically–relevant travelling wave solutions [El-Hachem et al. 2019]. To explore these ideas will now visualise the phase plane for each travelling wave shown previously in Figure 3.3. To show trajectories in the phase plane we solve Equations (3.11)–(3.12) numerically using Heun's method. A Matlab implementation of our algorithm to visualise these phase planes is available on GitHub. Unlike the full time–dependent solution of the PDE model where we treat κ as the input and c as the output of the numerical algorithm, here in the phase plane we treat c as the input into the numerical algorithm to generate the phase plane trajectory and we use this trajectory to estimate κ, as we will now explain. Phase planes for $c = 0.25, 0.50, 0.75$ and 1.00 are given in Figure 3.4(a)–(d), respectively. Similarly, phase planes for $c = -0.50, -1.00, -2.00$ and -2.99 are given in Figure 3.4(e)–(f), respectively. Each phase plane in Figure 3.4 corresponds to the particular PDE solution in Figure 3.3.

The phase planes in Figure 3.4(a)–(d) correspond to invading fronts with various values of $0 < c < 2$. As we previously describe [El-Hachem et al. 2019], these phase plane trajectories are usually neglected in the usual analysis of the Fisher–KPP model since they leave near $(1, 0)$ and eventually spiral into $(0, 0)$ as $z \to \infty$, implying that $U(z) < 0$ for certain intervals along the trajectory. In contrast, the travelling wave solution of the Fisher–Stefan model must also satisfy the Stefan condition at $U(z) = 0$, which means that we truncate the trajectory at $z = 0$ and only focus on that part of the trajectory in the fourth quadrant of the phase plane where $U(z) > 0$. Each trajectory in Figure 3.4(a)–(d) intersects the $V(z)$ axis at a special point, $(0, V^*)$, which corresponds to the Stefan condition where $U = 0$ and $c = -\kappa V^*$. Estimating V^* from the numerically–generated phase plane trajectory allows us to estimate κ. Following this approach we obtain estimates of κ for each value of c, and these estimates compare very well with the estimates used to generate the time–dependent PDE solutions in Figure 3.3. These phase planes explain why invading travelling waves for the Fisher–Stefan model are restricted to $0 < c < 2$ since setting $c > 2$ means that the origin is a stable node and the heteroclinic orbit between $(1, 0)$ and $(0, 0)$ never intersects the $V(z)$ axis, giving $c \to 2^-$ as $\kappa \to \infty$ [Du and Lin 2010, El-Hachem et al. 2019].

Figure 3.4: Phase plane for travelling wave solutions of the Fisher–Stefan model. Equilibrium points are shown as black discs, and the point at which the trajectory intersects the $V(z)$ axis are shown as pink discs. The numerical solution of the dynamical system, Equations (3.11)–(3.12) is shown in dashed orange and the travelling wave solution obtained from the numerical time–dependent PDE solutions, Equations (3.4)–(3.7) is superimposed in solid purple for the invading travelling waves in (a)–(d) and in solid green for the receding travelling waves in (e)–(h). The flow associated with the dynamical system is shown with blue vectors obtained using Matlab's quiver function.

For completeness we also show the remaining portion of the phase plane trajectory in Figure 3.4(a)–(d) that eventually spirals into $(0,0)$ as $z \to \infty$. Further, for each phase plane in Figure 3.3(a)–(d) we take the late time PDE solution from Figure 3.3(a)–(d) and transform these PDE solutions into a $(U(z), V(z))$ phase plane trajectory, and superimpose these curves in the phase planes in Figure 3.4(a)–(d). In each case the trajectory obtained by solving the dynamical system numerically is visually indistinguishable, at this scale, from the trajectory obtained by plotting the PDE solutions in the phase plane.

The phase planes in Figure 3.4(e)–(h) correspond to receding travelling waves with various $c < 0$. As we previously describe, these phase planes for $c < 0$ are not normally considered for the Fisher–KPP model since receding travelling wave solutions of the Fisher-KPP model are not possible. Here we see that we are interested in that part of the trajectory in the fourth quadrant that leaves $(0, V^*)$ and joins $(1, 0)$ as $z \to \infty$. Again, we can use this trajectory to estimate κ and the estimates from the phase plane compare well with the values used in the full time–dependent PDE solutions in Figure 3.3(e)–(h). For completeness we take the late–time PDE solutions in Figure 3.3(e)–(h) and superimpose these trajectories in Figure 3.4(e)–(h) where we see that the numerical solution of the trajectory obtained from the dynamical system is again visually indistinguishable from the trajectory obtained from the PDE solutions. Unlike the invading travelling wave solutions where linear stability analysis in the phase plane gives us the condition that $0 < c < 2$, there is no restriction on c in the phase plane so that the Fisher–Stefan model gives rise to receding travelling waves with $-\infty < c < 0$.

Now we have shown that both invading and receding travelling wave solutions of the Fisher–Stefan model can be studied in the phase plane, we will analyse the governing equations in the phase plane to provide more detailed insight into the relationship between κ and c. This will be important because estimates of κ are not available in the literature, whereas estimates of c are easier to obtain experimentally [Maini et al. 2004a, Maini et al. 2004b, Simpson et al. 2007].

3.4.3 Analysis

3.4.3.1 Exact solution for stationary waves

Here we solve for the shape of the stationary travelling wave when $c = 0$ by re–writing Equations (3.11)–(3.12) as

$$\frac{\mathrm{d}V}{\mathrm{d}U} = \frac{-cV - U(1 - U)}{V}, \tag{3.13}$$

where it is clear that an exact solution for $V(U)$ can be obtained when $c = 0$. This solution can be written as

$$V(U) = \pm\sqrt{-U^2 + \frac{2U^3 + 1}{3}}, \tag{3.14}$$

where, we are primarily interested in the negative solution since $V < 0$ at the leading edge. Equation (3.14) with $U(0) = 0$ can be integrated to give the shape of the stationary wave,

$$U(z) = \frac{3}{2}\left[\tanh\left(\frac{z}{2} - \mathrm{arctanh}\,\frac{\sqrt{3}}{3}\right)^2 - 1\right]. \tag{3.15}$$
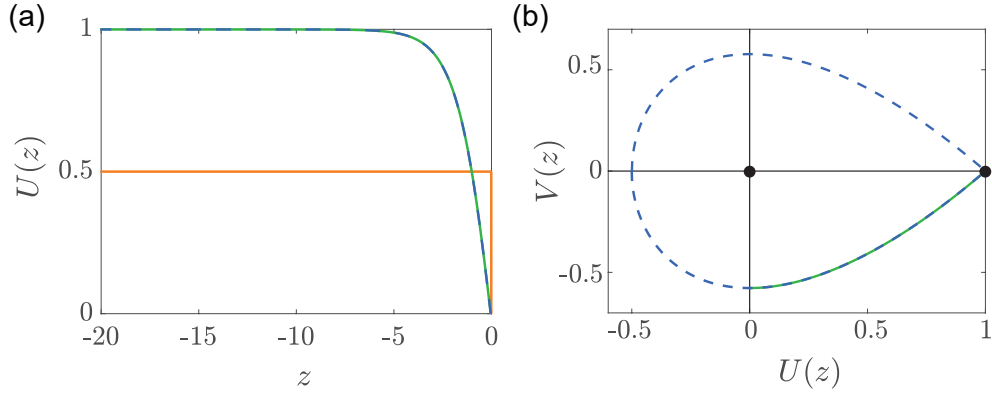
Figure 3.5: Exact solution for the stationary travelling wave, $c = 0$. (a) Comparison of the exact solution, Equation (3.15), in dashed blue with the numerical solution of Equations (3.4)–(3.7) with $\kappa = 0$ in solid green. The initial condition for the numerical solution of the PDE is in orange. (b) Comparison of the exact solution of the phase plane trajectory, Equation (3.14), in dashed blue, with the trajectory obtained by plotting the PDE solution in the phase plane in solid green. Equilibrium points in the phase plane are shown with black discs.

Results in Figure 3.5 compare these exact solutions for $c = 0$ with various numerical solutions. Firstly, in Figure 3.5(a) we show a time–dependent solution of Equations (3.4)–(3.7) with $\kappa = 0$ which evolves into a stationary wave that is visually indistinguishable from the exact solution, Equation (3.15), at this scale. The phase plane in Figure 3.5(b) shows the late–time PDE solution from Figure 3.5(a) plotted as a trajectory in the $(U(z), V(z))$ phase plane. In this phase plane we superimpose the exact solution, Equation (3.14), which forms a homoclinic orbit in the shape of a teardrop. The part of the homoclinic orbit in the fourth quadrant of the phase plane corresponds to the stationary wave, and we see that the numerical trajectory and the exact solution are indistinguishable at this scale. Just as we observed for the invading travelling waves in Figure 3.4, the stationary wave here corresponds to just one part of a trajectory in the phase plane. This is different to the usual phase plane analysis for either the Fisher-KPP or Porous–Fisher models where travelling wave solutions correspond to a complete trajectory, rather than just part of a trajectory.

3.4.3.2 Perturbation solution for slowly invading or receding travelling waves

Results in Section 3.4.3.1 show that we have an exact solution when $c = 0$. We now seek a perturbation solution for $|c| \ll 1$ by writing [Murray 1984],

$$V(U) = V_0(U) + cV_1(U) + c^2 V_2(U) + \mathcal{O}(c^3). \tag{3.16}$$

Substituting Equation (3.16) into Equation (3.13) gives,

$$\frac{\mathrm{d}V_0}{\mathrm{d}U}V_0 + U(1 - U) = 0, \qquad V_0(1) = 0, \tag{3.17}$$

$$\frac{\mathrm{d}V_1}{\mathrm{d}U}V_0 + \frac{\mathrm{d}V_0}{\mathrm{d}U}V_1 + V_0 = 0, \qquad V_1(1) = 0, \tag{3.18}$$

$$\frac{\mathrm{d}V_2}{\mathrm{d}U}V_0 + \frac{\mathrm{d}V_0}{\mathrm{d}U}V_2 + V_1\left(\frac{\mathrm{d}V_1}{\mathrm{d}U} + 1\right) = 0, \qquad V_2(1) = 0. \tag{3.19}$$

The solutions of these differential equations are

$$V_0(U) = \frac{\sqrt{3(2U+1)}}{3}(U - 1), \tag{3.20}$$

$$V_1(U) = \frac{-(U - 2)(1 + 2U)^{3/2} - 3\sqrt{3}}{5(U - 1)\sqrt{1 + 2U}}, \tag{3.21}$$

$$
\begin{aligned}
V_2(U) = {}& \frac{-18\sqrt{3}}{25(2U+1)^{3/2}(U-1)(\sqrt{6U+3}-3)^2(\sqrt{6U+3}+3)^2} \\
& \times \Bigg(-2U^3(6U^2 - 15U + 20) + 15U(U + 2) + 31 \\
& + \sqrt{6U + 3}\,[(2U + 1)(6U + 3) - 30U - 15] \\
& + (60U^3 - 90U^2 + 30)\ln\left[\frac{(\sqrt{6U+3}+3)(U-1)}{6(\sqrt{6U+3}-3)}\right]\Bigg).
\end{aligned}
\tag{3.22}
$$

Maple code to generate these solutions is available on GitHub. These three solutions can be used to truncate Equation (3.16) at different orders, and in doing so we will make use of the $\mathcal{O}(1)$, $\mathcal{O}(c)$ and $\mathcal{O}(c^2)$ perturbation solutions. Given our various approximate perturbation solutions for $V(U)$, we can either directly plot these solution in the phase plane and compare them with numerically–generated phase plane trajectories, or we can integrate these perturbation solutions numerically to give an approximation for the shape of the travelling wave, $U(z)$. To estimate the shape of the travelling wave we integrate the perturbation solution for $V(U)$ using Heun's method with $U(0) = 0$, and we integrate from $z = 0$ to $z = -Z$, where Z is taken to be sufficiently

large.

We now compare various perturbation solutions with phase plane trajectories and time–dependent PDE solutions for both invading and receding travelling waves. Figure 3.6 focuses on invading travelling wave with $c > 0$. Results in Figure 3.5(a)–(c) show the phase plane for $c = 0.25, 0.50$ and 0.75, respectively. The numerical solution of the dynamical system is shown in green, and is superimposed on the $\mathcal{O}(c)$ and $\mathcal{O}(c^2)$ perturbation solutions in yellow and blue, respectively. In these results there is a visual difference between the numerically–generated phase plane trajectories and the $\mathcal{O}(c)$ perturbation solutions, however the $\mathcal{O}(c^2)$ perturbation solution compares very well with the numerically–generated phase plane trajectories.
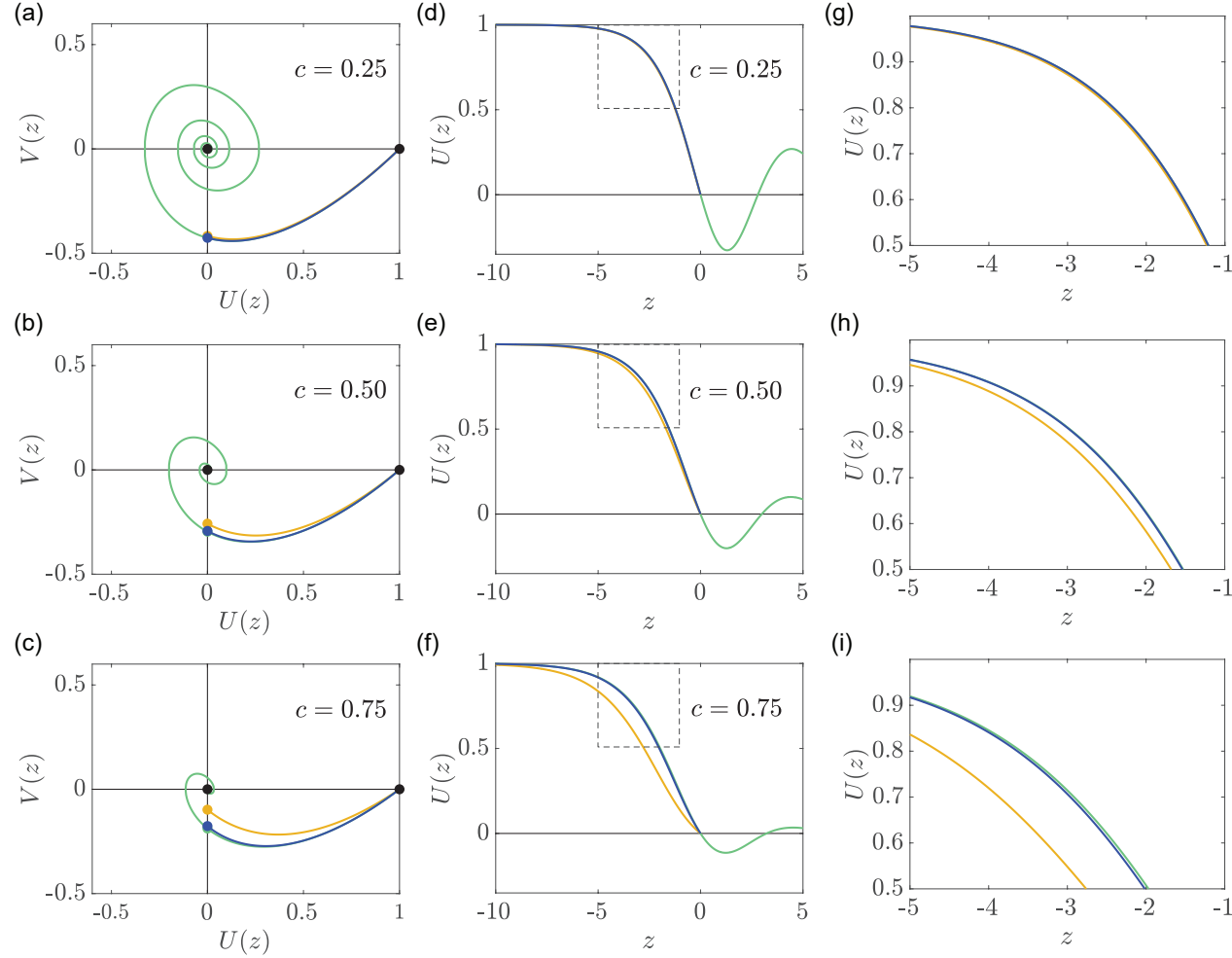
Figure 3.6: Perturbation solutions for slow invading travelling waves. (a)–(c) show the phase plane for $c = 0.25, 0.50$ and 0.75, respectively. Equilibrium points are shown with black discs. The numerical solution of Equations (3.11)–(3.12) are shown in green and the point at which these trajectories intersect the $V(z)$ axis are shown with a green disc. The $\mathcal{O}(c)$ and $\mathcal{O}(c^2)$ perturbation solutions are shown in yellow and blue, respectively. The intersection of the $V(z)$ for the $\mathcal{O}(c)$ and $\mathcal{O}(c^2)$ perturbation solutions are shown in a yellow and blue disc, respectively. Results in (d)–(f) compare the shape of the travelling wave profile, $U(z)$, obtained using the numerical solution of the phase plane trajectory (green) with the $\mathcal{O}(c)$ and $\mathcal{O}(c^2)$ perturbation solutions in yellow and blue, respectively. Results in (g)–(i) show magnified comparison of the three solutions in the regions highlighted by the dashed boxes in (d)–(f).

Results in Figure 3.6(d)–(f) compare the shape of the travelling wave, $U(z)$, using the numerical solution of the dynamical system in the phase plane with the results obtained from the $\mathcal{O}(c)$ and $\mathcal{O}(c^2)$ perturbation solutions. For the numerical solution of the dynamical system we deliberately show the invasion profile using the trajectory from $z = -15$ to $z = 5$, which includes the unphysical part of the trajectory, $z > 0$, where $U(z)$ is oscillatory. To make a clear distinction between the physical and unphysical parts of the invading profile we include a horizontal line at $U(z) = 0$. The horizontal line emphasise the fact that $U(z) > 0$ for $z < 0$, and $U(z)$ is oscillatory for $z > 0$. All three solutions are visually indistinguishable at the scale shown in Figure 3.6(d) where $c = 0.25$. For $c = 0.50$ and $c = 0.75$ we see a visually–distinct difference between the profiles from the phase plane trajectory and the $\mathcal{O}(c)$ perturbation solutions, whereas the $\mathcal{O}(c^2)$ perturbation solution gives an excellent approximation for these larger speeds. Results in Figure 3.6(g)–(i) show magnified comparisons of the shape of $U(z)$ corresponding to the dashed inset regions in Figure 3.6(d)–(f) where it is easier to see the distinction between the three solutions.

Results in Figure 3.7 for the receding travelling wave are presented in the exact same format as those in Figure 3.6. Here, in Figure 3.6 we consider $c = -0.5, -0.75$ and -1.00 and we see that the $\mathcal{O}(c^2)$ perturbation solution provides a very accurate approximation of both the phase plane trajectory and the shape of the receding travelling wave.
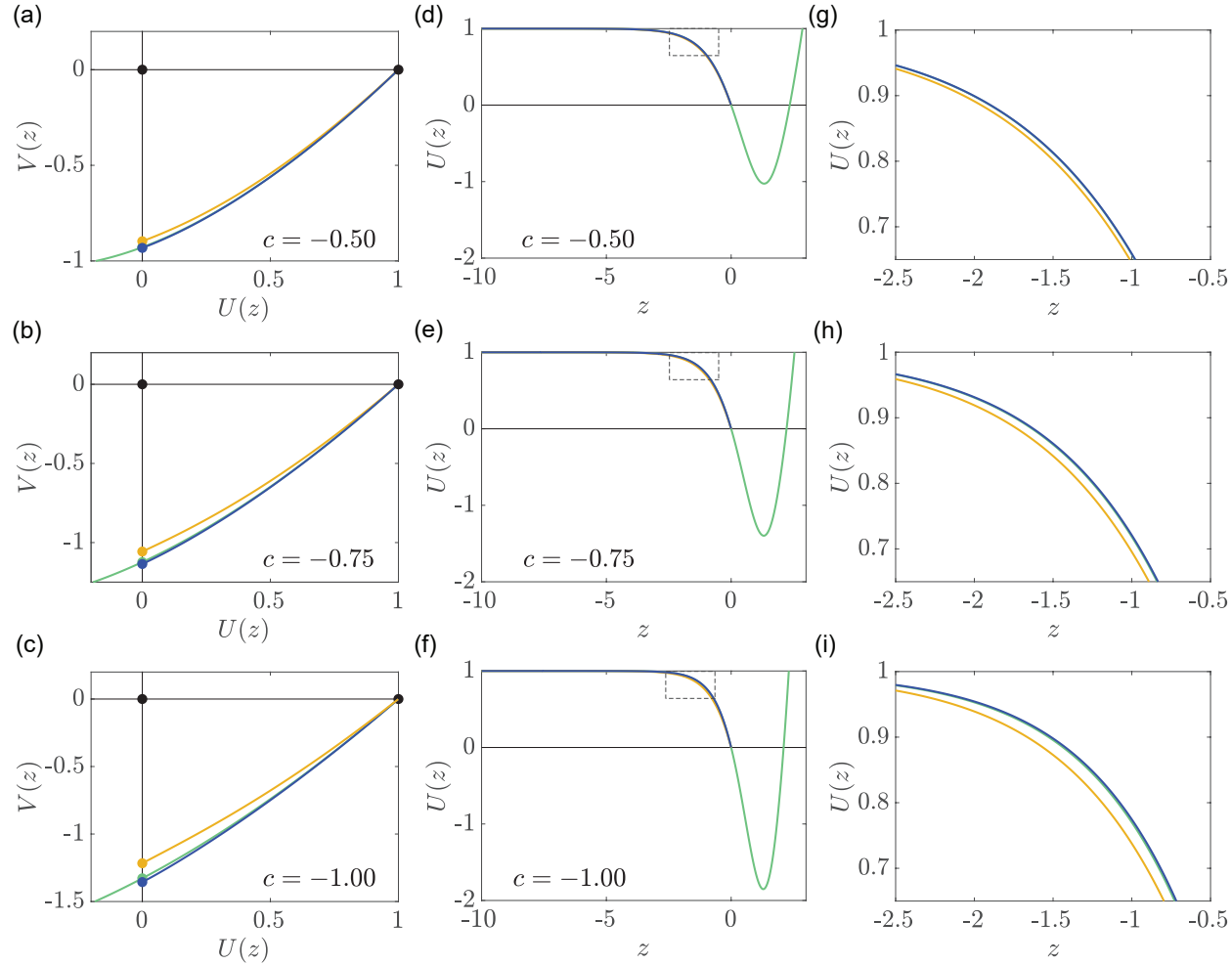
Figure 3.7: Perturbation solutions for slow receding travelling waves. (a)–(c) show the phase plane for $c = -0.50, -0.75$ and -1.00, respectively. Equilibrium points are shown with black discs. The numerical solution of Equations (3.11)–(3.12) are shown in green and the point at which these trajectories intersect the $V(z)$ axis are shown with a green disc. The $\mathcal{O}(c)$ and $\mathcal{O}(c^2)$ perturbation solutions are shown in yellow and blue, respectively. The intersection of the $V(z)$ for the $\mathcal{O}(c)$ and $\mathcal{O}(c^2)$ perturbation solutions are shown in a yellow and blue disc, respectively. Results in (d)–(f) compare the shape of the travelling wave profile, $U(z)$, obtained using the numerical solution of the phase plane trajectory (green) with the $\mathcal{O}(c)$ and $\mathcal{O}(c^2)$ perturbation solutions in yellow and blue, respectively. Results in (g)–(i) show magnified comparison of the three solutions in the regions highlighted by the dashed boxes in (d)–(f).

As we pointed out previously, one of the key conceptual limitations of using the Fisher–Stefan model is that, unlike applications in physical and material sciences [Crank 1987, Dalwadi et al. 2020, Hill 1987, Mitchell and O'Brien 2014], estimates of κ are not available. One way to address this limitation is to use our analysis to provide a relationship between κ and c, since the wave speed is relatively straightforward to measure [Maini et al. 2004a, Maini et al. 2004b, Simpson et al. 2007] and could be used to infer an estimate of κ. As noted previously, all travelling wave solutions of the Fisher–Stefan model satisfy $\kappa = -c/V(0)$, where $V = V(U)$. When $|c| \ll 1$ we can estimate $V(0)$ using our perturbation solutions and this provides various relationships between κ and c depending on the order of the perturbation solution for $V(0)$,

$$\mathcal{O}(1) : \kappa = \frac{-c}{V_0(0)}, \tag{3.23}$$

$$\mathcal{O}(c) : \kappa = \frac{-c}{V_0(0) + cV_1(0)}, \tag{3.24}$$

$$\mathcal{O}(c^2) : \kappa = \frac{-c}{V_0(0) + cV_1(0) + c^2V_2(0)}. \tag{3.25}$$

Substituting expressions for $V_0(0)$, $V_1(0)$ and $V_2(0)$ and expanding the resulting expressions for $|c| \ll 1$ gives

$$\mathcal{O}(1) : \kappa(c) = \sqrt{3}c + \mathcal{O}(c^2), \tag{3.26}$$

$$\mathcal{O}(c) : \kappa(c) = \sqrt{3}c - \frac{3}{5}(2 - 3\sqrt{3})c^2 + \mathcal{O}(c^3), \tag{3.27}$$

$$\mathcal{O}(c^2) : \kappa(c) = \sqrt{3}c - \frac{3}{5}(2 - 3\sqrt{3})c^2 \\ - \frac{9\sqrt{3}}{50}\left[10\ln\left(\frac{6}{2 + \sqrt{3}}\right) + 12\sqrt{3} - 31\right]c^3 + \mathcal{O}(c^4), \tag{3.28}$$

which provides a simple way to relate c and κ for $|c| \ll 1$. To explore the accuracy of these approximations we use numerical solutions in the phase plane to estimate κ in the interval $-1 < c < 1$ and show the numerically–determined relationship between c and κ in Figure 3.7. We also superimpose the various approximations, given by Equations (3.26)–(3.28) in Figure 3.7, where we see that Equation (3.28) is particularly accurate for $|c| \ll 0.5$.
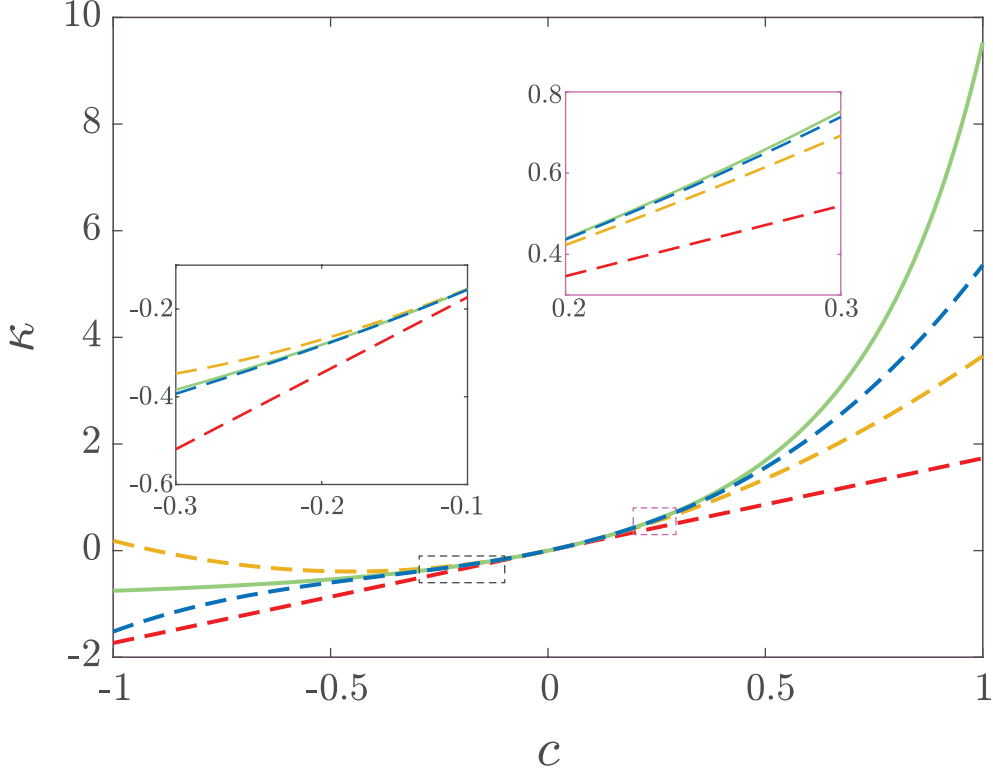
Figure 3.8: Relationship between c and κ for $|c| \ll 1$. The numerical estimate of κ as a function of c is given in solid green. Various perturbation approximations given by Equation (3.26)–(3.28) are given in dashed red, dashed yellow and dashed blue, respectively. The various relationships between c and κ are shown in two insets. The first inset, for $-0.3 < c < 0.1$, is outlined in black. The second inset, for $0.2 < c < 0.3$, is outlined in pink.

3.4.3.3 Perturbation solution for fast receding travelling waves

As noted in Section 3.4.1, preliminary numerical simulations of receding travelling waves in Figure 3.3(e)–(h) suggest the formation of a boundary layer as the speed c decreases. The second order boundary value problem governing the shape of these travelling waves can be written as

$$\frac{1}{c}\frac{\mathrm{d}^2 U}{\mathrm{d}z^2} + \frac{\mathrm{d}U}{\mathrm{d}z} + \frac{1}{c}U(1 - U) = 0, \quad -\infty < z < 0, \tag{3.29}$$

which is singular as $c \to -\infty$. Therefore, we will construct a matched asymptotic expansion [Murray 1984] by treating $1/c$ as a small parameter. The boundary conditions for this problem are $U(0) = 0$ and $U(z) = 1$ as $z \to -\infty$. Setting $1/c = 0$ and solving the resulting ODE gives the outer solution,

$$U(z) = 1, \tag{3.30}$$

which matches the boundary condition as $z \to -\infty$. To construct the inner solution near $z = 0$ we rescale the independent variable $\zeta = zc$. Therefore, in the boundary layer we have

$$\frac{d^2 U}{d\zeta^2} + \frac{dU}{d\zeta} + \frac{1}{c^2} U(1 - U) = 0, \quad -\infty < \zeta < 0. \quad (3.31)$$

Now expanding $U(\zeta)$ in a series we obtain

$$U(\zeta) = U_0(\zeta) + \frac{1}{c^2} U_1(\zeta) + \frac{1}{c^4} U_2(\zeta) + \mathcal{O}\left(\frac{1}{c^6}\right), \quad (3.32)$$

which we substitute into Equation (3.31) to give a family of boundary value problems,

$$\frac{d^2 U_0}{d\zeta^2} + \frac{dU_0}{d\zeta} = 0, \qquad U_0(0) = 0, \ U_0 \to 1 \text{ as } \zeta \to -\infty, \quad (3.33)$$

$$\frac{d^2 U_1}{d\zeta^2} + \frac{dU_1}{d\zeta} + U_0(1 - U_0) = 0, \qquad U_1(0) = 0, \ U_1 \to 0 \text{ as } \zeta \to -\infty, \quad (3.34)$$

$$\frac{d^2 U_2}{d\zeta^2} + \frac{dU_2}{d\zeta} + U_1(1 - 2U_0) = 0, \quad U_2(0) = 0, \ U_2 \to 0 \text{ as } \zeta \to -\infty. \quad (3.35)$$

The solution of these boundary value problems are

$$U_0(\zeta) = (1 - e^{-\zeta}), \quad (3.36)$$

$$U_1(\zeta) = \left(-\frac{1}{2} + \zeta\right) e^{-\zeta} + \frac{1}{2} e^{-2\zeta}, \quad (3.37)$$

$$U_2(\zeta) = \frac{e^{-\zeta}}{12} \left[11 - e^{-\zeta}\left(9 + 2e^{-\zeta}\right)\right] - \zeta e^{-\zeta}\left(e^{-\zeta} + \frac{1}{2}\zeta + \frac{1}{2}\right); \quad (3.38)$$

Maple code to generate these solutions is available on GitHub. Combining the inner and outer solution leads to $U(z) = U_0(z) + c^{-2} U_1(z) + c^{-4} U_2(z) + \mathcal{O}(c^{-6})$, where $U_0(z)$, $U_1(z)$, $U_2(z)$ correspond to Equations (3.36)–(3.38), respectively, written in terms of the original variable $z = \zeta/c$. By truncating this series at different orders we are able to compare $\mathcal{O}(1)$, $\mathcal{O}(c^{-2})$ and $\mathcal{O}(c^{-4})$ perturbation solutions.

Results in Figure 3.9 compare the numerical solutions of Equations (3.4)–(3.7) with various perturbation solutions for fast receding travelling waves. Results in Figure 3.9(a)–(c) show late–time numerical solutions of the PDE model in blue with $c = -2.00, -2.49$ and -2.99, respectively. In each subfigure, the $\mathcal{O}(1)$ and $\mathcal{O}(c^{-2})$ perturbation solutions are plotted, in red and yellow,

respectively. For these results we have not plotted the $\mathcal{O}(c^{-4})$ perturbation solution in order to keep Figure 3.9 easy to interpret. As expected we see that the match between the numerical and perturbation solutions improves as c decreases, and we see that the $\mathcal{O}(c^{-2})$ perturbation solutions are more accurate than the $\mathcal{O}(1)$ perturbation solutions. Results in Figure 3.9(d)–(f) show a magnified comparison of the three solutions and the regions shown are highlighted in the dashed box in Figure 3.9(a)–(c).
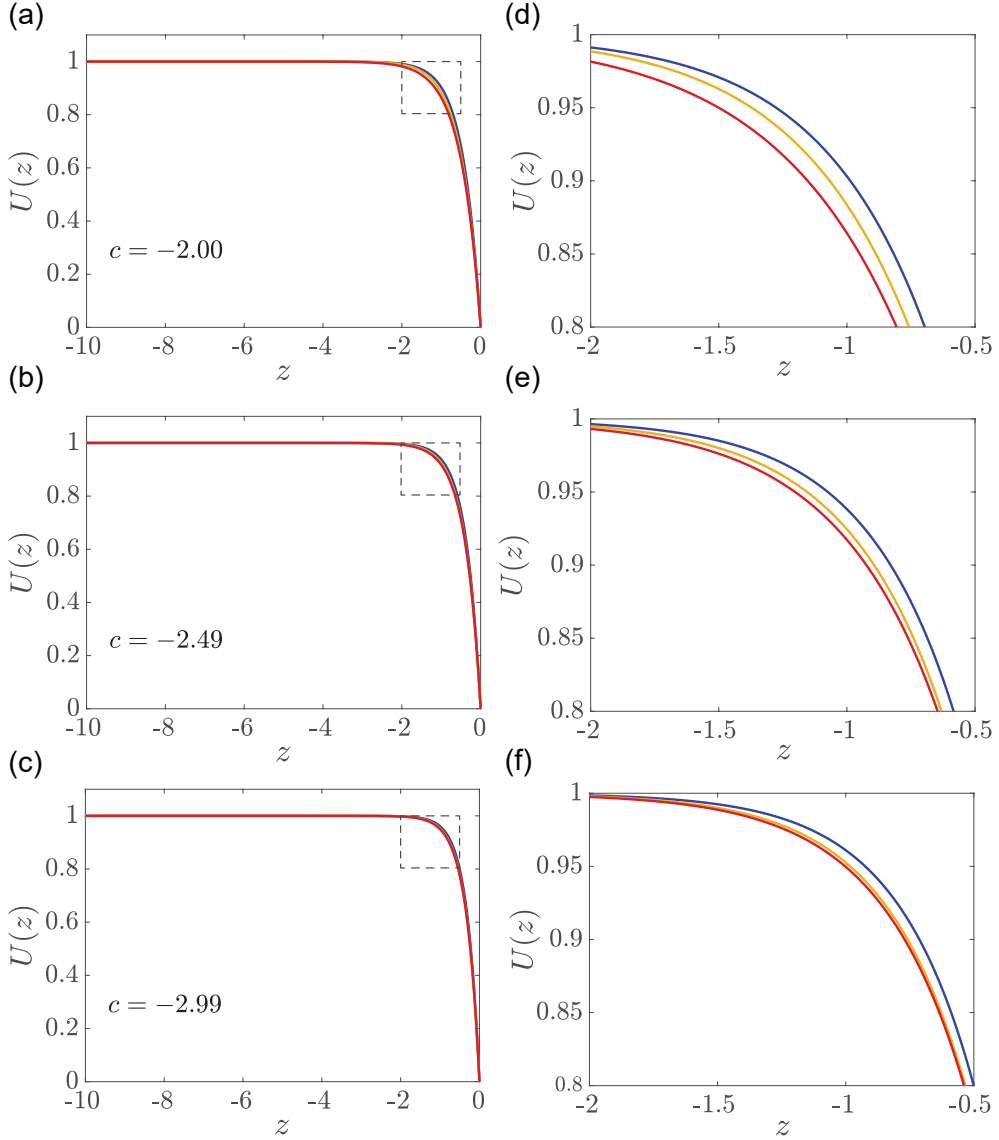
Figure 3.9: Perturbation solutions for slow receding travelling waves. (a)–(c) show plots of the shape of the travelling waves for $c = -2.00, -2.49$ and -2.99, respectively. Late time numerical solutions of Equations (3.4)–(3.7) are shown in blue, and the $\mathcal{O}(1)$ and $\mathcal{O}(c^{-2})$ perturbation solutions are plotted in red and yellow, respectively. (d)–(f) show the magnified regions highlighted by the dashed boxes in (a)–(c), respectively.

For all travelling wave solutions we have $\kappa = -c/V(0)$. As $c \to -\infty$ we can estimate $V(0)$ using our perturbation solutions to provide insight into the relationship between κ and c. We achieve this by evaluating the following expressions,

$$\mathcal{O}(1) : \kappa = \frac{-c}{\dfrac{\mathrm{d}U_0(0)}{\mathrm{d}z}}, \tag{3.39}$$

$$\mathcal{O}\left(\frac{1}{c^2}\right) : \kappa = \frac{-c}{\dfrac{\mathrm{d}U_0(0)}{\mathrm{d}z} + \dfrac{1}{c^2}\dfrac{\mathrm{d}U_1(0)}{\mathrm{d}z}}, \tag{3.40}$$

$$\mathcal{O}\left(\frac{1}{c^4}\right) : \kappa = \frac{-c}{\dfrac{\mathrm{d}U_0(0)}{\mathrm{d}z} + \dfrac{1}{c^2}\dfrac{\mathrm{d}U_1(0)}{\mathrm{d}z} + \dfrac{1}{c^4}\dfrac{\mathrm{d}U_2(0)}{\mathrm{d}z}}, \tag{3.41}$$

where we must differentiate our expressions for $U_0(z)$, $U_1(z)$ and $U_2(z)$ with respect to z. Substituting our perturbation solutions into Equations (3.39)–(3.41) and then expanding the resulting terms as $c \to -\infty$ gives

$$\mathcal{O}(1) : \kappa(c) = -1 + \mathcal{O}\left(\frac{1}{c^2}\right), \tag{3.42}$$

$$\mathcal{O}\left(\frac{1}{c^2}\right) : \kappa(c) = -1 + \frac{1}{2c^2} + \mathcal{O}\left(\frac{1}{c^4}\right), \tag{3.43}$$

$$\mathcal{O}\left(\frac{1}{c^4}\right) : \kappa(c) = -1 + \frac{1}{2c^2} - \frac{2}{3c^4} + \mathcal{O}\left(\frac{1}{c^6}\right), \tag{3.44}$$

which provides us with a simple way to relate κ and c as $c \to -\infty$. To explore the accuracy of these approximations we use numerical solutions in the phase plane to estimate κ in the interval $-10 < c < -2$ and show the numerically–determined relationship between c and κ in Figure 3.10. We also superimpose the various approximations, given by Equations (3.42)–(3.44) in Figure 3.10, where we see that $\kappa \to -1^+$ as $c \to -\infty$, and that Equation (3.44) gives an excellent approximation of κ for $c < -2$.
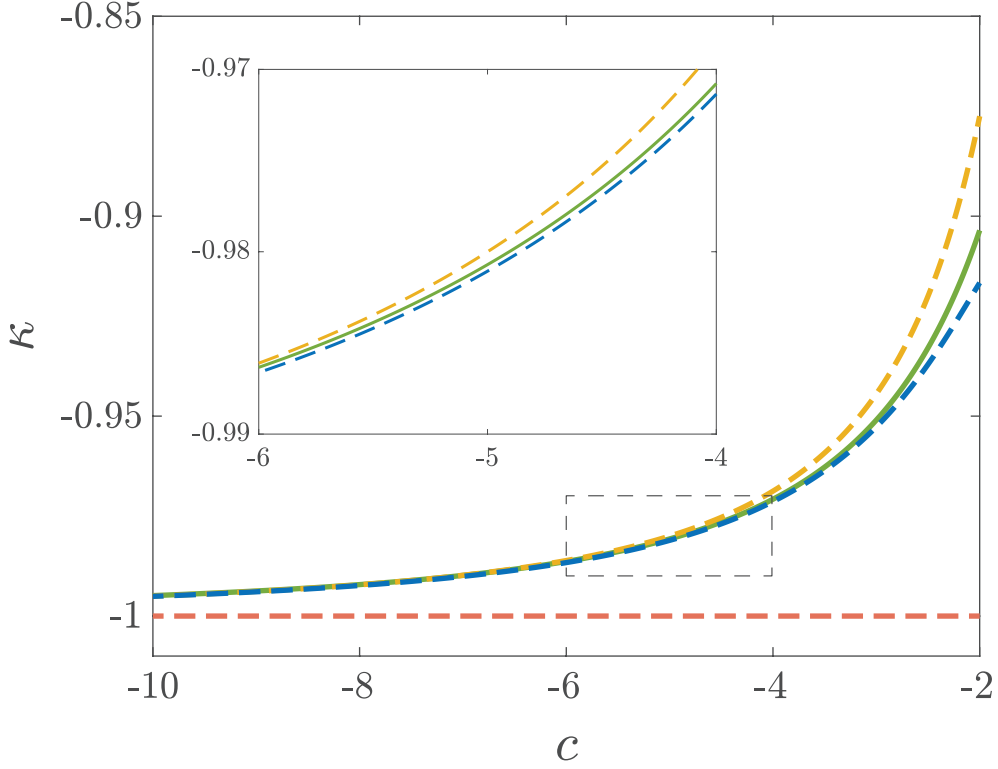
Figure 3.10: Relationship between c and κ near $c \to -\infty$. The numerical estimate of κ as a function of c is given in solid green. Various perturbation approximations given by Equation (3.42)–(3.44) are given in dashed red, dashed yellow and dashed blue, respectively. Various relationships between c and κ are shown in an inset, for $-6 < c < -4$.

In summary, in Sections 3.4.3.1–3.4.3.3 we provide analysis for the case of $c = 0$, $|c| \ll 1$ (slowly invading or slowly receding) and $-c \gg 1$ (fast receding), respectively. It is also possible to analyse the special case where $c = -\sqrt{5}/6$, where the solution can be written in terms of Weierstrass elliptic functions [McCue et al. 2021a].

3.5 Conclusion and Outlook

In this work we discuss approaches for modelling biological invasion and recession. The most commonly–used model to mimic biological invasion is the Fisher–KPP model [Edelstein-Keshet 2005, Murray 2002], and generalisations of the Fisher–KPP model, such as the Porous–Fisher model [Murray 2002, Witelski 1995]. While these single–species PDE models have been used to simulate biological invasion in various contexts, they cannot be used to simulate biological recession. As an alternative, we explore the Fisher–Stefan model [Du and Lin 2010, El-Hachem et al. 2019], which is a different generalisation of the

Fisher–KPP model obtained by reformulating the classical model as a moving boundary problem.

There are both advantages and disadvantages of reformulating the Fisher–KPP model as a moving boundary problem. One advantage of using the Fisher–Stefan model is that it involves a well–defined sharp front and it has the ability to model both biological invasion and recession. These advantages are both attractive because experimental observations of biological invasion typically report well–defined sharp fronts [Maini et al. 2004a, Maini et al. 2004b] and it is well–known that motile and proliferative populations can both invade and recede. The Fisher–KPP model cannot describe either of these observed features. A disadvantage of using the Fisher–Stefan model is the need to specify the constant, κ. While estimates of these kinds of parameters are well–known in the heat and mass transfer literature for modelling physical processes [Crank 1987, Dalwadi et al. 2020, Hill 1987, Mitchell and O'Brien 2014], there are no such estimates for these parameters in a biological or ecological context that we are aware of. Part of the motivation for the analysis in this work is to provide numerical and approximate analytical insight into the relationship between κ and c. We are motivated to do this because measurements of c are often reported [Maini et al. 2004a, Maini et al. 2004b, Simpson et al. 2007] and so understanding how to interpret an estimate of c in terms of κ is of interest. In summary, we show that slowly invading or receding travelling wave solutions of the Fisher-Stefan model move with speed $c \sim \kappa/\sqrt{3}$ as $\kappa \to 0$, whereas rapidly receding travelling wave solutions of the Fisher-Stefan model move with speed $c \sim 2^{-1}(\kappa + 1)^{-1/2}$ as $\kappa \to -1^{+}$.

In this work we compare the Fisher–KPP model and the Fisher–Stefan model and it is interesting to consider how these models can be used to interpret experimental observations. As discussed, experimental estimates of c are the most straightforward measurement to obtain in cell biology experiments. For example, Maini et al. [Maini et al. 2004a] use a scratch assay to obtain an estimate of $\hat{c}$, whereas Simpson et al. [Simpson et al. 2007] report estimates of $\hat{c}$ using observations of cell invasion within intact embryonic tissues. With these measurements of $\hat{c}$, it is possible to estimate the product of the diffusivity and the proliferation rate since $\hat{c} = 2\sqrt{\hat{\lambda}\hat{D}}$ for the Fisher–KPP model. A standard practice is to infer $\hat{\lambda}$ by assuming that a typical doubling time is,

say, 24 h, giving $\hat{\lambda} = \ln(2)/24$ /h. These two pieces of information can be used to estimate $\hat{D}$ by assuming that travelling wave solutions of the Fisher–KPP model are relevant and $\hat{c} = 2\sqrt{\hat{\lambda}\hat{D}}$. This approach was followed by Maini et al. [Maini et al. 2004a, Maini et al. 2004b] and Simpson et al. [Simpson et al. 2007]. Unfortunately this simple approach does not provide any certainty that the Fisher–KPP model is actually valid. Indeed, with more experimental effort it is possible to carefully analyse a cell proliferation assay to provide a separate estimate of $\hat{\lambda}$ [Browning et al. 2017], and to either track individual cells [Cai et al. 2007] or to chemically–inhibit proliferation [Simpson et al. 2013] to obtain an independent estimate of $\hat{D}$. If these more careful experiments are performed, it is then possible to examine if the relationship $\hat{c} = 2\sqrt{\hat{\lambda}\hat{D}}$ is indeed true. If this classical relationship does not hold and $\hat{c} < 2\sqrt{\hat{\lambda}\hat{D}}$, the Fisher–Stefan model provides a better explanation of the data since it is always possible to choose a value of $\hat{\kappa}$ to match independent estimates of $\hat{D}$, $\hat{\lambda}$ and $\hat{c}$.

In conclusion we would like to mention that all of the models discussed in this work make the very simple but extremely common assumption that the proliferation of individuals is given by a logistic source term. This assumption is widely invoked in many single species models of invasion, including the Fisher–KPP model [Maini et al. 2004a, Maini et al. 2004b, Simpson et al. 2007], the Porous–Fisher model [Buenzli et al. 2020, Sherratt and Murray 1990, Witelski 1995] and the Fisher–Stefan model [Du and Lin 2010, El-Hachem et al. 2019], as well as many more complicated multiple species analogues of these models [Chaplain et al. 2020, Painter and Sherratt 2003, Painter et al. 2015]. We acknowledge that there are other classes of models where different source terms are used, such as the bistable equation and various models that describe Allee effects [Courchamp et al. 2008, Fadai and Simpson 2020b, Fife 1979, Johnston et al. 2017, Lewis and Kareiva 1993, Taylor and Hastings 2005]. These models are similar to the classical Fisher–KPP model except that the quadratic source term is generalised to a cubic source term, and it is well–known that such single species models can be used to simulate both biological and invasion and retreat by changing the shape of the cubic source term. In this work we have deliberately not focused on Allee–type models so that we do not conflate models of Allee effects with the Fisher–Stefan model. Of course, it

would be very interesting to consider an extension of the Fisher–Stefan model with a more general source term [Browning et al. 2017, Tsoularis and Wallace 2002], such as an Allee effect. We anticipate many of the numerical, phase plane and perturbation tools developed in this work would also play a role in the analysis of a Fisher–Stefan–type model with a generalised source term. We leave this extension for future consideration.

3.6 Additional Material

3.6.1 Numerical methods

3.6.1.1 Partial differential equation

To obtain numerical solutions of the Fisher–Stefan equation

$$\frac{\partial u}{\partial t} = \frac{\partial^2 u}{\partial x^2} + u(1 - u), \tag{3.45}$$

for $0 < x < L(t)$ and $t > 0$, we first use a boundary fixing transformation $\xi = x/L(t)$ so that we have

$$\frac{\partial u}{\partial t} = \frac{1}{L^2(t)} \frac{\partial^2 u}{\partial \xi^2} + \frac{\xi}{L(t)} \frac{\mathrm{d}L(t)}{\mathrm{d}t} \frac{\partial u}{\partial \xi} + u(1 - u), \tag{3.46}$$

on the fixed domain, $0 < \xi < 1$, for $t > 0$. Here $L(t)$ is the length of the domain that we will discuss later. To close the problem we also transform the boundary conditions giving

$$\frac{\partial u}{\partial \xi} = 0 \quad \text{at} \quad \xi = 0, \tag{3.47}$$

$$u = 0 \quad \text{at} \quad \xi = 1. \tag{3.48}$$

We spatially discretise Equations (3.46)–(3.48) with a uniform finite difference mesh, with spacing $\Delta \xi$, approximating the spatial derivatives using a central finite difference approximation, giving

$$\frac{u_i^{j+1} - u_i^j}{\Delta t} = \frac{1}{(L^j)^2} \left(\frac{u_{i-1}^{j+1} - 2u_i^{j+1} + u_{i+1}^{j+1}}{\Delta \xi^2} \right)$$
$$+ \frac{\xi}{L^j} \left(\frac{L^{j+1} - L^j}{\Delta t} \right) \left(\frac{u_{i+1}^{j+1} - u_{i-1}^{j+1}}{2\Delta \xi} \right) + u_i^{j+1}(1 - u_i^{j+1}), \tag{3.49}$$

for $i = 2, \ldots, m - 1$, where $m = 1/\Delta \xi + 1$ is the total number of spatial nodes on the finite difference mesh, and the index j represents the time index so that $u_i^j \approx u(\xi, t)$, where $\xi = (i - 1) \Delta \xi$ and $t = j\Delta t$.

Discretising Equations (3.47)–(3.48) leads to

$$u_2^{j+1} - u_1^{j+1} = 0, \tag{3.50}$$

$$u_m^{j+1} = 0. \tag{3.51}$$

To advance the discrete system from time t to $t + \Delta t$ we solve the system of nonlinear algebraic equations, Equations (3.49)-(3.51), using Newton-Raphson iteration. During each iteration of the Newton–Raphson algorithm we estimate the position of the moving boundary using the discretised Stefan condition,

$$L^{j+1} = L^j - \frac{\Delta t \kappa}{L^j} \left(\frac{u_m^{j+1} - u_{m-1}^{j+1}}{\Delta \xi} \right). \tag{3.52}$$

Within each time step the Newton–Raphson iterations continue until the maximum change in the dependent variables is less than the tolerance ϵ. All results in this work are obtained by setting $\epsilon = 1 \times 10^{-8}$, $\Delta \xi = 1 \times 10^{-6}$ and $\Delta t = 1 \times 10^{-2}$, and we find that these values are sufficient to produce grid–independent results. However, we recommend that care be taken when using the algorithms on GitHub when considering larger values of κ, which can require a much denser mesh to give grid–independent results.

We use the time–dependent solutions to provide an estimate of the travelling wave speed c^*. The estimated wave speed is computed using the discretised position of the moving boundary such as $c^* = (L^{j+1} - L^j)/\Delta t$.

3.6.1.2 Phase plane

To construct the phase planes we solve Equations (3.11)–(3.12) numerically using Heun's method with a constant step size dz. In most cases we are interested in examining trajectories that either enter or leave the saddle $(1, 0)$ along the stable or unstable manifold, respectively. Therefore, it is important that the initial condition we chose when solving Equations (3.11)–(3.12) are on the appropriate stable or unstable manifold and sufficiently close to $(1, 0)$. To choose this point we use the MATLAB *eig* function [Mathworks 2021] to calculate the eigenvalues and eigenvectors for the particular choice of c of interest. The flow of the dynamical system are plotted on the phase planes using the MATLAB *quiver* function [Mathworks 2021].

3.6.2 Time–dependent PDE solutions with different initial conditions

Results in Figure 3.3 show a family of time–dependent solutions of the Fisher-Stefan model that lead to both invading and receding travelling waves for different choices of κ, but the same choice of initial condition, Equation (7) with $\alpha = 0.5$. Here, in Figures 3.11–3.13 we present analogous results except we change the initial condition by choosing $\alpha = 0.25, 0.75$ and 1.00, respectively. Comparing the shape of the long-time travelling wave solutions in Figure 3 with those here in Figures 3.11–3.13 confirms that the eventual travelling wave solutions are independent of the initial condition. Here, the time-dependent solution at $t = 30$ is sufficient to see this. For example, in Figure 3(g) with $\kappa = -0.9$, we eventually see that a receding travelling wave with $c = -2.00$ forms by $t = 30$. Results in Figure 3.11(g), Figure 3.12(g) and Figure 3.13(g) confirm that we obtain the same travelling wave, with the same long time wave speed, regardless of the initial condition. Of course, should the reader wish to experiment with other choices of initial condition, or if they wish to explore the time–dependent solutions in Figure 3 or Figures 3.11–3.13 for a longer duration of time, say $t = 40$, they may do so by downloading and running the MATLAB code provided on GitHub.
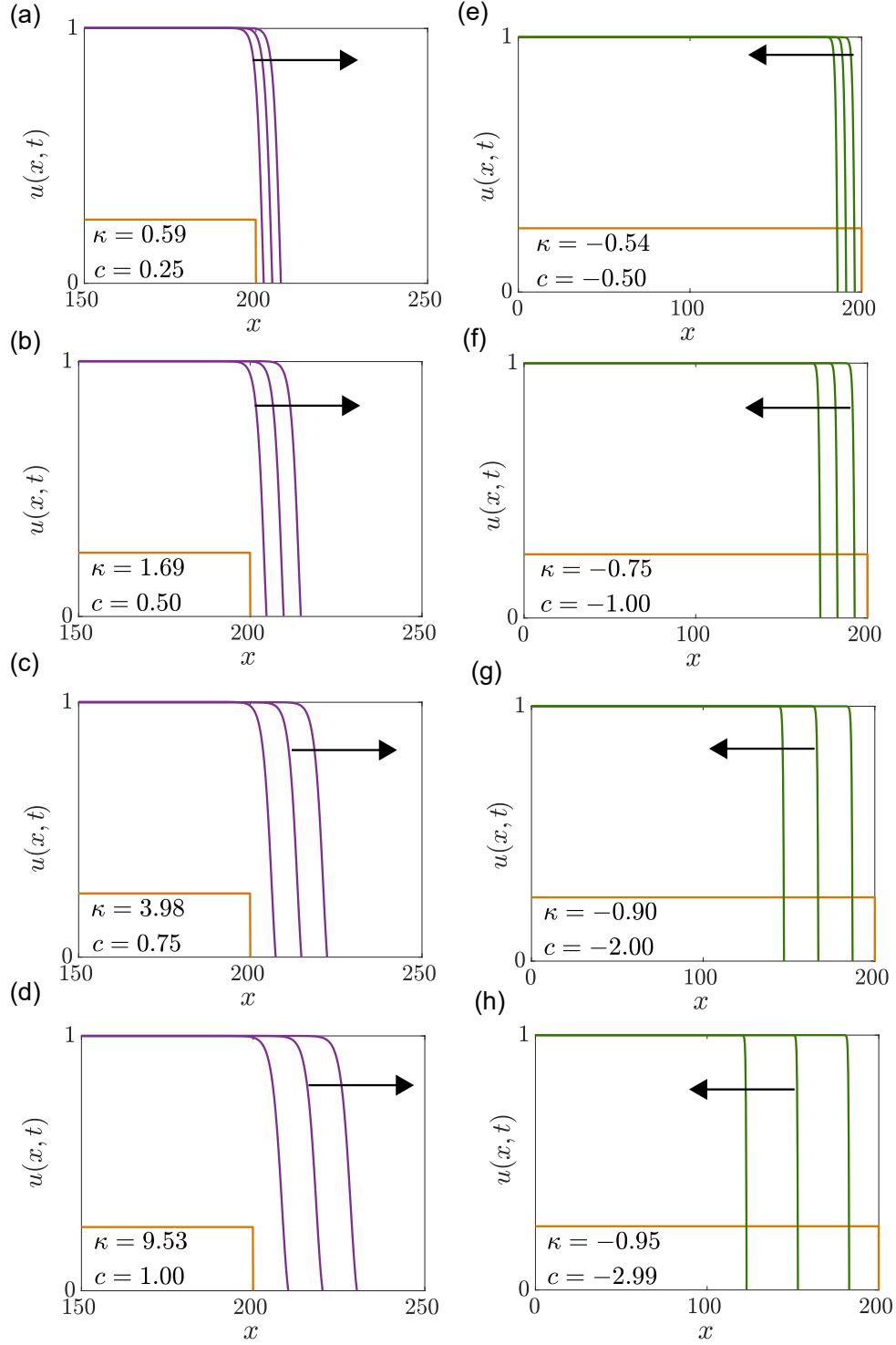
Figure 3.11: Late-time numerical solutions of the Fisher–Stefan model.
Numerical solutions of Equations (3.4)–(3.7) are given at $t = 0, 10, 20$ and 30. The
initial condition is given by Equation (3.7) with $\alpha = 0.25$ and $L(0) = 200$. Results
in (a)–(d) lead to invading travelling waves with $c = 0.25, 0.50, 0.75$ and 1.00, respec-
tively. These travelling waves are obtained by choosing $\kappa = 0.5859, 1.6879, 3.9823$
and 9.5315, respectively. Results in (e)–(h) lead to receding travelling waves with
$c = -0.50, -1.00, -2.00$ and -2.99, respectively. These receding travelling waves are
obtained by choosing $\kappa = -0.5387, -0.7529, -0.9036$ and -0.9510, respectively. Our
estimates of c correspond are obtained at late time, here $t = 30$. Note that estimates
of κ are reported in the caption to four decimal places, whereas the estimates given
in the subfigures are reported to two decimal places to keep the figure neat.

Figure 3.12: Late-time numerical solutions of the Fisher–Stefan model.
Numerical solutions of Equations (3.4)–(3.7) are given at $t = 0, 10, 20$ and 30. The initial condition is given by Equation (3.7) with $\alpha = 0.75$ and $L(0) = 200$. Results in (a)–(d) lead to invading travelling waves with $c = 0.25, 0.50, 0.75$ and 1.00, respectively. These travelling waves are obtained by choosing $\kappa = 0.5859, 1.6879, 3.9823$ and 9.5315, respectively. Results in (e)–(h) lead to receding travelling waves with $c = -0.50, -1.00, -2.00$ and -2.99, respectively. These receding travelling waves are obtained by choosing $\kappa = -0.5387, -0.7529, -0.9036$ and -0.9510, respectively. Our estimates of c correspond are obtained at late time, here $t = 30$. Note that estimates of κ are reported in the caption to four decimal places, whereas the estimates given in the subfigures are reported to two decimal places to keep the figure neat.
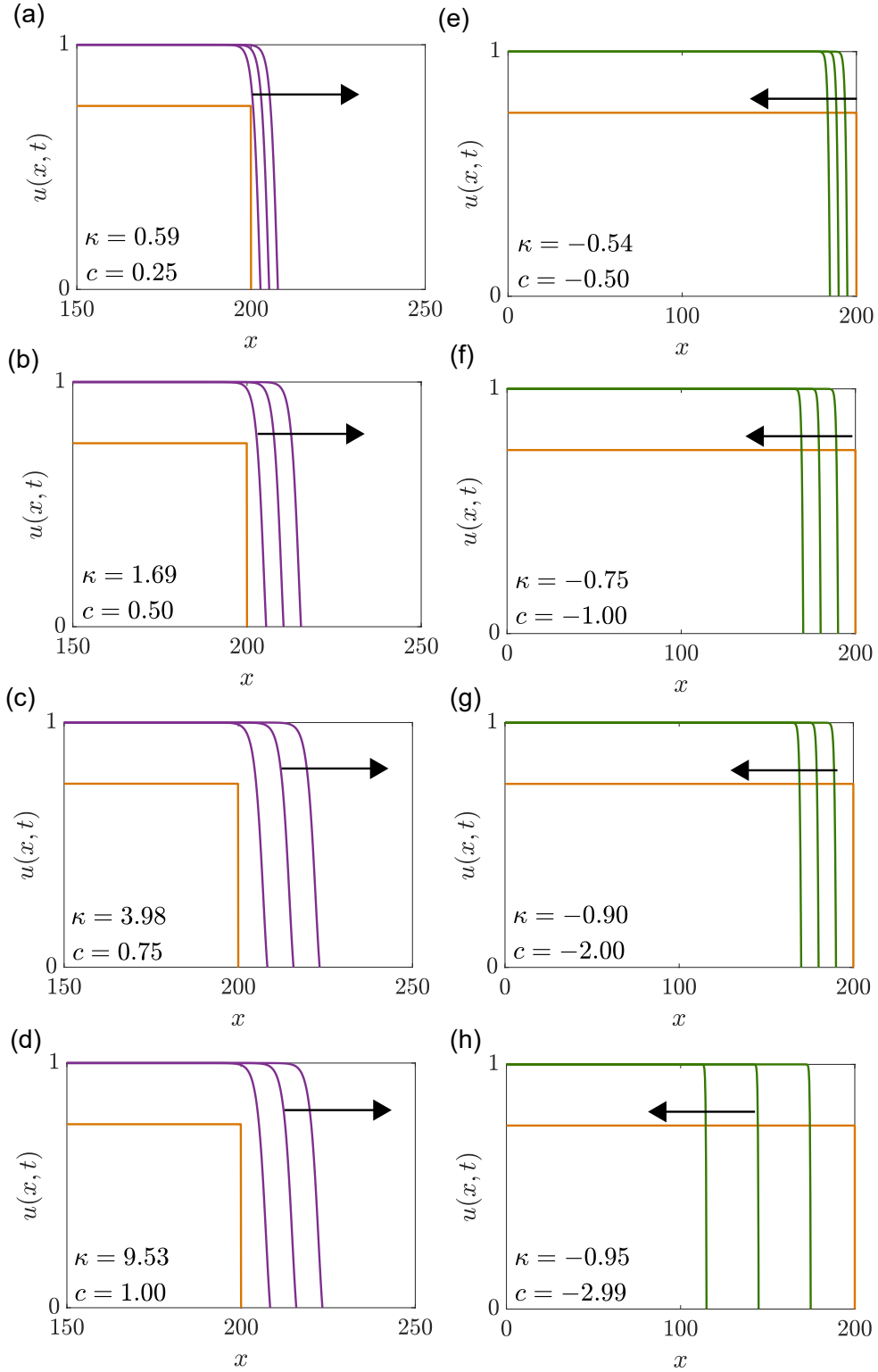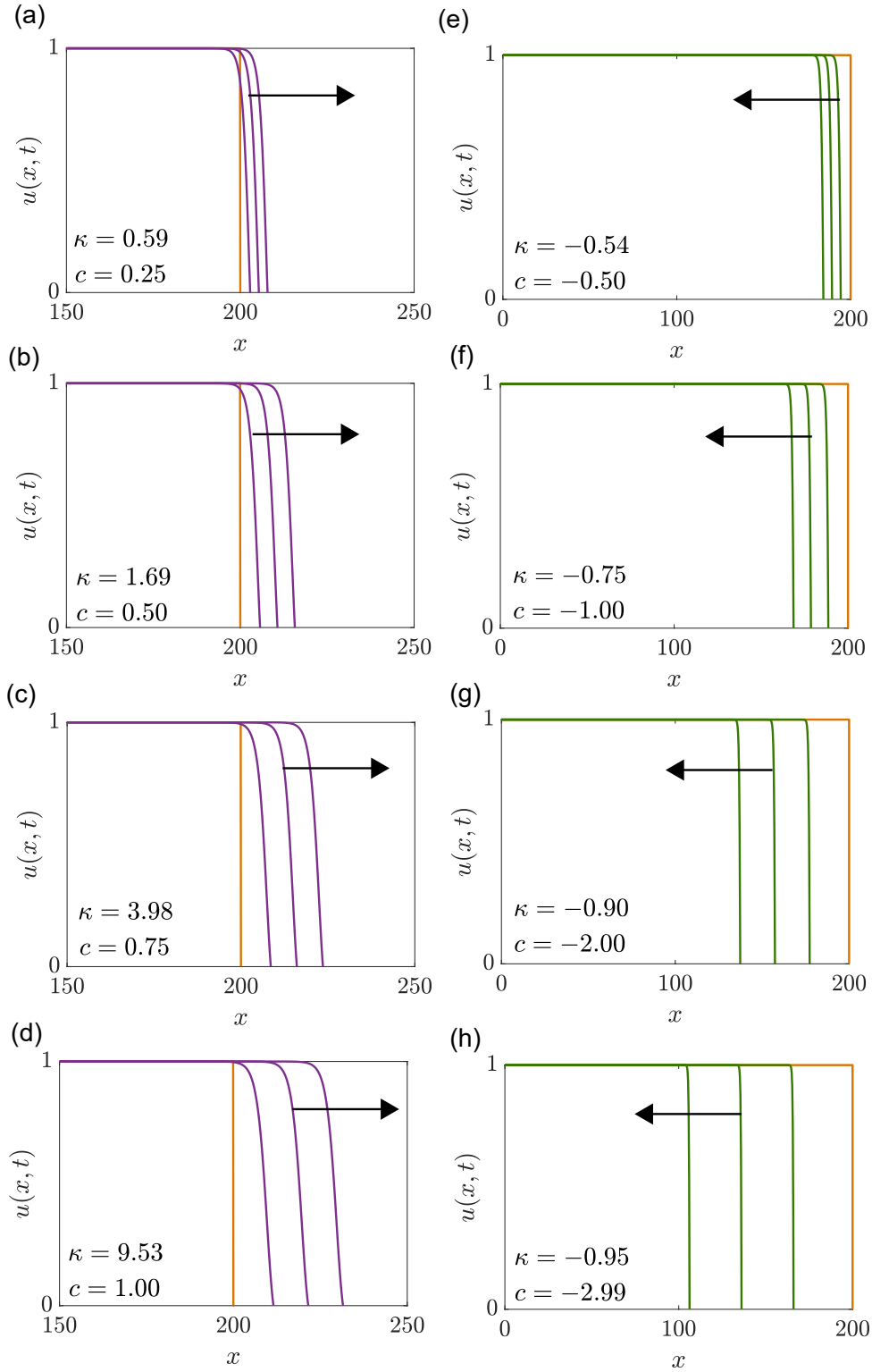
Figure 3.13: Late-time numerical solutions of the Fisher–Stefan model.
Numerical solutions of Equations (3.4)–(3.7) are given at $t = 0, 10, 20$ and 30. The
initial condition is given by Equation (3.7) with $\alpha = 1.00$ and $L(0) = 200$. Results
in (a)–(d) lead to invading travelling waves with $c = 0.25, 0.50, 0.75$ and 1.00, respec-
tively. These travelling waves are obtained by choosing $\kappa = 0.5859, 1.6879, 3.9823$
and 9.5315, respectively. Results in (e)–(h) lead to receding travelling waves with
$c = -0.50, -1.00, -2.00$ and -2.99, respectively. These receding travelling waves are
obtained by choosing $\kappa = -0.5387, -0.7529, -0.9036$ and -0.9510, respectively. Our
estimates of c correspond are obtained at late time, here $t = 30$. Note that estimates
of κ are reported in the caption to four decimal places, whereas the estimates given
in the subfigures are reported to two decimal places to keep the figure neat.

Results in Figures 3.3, 3.11–3.13 show late time–dependent solutions of the Fisher-Stefan model where the density profiles have reached a constant shape, recognisable visually, and a constant speed, computed numerically. Here, in Figure 3.14, we show solutions of the Fisher-Stefan model at early times, where the shape of the density profiles could be seen changing at each time step and where the calculated speed is still increasing or decreasing, for different initial conditions corresponding to Figures 3.3, 3.11–3.12.
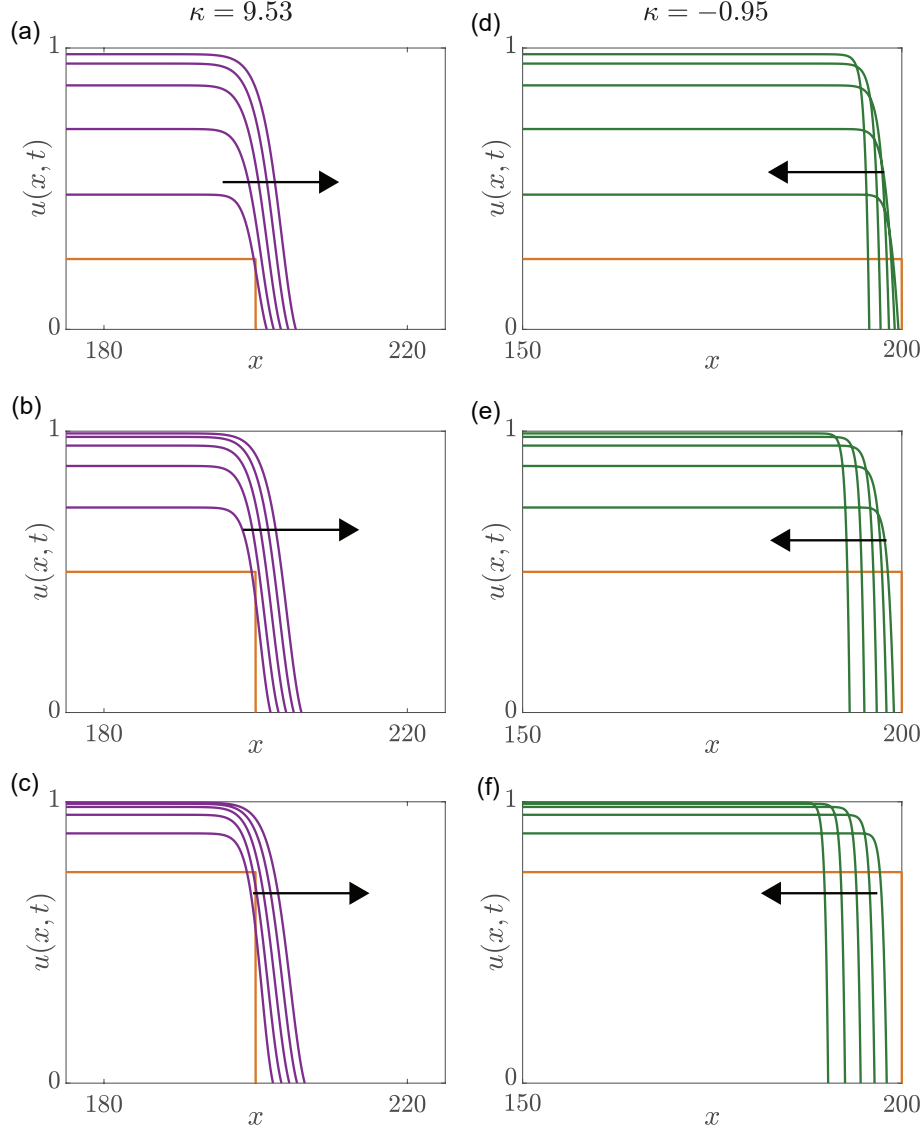

Figure 3.14: Time-dependant solutions of the Fisher–Stefan model at early times. Numerical solutions of Equations (3.4)–(3.7) are given at $t = 0, 1, 2, 3, 4$ and 5. The initial condition is given by Equation (3.7) where $L(0) = 200$ and where $\alpha = 0.25$ in (a) and (d), $\alpha = 0.5$ (b) and (e), and $\alpha = 0.75$ in (c) and (f), corresponding to initial condition of Figures 3.3, 3.11 and 3.12. The time-dependant solutions are obtained by choosing $\kappa = 9.5315$ in (a)–(c) and $\kappa = -0.9510$ in (d)–(f). Note that estimates of κ are reported in the caption to four decimal places, whereas the estimates given in the subfigures are reported to two decimal places to keep the figure neat.

Chapter 4

Non-vanishing sharp-fronted travelling wave solutions of the Fisher-Kolmogorov model

Statement of Contribution of Co-Authors for Thesis by Published Paper

The following is the suggested format for the required declaration provided at the start of any thesis chapter which includes a co-authored publication.

The authors listed below have certified that:

1. they meet the criteria for authorship and that they have participated in the conception, execution, or interpretation, of at least that part of the publication in their field of expertise;
2. they take public responsibility for their part of the publication, except for the responsible author who accepts overall responsibility for the publication;
3. there are no other authors of the publication according to these criteria;
4. potential conflicts of interest have been disclosed to (a) granting bodies, (b) the editor or publisher of journals or other publications, and (c) the head of the responsible academic unit, and
5. they agree to the use of the publication in the student's thesis and its publication on the QUT's ePrints site consistent with any limitations set by publisher requirements.
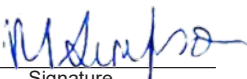
In the case of this chapter 4:

Please state the publication title and date of publication or status:

El-Hachem M, McCue SW, Simpson MJ, 2021. Non-vanishing sharp-fronted travelling wave solutions of the Fisher-Kolmogorov model. Submitted on 28 October 2021.

Contributor	Statement of contribution*
Maud El-Hachem *Maud Elh* 15/11/2021	Conceived and designed the study, performed all numerical and symbolic calculations, drafted the article, and gave final approval for publication.
Scott W McCue	Conceived and designed the study, drafted the article, and gave final approval for publication.
Matthew J Simpson	Conceived and designed the study, drafted the article, and gave final approval for publication.

Principal Supervisor Confirmation
I have sighted email or other correspondence from all Co-authors confirming their certifying authorship. (If the Co-authors are not able to sign the form please forward their email or other correspondence confirming the certifying authorship to the GRC). Professor Matthew Simpson _____ 16/11/2021 Name   Signature   Date

4.1 Abstract

The Fisher-KPP model, and generalisations thereof, involve simple reaction-diffusion equations for biological invasion that assume individuals in the population undergo linear diffusion with diffusivity D, and logistic proliferation with rate λ. For the Fisher-KPP model, biologically-relevant initial conditions lead to long-time travelling wave solutions that move with speed $c = 2\sqrt{\lambda D}$. Despite these attractive features, there are several biological limitations of travelling wave solutions of the Fisher-KPP model. First, these travelling wave solutions do not predict a well-defined invasion front. Second, biologically-relevant initial conditions lead to travelling waves that move with speed $c = 2\sqrt{\lambda D} > 0$. This means that, for biologically-relevant initial data, the Fisher-KPP model can not be used to study invasion with $c \neq 2\sqrt{\lambda D}$, or retreating travelling waves with $c < 0$. Here, we reformulate the Fisher-KPP model as a moving boundary problem and show that this reformulated model alleviates the key limitations of the Fisher-KPP model. Travelling wave solutions of the moving boundary problem predict a well-defined front that can propagate with *any* wave speed, $-\infty < c < \infty$. Here, we establish these results using a combination of high-accuracy numerical simulations of the time-dependent partial differential equation, phase plane analysis and perturbation methods. All software required to replicate this work is available on GitHub.

4.2 Introduction

The Fisher-Kolmogorov model, also known as the Fisher-KPP model, is a widely-used one-dimensional reaction-diffusion model that describes the spatial and temporal evolution of a population of motile and proliferative individuals with density $u(x, t)$ [Fisher 1937, Kolmogorov et al. 1937]. Individuals in the population are assumed to undergo diffusion with diffusivity D and logistic proliferation with proliferation rate λ, and have a carrying capacity density K.

The Fisher-KPP model and various extensions have been used to study a range of biological phenomena including various applications in cell biology [Sherratt and Murray 1990, Swanson et al. 2003, Painter and Sherratt 2003, Gatenby and Gawlinski 1996, Landman and Pettet 1998, Maini et al.

2004a, Maini et al. 2004b, Jin et al. 2016, Bitsouni et al. 2018, Warne et al. 2019] and ecology [Shigesada et al. 1951, Skellam 1951, Steel et al. 1998, Kot 2003]. From a mathematical point of view, the Fisher-KPP model is of high interest because it supports travelling wave solutions that have been widely studied using a range of mathematical techniques [Canosa 1973, El-Hachem et al. 2019, Murray 2002, Aronson and Weinberg 1978]. Despite the immense interest in travelling wave solutions of the Fisher-KPP model, there are various features of these solutions that are biologically unsatisfactory. For example, travelling wave solutions of the Fisher-KPP model are smooth and without compact support, and $u(x,t) \to 0$ as $x \to \infty$. This means that these travelling wave solutions do not provide a clear way to model the motion of a well-defined invasion front [Maini et al. 2004a, Maini et al. 2004b]. Furthermore, travelling wave solutions of the Fisher-KPP model that evolve from initial conditions with compact support lead to long-time travelling waves that move with speed $c = 2\sqrt{\lambda D}$ [Canosa 1973, Murray 2002]. Despite the fact that constant speed travelling wave-type behaviour can be observed and measured experimentally [Maini et al. 2004a, Maini et al. 2004b], simply observing travelling wave-type behaviour does not verify the relationship $c = 2\sqrt{\lambda D}$. Another limitation of the Fisher-KPP model is that travelling wave solutions always lead to invading fronts with $c > 0$ and $\partial u(x,t)/\partial t > 0$. In contrast, various applications in biology and ecology involve retreating fronts with $c < 0$ and $\partial u(x,t)/\partial t < 0$ [El-Hachem et al. 2021a], and these processes cannot be modelled using the Fisher-KPP model.

Various mathematical extensions have been proposed to overcome the biologically unsatisfactory features of the Fisher-KPP model. Perhaps the most widely known is to generalise the linear diffusion term in the Fisher-KPP model to a degenerate nonlinear diffusion term, giving rise to a model that is often called the Porous-Fisher model [Murray 2002, Sengers et al. 2007, Sánchez Garduño and Maini 1994, Sánchez Garduno and Maini 1995, Witelski 1994, Witelski 1995, McCue et al. 2019]. The Porous-Fisher model lead to sharp-fronted travelling wave solutions that can be used to model the motion of a well-defined front, such as those that are often observed experimentally [Maini et al. 2004a, Maini et al. 2004b]. With a nonlinear degenerate diffusivity $\mathcal{D}(u) = Du$, time-dependent solutions of the Porous-Fisher model with initial

conditions that have compact support leads to travelling waves that move with speed $c = \sqrt{\lambda D/2}$. Again, experimental measurements of the wave speed do not confirm the relationship $c = \sqrt{\lambda D/2}$. Similar to the Fisher-KPP model, the Porous-Fisher model cannot be used to study retreating fronts [El-Hachem et al. 2021a]. A second, less common approach to overcome the biologically unsatisfactory features of the Fisher-KPP model is to reformulate the model as a moving boundary problem on $x < s(t)$, where the density vanishes on the moving front, $u(s(t), t) = 0$, meaning that this moving boundary problem gives rise to a well-defined front that is consistent with experimental observations. This model, where the motion of $s(t)$ is driven by a classical one-phase Stefan condition $\mathrm{d}s(t)/\mathrm{d}t = -\kappa \partial u(s(t), t)/\partial x$ [Crank 1987, Hill 1987, Gupta 2017], has been called the Fisher-Stefan model [Du and Lin 2010, Du et al. 2014a, Du et al. 2014b, El-Hachem et al. 2019]. While moving boundary problems of this type are most often used to study certain physical and industrial phenomena [Mitchell and O'Brien 2014, Brosa Planella et al. 2019, Dalwadi et al. 2020, Brosa Planella et al. 2021], they are also used to study biological processes, such as tumour spheroid growth and wound healing [Ward and King 1997, Ward and King 1999, Gaffney and Maini 1999, Kimpton et al. 2013, Fadai and Simpson 2020a, Jin et al. 2021]. Setting $\kappa > 0$ in the Fisher-Stefan model can lead to travelling wave solutions with $0 < c < 2\sqrt{\lambda D}$. Unlike either the Fisher-KPP or Porous-Fisher models, the Fisher-Stefan model can be used to model retreating travelling waves with $c < 0$ simply by setting $\kappa < 0$ [El-Hachem et al. 2021a]. In summary, the Fisher-Stefan model can be used to study a wide range of travelling wave solutions with $-\infty < c < 2\sqrt{\lambda D}$. From this point of view, the Fisher-Stefan model is much more flexible than either the classical Fisher-KPP or Porous-Fisher models.

In this work we propose and analyse a generalisation of the Fisher-Stefan model that enables us to study travelling wave solutions with any wave speed, $-\infty < c < \infty$. This flexibility arises by generalising the boundary condition at the moving front, $x = s(t)$. The usual Fisher-Stefan model involves setting $u(s(t), t) = 0$ so that the solution vanishes at $x = s(t)$. Here, we set $u(s(t), t) = u_{\mathrm{f}}$, where $u_{\mathrm{f}} \in [0, 1)$. The density at the moving front is non-vanishing when $u_{\mathrm{f}} \in (0, 1)$, whereas the density at the moving front vanishes when we set $u_{\mathrm{f}} = 0$, in which case our model simplifies to the usual Fisher-Stefan model.

There are two different ways of motivating this kind of boundary condition, illustrated schematically in Figure 4.1 in the context of cellular invasion. First, in Figure 4.1(a)–(c), we think of a population of motile and proliferative cells that give rise to an invading front moving into an existing background population of cells ahead of the moving boundary with $u(s(t), t) = u_f$. Recall that the Fisher-KPP model is often used to model the invasion of one population of cells, such as a tumour cell population, into a surrounding population of healthy cells by simply modelling the invading population [Sherratt and Murray 1990, Swanson et al. 2003, Maini et al. 2004a, Maini et al. 2004b, Jin et al. 2016, Bitsouni et al. 2018, Warne et al. 2019] rather than explicitly modelling both populations [Gatenby and Gawlinski 1996, Landman and Pettet 1998, Painter and Sherratt 2003, El-Hachem et al. 2020, El-Hachem et al. 2021b]. Our approach can be thought of as a hybrid approach where we deal only with a PDE for the invading population, but we explicitly model the impact of the surrounding tissue by varying u_f. Another way in which we can interpret the schematic in Figure 4.1(a)–(c) is in terms of modelling wound healing. Here the main cell type of interest, such as fibroblast cells, could be invading a partial wound in which there is an existing population of fibroblasts at lower density. This existing population could be appropriate in the model when it is assumed the act of creating the partial wound does not remove all of the epidermal cells entirely.

The second way of motivating our mathematical model, shown schematically in Figure 4.1(d)–(f), is to think about modelling simple two-dimensional scratch assays, such as the experimental images reported by Jin et al. (2016) [Jin et al. 2016] in Figure 2(a)–(c) in their study. In these experiments the field-of-view is divided into vertical strips and the cell density is measured by counting the number of cells in each strip and dividing by the area of the strip. The cell density well–behind the front approaches some carrying capacity density and the cell density well ahead of the front is zero. Right at the front, however, the density is some intermediate density u_f, leading to a boundary condition $u = u_f$ in the continuum model.

Regardless of which biological scenario is used to motivate our mathematical model, the one-phase Stefan condition at $x = s(t)$ implies there is a local loss of the invading population at the leading edge. Regardless of the motiva-

tion for this model, our interest is in modelling the behaviour of the invading population in the region $x < s(t)$. While the schematic in Figure 4.1 is presented in terms of an invading front with $c > 0$, a similar schematic with very similar interpretations can be drawn for a retreating front with $c < 0$.
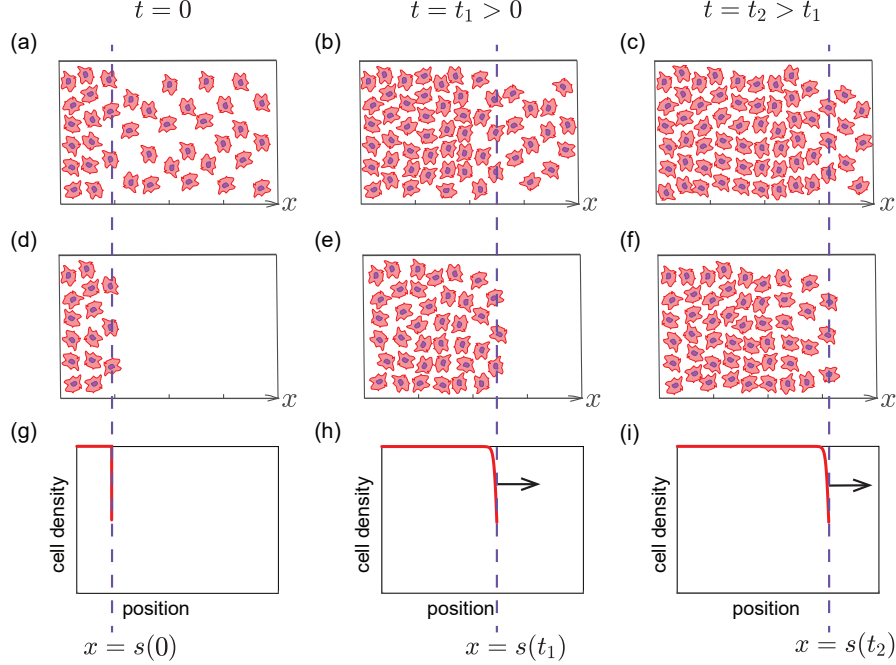

Figure 4.1: Schematic showing two interpretations of the non-vanishing Stefan model of invasion. (a)–(c) Evolution of a motile and proliferative cell population leading to an invading front moving into an initially occupied region. (d)–(f) Evolution of a motile and proliferative cell population leading to an invading front moving into an initially-vacant region. (g)–(i) Both schematics lead to an evolving density profile, moving in the positive x-direction with a non-vanishing, sharp-front density profile. Each column, from left-to-right, shows snapshots at different values of time, $t = 0, t_1$ and t_2, with $0 < t_1 < t_2$, and the position of the moving front, $x = s(t)$, is shown with three dashed vertical lines.

This work is organised as follows. We first introduce time-dependent solutions of the partial differential equation (PDE) model and we demonstrate that late-time numerical solutions give rise to a range of invading and retreating travelling waves. Following this numerical motivation, we show how these late-time PDE solutions are related to various trajectories in the classical Fisher-KPP phase plane [Murray 2002]. Focusing on the phase plane, we then obtain a range of solutions describing various travelling wave phenomena, including exact solutions for stationary waves, $c = 0$, and exact solutions for which the ordinary differential equation (ODE) governing the phase plane has the Painlevé property, $c = \pm 5/\sqrt{6}$ [Ablowitz and Zeppetella 1979, Kaliappan 1984, McCue et al. 2021a]. Building on these exact results, we then obtain

various approximate perturbation solutions that allow us to study: (i) slowly invading or retreating travelling waves, $|c| \ll 1$; (ii) fast retreating travelling waves, $-c \gg 1$; and, (iii) fast invading travelling waves, $c \gg 1$. At the outset, we acknowledge that one of the weaknesses of the Fisher-Stefan model is the lack of biological interpretation of the parameter κ and a absence of methods for measuring this parameter. Our analysis helps to overcome this limitation since our exact and perturbation solutions allow us to relate κ to the wave speed, c. This is a useful outcome because experimental measurements of c are relatively straightforward to obtain and so our analysis allows us to interpret such measurements of c in terms of κ, given that the density u_{f} of the population at the interface could also be inferred from experimental measurements [Jin et al. 2016].

4.3 Results and discussion

4.3.1 Mathematical model

We begin by studying the numerical solutions of the following non-dimensional moving boundary problem [Du and Lin 2010, Du et al. 2014a, Du et al. 2014b]

$$\frac{\partial u}{\partial t} = \frac{\partial^2 u}{\partial x^2} + u\left(1 - u\right), \quad 0 < x < s(t), \tag{4.1}$$

$$\frac{\partial u(0,t)}{\partial x} = 0, \quad u(s(t),t) = u_{\mathrm{f}}, \quad \frac{\mathrm{d}s(t)}{\mathrm{d}t} = -\kappa \frac{\partial u(s(t),t)}{\partial x}, \tag{4.2}$$

where $u(x,t) \geq 0$ is the population density [El-Hachem et al. 2019]. The length of the domain, $s(t)$, is determined as part of the solution through the classical one-phase Stefan condition. As we described in the Introduction, the key novelty here is to consider a non-vanishing boundary condition $u(s(t),t) = u_{\mathrm{f}} \in [0,1)$, which means that our model simplifies to the Fisher-Stefan model in the special case where $u_{\mathrm{f}} = 0$. While our travelling wave analysis is valid on an infinite domain, we study time-dependent travelling waves by working with a sufficiently large finite domain, $0 < x < s(t)$. For all time-dependent PDE solutions we consider the initial condition ,

$$u(x,0) = \begin{cases} 1, & 0 < x < \beta, \\ \dfrac{(1 - u_{\mathrm{f}})}{(s(0) - \beta)}(s(0) - x) + u_{\mathrm{f}}, & \beta < x < s(0), \end{cases} \tag{4.3}$$

which is a ramp-shaped function for which we must specify values of $\beta > 0$ and $s(0)$. While this work focuses on this linear ramp function, there are many other options for $u(x, 0)$. The key property of $u(x, 0)$ is that we have $u(x, 0) = 1$ near $x = 0$, and $u(s(0), 0) = u_\mathrm{f}$ at the front. Our choice of a linear ramp function is the simplest choice of initial condition to meet these properties, however other functional forms are possible, such as a nonlinear function of position. Preliminary numerical experimentation (not shown) indicates that the long–time travelling wave solutions of the mathematical model do not depend on these details. Note that when we study invading travelling waves we choose $s(0) = 1$, whereas when we study retreating travelling waves we choose $s(0) \gg 1$ [McCue et al. 2021b]. Full details of the numerical method to solve this moving boundary problem are given in Appendix A, and MATLAB software to implement these algorithms are available on GitHub.

4.3.2 Time dependent PDE solutions

Numerical results in Figure 4.2 show the evolution of $u(x, t)$ for various choices of κ. In all cases we see that the initial condition rapidly evolves into a constant speed, constant shape travelling wave solution. Results in the left column of Figure 4.2 are for $u_\mathrm{f} = 0.25$ while the results in the right column involve $u_\mathrm{f} = 0.75$. We see in all cases that the density is non-vanishing at the front of the profile, $x = s(t)$. Results in Figure 4.2(a)–(f) involve setting $\kappa > 0$ meaning that the time-dependent PDE solutions evolve to invading travelling wave solutions with $c > 0$. It is interesting to note that results in Figure 4.2(e)–(f) involve travelling wave solutions with $c = 0.50$, which is not possible with the usual nondimensional Fisher-KPP or Porous-Fisher models since travelling wave solutions for those models never move with such a slow wave speed [Murray 2002]. Results in Figure 4.2(g)–(h) involve $\kappa < 0$ and so lead to retreating travelling waves with $c < 0$. Again, neither of these results are possible using the Fisher-KPP or Porous-Fisher models [El-Hachem et al. 2021a]. Now that we have provided numerical evidence of this range of late-time travelling wave behaviour in terms of the time-dependent PDE solutions, we will analyse these travelling wave solutions using the phase plane.
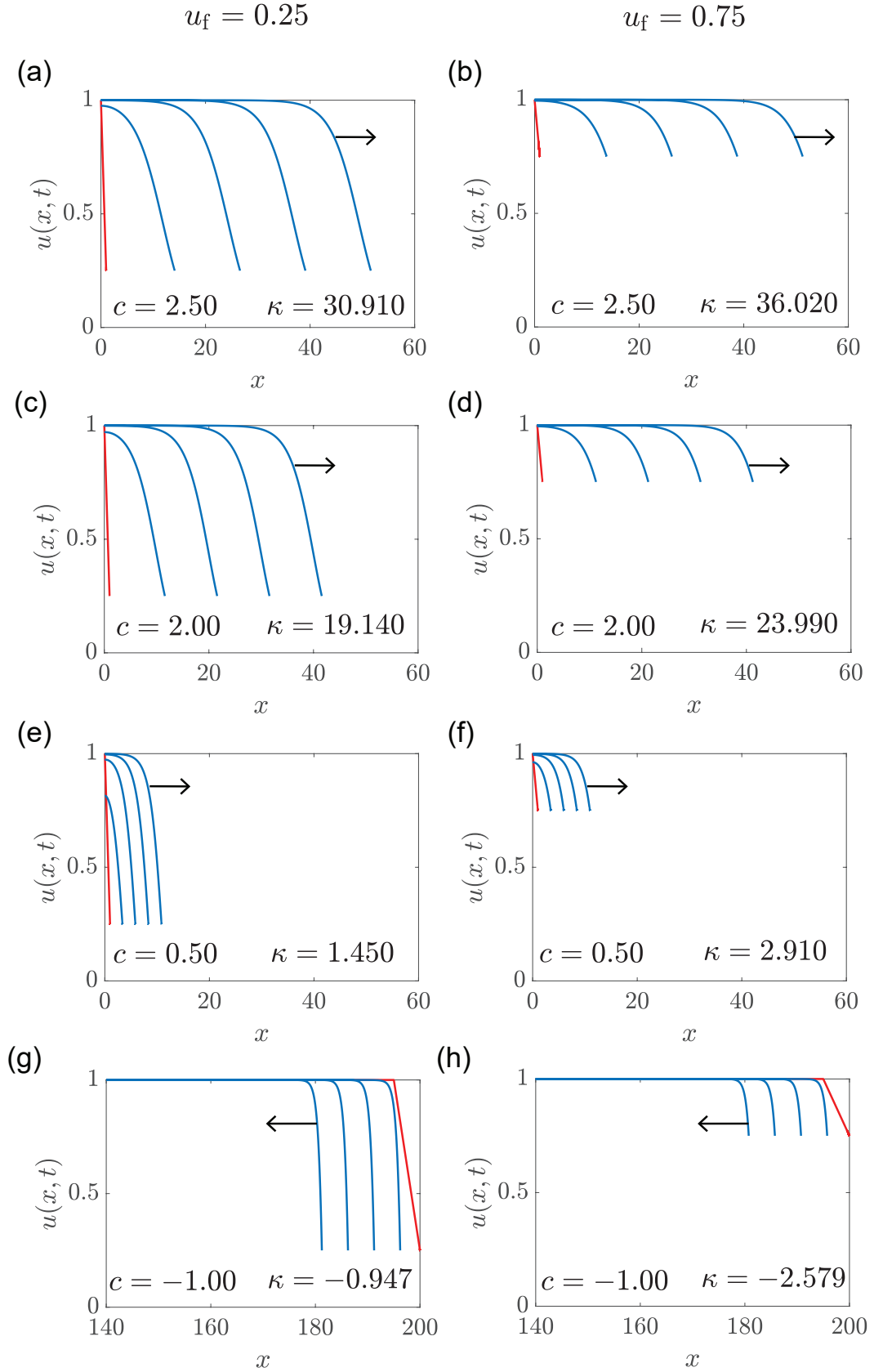
Figure 4.2: Time-dependant solutions of Equations (4.1)–(4.3). Density profiles $u(x,t)$ (blue) at times $t = 5, 10, 15$ and 20, evolving from the initial condition (red) with $s(0) = 1$ and $\beta = 0$ in (a)–(f), and $s(0) = 200$ and $\beta = 195$ in (g)–(h). Results in (a), (c) and (e) evolve into invading travelling wave solutions with $c = 2.50, 2.00$ and 0.50, respectively. Profiles in (a), (c) and (e) correspond to $u_{\mathrm{f}} = 0.25$ while profiles in (b), (d) and (f) correspond to $u_{\mathrm{f}} = 0.75$. Results in (g) and (h) evolve into retreating travelling wave solutions, both with $c = -1.00$. Profiles in (g) and (h) correspond to $u_{\mathrm{f}} = 0.25$ and $u_{\mathrm{f}} = 0.75$, respectively. The values of κ are given in each subfigure.

4.3.3 Phase plane analysis

In the usual way, we analyse travelling wave solutions by re-writing Equation (4.1) in terms of the travelling wave coordinate, $z = x - ct$ [Canosa 1973, Murray 2002]. We seek solutions of the form $u(x,t) = U(z)$ which leads to

$$\frac{\mathrm{d}^2U}{\mathrm{d}z^2} + c\frac{\mathrm{d}U}{\mathrm{d}z} + U(1-U) = 0, \quad -\infty < z < 0, \tag{4.4}$$

with boundary conditions

$$U(-\infty) = 1, \quad U(0) = u_{\mathrm{f}}, \quad c = -\kappa\frac{\mathrm{d}U(0)}{\mathrm{d}z}, \tag{4.5}$$

where, for convenience, we have chosen $z = 0$ to correspond to the moving boundary.

To proceed, we re-write Equation (4.4) as a first order dynamical system

$$\frac{\mathrm{d}U}{\mathrm{d}z} = V, \tag{4.6}$$

$$\frac{\mathrm{d}V}{\mathrm{d}z} = -cV - U(1-U), \tag{4.7}$$

which defines the well-known phase plane associated with travelling wave solutions of the Fisher-KPP model [Canosa 1973, Murray 2002]. Full details of how we obtain numerical trajectories in the phase plane are given in Appendix A. This phase plane involves two equilibrium points $(\bar{U}, \bar{V}) = (0,0)$ and $(\bar{U}, \bar{V}) = (1,0)$. Linearisation shows that $(\bar{U}, \bar{V}) = (0,0)$ is a stable spiral if $c^2 < 4$, and a stable node if $c^2 > 4$, whereas $(\bar{U}, \bar{V}) = (1,0)$ is a saddle for all c. Normally, in standard phase plane analysis of the Fisher-KPP model we reject travelling wave solutions with $c^2 < 4$ on physical grounds since the local behaviour about the origin implies that the density goes negative as the heteroclinic trajectory between $(1,0)$ and $(0,0)$ spirals into the origin. Here, we find that no such restriction is necessary as we will now explain.

Results in Figure 4.3(a), (c), (e) and (g) show the phase plane for $c = 2.5, 2, 0.5$ and -1, respectively. In each case the heteroclinic orbit between $(1,0)$ and $(0,0)$ is shown in dashed pink. In Figure 4.3(a) and (b) the heteroclinic orbit enters $(0,0)$ along the dominant eigenvector of the saddle node. In contrast, in Figure 4.3(e) we see the heteroclinic orbit spiraling into $(0,0)$, which is consistent with the linear analysis. Each phase plane is superimposed

with a vertical line at $U(z) = u_{\mathrm{f}} = 0.5$, and that part of the heteroclinic orbit where $U(z) < u_{\mathrm{f}}$ is shown as a thick blue line since this is the physically-relevant part of the trajectory corresponds to the travelling wave solution. In contrast, that part of the trajectory where $U(z) < u_{\mathrm{f}}$ is nonphysical, and does not form part of the travelling wave solution [El-Hachem et al. 2019]. Therefore, the travelling wave solutions correspond to a truncated heteroclinic orbit, and this truncation explains why the usual conditions relating to the linearisation about the origin are irrelevant when we consider working in a moving boundary framework.

The role of the Stefan condition in the phase plane is related to the point where the heteroclinic orbit intersects the vertical line where $U(z) = u_{\mathrm{f}}$. In the phase plane, the Stefan condition corresponds to $c = -\kappa\,\mathrm{d}U(0)/\mathrm{d}z$, which is equivalent to $c = -\kappa V(0)$. This means that if the intersection point of the heteroclinic orbit and the vertical line at u_{f} is $(U(0), V(0))$, then $\kappa = -c/V(0)$, which allows us to calculate κ from the phase plane. For completeness, results in Figure 4.3(b), (d), (f) and (h) show $U(z)$ corresponding to the heteroclinic orbits in Figure 4.3(a), (c), (e) and (g), respectively. In these plots we show $U(z)$ superimposed with horizontal lines at $U = 0$ (black) and $U = u_{\mathrm{f}}$ (pink). The physical part of the travelling wave for $U > u_{\mathrm{f}}$ and $z < 0$ is shown in solid blue, whereas the nonphysical part of the travelling wave for $z > 0$ is shown in dashed pink. Indeed, the unphysical part of the $U(z)$ profile in Figure 4.3(f) oscillates around $U = 0$ as $z \to \infty$. In all cases we superimpose a pink disc on the point $U = 0$ at $z = 0$, since this is the point where the Stefan condition applies.
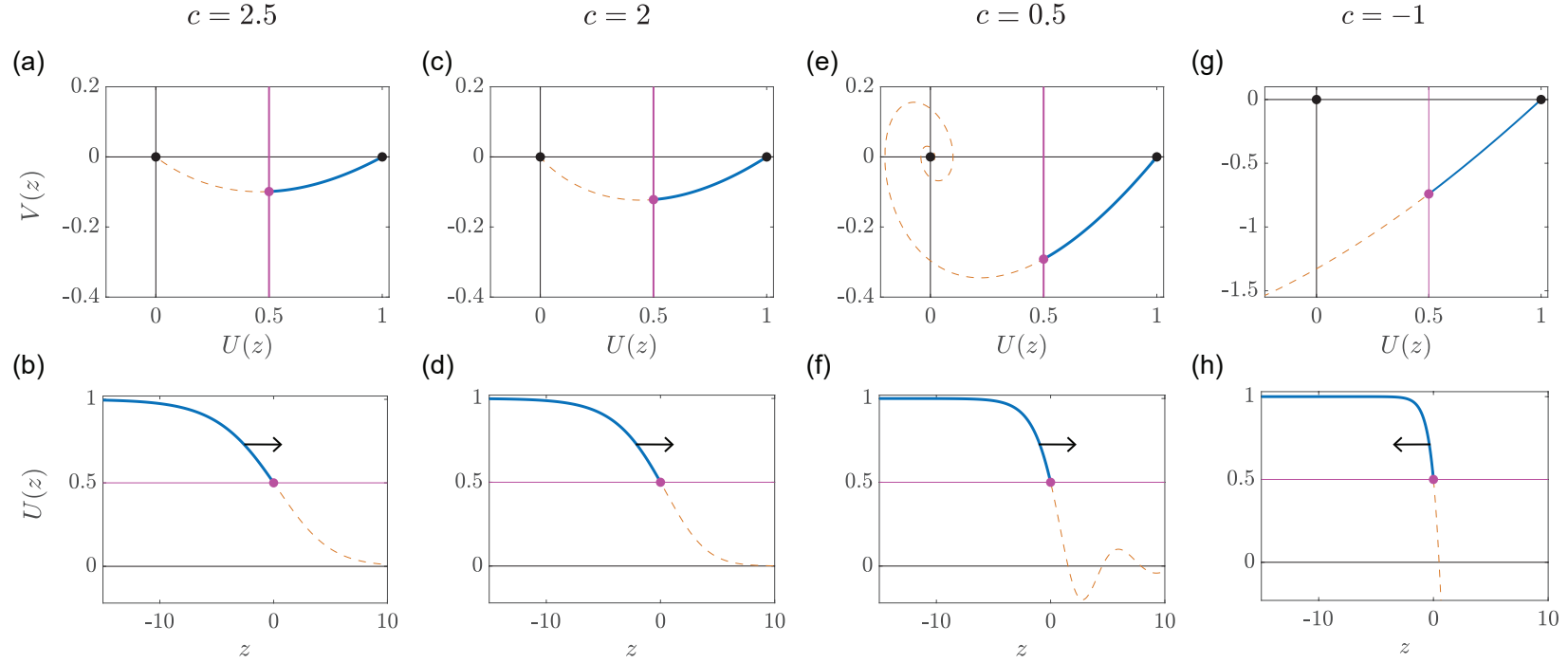
Figure 4.3: Phase planes for invading travelling waves with $u_\mathrm{f} = 0.5$. Phase planes in (a), (c), (e) and (g) show the trajectories corresponding to travelling wave $U(z)$, for $c = 2.5, 2, 0.5$ and -1 respectively (dashed orange), obtained by solving the dynamical system (4.6)–(4.7). Each trajectory is superimposed with a solid blue curve that is obtained from the late-time PDE solutions from Figure 4.2. In each phase plane we show the equilibrium points (black disc) and the point at which the trajectory intersects with the vertical line $U = u_\mathrm{f}$ (pink disc). Results in (b), (d), (f) and (h) show $U(z)$ for each phase plane in (a), (c), (e) and (g) respectively. These results are shifted so that the moving boundary is at $z = 0$. Horizontal lines at $U(z) = 0$ and $U(z) = u_\mathrm{f}$ are superimposed, and the location at which the $U(z)$ curve intersects with u_f are highlighted (pink disc).

Before proceeding, it is useful to remember the similarities and differences between the time-dependent PDE solutions and the phase plane analysis. To solve the time-dependent PDE model (4.1)–(4.3) we treat κ as an input parameter and the late-time PDE solutions allow us to estimate the wave speed, c, which is an output of the model. In contrast, when we study the heteroclinic orbit in the phase plane, we treat c as an input parameter into (4.6)–(4.7), and we use the resulting numerical phase plane trajectory to estimate $\kappa = -c/V(0)$, which is an output of the phase plane. Now that we have demonstrated the relationship between the time-dependent PDE solutions and the phase plane analysis for a range of c and u_f, we will now explore some exact results for special values of c and then develop some insightful perturbation approximations for limiting values of c.

4.3.4 Stationary wave, $c = 0$.

The exact shape of the stationary travelling wave for $c = 0$ can be obtained by re-writing Equations (4.6)–(4.7) as

$$\frac{\mathrm{d}V}{\mathrm{d}U} = \frac{-cV - U(1 - U)}{V}, \tag{4.8}$$

which can be solved when $c = 0$, giving

$$V(U) = \pm(1 - U)\sqrt{\frac{2U + 1}{3}}. \tag{4.9}$$

To proceed, we focus on $V(U) < 0$. Integrating Equation (4.9) with $U(0) = u_\mathrm{f}$ gives an expression for the shape of the stationary wave,

$$U(z) = \frac{3}{2}\left[\tanh\left(\frac{z}{2} - \mathrm{arctanh}\left[\sqrt{\frac{2u_\mathrm{f} + 1}{3}}\right]\right)\right]^2 - \frac{1}{2}, \tag{4.10}$$

Results in Figure 4.4(a) compare the exact stationary travelling wave solution, Equation (4.10), with a late-time numerical solution of Equations (4.1)–(4.3) with $\kappa = 0$ and $u_\text{f} = 0.5$, showing that the exact result is visually indistinguishable at this scale. The phase plane for $c = 0$ in Figure 4.4(b) shows the homoclinic orbit defined by Equation (4.9), where for completeness we show both the positive and negative branches. In this phase plane we show a vertical line at $u_\text{f} = 0.5$, and we also superimpose the late-time numerical solution of Equations (4.1)–(4.3) plotted in the phase plane coordinate. Here we see that the late-time PDE solution is indistinguishable from the truncated homoclinic orbit where $U(z) > u_\text{f}$ and $V(z) < 0$.
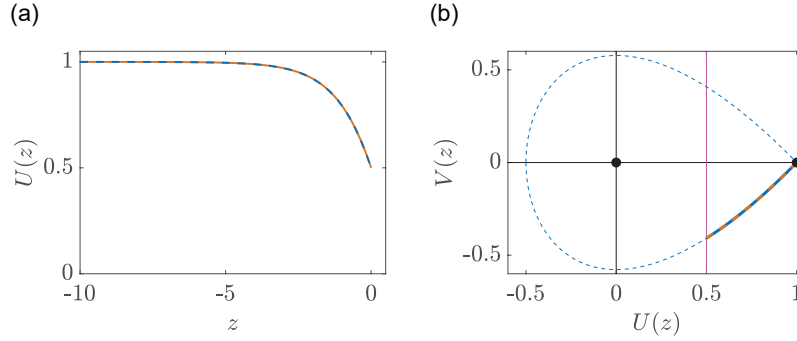
Figure 4.4: Exact solution for $c = 0$ with $u_\text{f} = 0.5$. (a) Comparison of the exact solution, Equation (4.10), (blue) with a late time numerical solution of Equations (4.1)–(4.3) (dashed orange) with $\kappa = 0$ and an initial condition with $s(0) = 10$ and $\beta = 1$. (b) Exact phase plane trajectory, Equation (4.9) (blue) superimposed with the trajectory obtained by plotting the late-time PDE solution in the phase plane (dashed orange). The exact homoclinic orbit is given (dashed blue), equilibrium points are highlighted (black discs) along with the vertical line at $U(z) = u_\text{f}$ (pink).

4.3.5 Solutions with the Painlevé property, $c = \pm 5/\sqrt{6}$.

While exact analytic solutions of Equation (4.4) are unknown for arbitrary values of c, it is well known that exact solutions can be written for values of c for which Equation (4.4) has the Painlevé property, $c = \pm 5/\sqrt{6}$. In these cases the solution of Equation (4.4) can be written in terms of the Weierstaß p-function [Ablowitz and Zeppetella 1979, McCue et al. 2021a], and in the case of $c = 5/\sqrt{6}$ it is remarkable that this solution can be written very simply in terms of exponential functions [Kaliappan 1984, Murray 2002],

$$U(z) = \left[1 + \left(-1 + \sqrt{\frac{1}{u_\text{f}}} \right) e^{z/\sqrt{6}} \right]^{-2}, \qquad (4.11)$$

which corresponds to

$$V(U) = -\frac{2U^{3/2}}{\sqrt{6}}\left(\sqrt{\frac{1}{U}} - 1\right).$$ (4.12)

These two expressions allow us to plot the heteroclinic orbit in the phase plane and to derive an expression for $\kappa = -c/V(u_{\mathrm{f}})$, namely

$$\kappa = \frac{5}{2u_{\mathrm{f}}^{3/2}\left(\sqrt{\frac{1}{u_{\mathrm{f}}}} - 1\right)}.$$ (4.13)

Results in Figure 4.5(a) show the exact travelling wave solution for $c = 5/\sqrt{6}$ and $u_{\mathrm{f}} = 0.5$ superimposed on a late-time PDE solution to make the point that the two travelling wave profiles are indistinguishable at this scale. The corresponding phase plane in Figure 4.5(b) compares the exact heteroclinic orbit with the physically-relevant part of that orbit where $U > u_{\mathrm{f}}$ from the late-time PDE solution. The match between the exact result and the numerically-generated phase plane trajectory is excellent. We note that Equation (4.13) allows us to explore how κ varies with u_{f}, for example setting $u_{\mathrm{f}} = 0.5$ leads to $\kappa = 5(2 + \sqrt{2}) \approx 17.071$.

For $c = -5/\sqrt{6}$ the exact solution can be written in terms of the Weierstaß p-function [McCue et al. 2021a],

$$U(z) = \mathrm{e}^{2z/\sqrt{6}}\wp\left(\mathrm{e}^{z/\sqrt{6}} - k; 0; g_3\right),$$ (4.14)

giving

$$V(z) = \frac{1}{\sqrt{6}}\mathrm{e}^{2z/\sqrt{6}}\left[2\wp\left(\mathrm{e}^{z/\sqrt{6}} - k; 0; g_3\right) + \mathrm{e}^{z/\sqrt{6}}\wp'\left(\mathrm{e}^{z/\sqrt{6}} - k; 0; g_3\right)\right],$$ (4.15)

where the two constants k and g_3 are obtained by solving Equation (4.14) with $U(0) = u_{\mathrm{f}}$ and $-2\pi k g_3^{1/6} = \Gamma(1/3)$ [Ablowitz and Zeppetella 1979], where $\Gamma(x)$ is the Gamma function. Results in Figure 4.5(c) show the exact travelling wave solution for $c = -5/\sqrt{6}$ and $u_{\mathrm{f}} = 0.5$ superimposed on a late-time PDE solution, and we see the two profiles are indistinguishable at this scale. The corresponding phase plane in Figure 4.5(d) compares exact phase plane trajectory with the physically-relevant part of the numerically-generated trajectory where $U > u_{\mathrm{f}}$. Again the match between the exact result and numerical result

is excellent. As before, the exact solution provides insight into the relationship between κ and u_{f} by setting $U(\alpha) - u_{\mathrm{f}} = 0$ for α and then calculating $\kappa = -5/[\sqrt{6}V(\alpha)]$. For example, with $u_{\mathrm{f}} = 0.5$ we have $\kappa = -1.7351$.
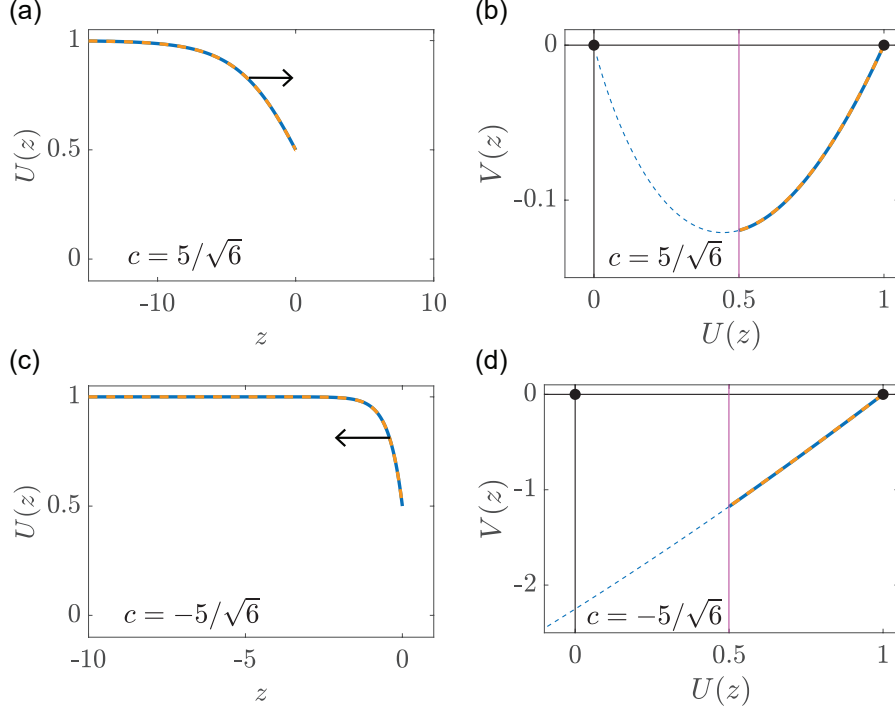

Figure 4.5: Exact solution for $c = \pm 5/\sqrt{6}$ with $u_{\mathrm{f}} = 0.5$. (a) and (c) Compare exact solutions given by Equations (4.11) and (4.14) for $c = \pm 5/\sqrt{6}$ respectively (blue), with a late time numerical solution of Equations (4.1)–(4.3) (dashed orange) with $\kappa = 17.0710$ and $\kappa = -1.7351$, respectively. (b) and (d) Compare the exact trajectories in the phase plane, Equations (4.12) and (4.14)-(4.15) for $c = \pm 5/\sqrt{6}$, respectively, superimposed with the trajectories obtained by plotting the late-time PDE solution in the phase plane (dashed orange). The phase plane trajectories are given (dashed blue), equilibrium points are highlighted (black discs) along with the vertical line at $U(z) = u_{\mathrm{f}}$ (pink).

4.3.6 Slow travelling waves

We now build upon the previous results for the stationary wave, $c = 0$, to develop insightful approximations for slowly invading or slowly retreating travelling wave solutions. Seeking a perturbation solution for $|c| \ll 1$, we substitute $V(U) \sim \sum_{n=0}^{\infty} c^n V_n(U)$ as $c \to 0$ into Equation (4.8) to give,

$$\frac{\mathrm{d}V_0}{\mathrm{d}U}V_0 + U(1 - U) = 0, \tag{4.16}$$

$$\frac{\mathrm{d}}{\mathrm{d}U}(V_1 V_0) + V_0 = 0, \tag{4.17}$$

$$\frac{\mathrm{d}}{\mathrm{d}U}(V_2 V_0) + V_1\left(\frac{\mathrm{d}V_1}{\mathrm{d}U} + 1\right) = 0, \tag{4.18}$$

113

with boundary conditions $V_0(1) = V_1(1) = V_2(1) = 0$. The solutions of these differential equations are

$$V_0(U) = \frac{\sqrt{3(2U+1)}(U-1)}{3}, \tag{4.19}$$

$$V_1(U) = \frac{-(U-2)(2U+1)^{3/2} - 3\sqrt{3}}{5(U-1)\sqrt{2U+1}}, \tag{4.20}$$

$$V_2(U) = \left(\frac{-18\sqrt{3}}{25(2U+1)^{3/2}(U-1)\left(\sqrt{3(2U+1)} - 3\right)^2 \left(\sqrt{3(2U+1)} + 3\right)^2} \right)$$

$$\left(\left[\frac{(U-1)^2(2U+1)}{2} \right] \ln \left[\frac{(U-1)\left(\sqrt{3(2U+1)} + 3\right)}{6\left(\sqrt{3(2U+1)} - 3\right)} \right] \right.$$

$$- 2U^3(6U^2 - 15U + 20) + 15U(U+2) + 31$$

$$\left. + 6(U-2)(2U+1)\sqrt{3(2U+1)} \right). \tag{4.21}$$
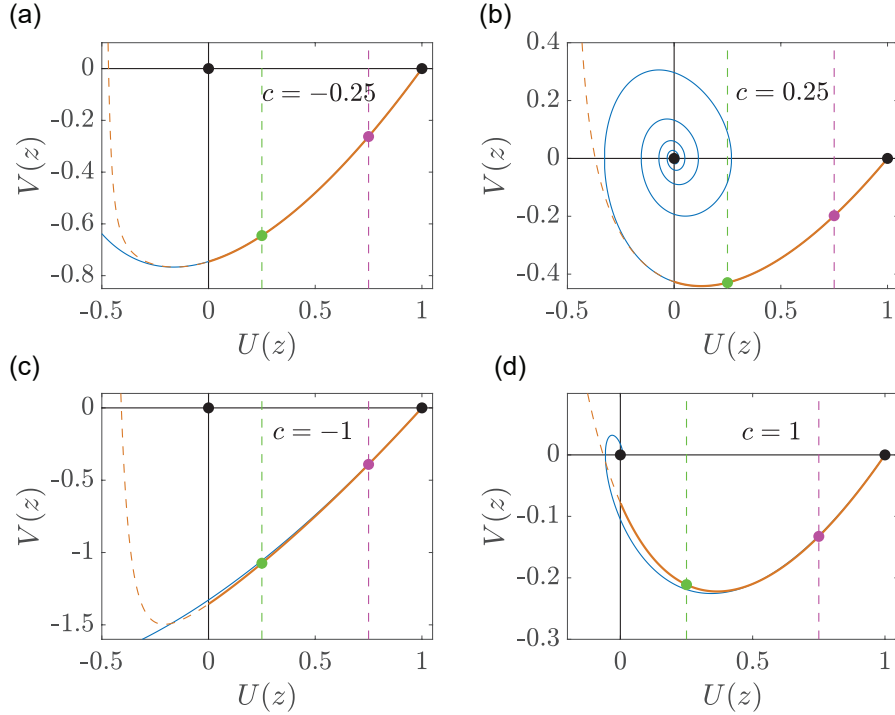
Figure 4.6: Perturbation solutions for $|c| \ll 1$. (a)–(d) show phase planes for $c = \mp 0.25$ and ∓ 1.00, respectively. Numerical solution of Equations (4.6)–(4.7) (blue) are superimposed on the perturbation solutions (orange). The intersection of the perturbation solutions with vertical lines at $U(z) = u_f = 0.25$ and $U(z) = u_f = 0.75$ are highlighted (green and pink discs). Equilibrium points are shown with black discs.

We now compare the accuracy of this $\mathcal{O}(c^3)$ perturbation solutions in Figure 4.6 for $c = \pm 0.25$ and $c = \pm 1$. The numerical solution of the dynamical system in each phase plane is shown in blue, whereas the perturbation solution is shown in orange. In all cases we include vertical lines at $u_f = 0.75$ (pink) and $u_f = 0.25$ (green) to illustrate the fact that the accuracy of the perturbation solution depends upon u_f as well as c. For example, in Figure 4.6(d) for $c = 1$ we see that the numerically-generated phase plane trajectory and the perturbation solution are visually indistinguishable for $U > 0.75$ meaning that the perturbation solution is very accurate for $u_f = 0.75$. In contrast, we see some visual discrepancy between the numerically-generated phase plane trajectory and the perturbation solution for smaller values of U, which means that the accuracy of the perturbation solution is reduced for $u_f = 0.25$. Nonetheless, for all values of c in Figure 4.6 the perturbation solution is very close to the numerically-generated phase plane trajectories. For completeness we compare $\mathcal{O}(c)$, $\mathcal{O}(c^2)$ and $\mathcal{O}(c^3)$ perturbation solutions for $c = \pm 0.25$ and $c = \pm 1$ in Appendix B.
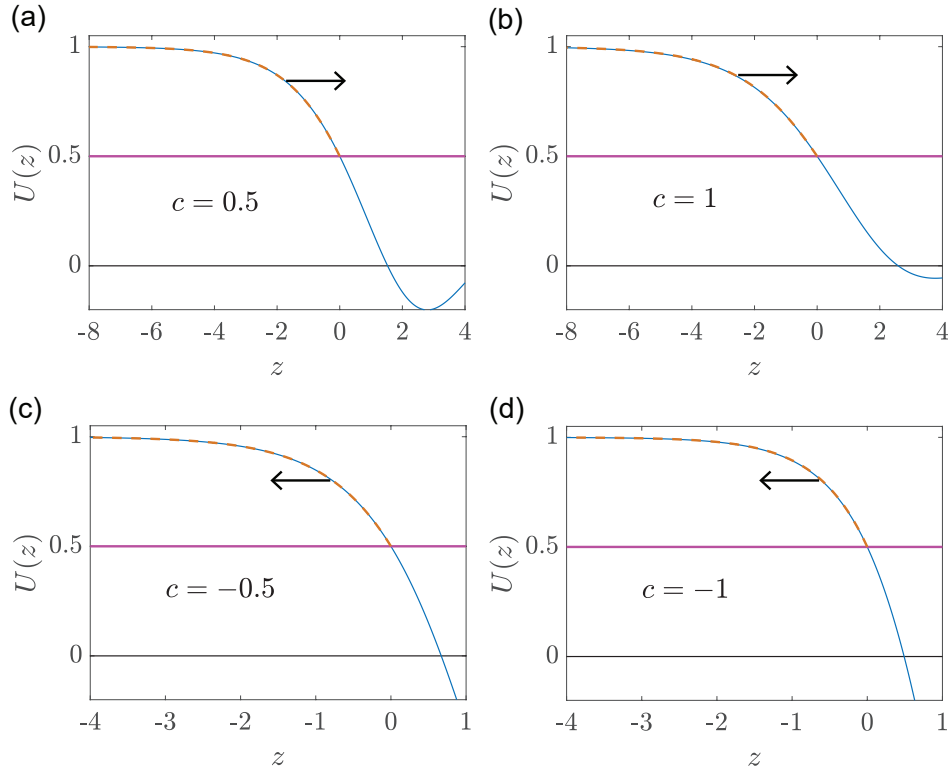

Figure 4.7: Perturbation solutions for slowly invading and retreating travelling waves. The shape of travelling wave profile, $U(z)$, obtained using the numerical solution of the phase plane trajectory (blue) is compared with perturbation solution in dashed orange, for $c = 0.5$ and 1 in (a)–(b) and $c = -0.5$ and -1 in (c)–(d).

A comparison of the two solutions in terms of the shape of $U(z)$, where we have numerically integrated the approximate $V(U)$ trajectories in the phase plane, is made in Figure 4.7. Here we compare the numerically-generated phase plane trajectory and the perturbation solution by numerically integrating $V(U)$ using the trapezoid rule. Plotted in this way, we see that the shape of the travelling wave obtained from the perturbation solution is indistinguishable from the shape of the travelling wave solution derived from the numerically-generated phase plane trajectory for $|c| \leq 1$.

Another way to test the accuracy of the perturbation solution is by comparing our numerical phase plane estimate κ with the result obtained from the perturbation solution, κ_p. Evaluating our $\mathcal{O}(c^3)$ perturbation approximation at $U = u_\mathrm{f}$, and then expanding the expression $\kappa = -c/V(u_\mathrm{f})$ in a series gives

$$
\begin{aligned}
\kappa_\mathrm{p} = {} & \frac{3}{\sqrt{3(2u_\mathrm{f}+1)}(1-u_\mathrm{f})}c + \frac{3}{5}\left[\frac{\left(2u_\mathrm{f}^2 - 3u_\mathrm{f} - 2\right)\left(\sqrt{2u_\mathrm{f}+1}\right) + 3\sqrt{3}}{(2u_\mathrm{f}+1)^{3/2}(1-u_\mathrm{f})^3}\right]c^2 \\
& - \left(\frac{18\sqrt{3}}{25\left(2u_\mathrm{f}+1\right)^{5/2}\left(\sqrt{3}\sqrt{2u_\mathrm{f}+1}+3\right)^2\left(\sqrt{3}\sqrt{2u_\mathrm{f}+1}-3\right)^2(1-u_\mathrm{f})^3}\right) \\
& + \left(90(2u_\mathrm{f}+1)(1-u_\mathrm{f})^2\ln\left[\frac{(u_\mathrm{f}-1)\left(\sqrt{3(2u_\mathrm{f}+1)}+3\right)}{6\left(\sqrt{3(2u_\mathrm{f}+1)}-3\right)}\right]\right. \\
& + 12u_\mathrm{f}^5 - 30\left(u_\mathrm{f}^4 + 6u_\mathrm{f}^3\right) + 5\left(39u_\mathrm{f}^2 + 42u_\mathrm{f}\right) + 279 \\
& \left. + 54(2u_\mathrm{f}+1)(u_\mathrm{f}-2)\sqrt{3(2u_\mathrm{f}+1)}\right)c^3 + \mathcal{O}\left(c^4\right),
\end{aligned}
$$

(4.22)

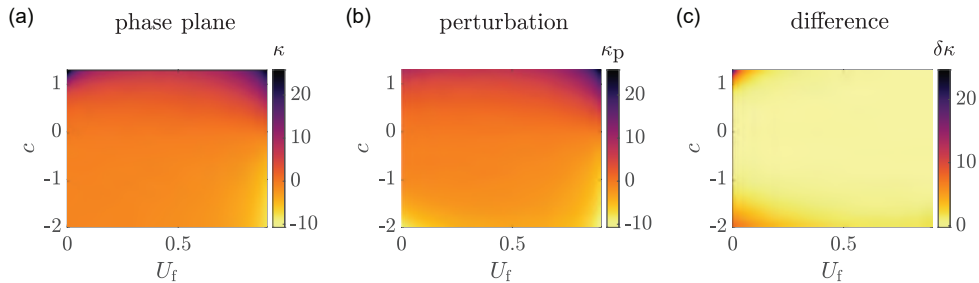which can be used to estimate κ provided we have experimental estimates of c and u_f.

Figure 4.8: κ **as a function of** c **and** u_f **for** $|c| \ll 1.$ (a) Heat map showing κ as a function of c and u_f where estimates of κ are obtained by solving Equations (4.6)–(4.7) in the phase. (b) Heat map showing κ_p from the perturbation solution, Equation (4.22). (c) Difference between the phase plane and perturbation estimates of κ, $\delta\kappa = \kappa - \kappa_\mathrm{p}$.

Figure 4.8(a) shows a heat map of κ as a function of c and u_f in the interval $-2 < c < 1$ obtained from the phase plane. The heat map in Figure 4.8(b) shows the same result obtained from the perturbation solution (4.22). The numerically-generated phase plane estimates are difficult to distinguish from the perturbation results, so we plot a heat map of $\delta\kappa = \kappa - \kappa_\text{p}$ in Figure 4.8(c) showing that the difference is small everywhere except for near $u_\text{f} = 0$.

4.3.7 Fast retreating travelling waves

We now examine fast retreating travelling wave solutions, $-c \gg 1$, by rewriting the governing boundary value problem as

$$\frac{1}{c}\frac{\mathrm{d}^2U}{\mathrm{d}z^2} + \frac{\mathrm{d}U}{\mathrm{d}z} + \frac{1}{c}U(1-U) = 0, \quad -\infty < z < 0, \tag{4.23}$$

which is singular as $c \to -\infty$. To address this problem we construct a matched asymptotic expansion by treating $1/c$ as a small parameter [Murray 1984]. The boundary conditions for this problem are $U(0) = u_\text{f}$ and $U(z) \to 1$ as $z \to -\infty$. Setting $1/c = 0$ and solving the resulting ODE gives the outer solution $U(z) = 1$, which matches the boundary condition as $z \to -\infty$. To construct the inner solution near $z = 0$, we rescale the independent variable $\zeta = zc$. Therefore, in the boundary layer we have

$$\frac{\mathrm{d}^2U}{\mathrm{d}\zeta^2} + \frac{\mathrm{d}U}{\mathrm{d}\zeta} + \frac{1}{c^2}U(1-U) = 0, \quad 0 < \zeta < \infty. \tag{4.24}$$

Substituting $U(\zeta) \sim \sum_{n=0}^{\infty} c^{-2n}U_n(\zeta)$ as $c \to -\infty$ into Equation (4.24) gives

$$\frac{\mathrm{d}^2U_0}{\mathrm{d}\zeta^2} + \frac{\mathrm{d}U_0}{\mathrm{d}\zeta} = 0, \tag{4.25}$$

$$\frac{\mathrm{d}^2U_1}{\mathrm{d}\zeta^2} + \frac{\mathrm{d}U_1}{\mathrm{d}\zeta} + U_0(1-U_0) = 0, \tag{4.26}$$

$$\frac{\mathrm{d}^2U_2}{\mathrm{d}\zeta^2} + \frac{\mathrm{d}U_2}{\mathrm{d}\zeta} + U_1(1-2U_0) = 0, \tag{4.27}$$

$$\frac{\mathrm{d}^2U_3}{\mathrm{d}\zeta^2} + \frac{\mathrm{d}U_3}{\mathrm{d}\zeta} + U_2(1-2U_0) - U_1^2 = 0, \tag{4.28}$$

where $U_0(0) = u_\text{f}$ and $U_1(0) = U_2(0) = U_3(0) = 0$, and $U_0(\zeta) \to 1$, $U_1(\zeta) \to 0$, $U_2(\zeta) \to 0$, and $U_3(\zeta) \to 0$ as $\zeta \to \infty$. The solution of these boundary value

problems are

$$U_0(\zeta) = (u_{\rm f} - 1){\rm e}^{-\zeta} + 1, \tag{4.29}$$

$$U_1(\zeta) = \left(\frac{u_{\rm f} - 1}{2}\right)\left[(u_{\rm f} - 1){\rm e}^{-2\zeta} + (-2\zeta - u_{\rm f} + 1){\rm e}^{-\zeta}\right], \tag{4.30}$$

$$U_2(\zeta) = \left(\frac{u_{\rm f} - 1}{12}\right)\left(\left[6\zeta(\zeta + 1 + u_{\rm f}) + 4u_{\rm f}^2 + 7u_{\rm f} - 11\right]{\rm e}^{-\zeta}\right.$$
$$\left. + (u_{\rm f} - 1)\left[-3(4\zeta + 2u_{\rm f} + 3){\rm e}^{-2\zeta} + 2(u_{\rm f} - 1){\rm e}^{-3\zeta}\right]\right), \tag{4.31}$$

$$U_3(\zeta) = \left(\frac{u_{\rm f} - 1}{144}\right)\left[\left(-24\zeta^3 - 108\zeta^2 - 12u_{\rm f}(3\zeta^2 + 13\zeta) - 4(12u_{\rm f}^2 + 21)\zeta\right.\right.$$
$$\left. -37u_{\rm f}^3 - 133u_{\rm f}^2 - 145u_{\rm f} + 315\right){\rm e}^{-\zeta}$$
$$+ \left(\left[3\left(4\left[12\left(\zeta^2 + u_{\rm f}\zeta\right) + 30\zeta + 19(u_{\rm f} + 1)\right] + 22u_{\rm f}^2\right)\right]{\rm e}^{-2\zeta}\right.$$
$$\left.\left. + \left[-4(9(2\zeta + u_{\rm f}) + 20){\rm e}^{-3\zeta} + 7(u_{\rm f} - 1){\rm e}^{-4\zeta}\right](u_{\rm f} - 1)\right)(u_{\rm f} - 1)\right]. \tag{4.32}$$
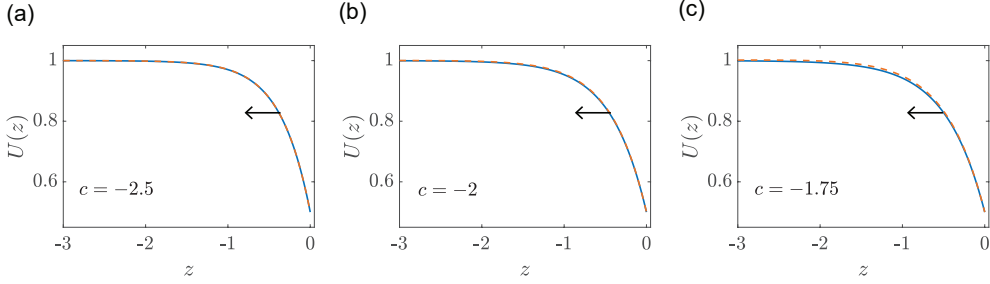
Figure 4.9: Perturbation solution for fast retreating travelling waves, $c \to -\infty$**.** (a)–(c) Perturbation solutions showing the shape of travelling waves for $c = -2.5, -2$ and -1.75, respectively (dashed orange) superimposed on late-time numerical solutions of Equations (4.1)–(4.3) (blue).

We now compare the accuracy of this $\mathcal{O}(c^{-8})$ perturbation solution in Figure 4.9 for $c = -2.5, -2$ and -1.75 where we superimpose a late-time numerical solution of Equations (4.1)–(4.3) onto the perturbation solution in terms of the re-scaled variable, $z = \zeta/c$. For this comparison we choose $u_{\rm f} = 0.5$, and we see that the numerical and perturbation solutions are visually indistinguishable for $c = -2.5$. Results for $c = -2$ and -1.75 show some small discrepancy between the numerical and perturbation profiles. Again, for completeness we compare $\mathcal{O}(c^{-2})$, $\mathcal{O}(c^{-4})$, $\mathcal{O}(c^{-6})$ and $\mathcal{O}(c^{-8})$ perturbation solutions for $c = -2.5, -2$ and -1.75 in Appendix B.

Again, we provide a further comparison between the accuracy of the perturbation solution in terms of estimating κ from the phase plane and the

perturbation solution, which gives

$$
\kappa_{\mathrm{p}} = \frac{-\left[1 - \dfrac{u_{\mathrm{f}}+1}{2c^2} + \dfrac{5u_{\mathrm{f}}^2 + 11u_{\mathrm{f}} + 8}{12c^4} + \dfrac{-57u_{\mathrm{f}}^3 - 197u_{\mathrm{f}}^2 - 281u_{\mathrm{f}} - 185}{144c^6}\right]}{1 - u_{\mathrm{f}}} + \mathcal{O}\left(\frac{1}{c^8}\right),
$$

(4.33)

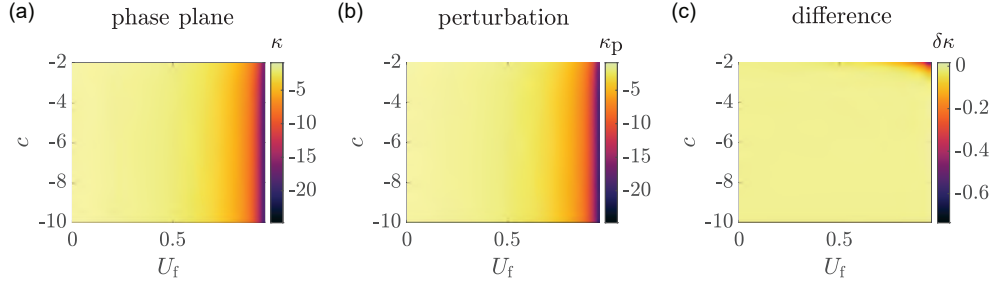which again allows us to estimate κ provided we have experimental estimates of c and u_{f}.

Figure 4.10: κ **as a function of** c **and** u_{f} **for** $c \to -\infty$**.** (a) Heat map showing κ as a function of c and u_{f} where estimates of κ are obtained by solving Equations (4.6)–(4.7) in the phase plane. (b) Heat map showing κ_{p} from the perturbation solution, Equation (4.33). (c) Difference between the phase plane and perturbation estimates of κ, $\delta\kappa = \kappa - \kappa_{\mathrm{p}}$.

Heat maps in Figure 4.10(a)–(b) compare numerical estimates of κ from the phase plane with the perturbation result (4.33). The heat map of $\delta\kappa = \kappa - \kappa_{\mathrm{p}}$ in Figure 4.10(c) shows that the $\mathcal{O}(c^{-8})$ perturbation solutions leads to extremely accurate solutions for κ for $c < -2$ for all u_{f}. Equation (4.33) reveals further information about the existence of travelling wave solutions for this model since we have $\kappa = -1/(1 - u_{\mathrm{f}})$ as $c \to -\infty$. Indeed, solving Equations (4.1)–(4.3) with $\kappa < -1/(1 - u_{\mathrm{f}})$ does not lead to constant speed, constant shape travelling wave solutions. Instead, for these cases the time-dependent solutions appear to undergo a form of finite-time blow-up, as explored in [McCue et al. 2021b].

4.3.8   Fast invading travelling waves

In Section 4.3.7 we saw that retreating travelling waves become increasingly steep as $c \to -\infty$. In this section we make use of the fact that, as noted by Murray [Murray 2002], invading travelling waves become increasingly flat as $c \to \infty$. This means that $V \to 0$ as $c \to \infty$. Following Canosa [Canosa 1973],

we re-write Equation (4.8) in terms of the re-scaled variable, $\tilde{V} = cV$, giving

$$\frac{\tilde{V}}{c^2}\frac{\mathrm{d}\tilde{V}}{\mathrm{d}U} + \tilde{V} + U(1 - U). \tag{4.34}$$

Assuming a solution of the form $\tilde{V}(U) \sim \sum_{n=0}^{\infty} c^{-2n}\tilde{V}_n(U)$ as $c \to \infty$ we obtain

$$\tilde{V}_0(U) = U^2 - U, \tag{4.35}$$

$$\tilde{V}_1(U) = -\tilde{V}_0(U)\frac{\mathrm{d}\tilde{V}_0(U)}{\mathrm{d}U} = -(2U^3 - 3U^2 + U), \tag{4.36}$$

$$\tilde{V}_2(U) = -\tilde{V}_0(U)\frac{\mathrm{d}\tilde{V}_1(U)}{\mathrm{d}U} - \tilde{V}_1(U)\frac{\mathrm{d}V_0(U)}{\mathrm{d}U} = -2(5U^4 - 10U^3 + 6U^2 - U), \tag{4.37}$$

which can also be written in terms of the original variable by remembering that $V = \tilde{V}/c$.
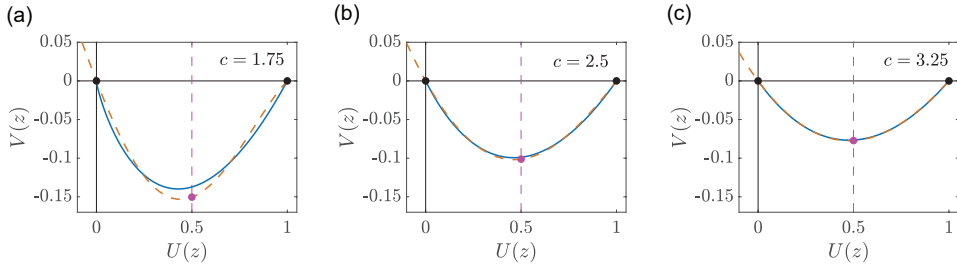
Figure 4.11: Phase plane perturbation solutions for fast retreating travelling waves, $c \to -\infty$. (a)–(c) Phase plane for $c = 1.75, 2.5$ and 3.25. Numerical solutions of Equations (4.6)–(4.7) (blue) are superimposed on the perturbation solutions (dashed orange). The intersection of the perturbation trajectory with the vertical line at $U(z) = u_\mathrm{f} = 0.5$ is highlighted (pink disc) and the equilibrium points also highlighted (black discs).

Results in Figure 4.11 compare numerically-generated phase plane trajectories with the $\mathcal{O}(c^{-6})$ perturbation solution in the phase plane for $c = 1.75, 2.5$ and 3.25. Here we see that the perturbation solution is very accurate for the two faster travelling wave speeds, but we see a visual discrepancy between the numerically-generated phase plane trajectory and the perturbation solution for $c = 1.75$.

As before, another test of the accuracy of the perturbation solution is to compare numerically-generated phase plane estimates of κ with the value

implied by the perturbation solution, which can be written as

$$\kappa_{\mathrm{p}} = \frac{\left(c^2 + 2u_{\mathrm{f}} - 1 - \dfrac{14u_{\mathrm{f}}(1 - u_{\mathrm{f}}) - 3}{c^2} + \dfrac{(2u_{\mathrm{f}} - 1)[24u_{\mathrm{f}}(u_{\mathrm{f}} - 1) + 5]}{c^4}\right)}{u_{\mathrm{f}}(1 - u_{\mathrm{f}})} + \mathcal{O}\left(\frac{1}{c^6}\right).$$
(4.38)
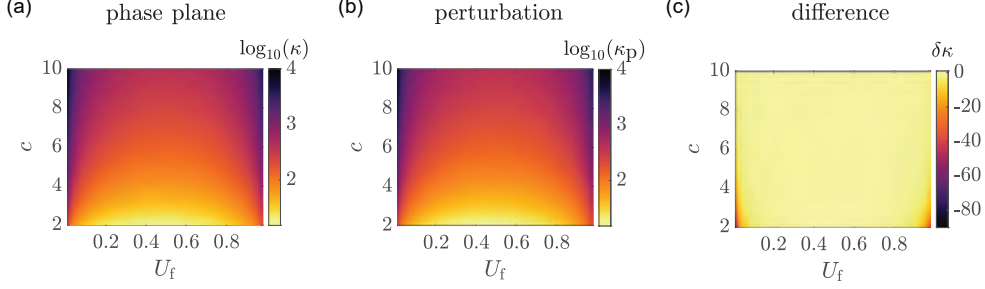
Figure 4.12: κ **as a function of** c **and** u_{f} **for** $c \to \infty$. (a) Heat map showing κ as a function of c and u_{f} where estimates of κ are obtained by solving Equations (4.6)–(4.7) in the phase. (b) Heat map showing κ_{p} from the perturbation solution, Equation (4.38). (c) Difference between the phase plane and perturbation estimates of κ, $\delta\kappa = \kappa - \kappa_{\mathrm{p}}$.

Heat maps in Figure 4.12(a)–(b) show κ and κ_{p} as a function of c and u_{f} using the phase plane and perturbation approaches, respectively. Visually we see no obvious distinction between the numerical and perturbation approximation of κ, and this is quantitatively confirmed in Figure 4.12(c) where we show a heat map of $\delta\kappa$ which is very close to zero for all $c \geq 2$.

To solve for the shape of the travelling wave as $c \to \infty$ we again follow Canosa [Canosa 1973] and write Equation (4.4) in terms of the re-scaled co-ordinate $\xi = z/c$,

$$\frac{1}{c^2}\frac{\mathrm{d}^2 U}{\mathrm{d}\xi} + \frac{\mathrm{d}U}{\mathrm{d}\xi} + U(1 - U) = 0, \quad -\infty < \xi < 0.$$
(4.39)

Assuming $U(\xi) \sim \displaystyle\sum_{n=0}^{\infty} c^{-2n} U_n(\xi)$ as $c \to \infty$, and substituting this expansion into Equation (4.39) we obtain

$$\frac{\mathrm{d}U_0}{\mathrm{d}\xi} + U_0(1 - U_0) = 0,$$
(4.40)

$$\frac{\mathrm{d}U_1}{\mathrm{d}\xi} + \frac{\mathrm{d}^2 U_0}{\mathrm{d}\xi^2} + U_1(1 - 2U_0) = 0,$$
(4.41)

with $U_0(0) = u_{\mathrm{f}}$ and $U_1(0) = 0$, and $U_0(\xi) = 1$ and $U_1(0) = 0$ as $\xi \to -\infty$.

121

The solutions of these differential equations are

$$U_0(\xi) = \frac{u_{\mathrm{f}}}{(1 - u_{\mathrm{f}})\mathrm{e}^{\xi} + u_{\mathrm{f}}}, \tag{4.42}$$

$$U_1(\xi) = \frac{u_{\mathrm{f}}(1 - u_{\mathrm{f}})\mathrm{e}^{\xi}\left(\xi - \ln\left[(1 - u_{\mathrm{f}})\mathrm{e}^{\xi} + u_{\mathrm{f}}\right]^2\right)}{\left[(1 - u_{\mathrm{f}})\,\mathrm{e}^{\xi} + u_{\mathrm{f}}\right]^2}. \tag{4.43}$$
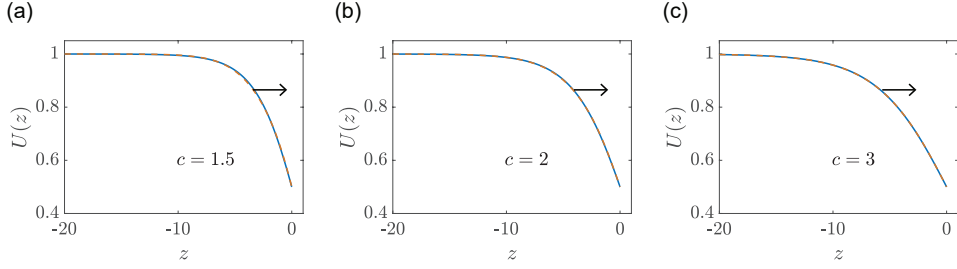
Figure 4.13: Perturbation solution for fast invading travelling waves, $c \to \infty$. (a)–(c) Perturbation solutions showing the shape of travelling waves for $c = 1.5, 2$ and 3, respectively (dashed orange) superimposed on late-time numerical solutions of Equations (4.1)–(4.3) (blue).

Results in Figure 4.13 show late-time numerical solutions of Equations (4.1)–(4.3) for $c = 1.5, 2$ and 3, each with $u_{\mathrm{f}} = 0.5$ in this case. These numerical travelling wave solutions are superimposed on the $\mathcal{O}(c^{-4})$ perturbation solution derived in this Section and we see that the shape of the travelling waves from perturbation solution provides an excellent approximation of the late-time PDE solutions for all c considered. This accuracy is remarkable given that the perturbation solutions are valid as $c \to \infty$, yet they match the numerical solutions extremely well for a value as small as $c = 1.5$. We note that all perturbation results here simplify to those given in our previous work for $u_{\mathrm{f}} = 0$ [El-Hachem et al. 2021a] in the limit $u_{\mathrm{f}} \to 0$.

4.4 Conclusions and future work

Despite the widespread popularity of the Fisher-KPP model as a prototype mathematical model of biological invasion, there are some key limitations of travelling wave solutions of this model that are inconsistent with experimental observations of invasive phenomena. For example, travelling wave solutions of the Fisher-KPP model do not give rise to a well-defined invasion front that arises naturally in many biological scenarios [Maini et al. 2004a, Maini et al. 2004b]. Further, biologically-relevant initial conditions lead to a very restric-

tive wave speed. In this work we show how to reformulate the Fisher-KPP model as a moving boundary problem on $x < s(t)$ with a classical one-phase Stefan condition defining the speed of the moving front. This approach leads to travelling wave solutions that involve a well-defined sharp front without the complication of introducing a degenerate nonlinear diffusivity. Furthermore, this moving boundary reformulation of the Fisher-KPP model gives rise to a wide range of travelling wave solutions that move with any speed, $-\infty < c < \infty$. This is a very interesting result since previous research focusing on retreating travelling wave solutions with $c < 0$ often involves the complication of working with a coupled systems of nonlinear reaction-diffusion equations [Painter and Sherratt 2003, El-Hachem et al. 2020, El-Hachem et al. 2021b], whereas here in the moving boundary framework we can simulate retreating travelling wave solutions in a single reaction-diffusion equation.

The important feature in our model (4.1)–(4.2) that leads to a family of travelling wave solutions for all $-\infty < c < \infty$ is the boundary condition $u = u_{\mathrm{f}}$ at $x = s(t)$. In previous studies of this Fisher-Stefan model, the parameter u_{f} was fixed to be $u_{\mathrm{f}} = 0$, whereas here we focus on $u_{\mathrm{f}} \in (0,1)$. For the case $u_{\mathrm{f}} = 0$, the wave speeds were restricted to $c < 2$, with the limiting value $c = 2$ corresponding to the well-known travelling wave solution to the traditional Fisher-KPP model. In our model (4.1)–(4.2) with $u_{\mathrm{f}} \in (0,1)$, the speed $c = 2$ plays no special role at all. Another important difference between the cases $u_{\mathrm{f}} = 0$ and $u_{\mathrm{f}} \in (0,1)$ is that for $u_{\mathrm{f}} = 0$ there is the possibility of population extinction for sufficiently small $s(0)$, leading to the so-called spreading-extinction dichotomy [Du and Lin 2010, Simpson 2020]. For $u_{\mathrm{f}} \in (0,1)$, this complication is not present.

A key limitation of reformulating the Fisher-KPP model as a moving boundary problem (4.1)–(4.2) is the interpretation and estimation of κ, which is a leakage parameter that describes how the population is lost ($\kappa > 0$) or gained ($\kappa < 0$) at the moving boundary. Here we seek to address this issue by using a range of exact and approximate perturbation solutions to estimate κ as a function of c, which is useful because the travelling wave speed is relatively straightforward to measure [Maini et al. 2004a, Maini et al. 2004b]. Our analysis gives three exact values for κ when $c = \pm 5\sqrt{6}$ and $c = 0$, and our perturbation solutions give expressions for κ in various limits. Compar-

ing our perturbation approximations with numerical estimates from the phase plane, our approximations for κ are accurate across the entire range of potential travelling wave speeds, $-\infty < c < \infty$. While we have compared our perturbation solutions with numerical results, it is possible that further work could be completed to extend their validity by, for example, introducing a Padé approximant [Van Dyke 1975].

While our analysis here focuses on invasion phenomena in one-dimensional geometries where we can obtain several exact and approximate perturbation solutions, future work could involve examining numerical solutions in two-dimensional geometries [King et al. 1999, McCue et al. 2003, McCue et al. 2005] since this would provide a more realistic description of populations of cells that invade outward from an initially-confined region [Treloar et al. 2014] as well as hole-closing problems that describe the closure of an initial gap in an otherwise uniform population [McCue et al. 2019].

4.5 Additional material

4.5.1 Numerical methods

4.5.1.1 Partial differential equations

To obtain numerical solutions of the Fisher–Stefan equation (4.1), we use a boundary fixing transformation $\xi = x/s(t)$ so that we have

$$\frac{\partial u}{\partial t} = \frac{1}{s^2(t)} \frac{\partial^2 u}{\partial \xi^2} + \frac{\xi}{s(t)} \frac{\mathrm{d}s(t)}{\mathrm{d}t} \frac{\partial u}{\partial \xi} + u(1-u), \tag{4.44}$$

on the fixed domain, $0 < \xi < 1$. Here $s(t)$ is the time–dependent length of the domain, and we will explain how we solve for this quantity later. To close the problem we also transform the boundary conditions giving

$$\frac{\partial u}{\partial \xi} = 0 \quad \text{at} \quad \xi = 0, \tag{4.45}$$

$$u = u_\mathrm{f} \quad \text{at} \quad \xi = 1. \tag{4.46}$$

The key to obtaining accurate numerical solutions of equation (4.1) is to take advantage of the fact that for many problems we consider $u(x,t)$ varies rapidly near $x = s(t)$, whereas $u(x,t)$ is approximately constant near $x = 0$. Motivated by this we discretize equation (4.44) using a variable mesh where the mesh spacing varies geometrically from $\delta\xi_\mathrm{min} = \xi_N - \xi_{N-1} = 1 - \xi_{N-1}$ at $\xi = 1$, to $\delta\xi_\mathrm{max} = \xi_2 - \xi_1 = \xi_2 - 0$ at $\xi = 0$. All results in this work are computed with $N = 5001$ mesh points with $\delta\xi_\mathrm{min} = 1 \times 10^{-6}$. With these constraints we solve for the geometric expansion factor 1.01 using MATLABS *fsolve* function which gives $\delta\xi_\mathrm{max} = 1.457 \times 10^{-3}$.

We spatially discretise equation (4.44) on the non-uniform mesh. At the ith internal mesh point we define $h_i^+ = \xi_{i+1} - \xi_i$ and $h_i^- = \xi_i - \xi_{i-1}$. For convenience we define $\alpha_i = 1/(h^-[h^+ + h^-])$, $\gamma_i = -1/(h^- h^+)$ and $\delta_i = 1/(h^+[h^+ + h^-])$, which gives

$$\begin{aligned}
\frac{u_i^{j+1} - u_i^j}{\Delta t} &= \frac{2}{(s^j)^2} \left[\alpha_i u_{i-1}^{j+1} + \gamma_i u_i^{j+1} + \delta_i u_{i+1}^{j+1} \right] \\
&+ \frac{\xi_i}{s^j} \left(\frac{s^{j+1} - s^j}{\Delta t} \right) \left[-\alpha_i h^+ u_{i-1}^{j+1} + \gamma_i (h^- - h^+) u_i^{j+1} + \delta_i h^- u_{i+1}^{j+1} \right] \\
&+ u_i^{j+1}(1 - u_i^{j+1}),
\end{aligned} \tag{4.47}$$

for $i = 2, \ldots, N-1$, where N is the total number of spatial nodes in the mesh, and index j represents the time index so that $u_i^j \approx u(\xi_i, j\Delta t)$.

Discretising the boundary conditions (4.45)–(4.46) gives

$$u_2^{j+1} - u_1^{j+1} = 0, \tag{4.48}$$

$$u_N^{j+1} = u_{\mathrm{f}}. \tag{4.49}$$

To advance the discrete system from time t to $t + \Delta t$ we solve the system (4.47)-(4.49), using Newton-Raphson iteration. During each iteration we estimate the position of the moving boundary using the discretised Stefan condition. Here we define $h_N^+ = \xi_N - \xi_{N-1}$, $h_N^- = \xi_{N-1} - \xi_{N-2}$, $\alpha_i = 1/(h^-[h^+ + h^-])$, $\gamma_i = -1/(h^- h^+)$ and $\delta_i = 1/(h^+[h^+ + h^-])$, which gives

$$s^{j+1} = s^j - \frac{\Delta t \kappa}{s^j} \left[-\alpha_i h^+ u_{N-2}^{j+1} + \gamma_i(h^- - h^+) u_{N-1}^{j+1} + \delta_i h^- u_{\mathrm{f}} \right]. \tag{4.50}$$

Within each time step Newton-Raphson iterations continue until the maximum change in the dependent variables is less than the tolerance ϵ. All results in this work are obtained by setting $\epsilon = 1 \times 10^{-10}$, and $\Delta t = 1 \times 10^{-3}$, and we find that these values are sufficient to produce grid–independent results. MATLAB software is available on GitHub so that these algorithms can be implemented to explore different choices of $\delta\xi_{\min}$, $\delta\xi_{\max}$, N, δt and ϵ. For certain problems in this work we the time–dependent solutions to provide an estimate of the velocity of the moving front, v. The estimated velocity is computed as $v = (s^{j+1} - s^j)/\Delta t$, and we find that v approaches as constant travelling wave speed, c, as t becomes sufficiently large.

4.5.1.2   Phase plane

To construct the phase planes we solve equations (4.6)-(4.7) numerically using Heun's method with a constant step size dz. In most cases we are interested in examining trajectories that either leave the saddle $(1, 0)$ along the unstable manifold. We chose the initial condition on the unstable manifold sufficiently close to $(1, 0)$. To choose this point we use the MATLAB *eig* function to calculate the eigenvalues and eigenvectors for the particular choice of c of interest.

4.5.2 Additional results

Additional time-dependent solutions of the moving boundary problem are given in Figure 4.14 where $u_{\text{f}} = 0.5$. In the main document we show results in Figure 4.2 for $u_{\text{f}} = 0.25$ and $u_{\text{f}} = 0.75$, and here we show results for another choice of u_{f} for completeness.
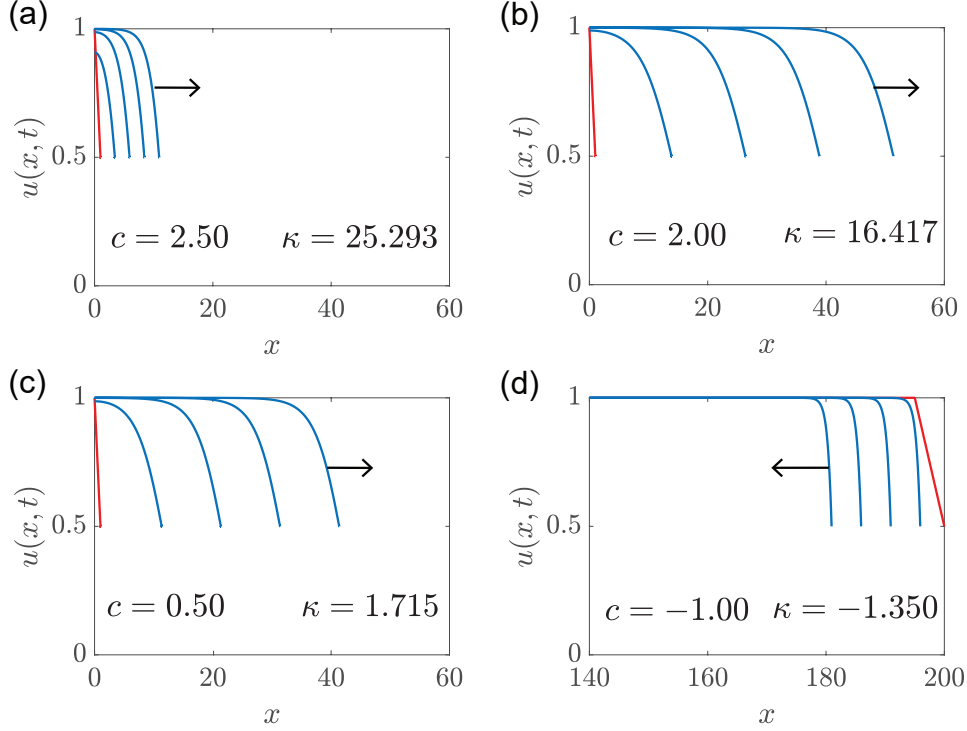

Figure 4.14: Time-dependant solutions of Equations (1.1)–(1.3) for $u_{\text{f}} = 0.5$. Density profiles $u(x, t)$ are illustrated in blue at times $t = 5, 10, 15, 20$. The initial condition is illustrated in red, where $s(0) = 1$ and $\beta = 0$ in (a)–(c), and $s(0) = 200$ and $\beta = 195$ in (d). Positive wave speeds $c = 0.50, 2.00$ and 2.50 are obtained by $\kappa = 1.715, 16.417$ and 25.293 and Negative wave speed $c = -1.00$ is obtained by $\kappa = -1.350$.
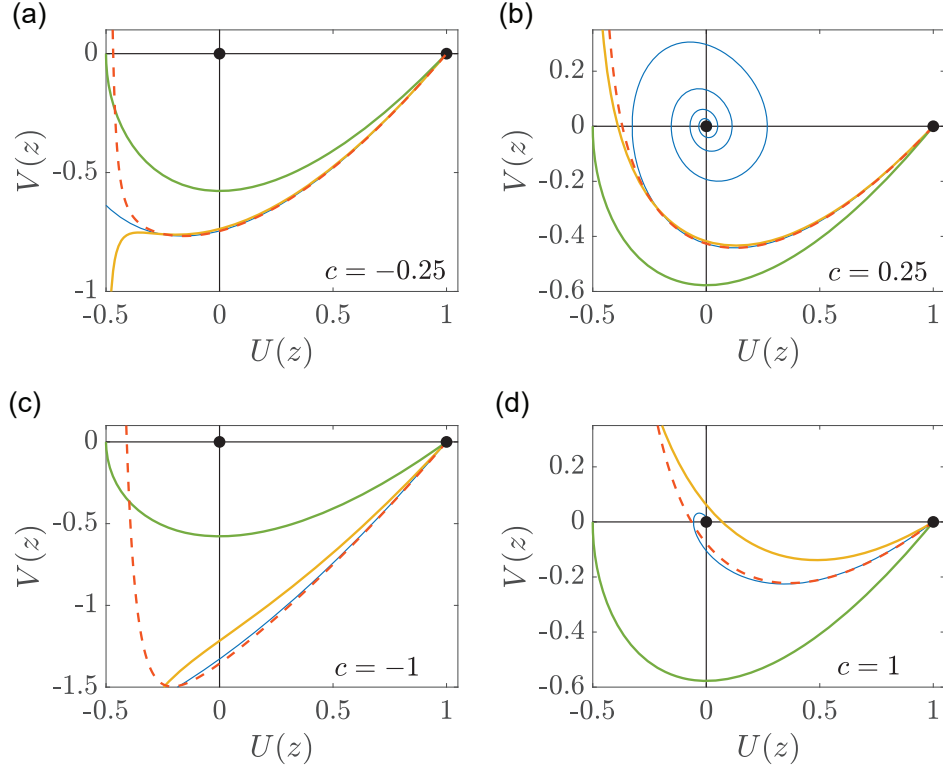
Figure 4.15: Additional perturbation solutions for $|c| \ll 1$. (a)–(d) show phase planes for $c = \mp 0.25$ and ∓ 1.00, respectively. Numerical solution of Equations (4.6)–(4.7) (blue) are superimposed on various perturbation solutions: $\mathcal{O}(c)$ in solid green; $\mathcal{O}(c^2)$ in solid yellow; and, $\mathcal{O}(c^3)$ in dashed orange. Equilibrium points are shown with black discs.

Results in Sections 4.3.6–4.3.7 compare several numerical trajectories in the phase plane with our various perturbation solutions. These comparisons do not explore the effect of truncation of the perturbation solutions since we always worked with the most terms possible. Additional results in Figure 4.15 replicate those in Figure 4.6 except here we show various perturbation solutions of different order: $\mathcal{O}(c)$ in solid green; $\mathcal{O}(c^2)$ in solid yellow; and, $\mathcal{O}(c^3)$ in dashed orange. For these particular choices of c we observe the importance of taking higher order terms in the perturbation solutions since the $\mathcal{O}(c)$ perturbation solution is relatively inaccurate in all cases considered.
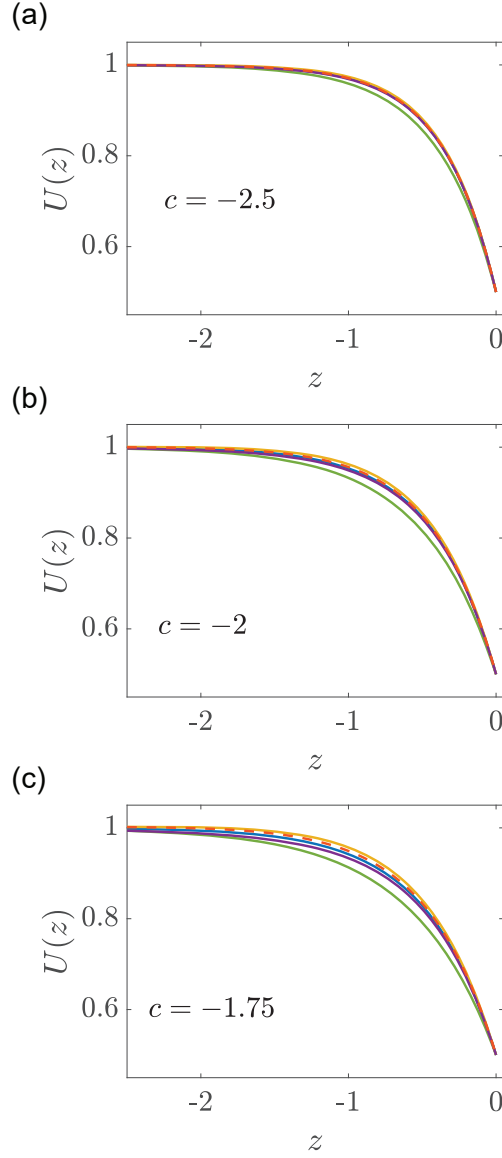
Figure 4.16: Additional perturbation solution for fast retreating travelling waves, $c \to -\infty$. (a)–(c) Perturbation solutions of different order of accuracy superimposed on late-time numerical solutions of Equations (4.1)–(4.3) in solid blue. Perturbation solutions include: $\mathcal{O}(c^{-2})$ in solid green; $\mathcal{O}(c^{-4})$ in solid yellow; $\mathcal{O}(c^{-6})$ in solid purple; and, $\mathcal{O}(c^{-8})$ in dashed orange. Results are compared for $c = -2.5, -2$ and -1.75, respectively, as indicated.

Results in Figure 4.16 replicate those in Figure 4.11 except here we show various perturbation solutions of different order: $\mathcal{O}(c^{-2})$ in solid green; $\mathcal{O}(c^{-4})$ in solid yellow; $\mathcal{O}(c^{-6})$ in solid purple; and, $\mathcal{O}(c^{-8})$ in dashed orange. Just like the comparisons in Figure 4.15, for these choices of c here we observe the importance of taking higher order terms in the perturbation solutions since the $\mathcal{O}(c^{-2})$ perturbation solution is relatively inaccurate, particularly for $c = -1.75$.

Chapter 5

A sharp-front moving boundary model for malignant invasion

Statement of Contribution of Co-Authors for Thesis by Published Paper

The following is the suggested format for the required declaration provided at the start of any thesis chapter which includes a co-authored publication.

The authors listed below have certified that:

1. they meet the criteria for authorship and that they have participated in the conception, execution, or interpretation, of at least that part of the publication in their field of expertise;
2. they take public responsibility for their part of the publication, except for the responsible author who accepts overall responsibility for the publication;
3. there are no other authors of the publication according to these criteria;
4. potential conflicts of interest have been disclosed to (a) granting bodies, (b) the editor or publisher of journals or other publications, and (c) the head of the responsible academic unit, and
5. they agree to the use of the publication in the student's thesis and its publication on the QUT's ePrints site consistent with any limitations set by publisher requirements.

In the case of this chapter 5:

Please state the publication title and date of publication or status:
El-Hachem M, McCue SW, Simpson MJ, 2020. A sharp-front moving boundary model for malignant invasion. *Physica D: Nonlinear Phenomena* **412**, 132639. Published on November 2020.

Contributor	Statement of contribution*
Maud El-Hachem *Maud Ell—* 15/11/2021	Conceived and designed the study, performed all numerical and symbolic calculations, drafted the article, and gave final approval for publication.
Scott W McCue	Conceived and designed the study, gave final approval for publication.
Matthew J Simpson	Conceived and designed the study, gave final approval for publication.

Principal Supervisor Confirmation

I have sighted email or other correspondence from all Co-authors confirming their certifying authorship.
(If the Co-authors are not able to sign the form please forward their email or other correspondence confirming the certifying authorship to the GRC).

Professor Matthew Simpson   _____   16/11/2021
Name   Signature   Date

Graduate Research Centre, Level 4, 88 Musk Ave, Kelvin Grove Qld 4059   Page 1 of 1
Current @ 20/02/2020   CRICOS No. 00213J

132

5.1 Abstract

We analyse a novel mathematical model of malignant invasion which takes the form of a two-phase moving boundary problem describing the invasion of a population of malignant cells into a population of background tissue, such as skin. Cells in both populations undergo diffusive migration and logistic proliferation. The interface between the two populations moves according to a two-phase Stefan condition. Unlike many reaction-diffusion models of malignant invasion, the moving boundary model explicitly describes the motion of the sharp front between the cancer and surrounding tissues without needing to introduce degenerate nonlinear diffusion. Numerical simulations suggest the model gives rise to very interesting travelling wave solutions that move with speed c, and the model supports both malignant invasion and malignant retreat, where the travelling wave can move in either the positive or negative x-directions. Unlike the well-studied Fisher-Kolmogorov and Porous-Fisher models where travelling waves move with a minimum wave speed $c \geq c^* > 0$, the moving boundary model leads to travelling wave solutions with $|c| < c^{**}$. We interpret these travelling wave solutions in the phase plane and show that they are associated with several features of the classical Fisher-Kolmogorov phase plane that are often disregarded as being nonphysical. We show, numerically, that the phase plane analysis compares well with long time solutions from the full partial differential equation model as well as providing accurate perturbation approximations for the shape of the travelling waves.

5.2 Introduction

Populations of motile and proliferative cells can give rise to moving fronts that are associated with cancer progression and malignant invasion [Swanson et al. 2003, Gatenby and Gawlinski 1996, Roose et al. 2007, Byrne 2010]. Similar invasive phenomena are associated with wound healing [Maini et al. 2004a, Maini et al. 2004b, Simpson et al. 2013], development [Simpson et al. 2007, Sengers et al. 2007] and ecology [Skellam 1951, Kot 2003, Bradshaw-Hajek and Broadbridge 2004]. Mathematically, these fronts are often studied using reaction-diffusion equations that are based upon the well-known Fisher-Kolmogorov model or extensions [Fisher 1937, Kolmogorov et al. 1937, Canosa 1973, Sher-

133

ratt and Murray 1990, Murray 2002]. While such models are able to capture certain important features, such as the formation of constant speed travelling wave solutions, there are other features of the standard Fisher-Kolmogorov model that are inconsistent with biological observations. For example, classical travelling wave solutions of the Fisher-Kolmogorov model on $-\infty < x < \infty$ do not involve a well-defined front because the travelling wave solutions do not have compact support and the cell density is always positive, with $u(x,t) \to 0$ as $x \to \infty$. Solutions of the Fisher-Kolmogorov model on $-\infty < x < \infty$ always lead to travelling waves for initial conditions with compact support, and these travelling waves lead to the colonisation of initially-vacant regions without ever retreating. These two features are inconsistent with many experimental observations.

Experimental images in Figure 5.1(a)–(b) show key features of malignant invasion. Here a population of motile and proliferative melanoma cells is placed onto the surface of human skin tissues (Figure 5.1(a)) that are maintained at an air-liquid interface to mimic the *in vivo* environment. At various times during these experiments, vertical cross sections through the skin tissues are imaged to show the melanoma cell population invading vertically downward into the surrounding skin cells. These images show the formation of a clear sharp front between the two subpopulations [Haridas 2017, Haridas et al. 2018]. The sharp front, highlighted by the arrow in Figure 5.1(b), shows that there is a particular depth at which the melanoma cell density vanishes. In reality, such malignant fronts can either invade into, or retreat from, the surrounding tissues [Hanahan and Weinberg 2000]. Neither of these biological features are consistent with travelling wave solutions of the classical Fisher-Kolmogorov model.

One way to extend the Fisher-Kolmogorov model to produce a well-defined front is to introduce nonlinear degenerate diffusion [Sengers et al. 2007, Murray 2002, Sherratt and Murray 1990, Sánchez Garduño and Maini 1994, Sánchez Garduno and Maini 1995, Witelski 1994, Witelski 1995, Sherratt and Marchant 1996, Harris 2004, Jin et al. 2016, Warne et al. 2019, McCue et al. 2019]. Such models, including the Porous-Fisher model, give rise to travelling wave solutions with a well-defined sharp front that always lead to advancing travelling waves that never retreat. One potential weakness of this approach is
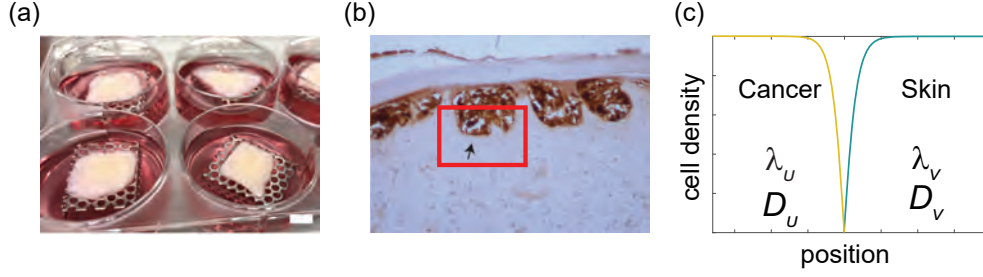
Figure 5.1: Experimental motivation and model schematic. (a) Experimental protocol where a population of motile and proliferative melanoma cells are placed onto the surface of human skin tissues kept at an air-liquid interface to simulate the *in vivo* environment. Scale bar is 6 mm. (b) Vertical cross section through the tissues in (a) highlighting the vertical downward invasion of melanoma cells (dark) into surrounding skin tissue (light). The sharp front separating the invading malignant population from the surrounding tissues is visually distinct and highlighted in the red rectangle. Images in (a)-(b) are reproduced from Haridas [Haridas 2017] with permission. (b) Schematic solution of a one-dimensional partial differential equation solution showing the spatial distribution of a population of cancer cells and skin cells separated by a sharp front. The cancer cells have density $u(x,t)$, diffusivity D_u and proliferation rate λ_u. The skin cells have density $v(x,t)$, diffusivity D_v and proliferation rate λ_v.

that the introduction of nonlinear degenerate diffusion leads to additional model parameters that can be difficult to estimate and interpret [Sherratt and Murray 1990, Warne et al. 2019, McCue et al. 2019, Simpson et al. 2011]. Another way to introduce a sharp front into the Fisher–Kolmogorov model is to recast the problem as a moving boundary problem [Crank 1987, Hill 1987, Gupta 2017, McCue et al. 2008]. This approach involves studying the Fisher-Kolmogorov model on $0 < x < L(t)$, and specifying that $u(L(t), t) = 0$ to give a well-defined front. In this approach a Stefan-condition is applied to determine the speed of the moving front [Crank 1987, Hill 1987, Gupta 2017, McCue et al. 2008]. Such models, sometimes called the Fisher-Stefan model [El-Hachem et al. 2019, Simpson 2020, Fadai and Simpson 2020a], have been extensively studied using rigorous analysis [Du and Lin 2010, Du and Guo 2011, Bunting et al. 2012, Du and Guo 2012, Du et al. 2014a, Du et al. 2014b, Du and Lou 2015] but have received far less attention in terms of how the solutions of such free boundary problems relate to biological observations. Interestingly, while free boundary problems are routinely used to study many problems in industrial and applied mathematics [Font et al. 2013, Mitchell and O'Brien 2014, Mitchell 2015, Dalwadi et al. 2020], they are less frequently encountered in the mathematical biology literature [Friedman 2008, Friedman 2014, Perthame et al. 2014, Perthame and Vauchelet 2015].

Of course, a key difference between the classical Fisher-Kolmogorov model

and the kinds of applications in Figure 5.1(a)-(b) is that the usual Fisher-Kolmogorov model deals with just one population of cells, whereas malignant invasion involves one population of cells invading into another population of cells. To model such applications, the Fisher-Kolmogorov model can be extended to a system of partial differential equations to represent the different cell types present [Gatenby and Gawlinski 1996, Landman and Pettet 1998, Perumpanani et al. 1999, Painter and Sherratt 2003, Simpson et al. 2006, Browning et al. 2019]. While the Fisher-Kolmogorov and Porous-Fisher models have been extended to deal with multiple interacting populations, the underlying issues associated with the single population models, described above, also apply to the multiple population analogue [Simpson et al. 2006].

In this work we study a mathematical model of cell invasion that involves describing two populations of cells as a moving boundary problem. A schematic of this model in Figure 5.1(c) shows that we consider two cell populations, such as a population of cancer cells invading into a population of skin cells, which is consistent with the experimental images in Figure 5.1(a)-(b). Cells in both populations undergo linear diffusion and proliferate logistically. The motion of the sharp front is governed by a two-phase Stefan condition [Crank 1987, Hill 1987, Gupta 2017, McCue et al. 2008, Mitchell and Vynnycky 2014, Mitchell 2015, Mitchel and Vynnycky 2016, Chang and Chen 2013, Yang 2015]. As we will show, various properties of the solutions of this model are consistent with experimental observations. Namely, this model leads to a well-defined front and travelling wave solutions that represent either malignant advance or retreat [Chang and Chen 2013, Yang 2015]. It is interesting that the travelling wave analysis of this model is intimately related with the classical phase plane associated with travelling wave solutions of the Fisher-Kolmogorov model. However, for our model we make use of certain trajectories in the classical phase plane that are normally discarded on the grounds of being nonphysical. Here, in the context of a moving boundary problem, these normally-discarded features play key roles in determining the travelling wave solutions.

5.3 Results and Discussion

From this point forward all dimensional variables and parameters are denoted with a circumflex, whereas nondimensional quantities are denoted using regular symbols.

5.3.1 Mathematical model

We consider a reaction-diffusion model of a population of cancer cells with density $\hat{u}(\hat{x}, \hat{t})$, and a population of skin cells with density $\hat{v}(\hat{x}, \hat{t})$. The system of equations can be written as

$$\frac{\partial \hat{u}}{\partial \hat{t}} = \hat{D}_u \frac{\partial^2 \hat{u}}{\partial \hat{x}^2} + \hat{\lambda}_u \hat{u} \left(1 - \frac{\hat{u}}{\hat{K}_u} \right), \quad -\hat{L}_u < \hat{x} < \hat{s}(\hat{t}), \tag{5.1}$$

$$\frac{\partial \hat{v}}{\partial \hat{t}} = \hat{D}_v \frac{\partial^2 \hat{v}}{\partial \hat{x}^2} + \hat{\lambda}_v \hat{v} \left(1 - \frac{\hat{v}}{\hat{K}_v} \right), \quad \hat{s}(\hat{t}) < \hat{x} < \hat{L}_v, \tag{5.2}$$

where the densities are functions of position, $\hat{x}$, and time, $\hat{t}$. Cancer cells undergo diffusive migration with diffusivity $\hat{D}_u > 0$, and proliferate logistically with rate $\hat{\lambda}_u > 0$ and carrying capacity density $\hat{K}_u > 0$. Similarly, skin cells undergo diffusive migration with diffusivity $\hat{D}_v > 0$ and proliferate logistically with rate $\hat{\lambda}_v > 0$ and carrying capacity density $\hat{K}_v > 0$. The model is defined on the $\hat{L}_u < \hat{x} < \hat{L}_v$, with a moving boundary $\hat{x} = \hat{s}(\hat{t})$ separating the population of cancer cells, $\hat{x} < \hat{s}(\hat{t})$, from the population of skin cells, $\hat{x} > \hat{s}(\hat{t})$. Typical values of a cell diffusivity are approximately 100-1000 μm^2/h [Johnston et al. 2015, Jin et al. 2016], whereas typical values of a cell proliferation rate are approximately 0.04-0.06 /h [Johnston et al. 2015, Jin et al. 2016].

Since we are interested in cell invasion we focus on travelling wave solutions of Equations (5.1)-(5.2) by setting $\hat{L}_u$ and $\hat{L}_v$ to be sufficiently large to model an infinite domain problem. The boundary conditions we consider are

$$\left. \frac{\partial \hat{u}}{\partial \hat{x}} \right|_{\hat{x}=-\hat{L}_u} = 0, \qquad \left. \frac{\partial \hat{v}}{\partial \hat{x}} \right|_{\hat{x}=\hat{L}_v} = 0, \tag{5.3}$$

$$\hat{u}(\hat{s}(\hat{t}), \hat{t}) = 0, \qquad \hat{v}(\hat{s}(\hat{t}), \hat{t}) = 0. \tag{5.4}$$

This means that we have no flux of cancer cells at the left-most boundary and no flux of skin cells at the right-most boundary, and the density of both populations is zero at the moving boundary, as in Figure 5.1(a).

We describe the motion of the moving boundary by a two-phase Stefan condition,

$$\frac{\mathrm{d}\hat{s}(\hat{t})}{\mathrm{d}\hat{t}} = -\hat{\kappa}_u \left.\frac{\partial \hat{u}}{\partial \hat{x}}\right|_{\hat{x}=\hat{s}(\hat{t})} - \hat{\kappa}_v \left.\frac{\partial \hat{v}}{\partial \hat{x}}\right|_{\hat{x}=\hat{s}(\hat{t})}. \tag{5.5}$$

Here the speed of the moving boundary is the sum of two terms: the first term on the right of Equation (5.5) is proportional to the spatial gradient of the cancer cell density at the moving boundary, $\hat{x} = \hat{s}(\hat{t})$, and the second term on the right of Equation (5.5) is proportional to the spatial gradient of the skin cell density at the moving boundary, $\hat{x} = \hat{s}(\hat{t})$. The constants of proportionality, $\hat{\kappa}_u$ and $\hat{\kappa}_u$, play an important role in relating the shape of the density profiles to the speed of the interface. We will consider the relationship between these constants and the speed of the interface later.

In this work we consider initial conditions given by

$$\hat{u}(\hat{x}, 0) = \hat{\phi}(\hat{x}) \quad \text{on} \quad -\hat{L}_u < \hat{x} < \hat{s}(\hat{t}), \tag{5.6}$$

$$\hat{v}(\hat{x}, 0) = \hat{\psi}(\hat{x}) \quad \text{on} \quad \hat{s}(\hat{t}) < \hat{x} < \hat{L}_v, \tag{5.7}$$

such that $\hat{\phi}(\hat{s}(0)) = \hat{\psi}(\hat{s}(0)) = 0$.

Real tumours are not one-dimensional, as is clear in Figure 5.1. Regardless, we expect the main features of this one-dimensional model to inform higher-dimensional versions. For example, travelling wave speeds may inform reasonable estimates of the speed of the moving boundary in more complex geometries. Alternatively, conditions for extinction (Section 5.3.7) should also inform two- and three-dimensional versions of the model. Therefore, we restrict our work here to focus on a one-dimensional model since working in this simpler geometry enables us to analyse the model more thoroughly than would be possible in a more general coordinate system. Further, as discussed, many important mathematical models of tumour growth and invasion provide important insight by working in a one-dimensional Cartesian geometry [Breward et al. 2002, Browning et al. 2019].

5.3.2 Nondimensional model

We nondimensionalise the dependent variables by writing $u = \hat{u}/\hat{K}_u$ and $v = \hat{v}/\hat{K}_v$, and we nondimensionalise the independent variables by writing $x = \hat{x}\sqrt{\hat{\lambda}_u/\hat{D}_u}$ and $t = \hat{\lambda}_u\hat{t}$. In this nondimensional framework our model can be

written as

$$\frac{\partial u}{\partial t} = \frac{\partial^2 u}{\partial x^2} + u(1 - u), \quad -L_u < x < s(t), \tag{5.8}$$

$$\frac{\partial v}{\partial t} = D\frac{\partial^2 v}{\partial x^2} + \lambda v(1 - v), \quad s(t) < x < L_v, \tag{5.9}$$

where the boundary conditions are given by

$$\left.\frac{\partial u}{\partial x}\right|_{x=-L_u} = 0, \qquad \left.\frac{\partial v}{\partial x}\right|_{x=L_v} = 0, \tag{5.10}$$

$$u(s(t), t) = 0, \qquad v(s(t), t) = 0, \tag{5.11}$$

$$\frac{\mathrm{d}s(t)}{\mathrm{d}t} = -\kappa_u \left.\frac{\partial u}{\partial x}\right|_{x=s(t)} - \kappa_v \left.\frac{\partial v}{\partial x}\right|_{x=s(t)}. \tag{5.12}$$

The nondimensional model has four parameters,

$$D = \frac{\hat{D}_v}{\hat{D}_u}, \quad \lambda = \frac{\hat{\lambda}_v}{\hat{\lambda}_u}, \quad \kappa_u = \frac{\hat{\kappa}_u \hat{K}_u}{\hat{D}_u}, \quad \kappa_v = \frac{\hat{\kappa}_v \hat{K}_v}{\hat{D}_u}. \tag{5.13}$$

In this framework, D is a relative diffusivity, and setting $D = 1$ means that the cancer cells and skin cells are equally motile. In contrast, setting $D > 1$ means that skin cells are more motile than cancer cells, while setting $D < 1$ models the situation where skin cells are less motile than cancer cells. Similar interpretations can be made for the relative proliferation rate λ.

We consider numerical solutions of Equations (5.8)-(5.9) on a domain with $L_u = 0$ and $L_v = L$, where L is chosen to be sufficiently large to facilitate the numerical simulation of travelling wave solutions. We chose piecewise initial conditions given by

$$u(x, 0) = \phi(x) = \begin{cases} \alpha, & 0 < x < \beta, \\ \alpha\left(1 - \dfrac{x - \beta}{s(0) - \beta}\right), & \beta < x < s(0), \end{cases} \tag{5.14}$$

$$v(x, 0) = \psi(x) = \begin{cases} \alpha\left(\dfrac{x - s(0)}{L - \beta - s(0)}\right), & s(0) < x < L - \beta, \\ \alpha, & L - \beta < x < L, \end{cases} \tag{5.15}$$

where the parameters $\alpha > 0$ and $\beta > 0$ control the shape of the piecewise initial density profile. These initial conditions correspond to an initial density of α when we are well away from the interface, $x = s(0)$. Near the interface we set the density to be a linear function of position. Typical initial conditions

139

in Figure 5.2 show how varying α, β and $s(0)$ affects the shape of the initial condition.
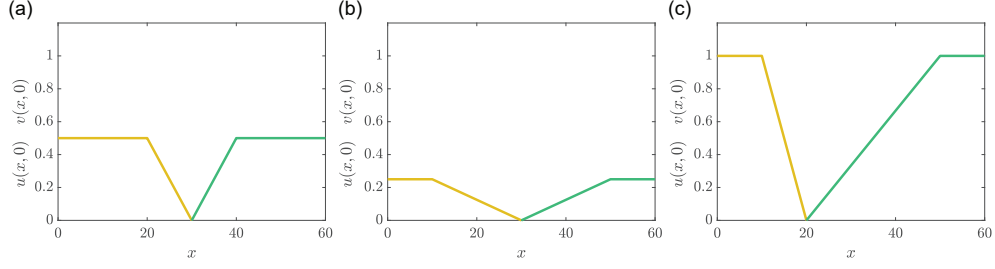
Figure 5.2: Initial condition. Three initial conditions on $0 < x < 60$ are shown for: (a) $\alpha = 0.5$, $\beta = 20$ and $s(0) = 30$; (b) $\alpha = 0.25$, $\beta = 10$ and $s(0) = 30$; and (c) $\alpha = 1$, $\beta = 10$ and $s(0) = 20$.

5.3.3 Numerical solution

To solve Equations (5.8)-(5.9) we use boundary fixing transformations to recast the moving boundary problem on two fixed domains. These transformations, $\xi = x/s(t)$ and $\eta = (x - s(t))/(L - s(t)) + 1$, allow us to re-write Equations (5.8)-(5.9) as,

$$\frac{\partial u}{\partial t} = \frac{1}{s^2(t)} \frac{\partial^2 u}{\partial \xi^2} + \frac{\xi}{s(t)} \frac{\mathrm{d}s(t)}{\mathrm{d}t} \frac{\partial u}{\partial \xi} + u(1 - u), \quad 0 < \xi < 1, \tag{5.16}$$

$$\frac{\partial v}{\partial t} = \frac{D}{(L - s(t))^2} \frac{\partial^2 v}{\partial \eta^2} + \left(\frac{2 - \eta}{L - s(t)} \right) \frac{\mathrm{d}s(t)}{\mathrm{d}t} \frac{\partial v}{\partial \eta} + \lambda v(1 - v), \quad 1 < \eta < 2, \tag{5.17}$$

so that we now have $u(\xi, t)$ on $0 < \xi < 1$ and $v(\eta, t)$ on $1 < \eta < 2$. The transformed boundary conditions are

$$\left. \frac{\partial u}{\partial \xi} \right|_{\xi=0} = 0, \qquad \left. \frac{\partial v}{\partial \eta} \right|_{\eta=2} = 0, \tag{5.18}$$

$$u(1, t) = 0, \qquad v(1, t) = 0, \tag{5.19}$$

$$\frac{\mathrm{d}s(t)}{\mathrm{d}t} = -\frac{\kappa_u}{s(t)} \left. \frac{\partial u}{\partial \xi} \right|_{\xi=1} - \frac{\kappa_v}{L - s(t)} \left. \frac{\partial v}{\partial \eta} \right|_{\eta=1}. \tag{5.20}$$

Equations (5.16)-(5.17) and the associated boundary conditions can now be solved numerically using a standard central difference approximation for the transformed spatial derivatives and a backward Euler approximation for the temporal derivatives. These details are given in the Additional Material.

5.3.4 Travelling wave solutions

Typically, we find that numerical solutions of Equations (5.8)-(5.12) evolve into constant speed, constant shape travelling waves, such as those shown in Figure 5.3(a). In this case we have $D = \lambda = 1$ so that the cancer cells and skin cells are equally motile and proliferative. The travelling wave profiles in Figure 5.3(a) are generated by choosing particular values of κ_u and κ_v that leads to an invading malignant population moving with positive speed, $c = 0.2$. In contrast, choosing different values of κ_u and κ_v can lead to a retreating malignant front, as in Figure 5.3(e), where we have a travelling wave with $c = -0.2$. These two numerical travelling wave solutions in Figure 5.3(a) and (e) are interesting, especially when we compare the properties of these travelling waves with the more familiar properties of the travelling wave solutions of the Fisher-Kolmogorov model where there are three important differences:

1. The moving boundary model (5.8)-(5.12) supports travelling wave solutions with well-defined sharp front whereas the Fisher-Kolmogorov model does not;

2. Travelling wave solutions of the moving boundary model (5.8)-(5.12) can either advance or retreat, whereas analogous travelling wave solutions of the Fisher-Kolmogorov model only ever advance;

3. Travelling wave solutions of the nondimensional moving boundary model (5.8)-(5.12) move with speed $|c| < 2$ whereas travelling wave solutions of the nondimensional Fisher-Kolmogorov model always lead to $c \geq 2$.

To provide further insight into the properties of the travelling wave solutions of Equations (5.8)-(5.9) we now use phase plane analysis.
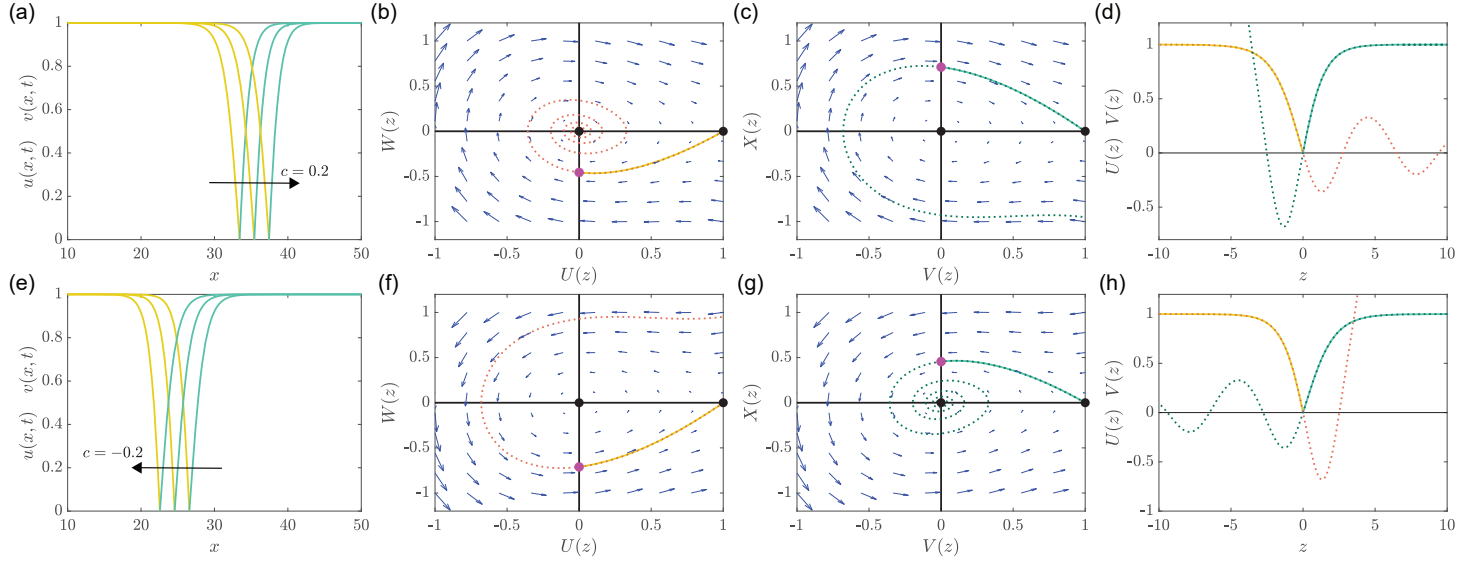
Figure 5.3: Travelling wave solutions for $D = \lambda = 1$. All partial differential equation solutions are obtained with $L = 60$, $\beta = 1$, $\alpha = 0.5$, $s(0) = 30$. Results in (a) correspond to $\kappa_u = 1.2195$ and $\kappa_v = 0.5$. Results in (e) correspond to $\kappa_u = 0.5$ and $\kappa_v = 1.2195$. Results in (a)-(d) correspond to $c = 0.2$ and results in (e)-(h) correspond to $c = -0.2$. Solutions of Equations (5.8)-(5.9) in (a) and (e) show $u(x,t)$ in solid yellow and $v(x,t)$ in solid green, at $t = 20, 30$ and 40. Phase planes in (b) and (f), and (c) and (g) show the trajectories corresponding to the $U(z)$ and $V(z)$ travelling waves, respectively. Relevant trajectories in (b)-(c) and (f)-(g) are shown in dashed lines upon which we superimpose the solid lines from the numerical solution of Equations (5.8)-(5.9) transformed into travelling wave coordinates. Results in (d) and (h) show $U(z)$ and $V(z)$ as a function of z where results from the phase plane are given in dashed lines superimposed upon the solutions of Equations (5.8)-(5.9) shifted so that the moving boundary is at $z = 0$. In the phase planes the equilibrium points are shown with a black disc and the intersection of the phase plane trajectory with the vertical axis is shown with a pink disc.

5.3.5 Phase plane analysis

To study travelling wave solutions of the moving boundary model we re-write the governing equations in the travelling wave coordinate, $z = x - ct$, and seek solutions of the form $U(z) = u(x - ct)$ and $V(z) = v(x - ct)$. Writing Equations (5.8)-(5.9) in the travelling wave coordinates leads to

$$\frac{\mathrm{d}^2 U}{\mathrm{d} z^2} + c \frac{\mathrm{d} U}{\mathrm{d} z} + U(1 - U) = 0, \quad -\infty < z < 0, \tag{5.21}$$

$$D \frac{\mathrm{d}^2 V}{\mathrm{d} z^2} + c \frac{\mathrm{d} V}{\mathrm{d} z} + \lambda V(1 - V) = 0, \quad 0 < z < \infty, \tag{5.22}$$

where the relevant boundary conditions are

$$U(-\infty) = 1, \quad U(0) = 0, \tag{5.23}$$

$$V(0) = 0, \quad V(\infty) = 1, \tag{5.24}$$

$$c = -\kappa_v \frac{\mathrm{d} V(0)}{\mathrm{d} z} - \kappa_u \frac{\mathrm{d} U(0)}{\mathrm{d} z}. \tag{5.25}$$

The travelling wave solution for the cancer population, $U(z)$, is described by Equations (5.21) and (5.23), while the travelling wave solution for the skin population, $V(z)$, is described by Equations (5.22) and (5.24). This means that the travelling wave solutions for $U(z)$ and $V(z)$ can be studied in two separate phase planes, and these two phase planes are coupled by Equation (5.25), which is associated with the Stefan condition at the moving interface.

To simplify our study of these two phase planes we note that Equation (5.21) for $U(z)$ is identical to Equation (5.22) for $V(z)$ when $D = \lambda = 1$. Therefore, it is sufficient for us to study Equation (5.22) for $V(z)$ and to recall that setting $D = \lambda = 1$ means that our analysis of this phase plane corresponds to $U(z)$. To make progress we re-write Equation (5.22) as a first-order system

$$\frac{\mathrm{d} V}{\mathrm{d} z} = X, \tag{5.26}$$

$$\frac{\mathrm{d} X}{\mathrm{d} z} = -\frac{c}{D} X - \frac{\lambda}{D} V(1 - V). \tag{5.27}$$

At this point we remark that Equation (5.26)-(5.27) defines a two-dimensional phase plane for $(V(z), X(z))$ that is identical to the phase plane associated with the well-studied travelling wave solutions of the Fisher-Kolmogorov model [Canosa 1973, Murray 2002]. Therefore, all the well-known properties of that phase

plane will play a role here in our study of Equations (5.8)-(5.9). In particular, the equilibrium points are $(0,0)$ and $(1,0)$. Linear stability shows that $(1,0)$ is a saddle for all c whereas $(0,0)$ is a stable node if $c \geq 2\sqrt{\lambda D}$ or a stable spiral for $c < 2\sqrt{\lambda D}$. Normally, when considering travelling wave solutions of the Fisher-Kolmogorov model, we are interested in the heteroclinic trajectory between $(1,0)$ and $(0,0)$, and the heteroclinic trajectory associated with the stable spiral at $(0,0)$ when $c < 2\sqrt{\lambda D}$ is ruled out on the basis of requiring $V(z) > 0$. This classical argument gives rise to the well-known condition that $c \geq 2\sqrt{\lambda D}$ for travelling wave solutions of the Fisher-Kolmogorov model [Canosa 1973, Murray 2002]. In contrast, for our moving boundary model we have a very different situation where, for example, the travelling wave in Figure 5.3(a) leads to $c = 0.2 < 2\sqrt{\lambda D}$.

To explore these solutions we show the phase plane corresponding to the travelling wave in Figure 5.3(a) in Figure 5.3(b)-(c) for the $U(z)$ and $V(z)$ population, respectively. In all phase planes, we generate the trajectories numerically using techniques described in the Additional Material. Figure 5.3(b) shows the $(U(z), W(z))$ phase plane, where $W(z) = \mathrm{d}U(z)/\mathrm{d}z$ and $c = 0.2$ to correspond with the travelling waves in Figure 5.3(a). The equilibrium points at $(1,0)$ and $(0,0)$ are highlighted, and the heteroclinic trajectory that leaves $(1,0)$ and spirals into $(0,0)$ is shown with a dotted line. Normally, when considering travelling wave solutions of the Fisher-Kolmogorov model, this heteroclinic trajectory would be regarded as nonphysical since it implies that $U(z) < 0$ for certain values of z along that trajectory. However, instead of rejecting this trajectory, the travelling wave solution for $U(z)$ in our moving boundary model simply corresponds to the portion of that heteroclinic trajectory in the fourth quadrant where $U(z) \geq 0$. The point where the trajectory intersects the $U(z) = 0$ axis corresponds to the slope of the travelling wave at the moving boundary, $(0, W^*(z))$. This point of intersection is important because it plays a role in satisfying Equation (5.25). To provide an additional check on our phase plane in Figure 5.3(b) we take the $u(x,t)$ travelling wave profile in Figure 5.3(a) and superimpose the $(U(z), W(z))$ profile calculated from that travelling wave as a solid line in the phase plane. This exercise shows that this solid curve is visually indistinguishable from the first part of the heteroclinic trajectory where $U(z) \geq 0$.

Figure 5.3(c) shows the $(V(z), X(z))$ phase plane associated with the $v(x,t)$ travelling wave profile in Figure 5.3(a). Again, we highlight the equilibrium points at $(1,0)$ and $(0,0)$ and we show the trajectory moving towards the saddle point at $(1,0)$ along the stable manifold. In the usual study of the Fisher-Kolmogorov model this trajectory is not normally considered because it is not associated with a heteroclinic trajectory, and indeed the phase plane in Figure 5.3(c) indicates that this trajectory originates far away from the relevant region of the phase plane. However, we find that part of the trajectory in the first quadrant where $V(z) \geq 0$, corresponds to the travelling wave solution for the $v(x,t)$ population. The point at which this trajectory intersects the $V(z) = 0$ axis, $(0, X^*(z))$, corresponds to the slope of the travelling wave at the moving boundary. Taking the two phase planes in Figure 5.3(b)-(c) together, the two intersection points $W^*(z)$ and $X^*(z)$ are such that they satisfy Equation (5.25), $c = -\kappa_v X^*(z) - \kappa_u W^*(z)$. Therefore, these two intersection points play a critical role in relating the speed of the travelling wave solution with the constants κ_u and κ_v.

To summarise the results in Figure 5.3(a)-(c), and to make an explicit connection between the physical solutions of the partial differential equation model and the nonphysical features of the phase plane trajectories, we superimpose various solutions in Figure 5.3(d). The solid green and solid yellow lines in Figure 5.3(d) show long time solutions of Equations (5.8)-(5.12) that are shifted so that the moving boundary is at $z = 0$. The dashed lines in Figure 5.3(d) shows the $U(z)$ and $V(z)$ associated with the relevant phase plane trajectories from Figure 5.3(b)-(c), respectively. In the case of the $U(z)$ trajectory we see that the shape of the trajectory matches the solution from Equations (5.8)-(5.9) where $z \leq 0$ and $U(z) \geq 0$. The phase plane trajectory of $U(z)$ for $z > 0$ is nonphysical since $U(z)$ oscillates about $U(z) = 0$ and this does not correspond to any part of the solution of Equations (5.8)-(5.9). In the case of the $V(z)$ profile we see that the shape of the phase plane trajectory matches the solution from Equations (5.8)-(5.9) where $z \geq 0$ and $V(z) \geq 0$. The phase plane trajectory of $V(z)$ for $z < 0$ is nonphysical since part of that trajectory involves $V(z) < 0$.

All results in Figure 5.3(a)-(d) correspond to choices of κ_u and κ_v that lead to $c = 0.2$. Results in Figure 5.3(e)-(h) correspond to different choices of κ_u

and κ_v such that the travelling wave leads to a receding front with $c = -0.2$. Numerical solutions of Equations (5.8)-(5.9) in Figure 5.3(e) show the travelling wave solutions and the phase planes in Figure 5.3(f)-(g) show the phase plane trajectories associated with the $U(z)$ and $V(z)$ travelling waves. Again, a summary comparing the physical travelling wave solutions from Equations (5.8)-(5.9) with the phase plane trajectories is given in Figure 5.3(h). This comparison shows that the travelling wave solutions of Equations (5.8)-(5.9) compare very well with the physical portion of the phase plane trajectories in Figure 5.3(f)-(g).

The first set of travelling wave solutions we report in Figure 5.3 correspond to the simplest possible case where $D = \lambda = 1$ so that the skin and cancer cells are equally motile and equally proliferative. Additional results are presented in Figures 5.4-5.5 for $D \neq 1$ and $\lambda = 1$, and for $D = 1$ and $\lambda \neq 1$, respectively. Results in Figure 5.4-5.5 are presented in the exact same format as in Figure 5.3 where we consider results for $c > 0$ and $c < 0$ separately in both cases. In all cases we find that the travelling wave solutions from Equations (5.8)-(5.9) compare very well with the physical portion of the phase plane trajectories and that the nonphysical portion of the phase plane trajectories do not play any role in the travelling wave solutions.

Experimenting with the numerical solutions of Equations (5.8)-(5.9) suggests that for a fixed choice of D and λ, the travelling wave speed depends on the choice of κ_u and κ_v. We find that numerical solutions of Equations (5.8)-(5.9) lead to travelling wave solutions with $-2 < c < 2$. For example, for any fixed positive κ_v, we find that $c \to 2^-$ as $\kappa_u \to \infty$ whereas $c \to -2^+$ as $\kappa_u \to -\infty$.
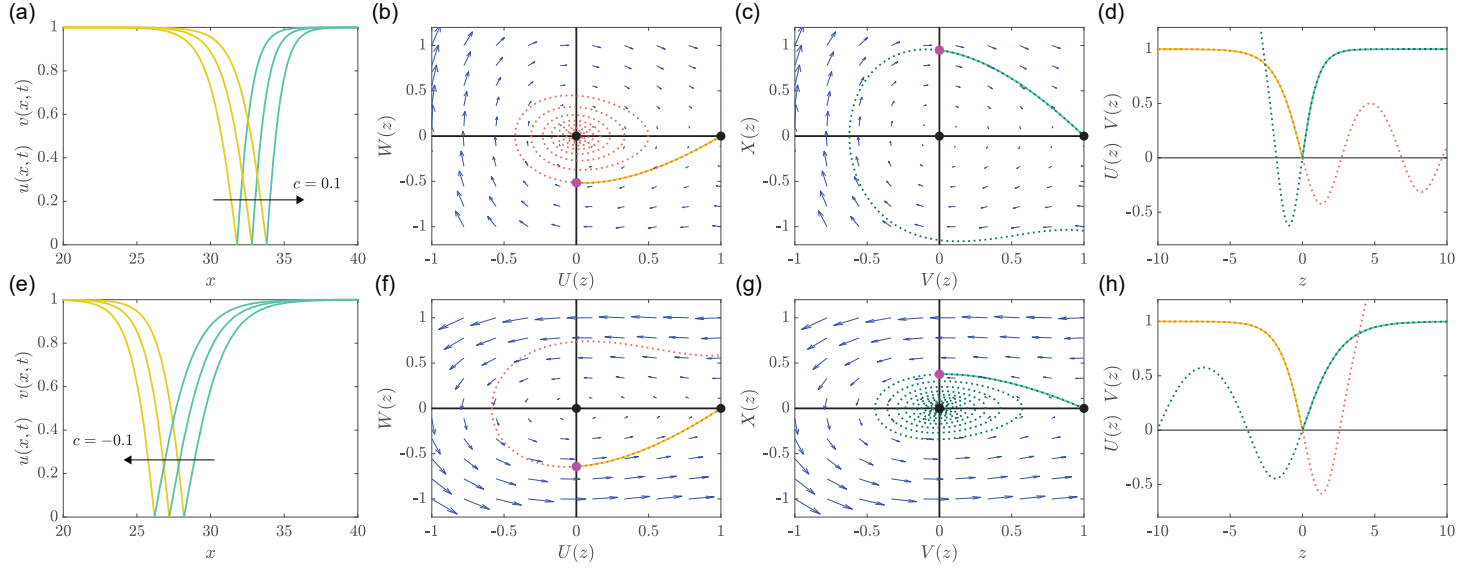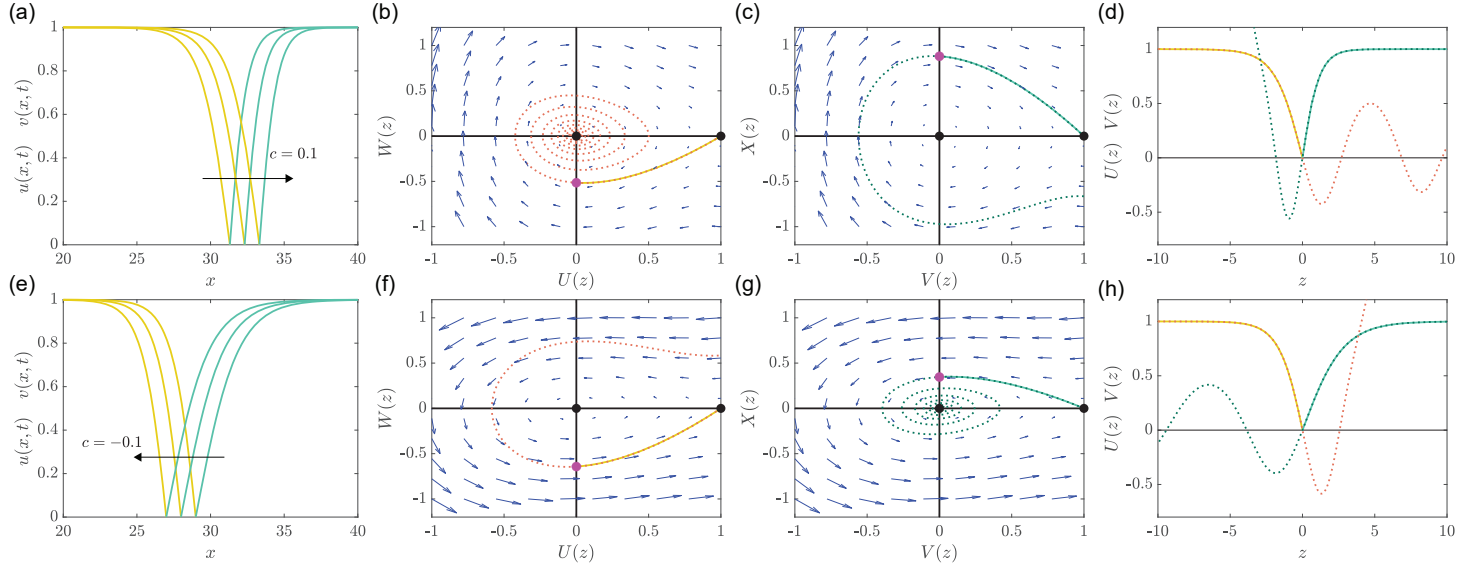
Figure 5.4: Travelling wave solutions for $D \neq 1$ and $\lambda = 1$. All partial differential equation solutions are obtained with $L = 60$, $\beta = 1$, $\alpha = 0.5$, $s(0) = 30$. Results in (a) correspond to $D = 0.5$, $\kappa_u = 1.1151$ and $\kappa_v = 0.5$. Results in (e) correspond to $D = 2$, $\kappa_u = 0.5$ and $\kappa_v = 1.1180$. Results in (a)-(d) correspond to $c = 0.1$ and results in (e)-(h) correspond to $c = -0.1$. Solutions of Equations (5.8)-(5.9) in (a) and (e) show $u(x,t)$ in solid yellow and $v(x,t)$ in solid green, at $t = 20, 30$ and 40. Phase planes in (b) and (f), and (c) and (g) show the trajectories corresponding to the $U(z)$ and $V(z)$ travelling waves, respectively. Relevant trajectories in (b)-(c) and (f)-(g) are shown in dashed lines upon which we superimpose the solid lines from the numerical solution of Equations (5.8)-(5.9) transformed into travelling wave coordinates. Results in (d) and (h) show $U(z)$ and $V(z)$ as a function of z where results from the phase plane are given in dashed lines superimposed upon the solutions of Equations (5.8)-(5.9) shifted so that the moving boundary is at $z = 0$. In the phase planes the equilibrium points are shown with a black disc and the intersection of the phase plane trajectory with the vertical axis is shown with a pink disc.

Figure 5.5: Travelling wave solutions for $D = 1$ and $\lambda \neq 1$. All partial differential equation solutions are obtained with $L = 60$, $\beta = 1$, $\alpha = 0.5$, $s(0) = 30$. Results in (a) correspond to $\lambda = 2$, $\kappa_u = 1.0502$ and $\kappa_v = 0.5$. Results in (e) correspond to $\lambda = 0.5$, $\kappa_u = 0.5$ and $\kappa_v = 1.2164$. Results in (a)-(d) correspond to $c = 0.1$ and results in (e)-(h) correspond to $c = -0.1$. Solutions of Equations (5.8)-(5.9) in (a) and (e) show $u(x, t)$ in solid yellow and $v(x, t)$ in solid green, at $t = 20, 30$ and 40. Phase planes in (b) and (f), and (c) and (g) show the trajectories corresponding to the $U(z)$ and $V(z)$ travelling waves, respectively. Relevant trajectories in (b)-(c) and (f)-(g) are shown in dashed lines upon which we superimpose the solid lines from the numerical solution of Equations (5.8)-(5.9) transformed into travelling wave coordinates. Results in (d) and (h) show $U(z)$ and $V(z)$ as a function of z where results from the phase plane are given in dashed lines superimposed upon the solutions of Equations (5.8)-(5.9) shifted so that the moving boundary is at $z = 0$. In the phase planes the equilibrium points are shown with a black disc and the intersection of the phase plane trajectory with the vertical axis is shown with a pink disc.

5.3.6 Perturbation solution for $|c| \ll 1$

All results in Figures 5.3–5.5 rely on numerical solutions of Equations (5.26)-(5.27) to explore trajectories in the phase plane. We now provide analytical insight by constructing approximate perturbation solutions to complement these numerical explorations. First we re-write Equations (5.26)-(5.27) as

$$\frac{\mathrm{d}X}{\mathrm{d}V} = \frac{-cX - \lambda V(1-V)}{DX}, \tag{5.28}$$

for which we seek a perturbation solution about $c = 0$. Substituting the expansion $X(V) = X_0(V) + cX_1(V) + \mathcal{O}(c^2)$ into Equation (5.28) leads to

$$\frac{\mathrm{d}X_0}{\mathrm{d}V} = -\frac{\lambda V(1-V)}{DX_0}, \tag{5.29}$$

$$\frac{\mathrm{d}X_1}{\mathrm{d}V} = \frac{\lambda X_1 V(1-V)}{DX_0^2} - \frac{1}{D}, \tag{5.30}$$

which can be solved exactly to give expressions for $X_0(V)$ and $X_1(V)$. With initial conditions $X_0(1) = 0$ and $X_1(1) = 0$, the two-term perturbation solution can be written as

$$X(V) = \pm\sqrt{\frac{\lambda}{D}\left(-V^2 + \frac{2V^3}{3} + \frac{1}{3}\right)} - c\frac{(2-V)(1+2V)^{3/2} - 3\sqrt{3}}{5D(1-V)\sqrt{1+2V}} + \mathcal{O}(c^2). \tag{5.31}$$

Retaining just the first term on the right of Equation (5.31) gives us an approximation that we refer to as an $\mathcal{O}(1)$ perturbation solution whereas retaining both terms on the right of Equation (5.31) gives us an approximation that we refer to as an $\mathcal{O}(c)$ perturbation solution. We will now explore both these solutions.

Results in Figure 5.6(a)-(b) show the $(U(z), W(z))$ and $(V(z), X(z))$ phase planes for $c = 0.05$, respectively. The numerically-generated trajectories are compared with both the $\mathcal{O}(1)$ and $\mathcal{O}(c)$ perturbation solutions. Here we see that the $\mathcal{O}(1)$ perturbation solution is a teardrop-shaped homoclinic trajectory to $(1, 0)$. In Figure 5.6(a) we see that the $\mathcal{O}(1)$ perturbation solution provides a reasonably accurate approximation of the numerical trajectory in the fourth quadrant for $U(W)$. Similarly, in Figure 5.6(b) we see that the $\mathcal{O}(1)$ perturbation solution is a reasonably accurate approximation of the numerical trajectory in the first quadrant for $V(X)$. We also superimpose the

149
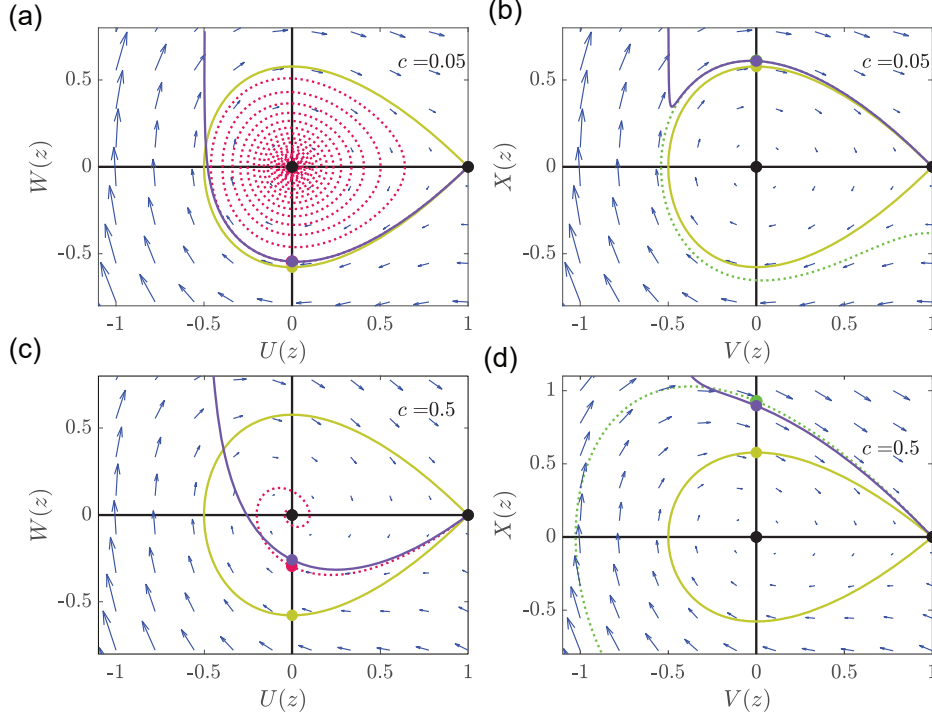
Figure 5.6: Perturbation solution in the phase plane when $c > 0$ and $D = \lambda = 1$. Phase planes in (a)-(b), (c)-(d) compare numerical phase plane trajectories and perturbation solutions for $c = 0.05$ and $c = 0.5$, respectively. Numerical estimates of the $U(W)$ and $V(X)$ trajectories are shown in dashed red and dashed green respectively. The $\mathcal{O}(1)$ and $\mathcal{O}(c)$ perturbation solutions are shown in solid yellow and solid purple, respectively. Equilibrium points are shown with black discs. The points at which the various solutions intersect the vertical axis are shown with various coloured discs corresponding to the colour of the particular trajectory.

$\mathcal{O}(c)$ perturbation solution in Figures 5.6(a)-(b) but it is difficult to visually distinguish between the $\mathcal{O}(1)$ and $\mathcal{O}(c)$ solutions for $c = 0.05$.

Results in Figure 5.6(c)-(d) show the $(U(z), W(z))$ and $(V(z), X(z))$ phase planes for $c = 0.5$, respectively. In both cases we see that the $\mathcal{O}(1)$ perturbation solutions do not provide an accurate approximation of the numerical trajectories, whereas the $\mathcal{O}(c)$ perturbation solutions compare very well with the physical part of the phase plane trajectories in both cases. The comparison of the numerical phase plane trajectories and the perturbation solutions in Figure 5.6 is given for the most fundamental case where $D = \lambda = 1$ and $c > 0$. Additional comparisons for other choices of D, λ and c are provided in the Additional Material.

The comparison of the numerical phase plane trajectories with the perturbation solutions in Figure 5.6 shows the shape of $W(U)$ and $X(V)$ in the phase plane. To explore how these solutions compare in the z plane, we integrate both sides of Equation (5.31) with respect to z numerically using a forward
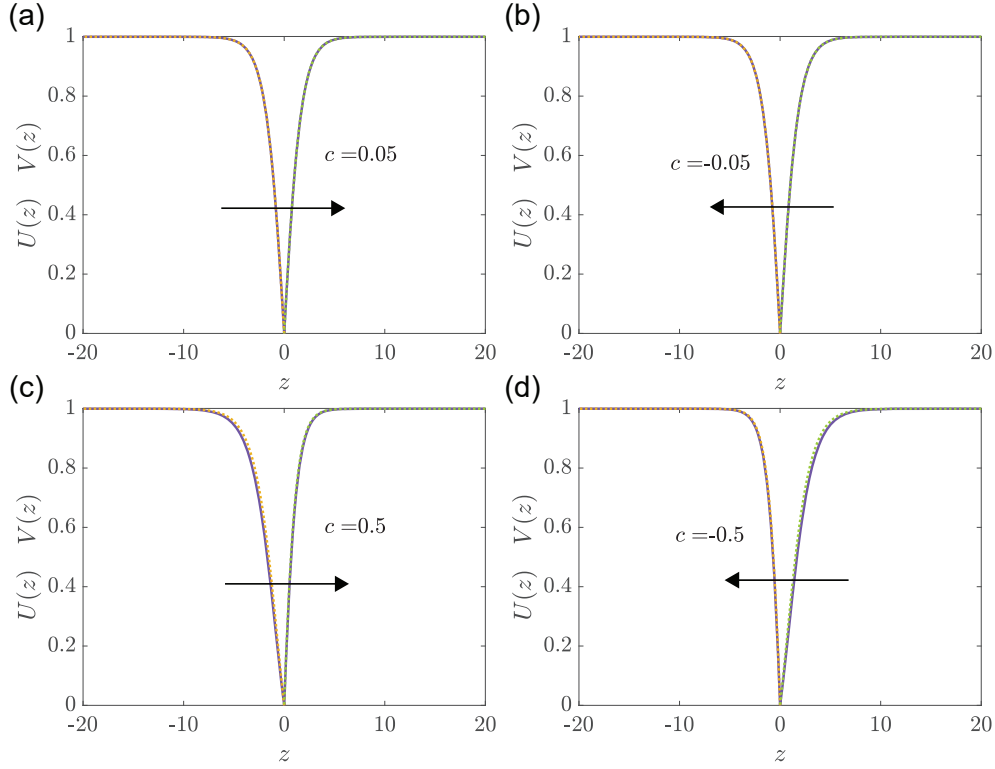
Figure 5.7: Perturbation solution for the shape of the travelling waves for $D = \lambda = 1$. Comparison of $U(z)$ and $V(z)$ from the $\mathcal{O}(c)$ perturbation solution (purple solid) with numerical estimates of the travelling wave obtained by solving Equations (5.8)-(5.9) and shifting the profiles so that $U(0) = V(0) = 0$. Numerical estimates of $U(z)$ and $V(z)$ are shown in dashed yellow and dashed green lines, respectively. Results are shown for: (a)–(b) $c = \pm 0.05$, and (c)–(d) $\pm c = -0.5$.

Euler approximation with constant step size, $\mathrm{d}z = 1 \times 10^{-3}$. This numerical integration leads to estimates of the shape of the travelling waves that can be compared with the shapes of the travelling wave obtained from long-time numerical solutions of Equations (5.8)-(5.9). Figure 5.7 compares the shape of both $V(z)$ and $U(z)$ obtained from the $\mathcal{O}(c)$ perturbation solution with those obtained from Equations (5.8)-(5.9), where we see that the shape of both the $V(z)$ and $U(z)$ profiles compare extremely well for $c = \pm 0.05$, as expected. It is also pleasing that the shape of the profiles compare quite well even for much larger values, $c = \pm 0.5$. All results in Figure 5.7 correspond to the simplest case where $D = \lambda = 1$ and additional comparisons for other choices of D and λ and are provided in the Additional Material.

5.3.7 Qualitatively different long time behaviour

All solutions in Figures 5.3-5.5 correspond to particular choices of $u(x, 0)$, $v(x, 0)$, κ_u and κ_v that lead to long time travelling wave solutions. However,

we note that numerical simulations and more rigorous analysis of the simpler single-phase Fisher-Stefan moving boundary problems gives rise to a *spreading-vanishing* dichotomy, whereby certain initial conditions and parameter values lead to population extinction as $t \rightarrow \infty$ [El-Hachem et al. 2019, Simpson 2020, Du and Lin 2010, Du and Guo 2011, Bunting et al. 2012, Du and Guo 2012, Du et al. 2014a, Du et al. 2014b, Du and Lou 2015]. The main focus of our current work is to study travelling wave solutions since we are interested in situations where both populations are present, such as the images in Figure 5.1(a)-(b). To complement these solutions in Figure 5.3–5.7 we now briefly consider additional numerical solutions of Equations (5.8)-(5.9) where similar extinction behaviour occurs in the two-phase problem.
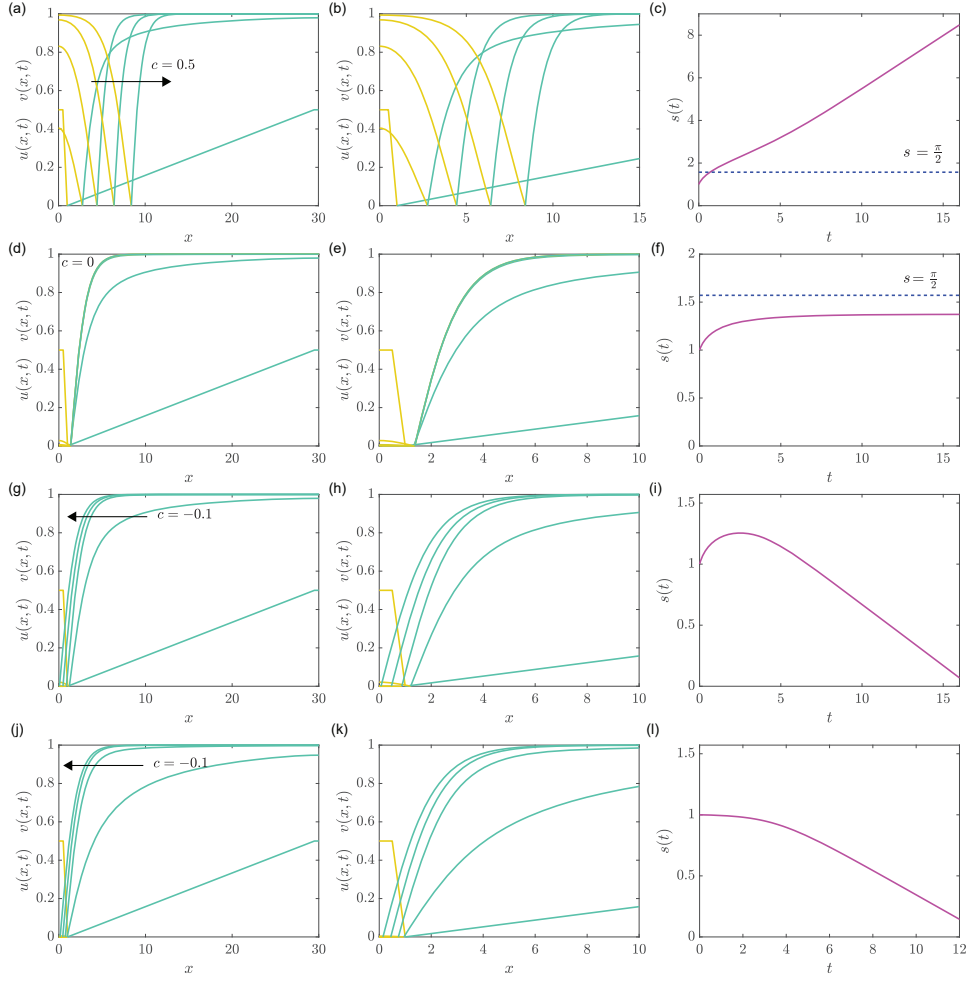
Figure 5.8: Additional solutions with qualitatively different long time behaviour. Four additional numerical solutions of Equations (5.8)–(5.9). Each solution corresponds to $D = 1$, $\lambda = 1$, with $L = 30$, $s(0) = 1$, $\beta = 0.5$, $\alpha = 0.5$. Results in each row correspond to different values of κ_u and κ_v: (a)–(c) corresponds to $\kappa_u = 2.2976$ and $\kappa_v = 0.1946$; (d)–(f) corresponds to $\kappa_u = 0.5$ and $\kappa_v = 0$; (g)–(i) corresponds to $\kappa_u = 0.5$ and $\kappa_v = 0.1946$; and (j)–(l) corresponds to $\kappa_u = 0.0001$ and $\kappa_v = 0.1946$. The profiles in (a)-(b), (d)-(e) and (g)-(h) are shown at $t = 0, 4, 8, 12$ and 16. The density profiles in (i)-(j) are shown at $t = 0, 3, 6, 9$ and 12. Profiles in the left column show the evolution of the solutions on $0 < x < 60$; profiles in the middle column show the details of these solutions on $0 < x < 10$, and profiles in the right column show the evolution of $s(t)$.

Figure 5.8 shows results for various initial conditions and/or values of κ_u and κ_v. The first set of results in Figure 5.8(a)–(c) shows a case in which $s(0) = 1$. Here we see the solution evolving to travelling wave profile with positive speed of the type we have discussed in some detail. An important point to make here is that $s(0) < \pi/2$, which is a critical length in the corresponding one-phase problem [El-Hachem et al. 2019, Simpson 2020]. Based on the previously reported studies of the one-phase problem, our interpretation of the solution in Figure 5.8(a)–(c) is that even though $s(0) < \pi/2$, travelling

153

wave solutions are still possible provided the initial mass $\int_0^{s(0)} u(x,0)\,dx$ is sufficiently large to overcome mass lost at the moving boundary. On the other hand, in Figure 5.8(d)–(f) the solution has the same parameter values as in Figure 5.8(a)–(c), except that κ_u and κ_v are now reduced. In this case the moving boundary $x = s(t)$ moves to the right and approaches a steady state value which is less than the critical length $\pi/2$, while the left population $u(x,t)$ goes extinct as $t \to \infty$. The extinction is caused by the fact that the rate at which mass associated with the $u(x,t)$ population is lost at $x = s(t)$ exceeds the rate at which the mass of $u(x,t)$ is gained by proliferation. These two examples are consistent with the spreading-vanishing dichotomy in the one-phase problem [El-Hachem et al. 2019, Simpson 2020].

Additional results in Figures 5.8(g)–(i) and (j)–(l) show two further solutions with different choices of κ_u and κ_v. In both these cases we see that the $u(x,t)$ profile eventually becomes extinct, whereas the $v(x,t)$ profile eventually forms a travelling wave solution with $c = -0.1$. Subtle differences, highlighted in Figure 5.8(i) and (l), show the temporal behaviour in terms of the movement of the interface, $s(t)$. The case in Figure 5.8(l) leads to a monotonically decreasing $s(t)$, whereas the case in Figure 5.8(i) leads to $s(t)$ that is initially increasing before eventually decreasing at later time. This kind of nonmonotone behaviour of $s(t)$ is very interesting because the standard single phase Fisher-Stefan model appears to only lead to monotone $s(t)$, whereas our two-phase analogue leads to more interesting and nuanced behaviours.

5.4 Conclusion

In this work we consider a novel mathematical model of cell invasion which takes the form of a two-phase moving boundary problem. This modelling strategy is both biologically relevant and mathematically novel. The moving boundary model leads to travelling wave solutions with a clearly defined moving front. This is advantageous over the classical Fisher–Kolmogorov model and extensions because travelling wave solutions of those models do not have this property. From a biological point of view, our model describes the migration and proliferation of two populations of cells, $u(x,t)$ and $v(x,t)$, and this allows us to model a population of cancer cells, $u(x,t)$, invading into a population of surrounding cells, $v(x,t)$. This scenario is relevant to melanoma

cells invading into surrounding skin cells, as shown in Figure 5.1(a)-(b). Interestingly, the moving boundary model leads to travelling wave solutions that move in either the positive or negative direction, meaning that we can simulate malignant invasion as well as malignant retreat. This is very different to travelling wave solutions of the Fisher-Kolmogorov and Porous-Fisher models because those models only ever predict malignant advance and never predict malignant retreat.

The two-phase moving boundary model is also very interesting mathematically. In this work we analyse travelling wave solutions where we show that the $U(z) = u(x - ct)$ and $V(z) = v(x - ct)$ travelling waves can be analysed in two separate phase planes. These two phase planes are identical to the phase plane that arises in the classical analysis of travelling wave solutions of the Fisher-Kolmogorov model. There are two equilibria: (i) $(1, 0)$ is a saddle for all c; and (ii) $(0, 0)$ is a stable node if $c \geq 2\sqrt{\lambda D}$ or a stable spiral for $c < 2\sqrt{\lambda D}$. Normally, in the case of travelling waves solutions of the Fisher–Kolmogorov model we are interested in a heteroclinic trajectory between these two equilibria and so we require $c \geq 2\sqrt{\lambda D}$ to avoid the nonphysical negative densities that arise from spirals in the phase plane. In contrast, travelling wave solutions of our moving boundary model have $c < 2\sqrt{\lambda D}$ and so these normally-discarded trajectories turn out to be very useful.

For our two-phase moving boundary model we use numerical simulations and perturbation methods to confirm that the travelling wave solutions for $U(z)$ and $V(z)$ are associated with trajectories in the classical Fisher–Kolmogorov phase plane that are normally disregarded as being nonphysical. In the cases we consider with $c > 0$, the $U(z)$ travelling wave is associated with the heteroclinic trajectory that leaves $(1, 0)$ along the unstable manifold and eventually spiralling into $(0, 0)$. Here we have the restriction that the travelling wave solution is only associated with the first part of that trajectory where $U(z) > 0$. Similarly, the $V(z)$ travelling wave is associated with the trajectory that approaches $(1, 0)$ along the stable manifold. Here we have the restriction that the travelling wave is associated with part of the trajectory where $V(z) > 0$. For travelling wave solutions with $c < 0$, it is the other way around: the $U(z)$ travelling wave is associated with the trajectory that eventually moves into $(1, 0)$ from infinity, whereas the $V(z)$ travelling wave is associated with the trajectory

that eventually spirals into $(0,0)$. It is very interesting that both these trajectories come from the phase plane for the well–studied Fisher–Kolmogorov equation, except that these trajectories are not normally considered in any detail. While certain aspects have been studied more rigorously [Chang and Chen 2013, Yang 2015], these previous studies do not provide visualisations of numerical solutions of the partial differential equation models, nor do they make use of traditional phase plane analysis or perturbation methods to provide approximate expressions for the solutions of the models.

There are many ways that our study could be extended to incorporate additional features. For example, from a practical point of view, all work presented here involves applying these models in a standard one-dimensional Cartesian geometry and it would also be interesting to apply these models in a radial geometry to study the outward invasion of a spherical tumour or the closure of a disc-shaped wound [Treloar et al. 2014]. Another practical consideration is that it is relatively straightforward to make experimental measurements of the invasion speed c [Maini et al. 2004a, Maini et al. 2004b], the cell diffusivity [Johnston et al. 2015] and cell proliferation rates [Johnston et al. 2015]. With this information, our model could be used to provide estimates of the coefficients κ_u and κ_v. Further considerations could be to explicitly model how malignant cells produce proteases and other chemical signals and to explore how such signals can be incorporated into the evolution equation for the moving boundary [Smallbone et al. 2005, Holder et al. 2014]. From a more mathematical point of view, additional questions of interest are to precisely study under which conditions solutions go to travelling waves or become extinct, to relax the assumption that the contact point corresponds to zero cell density, and to study the limit $t \to \infty$ with care to determine how quickly travelling wave solutions develop.

5.5 Additional material

5.5.1 Numerical methods

Liberally commented MATLAB implementations of all numerical algorithms used to generate the solutions of the differential equations in this work are available on GitHub.

5.5.1.1 Partial differential equation

As we explained in the main document, the partial differential equation models are transformed to a fixed domain, Equations (5.8)-(5.9) on $0 \leq \xi \leq 1$ and $1 \leq \eta \leq 2$, respectively. To solve these transformed partial differential equations we discretize the ξ and η domains uniformly. In principle we use m equally-spaced mesh points for ξ, $m = 1/\Delta\xi + 1$, and n equally-spaced mesh points for η, $n = 1/\Delta\eta + 1$. In practice we usually implement the numerical solution with $m = n$ by setting $\Delta\xi = \Delta\eta$. This is convenient, but not necessary.

Using a central difference approximation for the transformed spatial variable and an implicit Euler approximation for the temporal derivatives [Simpson et al. 2005, Simpson et al. 2007], at the central nodes on both meshes we have

$$
\begin{aligned}
\frac{u_i^{j+1} - u_i^j}{\Delta t} &= \frac{\left(u_{i+1}^{j+1} - 2u_i^{j+1} + u_{i-1}^{j+1}\right)}{(s^{j+1}\Delta\xi)^2} \\
&\quad + \frac{\xi_i \left(s^{j+1} - s^j\right)\left(u_{i+1}^{j+1} - u_{i-1}^{j+1}\right)}{2s^{j+1}\Delta t \Delta\xi} \\
&\quad + u_i^{j+1}\left(1 - u_i^{j+1}\right), \quad i = 2, \dots, m-1,
\end{aligned}
\tag{5.32}
$$

$$
\begin{aligned}
\frac{v_i^{j+1} - v_i^j}{\Delta t} &= \frac{D\left(v_{i+1}^{j+1} - 2v_i^{j+1} + v_{i-1}^{j+1}\right)}{\left((L - s^{j+1})\Delta\eta\right)^2} \\
&\quad + \frac{(2 - \eta_i)\left(v_{i+1}^{j+1} - v_{i-1}^{j+1}\right)\left(s^{j+1} - s^j\right)}{2\Delta t \Delta\eta \left(L - s^{j+1}\right)} \\
&\quad + \lambda v_i^{j+1}\left(1 - v_i^{j+1}\right), \quad i = 2, \dots, n-1,
\end{aligned}
\tag{5.33}
$$

where the subscript i denotes the mesh point and the superscript j denotes the time, where $t = j\Delta t$.

To enforce the boundary conditions we set $\partial u/\partial\xi = 0$ at $\xi = 0$ and $\partial v/\partial\eta = 0$ at $\eta = 2$, further we set $u = v = 0$ at the moving boundary where $\xi = \eta = 1$, leading to

$$
u_2^{j+1} = u_1^{j+1}, \quad v_n^{j+1} = v_{n-1}^{j+1}, \quad u_m^{j+1} = v_1^{j+1} = 0.
\tag{5.34}
$$

To advance the discrete system from time t to $t + \Delta t$ we solve the system of nonlinear algebraic equations, Equations (5.32)-(5.34), using Newton-Raphson iteration [Burden and Faires 2011]. During each iteration of the Newton-Raphson algorithm we estimate the position of the moving boundary using

the discretised Stefan condition,

$$\frac{s^{j+1} - s^j}{\Delta t} = -\kappa_u \frac{u_m^{j+1} - u_{m-1}^{j+1}}{s^{j+1}\Delta\xi} - \kappa_v \frac{v_2^{j+1} - v_1^{j+1}}{\left(L - s^{j+1}\right)\Delta\eta}. \tag{5.35}$$

Within each time step the Newton-Raphson iterations continue until the maximum change in the dependent variables is less than the tolerance ϵ. All results in this work are obtained by setting $\epsilon = 1 \times 10^{-8}$, $\Delta\xi = \Delta\eta = 2.5 \times 10^{-4}$ and $\Delta t = 1 \times 10^{-3}$, and we find that these values are sufficient to produce grid-independent results. However, we recommend that care be taken when using the algorithms on GitHub for different choices of parameters, especially when considering larger values of κ_u and κ_v, which can require a much denser mesh to give grid-independent results.

5.5.1.2 Phase plane

To construct the phase planes we solve Equations (5.26)–(5.27) numerically using Heun's method with a constant step size $\mathrm{d}z$. In most cases we are interested in examining trajectories that either enter or leave the saddle $(1, 0)$ along the stable or unstable manifold, respectively. Therefore, it is important that the initial condition we chose when solving Equations (5.26)–(5.27) are on the appropriate stable or unstable manifold and sufficiently close to $(1, 0)$. To choose this point we use the MATLAB *eig* function [Mathworks 2021] to calculate the eigenvalues and eigenvectors for the particular choice of c, D and λ of interest. The flow of the dynamical system are plotted on the phase planes using the MATLAB *quiver* function [Mathworks 2021].

5.5.2 Additional results

Results in Figure 6 are presented for $D = \lambda = 1$ and $c > 0$ only. Similarly, results in Figure 7 are presented for $D = \lambda = 1$ only. In Section 5.5.2.1 we present additional results where $D \neq 1$, $\lambda \neq 1$ and $c < 0$. Similarly in Section 5.5.2.2 we present additional results where $D \neq 1$ and $\lambda \neq 1$. In all cases we have a good match between the perturbation solutions and numerical solutions provided that the wavespeed is sufficiently close to zero, as expected.

5.5.2.1 Additional perturbation results in the phase plane
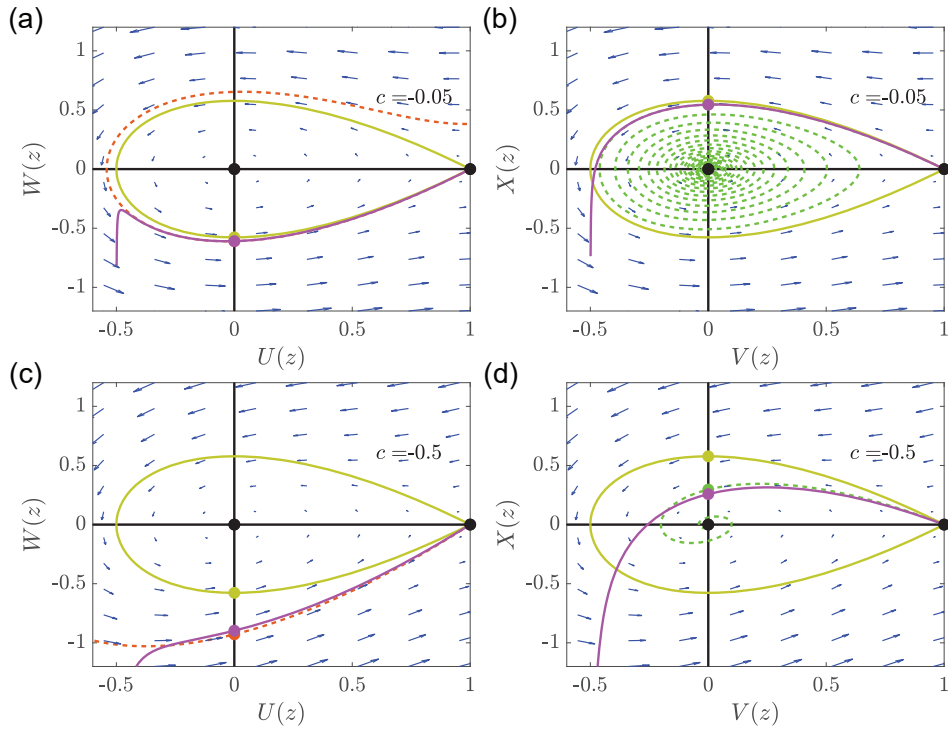
Figure 5.9: Perturbation solution for the phase plane trajectories when $c < 0$ and $D = \lambda = 1$. Phase planes in (a)-(b), (c)-(d) compare numerical phase plane trajectories and perturbation solutions for $c = -0.05$ and $c = -0.5$, respectively. Numerical estimates of the $U(W)$ and $V(X)$ trajectories are shown in dashed red and dashed green respectively. The $\mathcal{O}(1)$ and $\mathcal{O}(c)$ perturbation solutions are shown in solid yellow and solid purple, respectively. Equilibrium points are shown with black discs. The points at which the various solutions intersect the vertical axis are shown with various coloured discs corresponding to the colour of the particular trajectory.
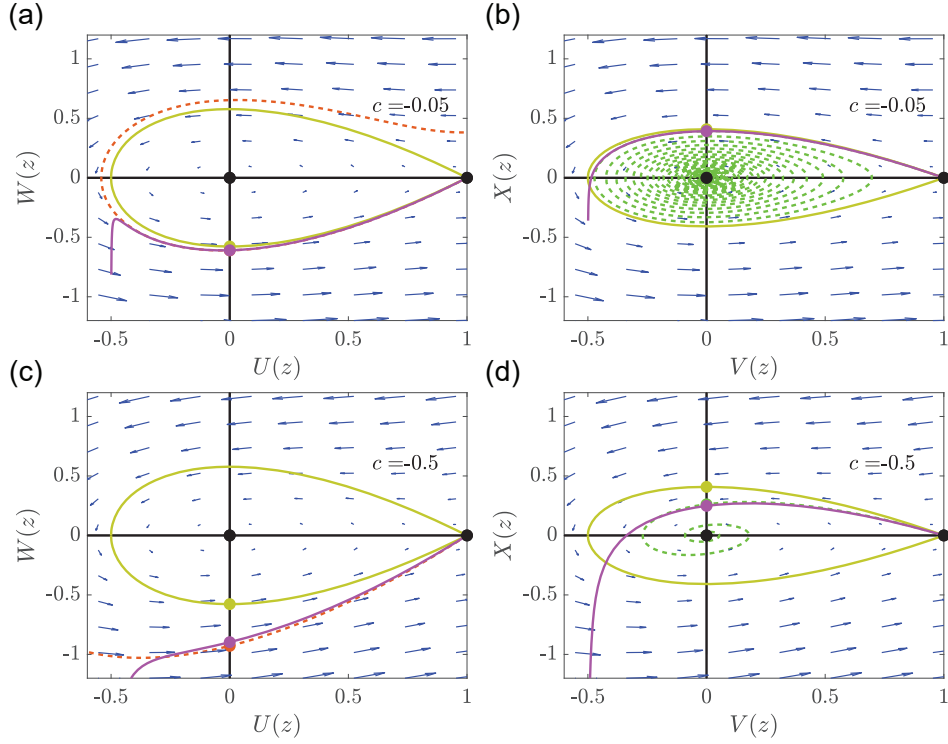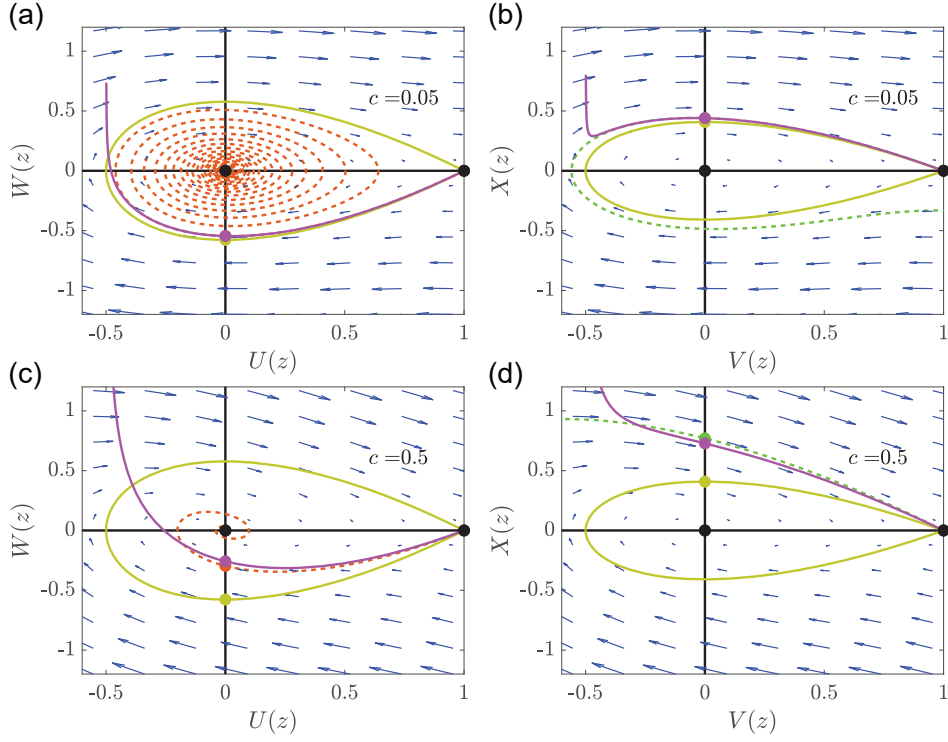
159
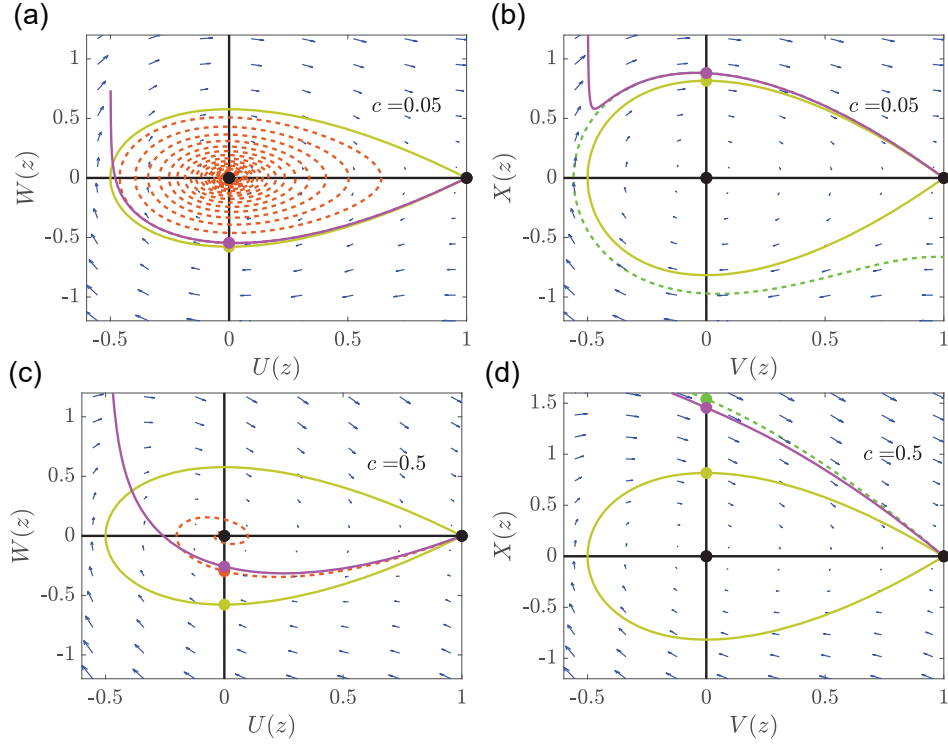
Figure 5.10: Perturbation solution for the phase plane trajectories when
$c > 0$**,** $D = 0.5$ **and** $\lambda = 1$**.** Phase planes in (a)-(b), (c)-(d) compare numerical phase plane trajectories and perturbation solutions for $c = 0.05$ and $c = 0.5$, respectively. Numerical estimates of the $U(W)$ and $V(X)$ trajectories are shown in dashed red and dashed green respectively. The $\mathcal{O}(1)$ and $\mathcal{O}(c)$ perturbation solutions are shown in solid yellow and solid purple, respectively. Equilibrium points are shown with black discs. The points at which the various solutions intersect the vertical axis are shown with various coloured discs corresponding to the colour of the particular trajectory.
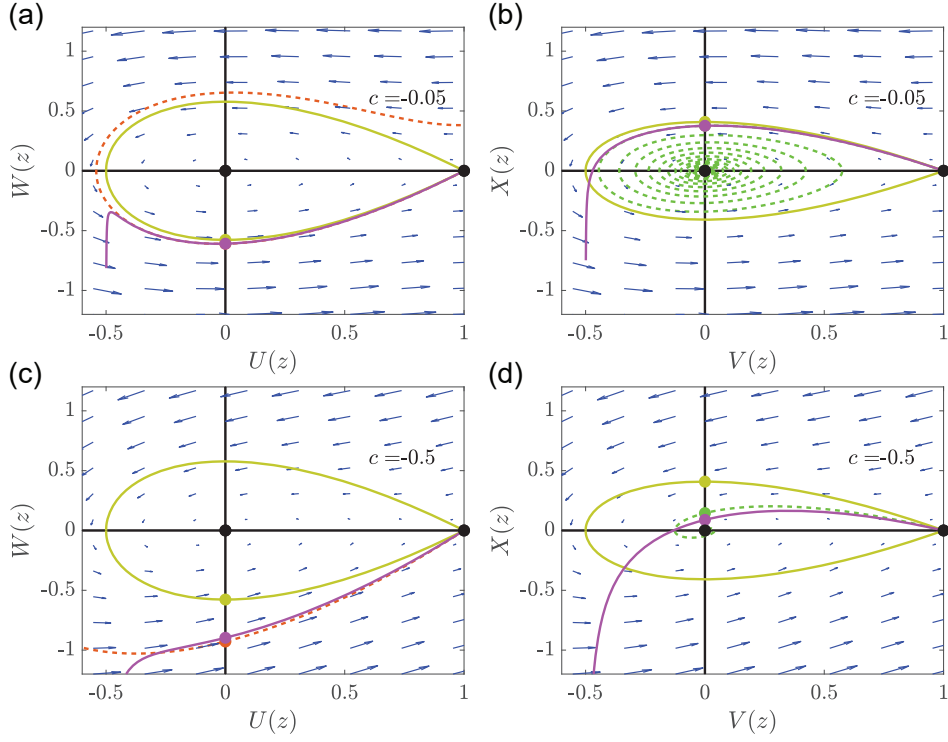
160

Figure 5.11: Perturbation solution for the phase plane trajectories when $c < 0$, $D = 0.5$ and $\lambda = 1$. Phase planes in (a)-(b), (c)-(d) compare numerical phase plane trajectories and perturbation solutions for $c = -0.05$ and $c = -0.5$, respectively. Numerical estimates of the $U(W)$ and $V(X)$ trajectories are shown in dashed red and dashed green respectively. The $\mathcal{O}(1)$ and $\mathcal{O}(c)$ perturbation solutions are shown in solid yellow and solid purple, respectively. Equilibrium points are shown with black discs. The points at which the various solutions intersect the vertical axis are shown with various coloured discs corresponding to the colour of the particular trajectory.

Figure 5.12: Perturbation solution for the phase plane trajectories when $c > 0$, $D = 2$ and $\lambda = 1$. Phase planes in (a)-(b), (c)-(d) compare numerical phase plane trajectories and perturbation solutions for $c = 0.05$ and $c = 0.5$, respectively. Numerical estimates of the $U(W)$ and $V(X)$ trajectories are shown in dashed red and dashed green respectively. The $\mathcal{O}(1)$ and $\mathcal{O}(c)$ perturbation solutions are shown in solid yellow and solid purple, respectively. Equilibrium points are shown with black discs. The points at which the various solutions intersect the vertical axis are shown with various coloured discs corresponding to the colour of the particular trajectory.
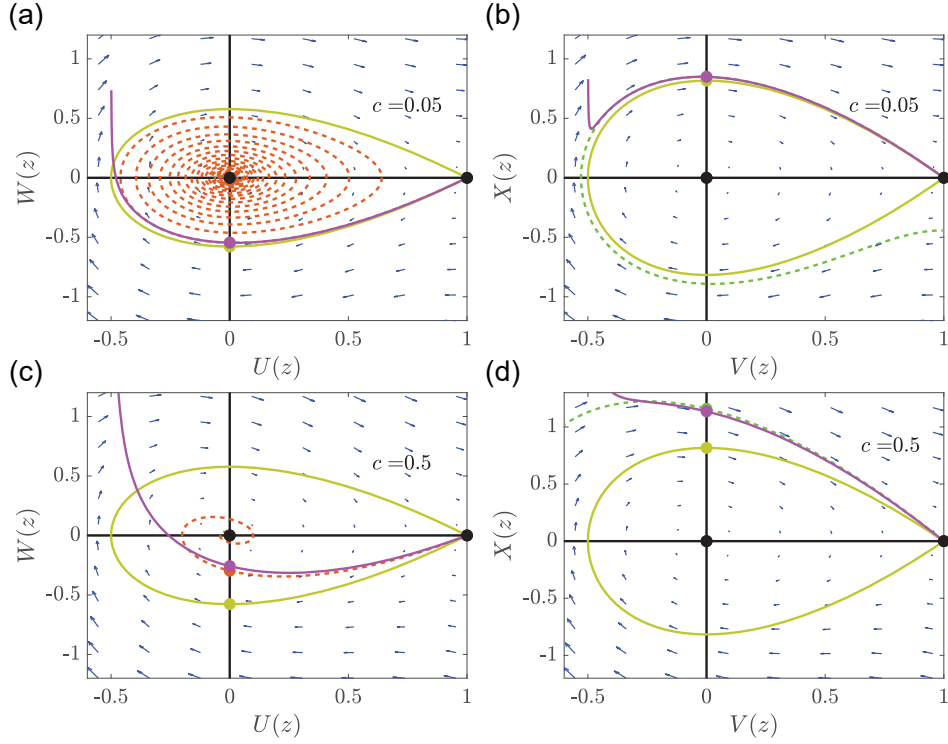
Figure 5.13: Perturbation solution for the phase plane trajectories when $c < 0$, $D = 2$ and $\lambda = 1$. Phase planes in (a)-(b), (c)-(d) compare numerical phase plane trajectories and perturbation solutions for $c = -0.05$ and $c = -0.5$, respectively. Numerical estimates of the $U(W)$ and $V(X)$ trajectories are shown in dashed red and dashed green respectively. The $\mathcal{O}(1)$ and $\mathcal{O}(c)$ perturbation solutions are shown in solid yellow and solid purple, respectively. Equilibrium points are shown with black discs. The points at which the various solutions intersect the vertical axis are shown with various coloured discs corresponding to the colour of the particular trajectory.
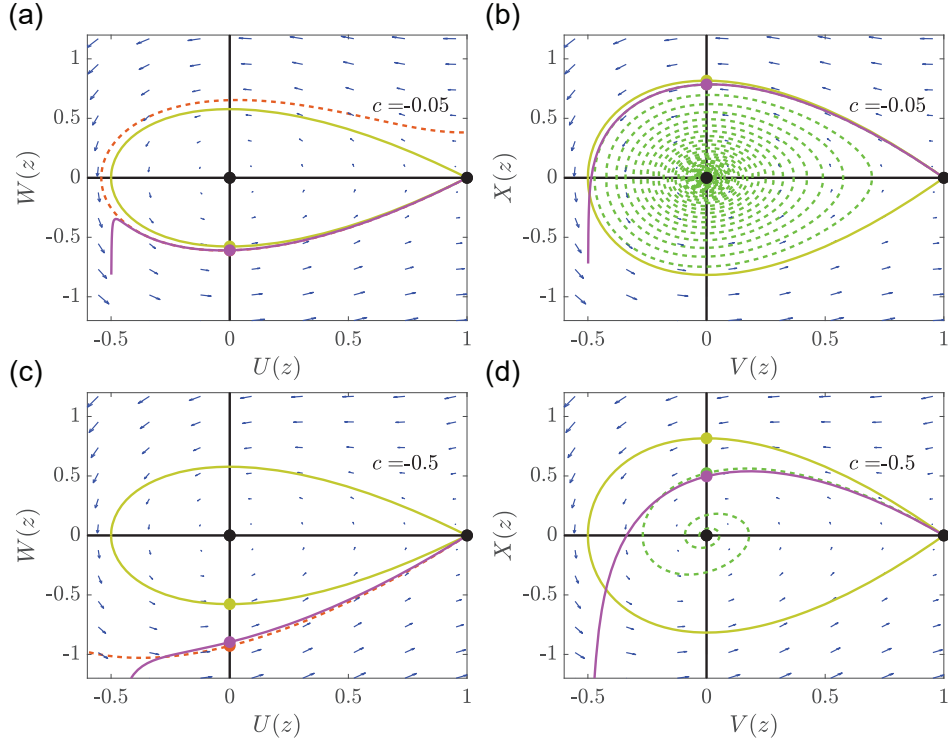
163

Figure 5.14: Perturbation solution for the phase plane trajectories when $c > 0$, $D = 1$ and $\lambda = 0.5$. Phase planes in (a)-(b), (c)-(d) compare numerical phase plane trajectories and perturbation solutions for $c = 0.05$ and $c = 0.5$, respectively. Numerical estimates of the $U(W)$ and $V(X)$ trajectories are shown in dashed red and dashed green respectively. The $\mathcal{O}(1)$ and $\mathcal{O}(c)$ perturbation solutions are shown in solid yellow and solid purple, respectively. Equilibrium points are shown with black discs. The points at which the various solutions intersect the vertical axis are shown with various coloured discs corresponding to the colour of the particular trajectory.

Figure 5.15: Perturbation solution for the phase plane trajectories when $c < 0$, $D = 1$ and $\lambda = 0.5$. Phase planes in (a)-(b), (c)-(d) compare numerical phase plane trajectories and perturbation solutions for $c = -0.05$ and $c = -0.5$, respectively. Numerical estimates of the $U(W)$ and $V(X)$ trajectories are shown in dashed red and dashed green respectively. The $\mathcal{O}(1)$ and $\mathcal{O}(c)$ perturbation solutions are shown in solid yellow and solid purple, respectively. Equilibrium points are shown with black discs. The points at which the various solutions intersect the vertical axis are shown with various coloured discs corresponding to the colour of the particular trajectory.

Figure 5.16: Perturbation solution for the phase plane trajectories when $c > 0$, $D = 1$ and $\lambda = 2$. Phase planes in (a)-(b), (c)-(d) compare numerical phase plane trajectories and perturbation solutions for $c = 0.05$ and $c = 0.5$, respectively. Numerical estimates of the $U(W)$ and $V(X)$ trajectories are shown in dashed red and dashed green respectively. The $\mathcal{O}(1)$ and $\mathcal{O}(c)$ perturbation solutions are shown in solid yellow and solid purple, respectively. Equilibrium points are shown with black discs. The points at which the various solutions intersect the vertical axis are shown with various coloured discs corresponding to the colour of the particular trajectory.

Figure 5.17: Perturbation solution for the phase plane trajectories when $c < 0$, $D = 1$ and $\lambda = 2$. Phase planes in (a)-(b), (c)-(d) compare numerical phase plane trajectories and perturbation solutions for $c = -0.05$ and $c = -0.5$, respectively. Numerical estimates of the $U(W)$ and $V(X)$ trajectories are shown in dashed red and dashed green respectively. The $\mathcal{O}(1)$ and $\mathcal{O}(c)$ perturbation solutions are shown in solid yellow and solid purple, respectively. Equilibrium points are shown with black discs. The points at which the various solutions intersect the vertical axis are shown with various coloured discs corresponding to the colour of the particular trajectory.

### 5.5.2.2 Additional perturbation results presented in the z coordinate
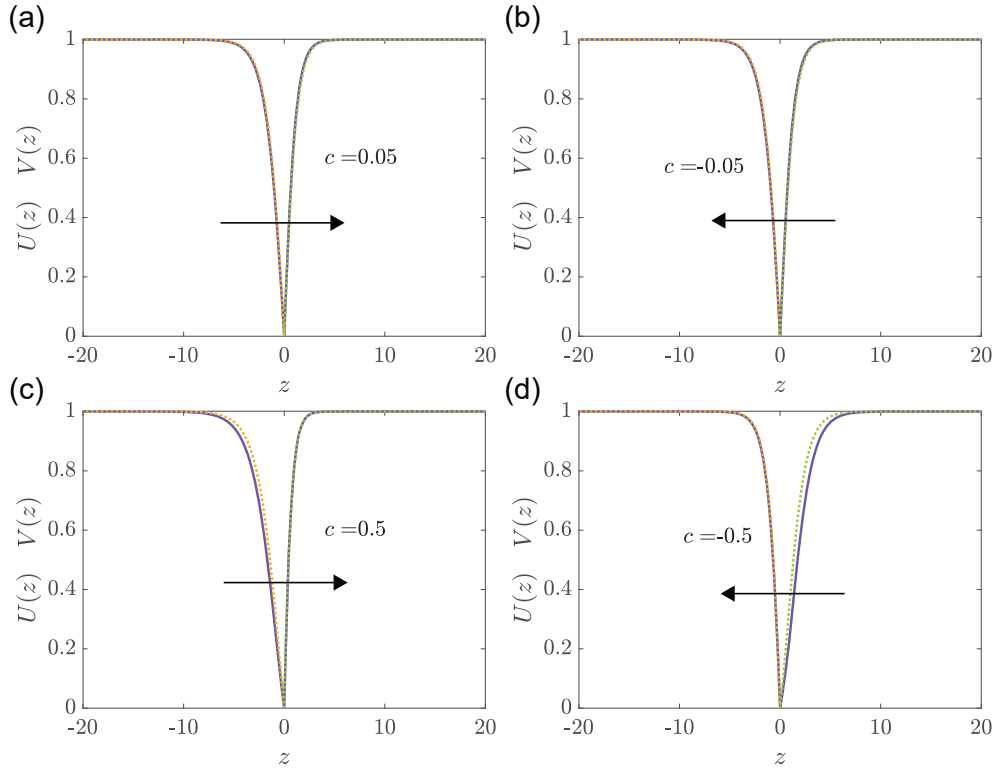
Figure 5.18: Perturbation solution for the shape of the travelling waves when $D = 0.5$ and $\lambda = 1$. Comparison of $U(z)$ and $V(z)$ from the $\mathcal{O}(c)$ perturbation solution (purple solid) with numerical estimates obtained by solving Equations (16)-(17) that are shifted so that $U(0) = V(0) = 0$. Numerical estimates of $U(z)$ and $V(z)$ are shown in dashed yellow and dashed green lines, respectively. Results are shown for: (a) $c = 0.05$; (b) $c = -0.05$; (c) $c = 0.5$; and (d) $c = -0.5$.
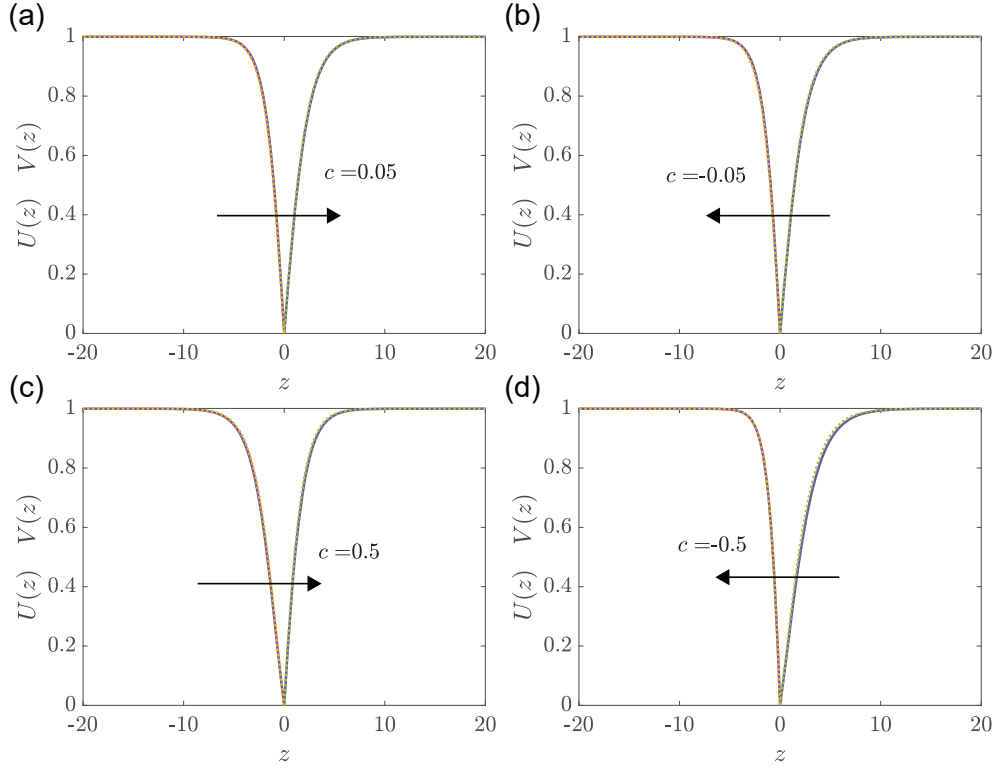
Figure 5.19: Perturbation solution for the shape of the travelling waves when $D = 2$ and $\lambda = 1$. Comparison of $U(z)$ and $V(z)$ from the $\mathcal{O}(c)$ perturbation solution (purple solid) with numerical estimates obtained by solving Equations (16)-(17) that are shifted so that $U(0) = V(0) = 0$. Numerical estimates of $U(z)$ and $V(z)$ are shown in dashed yellow and dashed green lines, respectively. Results are shown for: (a) $c = 0.05$; (b) $c = -0.05$; (c) $c = 0.5$; and (d) $c = -0.5$.
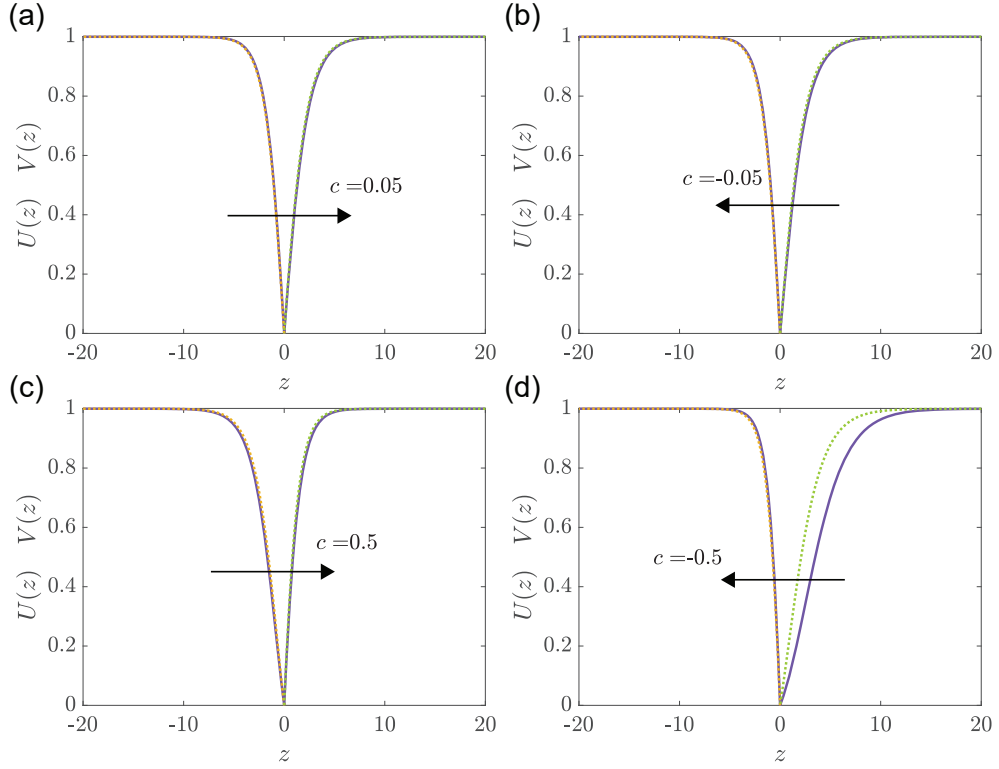
Figure 5.20: Perturbation solution for the shape of the travelling waves when $D = 1$ and $\lambda = 0.5$. Comparison of $U(z)$ and $V(z)$ from the $\mathcal{O}(c)$ perturbation solution (purple solid) with numerical estimates obtained by solving Equations (16)-(17) that are shifted so that $U(0) = V(0) = 0$. Numerical estimates of $U(z)$ and $V(z)$ are shown in dashed yellow and dashed green lines, respectively. Results are shown for: (a) $c = 0.05$; (b) $c = -0.05$; (c) $c = 0.5$; and (d) $c = -0.5$.
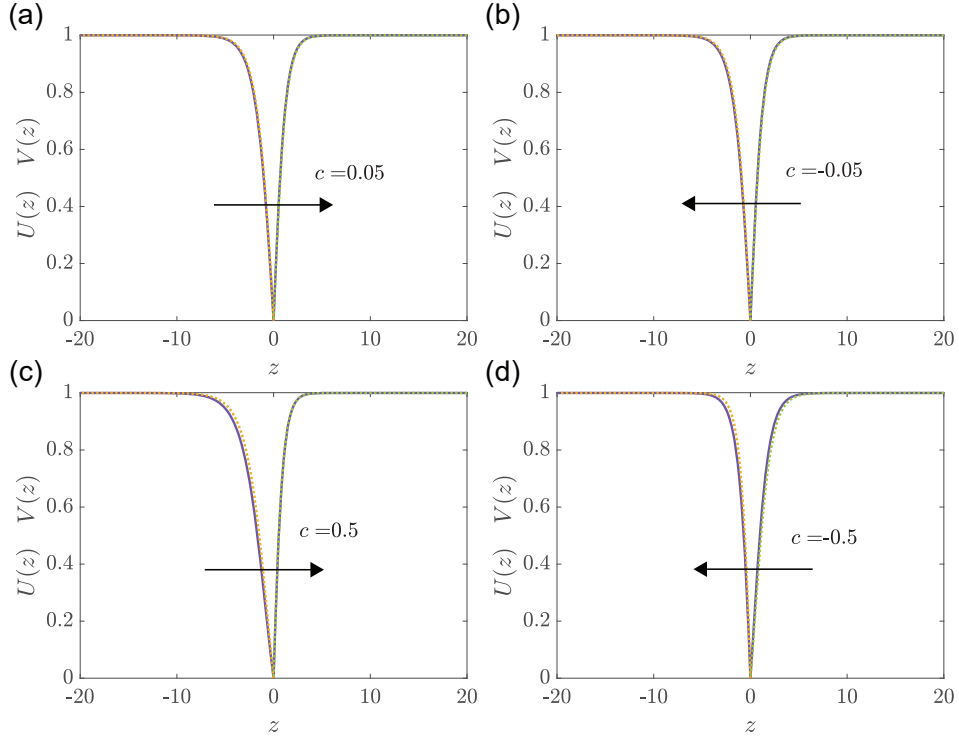
Figure 5.21: Perturbation solution for the shape of the travelling waves when $D = 1$ and $\lambda = 2$. Comparison of $U(z)$ and $V(z)$ from the $\mathcal{O}(c)$ perturbation solution (purple solid) with numerical estimates obtained by solving Equations (16)-(17) that are shifted so that $U(0) = V(0) = 0$. Numerical estimates of $U(z)$ and $V(z)$ are shown in dashed yellow and dashed green lines, respectively. Results are shown for: (a) $c = 0.05$; (b) $c = -0.05$; (c) $c = 0.5$; and (d) $c = -0.5$.

Chapter 6

Travelling wave analysis of cellular invasion into surrounding tissues

Statement of Contribution of Co-Authors for Thesis by Published Paper

The following is the suggested format for the required declaration provided at the start of any thesis chapter which includes a co-authored publication.

The authors listed below have certified that:

1. they meet the criteria for authorship and that they have participated in the conception, execution, or interpretation, of at least that part of the publication in their field of expertise;
2. they take public responsibility for their part of the publication, except for the responsible author who accepts overall responsibility for the publication;
3. there are no other authors of the publication according to these criteria;
4. potential conflicts of interest have been disclosed to (a) granting bodies, (b) the editor or publisher of journals or other publications, and (c) the head of the responsible academic unit, and
5. they agree to the use of the publication in the student's thesis and its publication on the QUT's ePrints site consistent with any limitations set by publisher requirements.

In the case of this chapter 6:

Please state the publication title and date of publication or status:
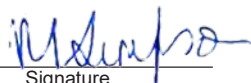
El-Hachem M, McCue SW, Simpson MJ, 2021. Travelling wave analysis of cellular invasion into surrounding tissues. *Physica D: Nonlinear Phenomena* **428**, 133026. Published on December 2021.

Contributor	Statement of contribution*
Maud El-Hachem *Maud Ellh* 15/11/2021	Conceived and designed the study, performed all numerical and symbolic calculations, drafted the article, and gave final approval for publication.
Scott W McCue	Conceived and designed the study, gave final approval for publication.
Matthew J Simpson	Conceived and designed the study, gave final approval for publication.

Principal Supervisor Confirmation

I have sighted email or other correspondence from all Co-authors confirming their certifying authorship.
(If the Co-authors are not able to sign the form please forward their email or other correspondence confirming the certifying authorship to the GRC).

Professor Matthew Simpson   *[signature]*   16/11/2021
Name   Signature   Date

6.1 Abstract

Single-species reaction-diffusion equations, such as the Fisher-KPP and Porous-Fisher equations, support travelling wave solutions that are often interpreted as simple mathematical models of biological invasion. Such travelling wave solutions are thought to play a role in various applications including development, wound healing and malignant invasion. One criticism of these single-species equations is that they do not explicitly describe interactions between the invading population and the surrounding environment. In this work we study a reaction-diffusion equation that describes malignant invasion which has been used to interpret experimental measurements describing the invasion of malignant melanoma cells into surrounding human skin tissues [Browning et al. 2019]. This model explicitly describes how the population of cancer cells degrade the surrounding tissues, thereby creating free space into which the cancer cells migrate and proliferate to form an invasion wave of malignant tissue that is coupled to a retreating wave of skin tissue. We analyse travelling wave solutions of this model using a combination of numerical simulation, phase plane analysis and perturbation techniques. Our analysis shows that the travelling wave solutions involve a range of very interesting properties that resemble certain well-established features of both the Fisher-KPP and Porous-Fisher equations, as well as a range of novel properties that can be thought of as extensions of these well-studied single-species equations. Matlab software to implement all calculations is available at GitHub.

6.2 Introduction

The Fisher-KPP model [Fisher 1937, Kolmogorov et al. 1937] is a very simple prototype mathematical model of biological invasion that describes the spatial and temporal evolution of a population where individuals undergo migration by linear diffusion and proliferation via logistic growth. The Porous-Fisher model is an extension of the Fisher-KPP model where the linear diffusion term is generalised to a nonlinear degenerate diffusion term with a power law diffusivity [Murray 2002, Sánchez Garduño and Maini 1994, Witelski 1994, Witelski 1995, McCue et al. 2019]. Such single species partial differential equation (PDE) models have had a major influence on the study

of biological populations, both in cell biology [Sherratt and Murray 1990, Maini et al. 2004a, Swanson et al. 2003, Sengers et al. 2007, Gerlee and Nerlander 2012, Jin et al. 2020, Lagergren et al. 2021a, Largergren et al. 2021b] and in ecology [Skellam 1951, Lewis and Kareiva 1993, Holmes et al. 1994, Shigesada et al. 1951, Steel et al. 1998, Kot 2003, Levin et al. 2003], since these models gives rise to travelling wave solutions that are thought to represent invasion waves [Canosa 1973, Murray 2002]. While influential, an obvious limitation of such single species models is that they focus on the properties of the invading population alone, and neglect interactions between the invasive population and the environment, or interactions between the invasive population and other populations of interest. To overcome this limitation, a number of extended multi-species models that explicitly describe coupling between the invasive population and the environment or other populations of interest have been proposed, for example [Painter and Sherratt 2003, Byrne and Preziosi 2003, Byrne et al. 2003]. While this work is focused on models of invasion in the context of cancer biology, similar continuum mathematical models are developed and deployed in the ecology literature [Amor and Fort 2010, Amor et al. 2017, Fort 2012, Muller et al. 2014].
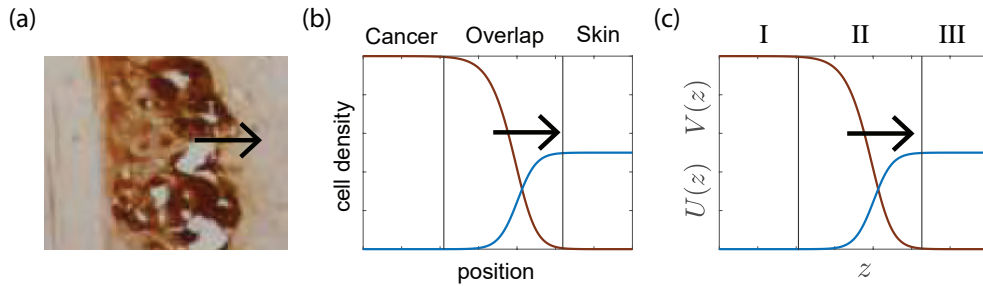
Figure 6.1: Experimental motivation and mathematical model schematic.
(a) Cross section through human skin tissues showing the invasion of melanoma cells (dark brown) into surrounding skin tissue (light brown). The direction of invasion is shown with the arrow. This image is reproduced from Haridas [Haridas 2017] with permission. (b) Schematic solution of a one-dimensional PDE model showing the spatial distribution of cell populations during invasion. To be consistent with the experiments in (a), the density of cancer cells (brown) moves in the direction of the black arrow, and this invasion is associated with the retreat of the density of surrounding skin tissues (blue). The overlap region involves a visually-distinct region where both populations are present at the same location. (c) Shows travelling wave solutions for the cancer cell density $U(z)$, and the skin cell density $V(z)$, on $-\infty < z < \infty$. In this work we will refer to three different regions of the domain: (i) region I is the *invaded* region where $U(z) \to 1$ and $V(z) \to 0$ as $z \to -\infty$; (ii) region II is the *overlap* region where $U(z) > 0$ and $V(z) > 0$; and, (iii) region III is the uninvaded region where $U(z) \to 0$ and $V(z) \to \mathcal{V}$ as $z \to \infty$.

One area of research where coupled mathematical models of invasion have played an important role is in the study of cancer biology where the invasion of a population of malignant cells is tightly coupled to the degradation of surrounding tissues. The experimental image in Figure 6.1(a) shows a population of highly aggressive melanoma cells growing within and invading into human skin tissues [Haridas 2017, Haridas et al. 2018]. During these experiments, melanoma cells simultaneously migrate and proliferate to form an invading front, and this invasion is tightly coupled to the biochemical breakdown of the surrounding tissues by proteases released by the melanoma cells. From a mathematical modelling point of view, this kind of process leads to conceptual models like that shown in Figure 6.1(b) where we think of a density profile of invading cancer cells that is coupled to the retreat of a population of surrounding skin cells. In this schematic we identify three regions: *region* I is the invading region; *region* II is the overlap region; and, *region* III is the uninvaded region. Throughout this work we refer to the density of invading cells as $\hat{u}$ and the density of surrounding tissues as $\hat{v}$.

One of the first mathematical models of cellular invasion was proposed by Gatenby and Gawlinski [Gatenby and Gawlinski 1996], who present a coupled system of PDEs that described the spatial and temporal development of tumour tissue, normal tissue and excess hydrogen ion concentration. Numerical exploration and phase plane analysis suggested the formation of a pH gradient across the tumour-host interface, leading to a hypocellular interstitial gap at the tumour-host interface. This gap was then verified using both *in vitro* and *in vivo* data. A similar model of cellular migration coupled to the degradation of surrounding tissues in the context of developmental biology was later proposed by Landman and Pettet [Landman and Pettet 1998]. In this case the simpler mathematical model was solved exactly to reveal details of the coupling between the invading population and the degradation of surrounding tissues. Since these first two mathematical models were proposed and analysed in the late 1990s, a range of more detailed mathematical models have since studied to examine different aspects of cellular invasion [Perumpanani et al. 1999, Marchant et al. 2000, Smallbone et al. 2005, Landman et al. 2008, Anderson and Quaranta 2008, Astanin and Preziosi 2009, Fasano et al. 2009, Byrne 2010, Tindall et al. 2012, Holder et al. 2014, Holder and Rodrigo 2015].

Despite the fact that mathematical models of cellular invasion into surrounding tissues had been considered for over twenty years, it was not until 2019 that one of these models was first quantitatively calibrated to experimental data. In 2019, Browning and co-workers [Browning et al. 2019] examined a simplified model based on Gatenby and Gawlinski's earlier, more general modelling framework [Gatenby and Gawlinski 1996]. In this work, Browning took experimental data describing time-series measurements of melanoma invasion into human tissues (Figure 1(a)) and used a Bayesian sequential learning approach to estimate the diffusivity of the melanoma cells, the proliferation rate of the melanoma cells and the rate at which melanoma cells degraded the surrounding skin tissues [Browning et al. 2019]. This 2019 study was different to many previous mathematical studies of cellular invasion since Browning did not consider any travelling wave solutions or travelling wave analysis. In the present study we re-visit the model proposed by Browning and explore various travelling wave solutions of that model. Using a combination of numerical methods to solve the full time-dependent PDE model, phase plane analysis and perturbation methods, we reveal several novel features of the travelling wave solutions of this model. In particular we unearth many important parallels and differences between the travelling wave solutions of the invasion model and the very well-studied Fisher-KPP model. There are two aspects of our analysis that are of particular interest. First, we show that travelling wave solutions of the invasion model that involves three dimensional phase space can be approximated using the simpler Fisher-KPP phase plane. Second, we show that Browning's model of invasion leads to travelling wave solutions that are reminiscent of travelling wave solutions of a moving boundary type model [Ward and King 1997, Byrne and Chaplain 1997, Gaffney and Maini 1999].

6.3 Mathematical model and preliminary simulations

6.3.1 Browning's model of cellular invasion

In 2019, Browning and co-workers [Browning et al. 2019] proposed the following simple dimensional model to describe the invasion of melanoma cells into

surrounding skin tissue,

$$\frac{\partial \hat{u}}{\partial \hat{t}} = \hat{D}\frac{\partial}{\partial \hat{x}}\left[\left(1 - \frac{\hat{v}}{\hat{K}}\right)\frac{\partial \hat{u}}{\partial \hat{x}}\right] + \hat{\lambda}\hat{u}\left(1 - \frac{\hat{u} + \hat{v}}{\hat{K}}\right), \qquad 0 < \hat{x} < \infty, \qquad (6.1)$$

$$\frac{\partial \hat{v}}{\partial \hat{t}} = -\hat{\gamma}\hat{u}\hat{v}, \qquad\qquad\qquad\qquad 0 < \hat{x} < \infty, \qquad (6.2)$$

where $\hat{u}(\hat{x}, \hat{t}) > 0$ is the density of melanoma cells, and $\hat{v}(\hat{x}, \hat{t}) > 0$ is the density of skin cells. Throughout this work we use a circumflex to indicate dimensional parameters and variables.

Equation (6.1) governs the evolution of the cell density, and we see that the melanoma cells move according to a nonlinear diffusion term, with diffusivity $\hat{D} > 0$ [μm^2 h^{-1}]. The nonlinear diffusivity function decreases linearly with the skin density such that the diffusion of melanoma cells vanishes if the skin density reaches the carrying capacity density, $\hat{v}(\hat{x}, \hat{t}) = \hat{K} > 0$. Further, equation (6.1) specifies that the melanoma cells grow logistically, with rate $\hat{\lambda} > 0$ [h^{-1}], such that the net proliferation rate is a linearly decreasing function of the total cell density, $\hat{u}(\hat{x}, \hat{t}) + \hat{v}(\hat{x}, \hat{t})$. Equation (6.2) governs the evolution of the skin density such that melanoma cells degrade skin cells at a rate governed by $\hat{\gamma} \geq 0$ [μm^{2}cells^{-1}h^{-1}]. This two-species PDE model is a simplification of a three-species PDE extension that is fully described in the Additional Material document reported by Browning et al. [Browning et al. 2019].

Since we are interested in travelling wave solutions we pose Equations (6.1)–(6.2) on $0 < \hat{x} < \infty$, however when we generate numerical solutions we take the usual approach and examine solutions on a truncated domain, $0 < \hat{x} < \hat{L}$. For all numerical solutions, we specify no-flux boundary conditions for $\hat{u}(\hat{x}, \hat{t})$, so that $\partial \hat{u}(0, \hat{t})/\partial \hat{x} = \partial \hat{u}(\hat{L}, \hat{t})/\partial \hat{x} = 0$. Note that since Equation (6.2) does not involve any spatial derivatives, we do not need to specify any boundary conditions for $\hat{v}(\hat{x}, \hat{t})$. The choice of $\hat{L}$ is unimportant provided that it is chosen to be sufficiently large [El-Hachem et al. 2021a]. Matlab software on GitHub can be used to explore different choices of $\hat{L}$ for all problems that we consider, and full details of the numerical algorithms are outlined in the Appendix.

The mathematical model is nondimensionalised by introducing $u = \hat{u}/\hat{K}$, $v = \hat{v}/\hat{K}$, $x = \hat{x}\sqrt{\hat{\lambda}/\hat{D}}$, $t = \hat{\lambda}\hat{t}$, and $\gamma = \hat{K}\hat{\gamma}/\hat{\lambda}$, which gives

$$\frac{\partial u}{\partial t} = \frac{\partial}{\partial x}\left[(1-v)\frac{\partial u}{\partial x}\right] + u(1-u-v), \qquad 0 < x < \infty \qquad (6.3)$$

$$\frac{\partial v}{\partial t} = -\gamma u v, \qquad\qquad\qquad 0 < x < \infty, \qquad (6.4)$$

which means that the nondimensional PDE model requires the specification of just one model parameter, $\gamma \geq 0$.

For the first part of the study, we specify initial conditions such that the initial distribution of skin density is a constant, and the initial distribution of melanoma cells has compact support,

$$u(x,0) = \alpha\left[1 - H(x - \beta)\right], \qquad (6.5)$$

$$v(x,0) = \mathcal{V}, \qquad (6.6)$$

where $H(x)$ is the usual Heaviside function and $\beta > 0$ is a constant so that we have $u(x,0) = \alpha$ for $x < \beta$ and $u(x,0) = 0$ for $x > \beta$. The initial density of skin, $0 \leq \mathcal{V} \leq 1$, is set to be a constant that does not depend upon position. In summary, the non-dimensional invasion model involves one model parameter, $\gamma \geq 0$, and when we specify the initial conditions we introduce another parameter, $0 \leq \mathcal{V} \leq 1$, that we will study. In general, we interpret γ as the rate at which cancer cells degrade skin tissues, and $\mathcal{V}$ is the density of skin tissues in the far field ahead of the invading front. Most of our analysis will be concerned with how varying γ and $\mathcal{V}$ influence the shape and speed of the resulting travelling wave solutions. Setting the upper value of $\mathcal{V} = 1$ implies that the maximum density of skin cells is the same as the maximum density of cancer cells. This assumption may be biologically realistic as skin cells and cancer cells are often similar in shape and size [Haridas 2017].

The first part of this work focuses on travelling wave solutions of the invasion model that arise from initial conditions given by Equations (6.5)–(6.6) since this form of initial condition with compact support is biologically-relevant [Haridas 2017, Haridas et al. 2018]. Once we have characterised this first family of travelling wave solutions, we will then study another family of travelling wave solutions where $u(x,0)$ decays to zero as $x \to \infty$. While this

second family of travelling wave solutions are mathematically interesting, the fact that these travelling wave solutions that arise from exponentially decaying initial conditions means that this second set of travelling waves are more difficult to interpret biologically since this kind of special initial condition is not relevant in practice. To study this second family of travelling wave solutions we work with an initial condition given by

$$u(x,0) = \begin{cases} \alpha, & x < \beta, \\ \alpha \exp[-a(x-\beta)], & x \geq \beta, \end{cases} \tag{6.7}$$

$$v(x,0) = \mathcal{V}, \tag{6.8}$$

where $a > 0$ is a constant that we vary so that we can understand how travelling wave solutions of the invasion model depend upon the initial spatial decay of u.

One of the main themes of our work is to highlight surprising similarities and differences between the invasion model (6.3)–(6.4) and some well-studied single-species models. For example, setting $\mathcal{V} = 0$ reduces the invasion model to the well-known Fisher-KPP model [Fisher 1937, Kolmogorov et al. 1937, Murray 2002],

$$\frac{\partial u}{\partial t} = \frac{\partial^2 u}{\partial x^2} + u(1-u). \tag{6.9}$$

As we pointed out in Section 6.2, the Fisher-KPP model is a simplified mathematical model of biological invasion that ignores any interaction between the invading population and the local environment. In this work, we study travelling wave solutions of Equations (6.3)–(6.4) and we find there are important similarities and differences with travelling wave solutions of the Fisher-KPP model, so it is useful to explicitly note the connection between these two mathematical models at the outset. There are also interesting, but perhaps less obvious, connections between the invasion model and the Porous-Fisher model [Murray 2002, Sánchez Garduño and Maini 1994, Witelski 1994, Witelski 1995, McCue et al. 2019],

$$\frac{\partial u}{\partial t} = \frac{\partial}{\partial x}\left[u\frac{\partial u}{\partial x}\right] + u(1-u). \tag{6.10}$$

We will now begin to explore these relationships.

6.3.2 Time-dependant solutions

We begin our study of the invasion model by computationally exploring various travelling wave solutions of (6.3)–(6.4) to develop an intuitive understanding of how their shape and speed depend upon the choice of γ and $\mathcal{V}$. Full details of the numerical method used to solve the PDE model is given in the Appendix, and MATLAB software to study time-dependent solutions of (6.3)–(6.4) is available on GitHub.

In the first instance we focus on travelling wave solutions with initial condition given by Equations (6.5)–(6.6) so that the initial cancer density profile has compact support. Time-dependent solutions are shown in Figure 6.2(a)–(d) for $\mathcal{V} = 0.5$ for a range of γ. Additional time-dependent solutions are shown in Figure 6.2(e)–(h) for $\mathcal{V} = 1$ for a range of γ. In all cases we see that the time-dependent solutions of Equations (6.3)–(6.4) evolve to constant-speed travelling wave solutions, and in each subfigure we give a numerical estimate of the travelling wave speed, c.
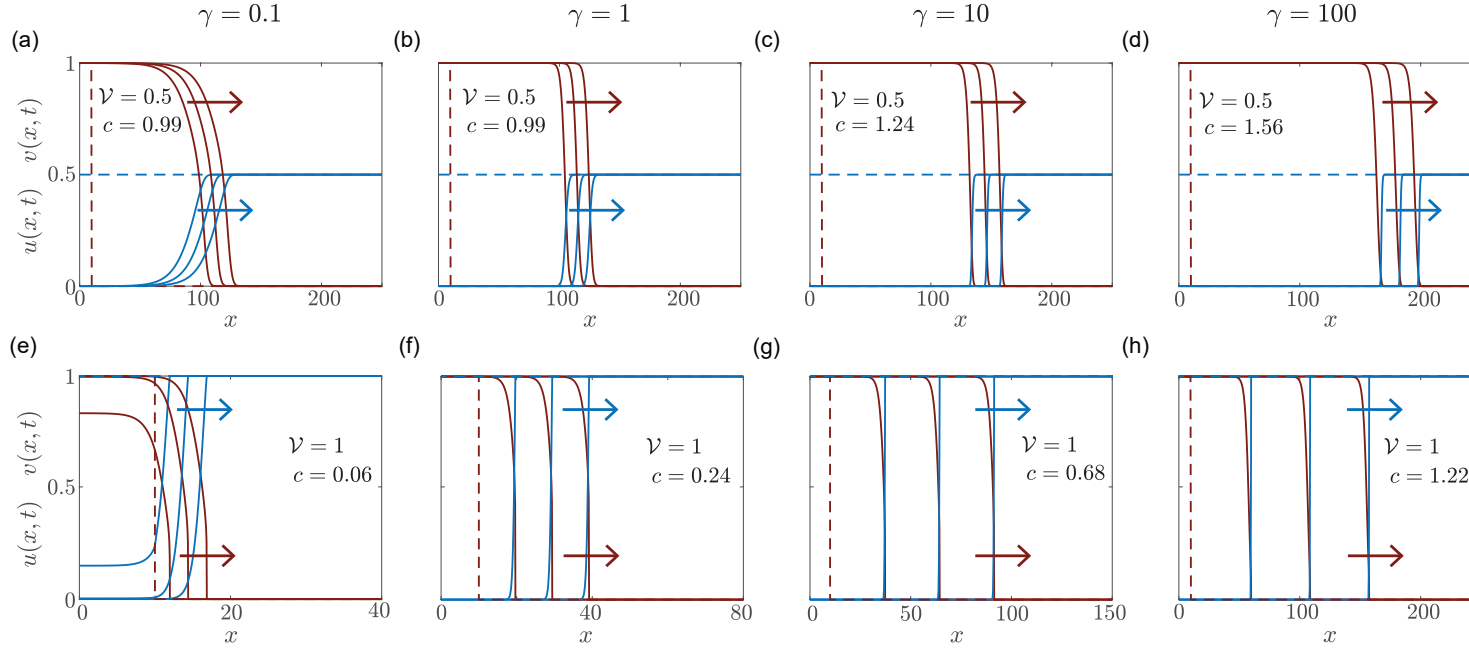
Figure 6.2: Time-dependant solutions of Equations (6.3)–(6.4) for different γ and $\mathcal{V}$. Results in (a)–(d) correspond to $\mathcal{V} = 0.5$, while results in (e)–(h) correspond to $\mathcal{V} = 1$. Solutions in (a) and (e), (b) and (f), (c) and (g), and (d) and (h) correspond to $\gamma = 0.1, 1, 10$ and 100, respectively. Density profiles for $u(x,t)$ are shown in brown, and profiles of $v(x,t)$ are shown in blue. Results in (a)–(d) are shown at $t = 0, 100, 110, 120$ and the invasion front moves in the positive x-direction, whereas results in (e)–(h) are shown at $t = 0, 40, 80, 120$. For each solution we show the initial condition in dashed lines, and the subsequent solutions for $t > 0$ are shown in solid lines. All PDE solutions are obtained using $\Delta x = \Delta t = 1 \times 10^{-3}$.

Results in Figure 6.2(a)–(d) highlight several interesting properties of these travelling wave solutions, especially when we compare them with the well-known travelling wave solutions of the Fisher-KPP model (6.9). Each travelling wave solution in Figure 6.2(a)–(d) leads to profiles for $u(x, t)$ that are smooth since they are differentiable everywhere on the domain, and they do not have compact support since they decay to zero in the far field, $u(x, t) \to 0^+$ as $x \to \infty$. In this regard, the shape of these travelling wave solutions is similar to those for the Fisher-KPP model [Murray 2002, Canosa 1973]. However, in the invasion model we see that the speed of the travelling wave depends upon the decay rate, γ, in a rather unexpected way. First, results in Figure 6.2(a)–(b) suggest that for sufficiently small $\gamma < \gamma_c$, the speed of the travelling wave is independent of γ. Second, results in Figure 6.2(c)–(d) indicate that for sufficiently large $\gamma > \gamma_c$, the travelling wave speed increases with γ. It is of interest to note that all values of γ considered in Figure 6.2(a)–(d) lead to travelling wave solutions with $c < 2$. This is very different to travelling wave solutions of the dimensionless Fisher-KPP model that evolve from initial conditions with compact support since these travelling waves always have $c = 2$ [Murray 2002, Canosa 1973].

Results in Figure 6.2(e)–(h) for $\mathcal{V} = 1$ show that the invasion model leads to non-smooth travelling wave solutions that have compact support. These solutions are non-smooth since they contain a well defined front and $u(x, t)$ is not differentiable at the location of the front, $x = X$ (sometimes called the contact point). These solutions have compact support since $u(x, t) > 0$ for $x < X$, and $u(x, t) = 0$ for $x \geq X$. From this point of view, the shape of the travelling wave solutions in Figure 6.2(e)–(h) is reminiscent of the shape of travelling wave solutions of the Porous-Fisher model (6.10). Comparing the speeds of the travelling wave solutions in Figure 6.2(e)–(h) indicates that c increases with γ but, unlike the results in Figure 6.2(a)–(d), we do not see any evidence that the wave speed is independent of γ for any of the values considered. As with Figure 6.2(a)–(d), all values of γ explored in Figure 6.2(e)–(h) lead to travelling wave solutions with $c < 2$, which, again, is very different to travelling wave solutions of the dimensionless Fisher-KPP equation (6.9).

In summary, preliminary numerical explorations reveal that we obtain smooth travelling wave solutions of the invasion model for $\mathcal{V} < 1$ whereas
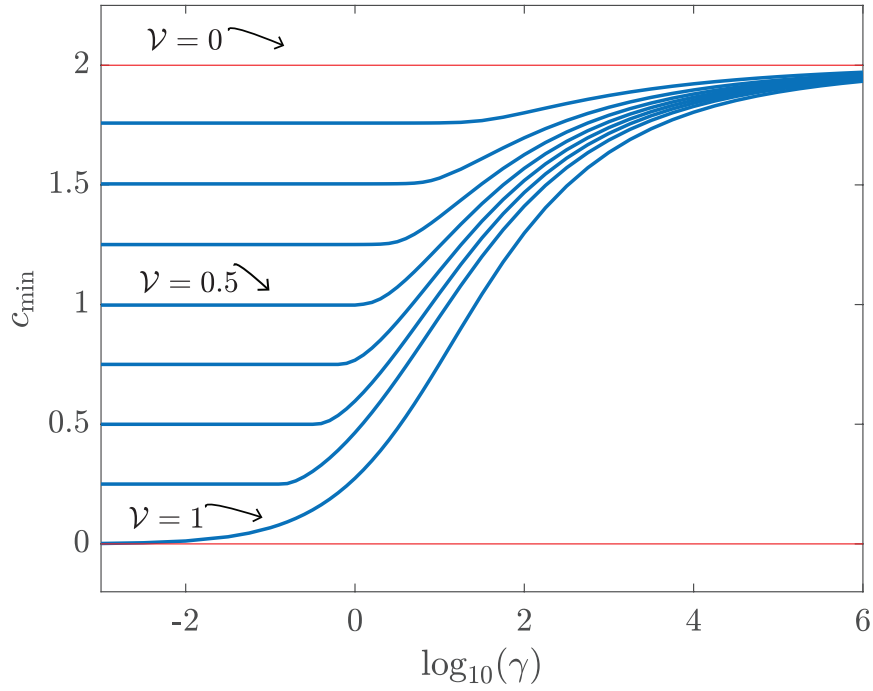
Figure 6.3: Relationship between the minimum travelling wave speed $c_{\min}$, γ and $\mathcal{V}$. Numerical estimates of $c_{\min}$ are obtained by solving Equations (6.3)–(6.4) with initial conditions (6.5)–(6.6), with $\alpha = 1$ and $\beta = 10$. Numerical solutions of the PDE model are obtained with $\Delta x = \Delta t = 1 \times 10^{-2}$, for $1 \times 10^{-3} \leq \gamma \leq 1 \times 10^{6}$ and $\mathcal{V} = 1/8, 2/8, 3/8, 4/8, 5/8, 6/8, 7/8$ and 1.

we obtain non-smooth travelling waves with compact support when $\mathcal{V} = 1$. While the former are similar in shape to the travelling wave solutions of the Fisher-KPP model and the latter are similar in shape to the travelling wave solutions of the Porous-Fisher model, the speed of the travelling waves of the invasion model are very different to the well-known bounds on travelling wave solutions of the Fisher-KPP and Porous-Fisher models. The relationship between c, γ and $\mathcal{V}$ is summarised in Figure 6.3 where we estimate the long time travelling wave speed c from a large number of simulations where $u(x, 0)$ has compact support, given by Equations (6.5)–(6.6. As we will establish later in Section 6.6, this means that these estimates of c correspond to the minimum wave speed, $c_{\min}$. Remembering that the Fisher-KPP model has a very simple minimum wave speed, $c_{\min} = 2$ [Murray 2002, Canosa 1973], here we see that the minimum wave speed for the invasion model is a relatively complicated function of $\mathcal{V}$ and γ and we will devote much of this work to understanding this relationship in different limiting cases. As noted in Section 6.3.1, setting $\mathcal{V} = 0$ means that the invasion model simplifies to the Fisher-KPP model and

so we obtain $c = c_{\min} = 2$ regardless of γ. Interestingly, for all choices of γ and $\mathcal{V} > 0$ we observe travelling wave solutions with a minimum wave speed that is less than the minimum travelling wave speed for the Fisher-KPP model, and we will return to this point later. For intermediate values of $0 < \mathcal{V} < 1$ we see that $c_{\min}$ is a decreasing function of $\mathcal{V}$, but independent of γ provided that γ is sufficiently small. In contrast for intermediate values of $0 < \mathcal{V} < 1$ we see that $c_{\min}$ increases with γ, and approaches $c_{\min} = 2$ for large γ. Finally, for $\mathcal{V} = 1$, there appears to be no positive value of γ where the wave speed is independent of γ, meaning that we have with $c_{\min} \to 0^+$ as $\gamma \to 0^+$, and $c_{\min} \to 2^-$ as $\gamma \to \infty$. The key features of the travelling wave solutions of the invasion model, and their relationship to the well-studied travelling wave solutions of the Fisher-KPP and Porous-Fisher models are summarised in Table 6.1.

Table 6.1: Comparing key features of travelling wave solutions of the invasion model with travelling wave solutions of the Fisher-KPP model and the Porous-Fisher model.

Fisher-KPP (6.9)	Porous-Fisher (6.10)	Invasion model	
		$\mathcal{V} < 1$	$\mathcal{V} = 1$
Smooth No compact support	Sharp-fronted Compact support	Smooth No compact support	Sharp-fronted Compact support
$c_{\min} = 2$	$c_{\min} = \dfrac{1}{\sqrt{2}}$	$c_{\min} = 2(1 - \mathcal{V}), \quad \gamma < \gamma_{\mathrm{c}}$ $\displaystyle\lim_{\gamma \to \infty} c_{\min} = 2^-$	$\displaystyle\lim_{\gamma \to 0^+} c_{\min} = 0^+$ $\displaystyle\lim_{\gamma \to \infty} c_{\min} = 2^-$

6.4 Travelling wave analysis

We now attempt to formalise these preliminary numerical results by analysing travelling wave solutions of Equations (6.3)–(6.4) in the phase-space.

6.4.1 Preamble

To study the travelling wave solutions of Equations (6.3)–(6.4) we seek solutions in the form $u(x,t) = U(z)$ and $V(x,t) = V(z)$, where z is the usual travelling wave variable, $z = x - ct$. Re-writing the governing equations in terms of the travelling wave coordinate gives

$$\frac{\mathrm{d}}{\mathrm{d}z}\left[(1-V)\frac{\mathrm{d}U}{\mathrm{d}z}\right] + c\frac{\mathrm{d}U}{\mathrm{d}z} + U(1 - U - V) = 0, \quad -\infty < z < \infty, \quad (6.11)$$

$$c\frac{\mathrm{d}V}{\mathrm{d}z} - \gamma UV = 0, \quad -\infty < z < \infty, \quad (6.12)$$

with boundary conditions $U(z) \to 1$ and $V(z) \to 0$ as $z \to -\infty$, and $U(z) \to 0$ and $V(z) \to \mathcal{V}$ as $z \to \infty$. At this point it is worthwhile to observe that if the solution $U(z)$ is known, we can solve Equation (6.12) to give,

$$V(z) = \mathcal{V}\exp\left\{\left(\frac{\gamma}{c}\int_z^\infty U(\xi)\,\mathrm{d}\xi\right)\right\}. \quad (6.13)$$

To study this boundary value problem in phase space we re-write Equations (6.11)–(6.12) as a first order system

$$\frac{\mathrm{d}U}{\mathrm{d}z} = W, \quad (6.14)$$

$$\frac{\mathrm{d}V}{\mathrm{d}z} = \frac{\gamma UV}{c}, \quad (6.15)$$

$$\frac{\mathrm{d}W}{\mathrm{d}z} = \frac{1}{(1-V)}\left[\frac{\gamma UVW}{c} - cW - U(1 - U - V)\right], \quad (6.16)$$

with boundary conditions $U \to 1, V \to 0$ and $W \to 0$ as $z \to -\infty$, and $U \to 0, V \to \mathcal{V}$ and $W \to 0$ as $z \to \infty$. There are two equilibrium points of this dynamical system: (i) $(\bar{U}, \bar{V}, \bar{W}) = (1, 0, 0)$ corresponding to $z \to -\infty$; and, (ii) $(\bar{U}, \bar{V}, \bar{W}) = (0, \mathcal{V}, 0)$ for $\mathcal{V} < 1$, corresponding to $z \to \infty$. Before we proceed it is useful to remark that the dynamical system is singular when $\mathcal{V} = 1$, whereas there is no such singularity for $\mathcal{V} < 1$. Therefore, just like we did in Section 6.3, we will treat these two cases separately.

6.4.2 $\mathcal{V} < 1$

Setting $\mathcal{V} < 1$ leads to smooth travelling wave solutions that we will analyse in phase space. Since the travelling wave solutions are smooth the phase plane is non-singular. We refer to this as a traditional phase space since we do not have to consider any nonsingularities, and we proceed by analysing Equations (6.14)–(6.16) directly. Eigenvalues of the linearised dynamical system about $(\bar{U}, \bar{V}, \bar{W}) = (1, 0, 0)$ are given by the roots of $\lambda^3 - (\gamma - c^2)\lambda^2/c - (1+\gamma)\lambda + \gamma/c = 0$, so that we have $\lambda_1 = \gamma/c$ and $\lambda_{2,3} = (-c \pm \sqrt{c^2 + 4})/2)$. These eigenvalues are all real with $\lambda_1 > 0$, $\lambda_2 > 0$ and $\lambda_3 < 0$, which means that the equilibrium point $(\bar{U}, \bar{V}, \bar{W}) = (1, 0, 0)$ is a three-dimensional saddle for all values of c and γ [Wiggins 2003]. Note that the analogous phase plane analysis for travelling wave solutions of the Fisher-KPP model (6.9) involves an equilibrium point corresponding to the invaded region that is a two-dimensional saddle for all c [Murray 2002].

Eigenvalues of the linearised dynamical system about $(\bar{U}, \bar{V}, \bar{W}) = (0, \mathcal{V}, 0)$ are given by the roots of $\lambda^3 + c\lambda^2/(\mathcal{V} - 1) + \lambda = 0$, so that we have $\lambda_1 = 0$ and $\lambda_{2,3} = (-c \pm \sqrt{c^2 - 4(1 - \mathcal{V})^2})/[2(1 - \mathcal{V})]$. In this case λ_2 and λ_3 are real negative numbers when $c \geq 2(1 - \mathcal{V})$, whereas they are complex conjugates when $c < 2(1 - \mathcal{V})$. This means that the equilibrium point associated with the uninvaded region is a non-hyperbolic stable node when $c \geq 2(1 - \mathcal{V})$ and a non-hyperbolic stable spiral when $c < 2(1 - \mathcal{V})$. Since we are interested in travelling waves with $U(z) > 0$, this condition defines a minimum wave speed, $c_{\min} = 2(1 - \mathcal{V})$. Again, note that the analogous phase plane analysis of the Fisher-KPP model also involves the equilibrium point corresponding to the uninvaded region bifurcating from a stable node to a stable spiral, and this defines an analogous minimum wave speed, $c_{\min} = 2$ [Murray 2002].

The phase space analysis leading to a minimum wave speed condition, $c_{\min} = 2(1 - \mathcal{V})$ is consistent with our numerical results in Figure 6.3 computed with initial conditions with compact support. In particular, for sufficiently small $\gamma < \gamma_c$ we have travelling wave solutions that move with the minimum wave speed, $c_{\min} = 2(1 - \mathcal{V})$, and this speed is independent of γ. For large $\gamma > \gamma_c$ our numerical results lead to travelling wave solutions with $c > c_{\min} = 2(1 - \mathcal{V})$, which is again consistent with the phase space analysis. Unfortunately, this analysis provides no insight into the behaviour of the wave speed for

sufficiently large γ, nor the critical value, γ_c, where the wave speed dependence upon γ changes. Alternatively, simply set $\gamma = 0$ in Equations (6.3)–(6.4) uncouples the system. Seeking travelling wave solutions of this uncoupled system leads to Fisher-KPP-like phase plane analysis, giving $c_{\min} = 2(1 - \mathcal{V})$ which corroborates our previous result. Unfortunately, this simpler approach provides no insight when $\gamma > 0$.

Biologically, setting $\mathcal{V} < 1$ corresponds to the situation where the density of the skin tissue ahead of the invading front of is lower than the carrying capacity of the invading population. Intuitively, we might anticipate that the speed of the invading front would decrease with $\mathcal{V}$ and increase with γ. While the first of these intuitive expectations is consistent with our analysis and numerical observations, the second point highlights the value of our mathematical analysis and numerical explorations since our finding that the minimum wave speed is independent of γ, for sufficiently small $\gamma < \gamma_c$, is not at all obvious. The implication of this finding is that interventions seeking to reduce the decay rate to zero would not stop the invasion since $c_{\min} > 0$ when $\gamma = 0$.

6.4.3 $\mathcal{V} = 1$

Setting $\mathcal{V} = 1$ leads to nonsmooth travelling wave solutions and a singularity in Equations (6.14)–(6.16). We proceed by defining a new independent variable ζ , $(1-V)\mathrm{d}(\cdot)/\mathrm{d}z = \mathrm{d}(\cdot)/\mathrm{d}\zeta$ [Murray 2002], so that the desingularised dynamical system is given by

$$\frac{\mathrm{d}U}{\mathrm{d}\zeta} = W(1 - V), \tag{6.17}$$

$$\frac{\mathrm{d}V}{\mathrm{d}\zeta} = \left(\frac{\gamma U V}{c}\right)(1 - V), \tag{6.18}$$

$$\frac{\mathrm{d}W}{\mathrm{d}\zeta} = \left(\frac{\gamma U V - c^2}{c}\right) W - U(1 - U - V), \tag{6.19}$$

with boundary conditions $U \to 1, W \to 0$ and $V \to 0$ as $\zeta \to -\infty$, and $U \to 0, W \to 0$ and $V \to \mathcal{V}$ as $\zeta \to \infty$. Similar to before, given $U(\zeta)$, the solution for $V(\zeta)$ can be written as

$$V(\zeta) = \frac{1}{A \exp\left\{\left(-\dfrac{\gamma}{c} \displaystyle\int_{\zeta}^{\infty} U(\eta)\, \mathrm{d}\eta\right)\right\} + 1}, \tag{6.20}$$

where A is an integration constant.

Eigenvalues of the linearised dynamical system around $(\bar{U}, \bar{V}, \bar{W}) = (1, 0, 0)$ are roots of $\lambda^3 - (\gamma - c^2)\lambda^2/c - (1 + \gamma)\lambda + \gamma/c = 0$, leading to $\lambda_1 = \gamma/c$, $\lambda_{2,3} = (-c \pm \sqrt{c^2 + 4})/2)$. This means that λ_2 and λ_3 are real numbers with opposite sign, and so $(\bar{U}, \bar{V}, \bar{W}) = (1, 0, 0)$ is a saddle. The eigenvalues of the linearised dynamical system around $(\bar{U}, \bar{V}, \bar{W}) = (0, 1, 0)$ are roots of $c\lambda^2 + \lambda^3 = 0$, leading to $\lambda_1 = -c$, $\lambda_2 = \lambda_3 = 0$, which means that the uninvaded equilibrium point is always a degenerate stable node. Unlike the previous case where $\mathcal{V} < 1$, here there is no restriction on a minimum wave speed to ensure $U(\zeta) > 0$. One way of interpreting this result is that $c_{\min} = 0$ which is consistent with the numerical results in Figure 6.3 where we have $c > c_{\min} = 0$ when $\mathcal{V} = 1$.

Biologically, setting $\mathcal{V} = 1$ corresponds to the situation where the density of the skin tissue ahead of the invading front is identical to the carrying capacity of the invading population. In this situation we see that $c_{\min} \to 0^+$ as $\gamma \to 0^+$, such that $\gamma_c = 0$ and there is no interval of γ for which the minimum wave speed is independent of γ. The implication of this finding is that interventions seeking to reduce the decay rate to $\gamma = 0$ would eventually stop the invasion since $c_{\min} \to 0^+$ as $\gamma \to 0^+$.

6.5 Limiting cases

As we pointed out in Section 6.3.1, we are primarily interested in understanding how travelling wave solutions of the invasion model (6.3)–(6.4) depend upon choices of γ and $\mathcal{V}$. We will start by considering limits of fast and slow decay, $\gamma \gg 1$ and $\gamma \ll 1$, respectively, and consider differences between $\mathcal{V} = 1$ and $\mathcal{V} < 1$ as appropriate.

6.5.1 Fast decay: $\gamma \gg 1$

Preliminary numerical results in Figure 6.2 indicate that the width of the overlap region (region II) decreases with γ. This trend is evident in Figure 6.2(a)–(d) for $\mathcal{V} < 1$ as well as in Figure 6.2(e)–(h) where $\mathcal{V} = 1$. One way to interpret this observation is that the overlap between the $U(z)$ and $V(z)$ profiles becomes negligible as γ increases.

Given our previous discussion in Section 6.3.1 where we observed that

setting $\mathcal{V} = 0$ means that the evolution equation for $u(x, t)$ simplifies to the Fisher-KPP model (6.9), we anticipate that the solution of the dynamical system associated with travelling wave solutions of the invasion model for $\gamma \gg 1$ can be approximated by the solution of the dynamical system associated with travelling wave solutions of the Fisher-KPP model,

$$\frac{\mathrm{d}^2 U}{\mathrm{d}z^2} + c\frac{\mathrm{d}U}{\mathrm{d}z} + U(1 - U) = 0, \tag{6.21}$$

with boundary conditions $U \to 1$ as $z \to -\infty$, and $U \to 0$ as $z \to \infty$. In the usual way, this second-order boundary value problem can be re-written in terms of a first order system

$$\frac{\mathrm{d}U}{\mathrm{d}z} = W, \tag{6.22}$$

$$\frac{\mathrm{d}W}{\mathrm{d}z} = -cW - U(1 - U), \tag{6.23}$$

with boundary conditions $U \to 1$ and $W \to 0$ as $z \to -\infty$, and $U \to 0$ and $W \to 0$ as $z \to -\infty$. There are two equilibrium points: (i) $(\bar{U}, \bar{W}) = (1, 0)$ that is associated with the invaded region; and, (ii) $(\bar{U}, \bar{W}) = (0, 0)$ that is associated with the uninvaded region.
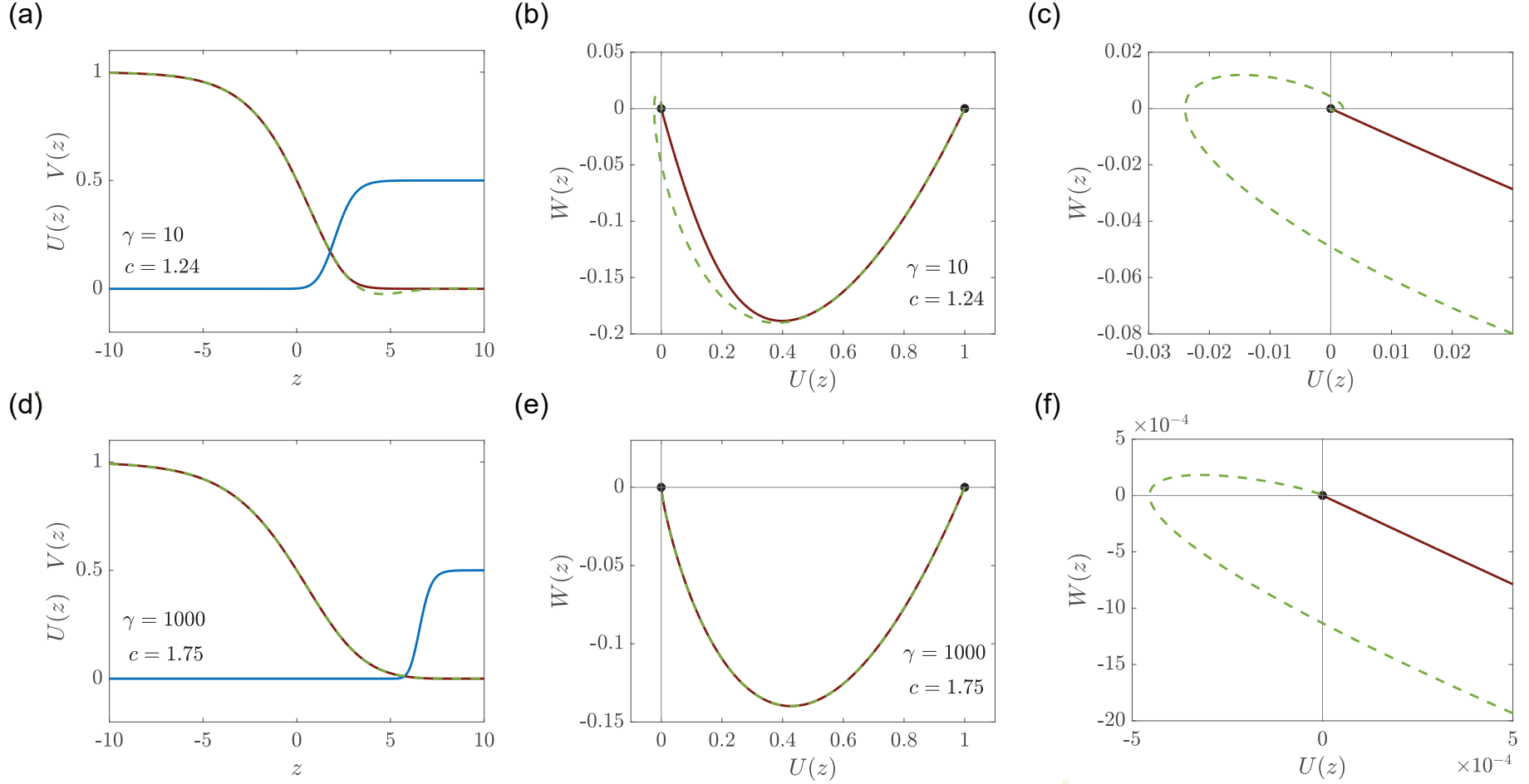
Figure 6.4: Travelling wave solutions of the invasion model with $\gamma \gg 1$ and $\mathcal{V} < 1$. (a) and (d) show late-time numerical solutions of Equations (6.3)–(6.4) with $\gamma = 10$ and $\gamma = 1000$, respectively. The solution for $U(z)$ is shown in solid brown and the solution for $V(z)$ is shown in solid blue. The approximate solution for $U(z)$ obtained from the Fisher-KPP phase plane is shown in dashed green. (b) and (c) show a projection of the (U, V, W) phase space for the invasion model projected onto the (U, W) plane together with the projection of the three-dimensional heteroclinic orbit in solid brown. The trajectory from Fisher-KPP phase plane is shown in dashed green. (c) and (f) show magnified regions near the origin in (b) and (e), respectively.

In this section we demonstrate a relationship between the three-dimensional dynamical system and phase space for the invasion model with the far simpler two-dimensional dynamical system and phase plane for the simpler Fisher-KPP model. To motivate this we compare various solutions for $\gamma = 10$ and 1000 with $\mathcal{V} = 0.5$ in Figure 6.4, and a separate set of comparisons are made for $\gamma = 10$ and 1000 with $\mathcal{V} = 1$ in Figure 6.5.

Results in Figure 6.4(a) and (d) show the long-time numerical solutions of the invasion model (6.3)–(6.4) with $\gamma = 10$ and $\gamma = 1000$, respectively. Comparing the shapes of these two travelling wave solutions confirms that the width of region II decreases with γ. In particular, the travelling wave profile in Figure 6.4(d) confirms that the overlap between the invading cancer density and the retreating skin density is barely noticeable at this scale. These travelling wave profiles in Figure 6.4(a) and (d) are first generated and plotted in the three-dimensional (U, V, W) phase space, and a projection of this phase space and the trajectory is plotted in the (U, W) plane. This projection looks like a two-dimensional heteroclinic orbit between $(\bar{U}, \bar{W}) = (1, 0)$ and $(\bar{U}, \bar{W}) = (0, 0)$. To make the connection with the simpler Fisher-KPP model explicit, we superimpose a numerical trajectory obtained from the Fisher-KPP phase plane (6.22)–(6.23) for the appropriate value of c obtained from the long-time numerical solutions of (6.3)–(6.4). In both cases we see that the projection of the trajectory associated with the invasion model and the trajectory associated with the simpler Fisher-KPP model compare very well, particularly in Figure 6.4(e) where $\gamma = 1000$. The main discrepancy between the trajectories is near the origin. Additional comparisons in Figure 6.4(c) and (f) to show details of the trajectories near the origin where the differences are clear. Indeed, in both cases we see that the trajectory for the simpler Fisher-KPP model spirals into the origin, whereas the trajectory for the invasion model does not [Murray 2002].

Overall, the results in Figure 6.4 reveal a novel application of the well-known phase plane for travelling wave solutions of the Fisher-KPP model since we show that trajectories in this phase plane provide a good approximation to projections of the three-dimensional trajectories associated with travelling wave solutions of the more complicated invasion model (6.3)–(6.4). This comparison is mathematically interesting since standard phase plane

analysis of travelling wave solutions to the Fisher-KPP model are limited to $c \geq 2$, given, the heteroclinic trajectories for $c < 2$ are disregarded on physical grounds [Murray 2002], but here we find that these trajectories provide a good approximation for the shape of travelling wave solutions to the more complicated invasion model. To highlight the value of this approximation, we take the (U, W) trajectory from the Fisher-KPP phase plane and plot the profile as a function of z in Figure 6.4(a) and (d), where we see that the profile obtained from the simpler Fisher-KPP model approximates the shape of travelling wave profile for the full invasion model. This approximation is particularly accurate in Figure 6.4(d) for $\gamma = 1000$. In contrast, while the Fisher-KPP approximation in Figure 6.4(a) is quite reasonable where $z < 2$, it is relatively poor in the region $2 < z < 5$ because of the more pronounced oscillation.
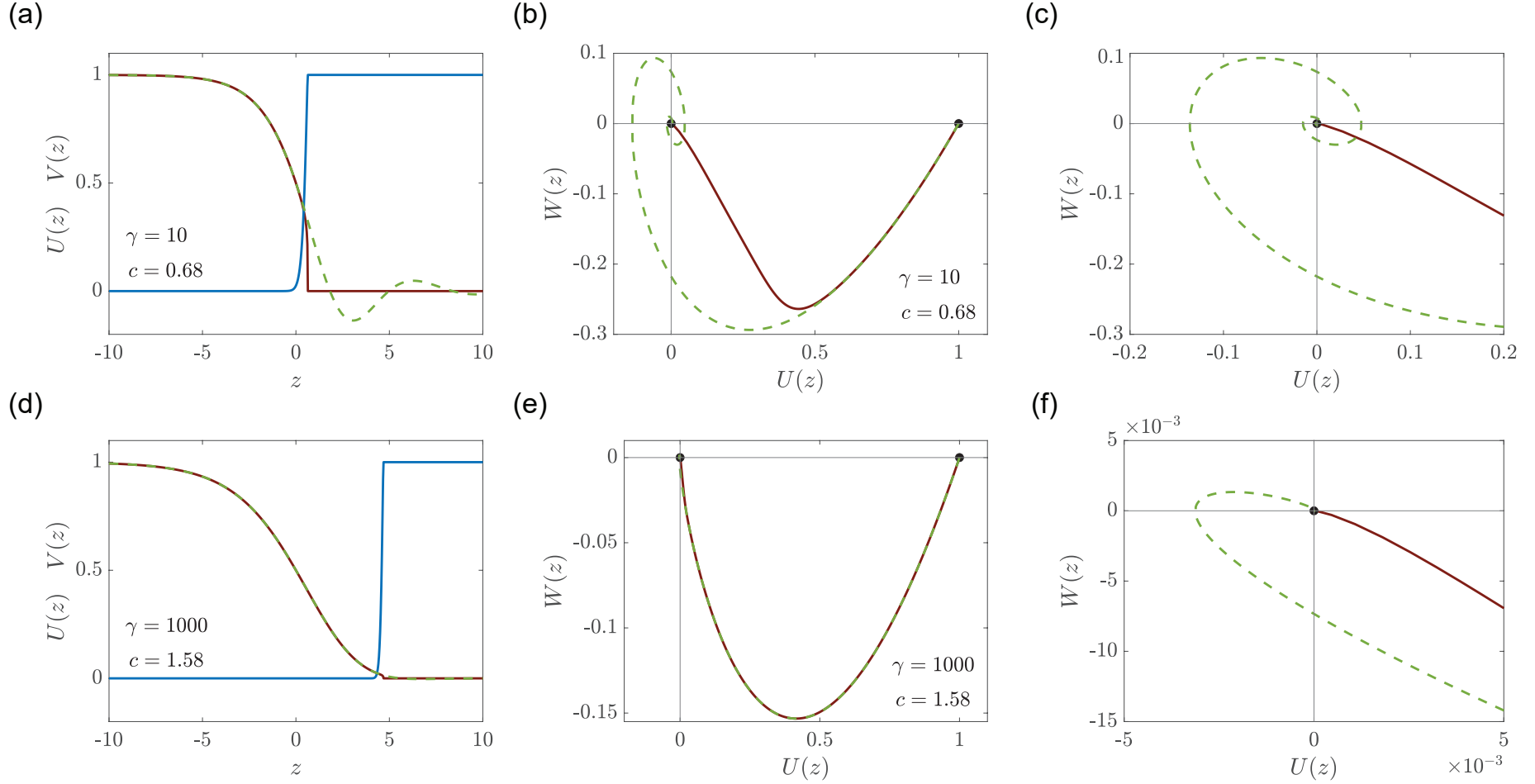
Figure 6.5: Travelling wave solutions of the invasion model with $\gamma \gg 1$ and $\mathcal{V} = 1$. (a) and (d) show late-time numerical solutions of Equations (6.3)–(6.4) with $\gamma = 10$ and $\gamma = 1000$, respectively. The solution for $U(z)$ is shown in solid brown and the solution for $V(z)$ is shown in solid blue. The approximate solution for $U(z)$ obtained from the Fisher-KPP phase plane is shown in dashed green. (b) and (c) show a projection of the (U, V, W) phase space for the invasion model projected onto the (U, W) plane together with the projection of the three-dimensional heteroclinic orbit in solid brown. The trajectory from Fisher-KPP phase plane is shown in dashed green. (c) and (f) show magnified regions near the origin in (b) and (e), respectively.

Results in Figure 6.5 are presented in the exact same format as the results in Figure 6.4, except that here we have $\mathcal{V} = 1$ so we have sharp-fronted travelling wave solutions. Comparing the shape of the travelling wave solutions in Figure 6.5(a) and (d) again confirms that the width of the overlap region decreases with γ. The projections of the three-dimensional phase space onto the (U, W) plane in Figure 6.5(b) and (e) take the form of a two-dimensional heteroclinic orbit between $(\bar{U}, \bar{W}) = (1, 0)$ and $(\bar{U}, \bar{W}) = (0, 0)$. Comparing the projections of the three-dimensional trajectory with the numerical trajectory obtained from the Fisher-KPP model (6.22)–(6.23), confirms that the simpler dynamical system provides a good approximation to the three-dimensional dynamical system when γ is large, with only small discrepancies near the origin, as shown in Figure 6.5(c) and (f). In this case, comparing the $U(z)$ profiles in Figure 6.5(d) shows that the entire shape of the travelling wave is approximated very well when $\gamma = 1000$, but we see a more clear discrepancy in Figure 6.5(a) for $\gamma = 10$ since this leads to $c = 0.68$ and more pronounced oscillations about $U = 0$ at the front of the travelling wave.

6.5.2 Slow decay: $\gamma \ll 1$

We now turn our attention to the limit where cancer cells consume skin cells very slowly, $\gamma \ll 1$. In this limit we find that it is necessary to treat the cases $\mathcal{V} < 1$ and $\mathcal{V} = 1$ separately, as we will now illustrate.

6.5.2.1 $\gamma \ll 1$ and $\mathcal{V} < 1$

Preliminary numerical results in Figure 6.2(a)–(d) show that the width of region II, the overlap region, increases as $\gamma \to 0$. To analyse this behaviour we seek a perturbation solution by treating γ as a small parameter, and it is useful to recall from Section 6.3 that when $\mathcal{V} < 1$ we have $c = c_{\min} = 2(1 - \mathcal{V})$ for $\gamma < \gamma_c$ so that we take $c = c_{\min}$ in our small γ analysis. Re-scaling the dependent variable $\tilde{z} = \gamma z$ gives

$$\gamma^2 \frac{\mathrm{d}}{\mathrm{d}\tilde{z}} \left[(1 - V) \frac{\mathrm{d}U}{\mathrm{d}\tilde{z}} \right] + c_{\min} \gamma \frac{\mathrm{d}U}{\mathrm{d}\tilde{z}} + U(1 - U - V) = 0, \quad -\infty < \tilde{z} < \infty, \quad (6.24)$$

$$c_{\min} \frac{\mathrm{d}V}{\mathrm{d}\tilde{z}} - UV = 0, \quad -\infty < \tilde{z} < \infty. \quad (6.25)$$

We now seek perturbation solutions of the form

$$U(\tilde{z}) = U_0(\tilde{z}) + \gamma U_1(\tilde{z}) + \mathcal{O}(\gamma^2), \tag{6.26}$$

$$V(\tilde{z}) = V_0(\tilde{z}) + \gamma V_1(\tilde{z}) + \mathcal{O}(\gamma^2). \tag{6.27}$$

Substituting these expansions into Equation (6.24) shows that we have $U_0(1 - U_0 - V_0) = 0$ at leading order, so that $V_0(\tilde{z}) + U_0(\tilde{z}) = 1$. The differential equations governing the terms in the perturbation solution are therefore given by

$$c_{\min}\frac{\mathrm{d}U_0}{\mathrm{d}\tilde{z}} + U_0(1 - U_0) = 0, \tag{6.28}$$

$$c_{\min}\frac{\mathrm{d}U_0}{\mathrm{d}\tilde{z}} - U_0(U_1 + V_1) = 0, \tag{6.29}$$

$$c_{\min}\frac{\mathrm{d}V_1}{\mathrm{d}\tilde{z}} - V_1(2U_0 - 1) + V_0^2 = 0. \tag{6.30}$$

with boundary conditions $U_0 \to 1, V_0 \to 0, U_1 \to 0, V_1 \to 0$ as $\tilde{z} \to -\infty$, $U_0 \to 0, V_0 \to \mathcal{V}, U_1 \to 0, V_1 \to 0$ as $\tilde{z} \to \infty$.

We solve these differential equations using the following strategy. Equation (6.28) can be solved for $U_0(\tilde{z})$ directly using separation of variables, and from this we can evaluate $V_0(\tilde{z}) = 1 - U_0(\tilde{z})$. Given the $\mathcal{O}(1)$ solutions, we simply rearrange Equation (6.29) to obtain $U_1(z)$ directly, and the solution of Equation (6.29) is obtained using an integrating factor. In summary, the solutions of these differential equations are

$$U_0(\tilde{z}) = \frac{1}{1 + \left(\dfrac{\mathcal{V}}{1 - \mathcal{V}}\right)\exp\left\{\left(\dfrac{\tilde{z}}{c_{\min}}\right)\right\}},$$

$$V_0(\tilde{z}) = \frac{1}{1 + \left(\dfrac{1 - \mathcal{V}}{\mathcal{V}}\right)\exp\left\{\left(-\dfrac{\tilde{z}}{c_{\min}}\right)\right\}}, \tag{6.31}$$

$$U_1(\tilde{z}) = \frac{-\mathcal{V}\exp\left\{\dfrac{\tilde{z}}{c_{\min}}\right\}}{\left(\mathcal{V}\left[\exp\left\{\left(\dfrac{\tilde{z}}{c_{\min}}\right)\right\} - 1\right] + 1\right)^2},$$

$$V_1(\tilde{z}) = \frac{\mathcal{V}^2\left[1 - \exp\left\{\left(\dfrac{\tilde{z}}{c_{\min}}\right)\right\}\right]\exp\left\{\left(-\dfrac{\tilde{z}}{c_{\min}}\right)\right\}}{\left[\exp\left\{\left(-\dfrac{\tilde{z}}{c_{\min}}\right)\right\}(\mathcal{V} - 1) - \mathcal{V}\right]^2}. \tag{6.32}$$

where we have evaluated the constants of integration by setting $V(0) = \mathcal{V}/2$.

Results in Figure 6.6 show long-time solutions of (6.3)–(6.4) in (a), (d) and (g) for $\gamma = 0.1, 0.01$ and 0.005, respectively. Comparing the shapes of these travelling waves confirms that the width of the overlap region increases as γ decreases. Results in Figure 6.6(b), (e) and (h) compare the shape of the late-time PDE solutions with the $\mathcal{O}(\gamma)$ perturbation solutions, and we see that the accuracy of the approximate perturbation solutions improves as γ decreases, as expected. Results in Figure 6.6(c), (f) and (i) compare the numerical solutions and the perturbation solutions within the regions highlighted by the dashed rectangles in Figure 6.6(b), (e) and (h). Again, we see the accuracy of the perturbation solution increases as γ decreases, and the perturbation solution captures the sharp transition region reasonably accurately as $\gamma \to 0$.
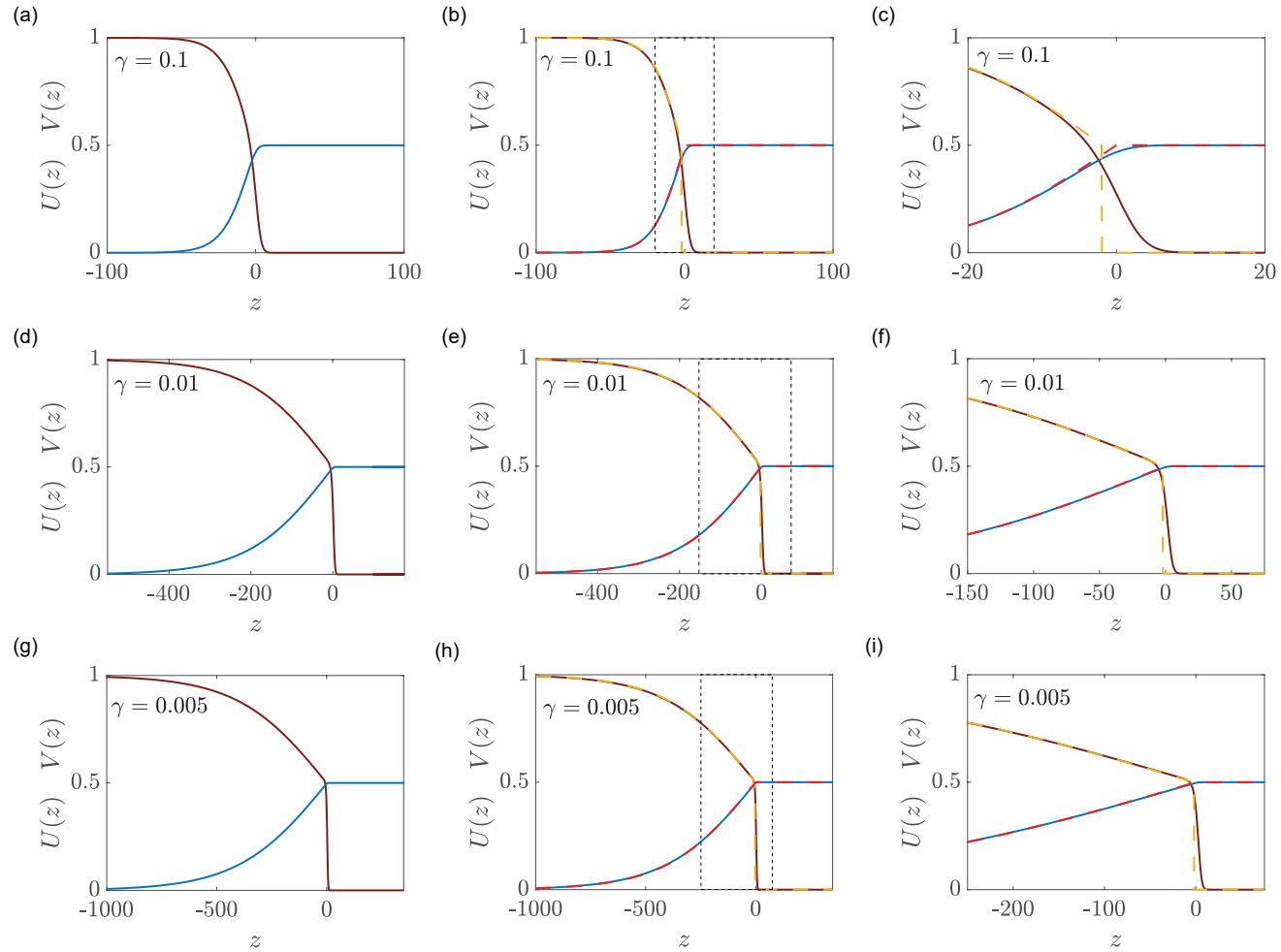
Figure 6.6: Comparison of PDE solutions with perturbation solution when $\gamma \ll 1$ and $\mathcal{V} = 0.5$. Travelling wave solutions $U(z)$ and $V(z)$ obtained from PDE with $\Delta x = \Delta t = 1 \times 10^{-2}$, $\gamma = 0.1$ in (a)–(c), $\gamma = 0.01$ in (d)–(f) and $\gamma = 0.005$ in (g)–(i) are illustrated in solid brown and solid blue for $U(z)$ and $V(z)$ respectively. $\mathcal{O}(\varepsilon)$ perturbation solution is illustrated in dashed yellow respectively for $U(z)$ and in dashed red for $V(z)$. Solutions shown in (c),(f) and (i) are magnification of region of interest in (b),(e) and (h) respectively.

6.5.3 $\gamma \ll 1$ and $\mathcal{V} = 1$

To analyse the shape of the travelling wave for $\gamma \ll 1$ with $\mathcal{V} = 1$ we consider the desingularised system

$$\frac{\mathrm{d}^2 U}{\mathrm{d}\zeta^2} + c\frac{\mathrm{d}U}{\mathrm{d}\zeta} + U(1 - V)(1 - U - V) = 0, \tag{6.33}$$

$$\frac{\mathrm{d}V}{\mathrm{d}\zeta} - \frac{\gamma UV}{c}(1 - V) = 0, \tag{6.34}$$

with boundary conditions $U \to 1, V \to 0$ as $\zeta \to -\infty$, $U \to 0, V \to 1$ as $\zeta \to \infty$.

Numerical results in Figure 6.2 show that when $\mathcal{V} = 1$ we have $c \to 0$ as $\gamma \to 0$, so we write $c = \tilde{c}\gamma$ so that $\tilde{c}$ is $\mathcal{O}(1)$. Like in the previous section, we re-scale the independent variable $\tilde{\zeta} = \gamma\zeta$ to give

$$\frac{\mathrm{d}^2 U}{\mathrm{d}\tilde{\zeta}^2} + \tilde{c}\gamma\frac{\mathrm{d}U}{\mathrm{d}\tilde{\zeta}} + U(1 - U - V)(1 - V) = 0, \qquad -\infty < \tilde{\zeta} < \infty \tag{6.35}$$

$$\tilde{c}\frac{\mathrm{d}V}{\mathrm{d}\tilde{\zeta}} - UV(1 - V) = 0, \qquad -\infty < \tilde{\zeta} < \infty, \tag{6.36}$$

with boundary conditions $U \to 1, V \to 0$ as $\tilde{\zeta} \to -\infty$, $U \to 0, V \to 1$ as $\tilde{\zeta} \to \infty$.

Seeking a perturbation solution of the form

$$U(\tilde{\zeta}) = U_0(\tilde{\zeta}) + \gamma U_1(\tilde{\zeta}) + \mathcal{O}(\gamma^2), \tag{6.37}$$

$$V(\tilde{\zeta}) = V_0(\tilde{\zeta}) + \gamma V_1(\tilde{\zeta}) + \mathcal{O}(\gamma^2), \tag{6.38}$$

leads to a system of coupled differential equations for the leading order terms,

$$\frac{\mathrm{d}^2 U_0}{\mathrm{d}\tilde{\zeta}^2} + U_0(1 - U_0 - V_0)(1 - V_0) = 0, \tag{6.39}$$

$$\tilde{c}\frac{\mathrm{d}V_0}{\mathrm{d}\tilde{\zeta}} - U_0 V_0(1 - V_0) = 0, \tag{6.40}$$

with boundary conditions $U_0 \to 1, V_0 \to 0$ as $\tilde{\zeta} \to -\infty$, $U_0 \to 0, V_0 \to 1$ as $\tilde{\zeta} \to \infty$. Unfortunately we are unable to obtain a closed-form solution of Equations (6.39)–(6.40) and we do not proceed further with this approach.

6.6 Fast travelling waves, $c > c_{\text{min}}$

Our focus so far has been on the long-time limit of the time-dependent solutions of (6.3)–(6.4) with initial conditions given by Equations (6.5)–(6.6) so that $u(x,0)$ has compact support. This leads to travelling wave solutions with the minimum wave speed, c_{min}. We now examine travelling wave solutions of the same model but with initial conditions given by Equations (6.7)–(6.8), where $a > 0$ controls the far-field decay rate of $u(x,0)$. Results in Figure 6.7 summarise the numerically-observed travelling wave speed, c, for $a = 0.1, 0.25, 0.5$ and 1, as a function of $\mathcal{V}$ and γ as indicated. Comparing these results with those in Figure 6.3 for initial conditions with compact support, we see that some general features of the relationship between c, $\mathcal{V}$ and γ are maintained, while other features are different. In general we see that c is a decreasing function of a, and that all results suggest that c is independent of γ for sufficiently small γ when $\mathcal{V} < 1$. As γ increases, we see that c increases with γ, but that the limiting value of c as $\gamma \to \infty$ depends upon the decay rate, a. Careful comparison of the results in Figure 6.7(d) for $a = 1$ shows that different choices of γ and $\mathcal{V}$ lead to the exact same travelling wave speed as in Figure 6.3 for initial conditions with compact support, which can be thought of as letting $a \to \infty$ in (6.7)–(6.8). We will now explain some of these observed trends analytically. To understand the relationship between the decay rate of the initial condition and the asymptotic wave speed, c, we examine the leading edge of the travelling wave where $u \ll 1$, giving

$$\frac{\partial \tilde{u}}{\partial t} = (1 - \tilde{v})\frac{\partial^2 \tilde{u}}{\partial x^2} + (1 - \tilde{v})\tilde{u}, \tag{6.41}$$

$$\frac{\partial \tilde{v}}{\partial t} = -\gamma \tilde{u}\tilde{v}. \tag{6.42}$$

Assuming the travelling wave solution takes the form $\tilde{u} \sim \exp[-a(x - ct)]$ for large x, substituting this into Equation (6.41) gives

$$c = (1 - \mathcal{V})\left(a + \frac{1}{a}\right). \tag{6.43}$$

This dispersion relationship is similar to the analogous result for the Fisher-KPP model [Murray 2002]. This simple relationship explains some of the observations in Figure 6.7 where we see that c is independent of γ for $\gamma <$

γ_c. Indeed, this constant speed is given by Equation (6.43). Unfortunately, this dispersion relationship does not provide any insight into the relationship between c, $\mathcal{V}$ and γ for $\gamma > \gamma_c$, nor any insight into the shape of the resulting travelling waves.
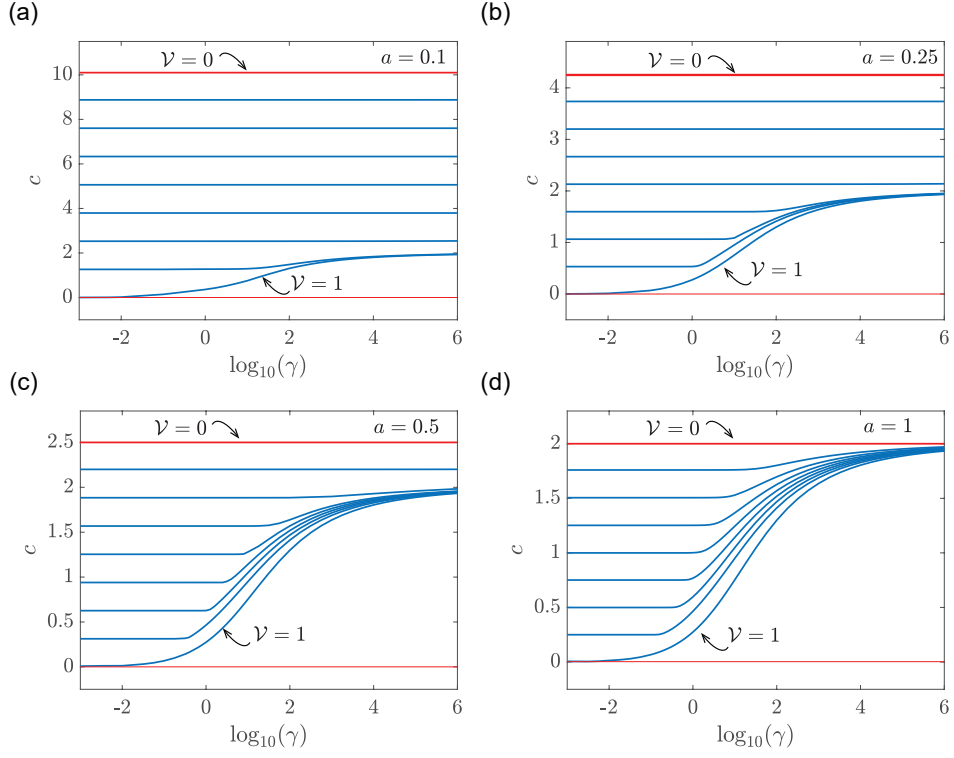
Figure 6.7: Relationship between c, γ and $\mathcal{V}$ for slowly decaying initial $u(x,0)$. Numerical estimates of c are obtained from long-time solutions of Equations (6.3)–(6.4) with the initial condition given by Equations (6.7)–(6.8). Results are presented with $\beta = 10$ and $a = 0.1, 0.25, 0.5$ and 1, as indicated. Time-dependent PDE solutions are obtained using $\Delta x = \Delta t = 1 \times 10^{-2}$, for $1 \times 10^{-3} \leq \gamma \leq 1 \times 10^{6}$ and $\mathcal{V} = 1/8, 2/8, 3/8, 4/8, 5/8, 6/8, 7/8$ and 1.

To address the shape of the travelling waves for $c > c_{\min}$ we extend the approach of Canosa [Canosa 1973] who noted that travelling wave solutions of the Fisher-KPP model become increasingly wide as $c \to \infty$. Our numerical simulation results suggest that travelling wave solutions of the invasion model behave similarly, so we explore this behaviour by re-scaling the independent variable, $\bar{z} = z/c$, giving

$$\frac{\mathrm{d}U}{\mathrm{d}\bar{z}} + \frac{1}{c^2}\frac{\mathrm{d}}{\mathrm{d}\bar{z}}\left[(1-V)\frac{\mathrm{d}U}{\mathrm{d}\bar{z}}\right] + U(1 - U - V) = 0, \quad -\infty < \bar{z} < \infty, \quad (6.44)$$

$$\frac{\mathrm{d}V}{\mathrm{d}\bar{z}} - \gamma UV = 0, \quad -\infty < \bar{z} < \infty, \quad (6.45)$$

with boundary conditions $U(\bar{z}) \to 1$ and $V(\bar{z}) \to 0$ as $\bar{z} \to -\infty$, and $U(\bar{z}) \to 0$ and $V(\bar{z}) \to \mathcal{V}$ as $\bar{z} \to \infty$. In this re-scaled coordinate we seek perturbation solutions in terms of the small parameter $\varepsilon = 1/c^2$,

$$U(\bar{z}) = U_0(\bar{z}) + \varepsilon U_1(\bar{z}) + \mathcal{O}(\varepsilon^2), \quad (6.46)$$

$$V(\bar{z}) = V_0(\bar{z}) + \varepsilon V_1(\bar{z}) + \mathcal{O}(\varepsilon^2). \quad (6.47)$$

Substituting Equations (6.46)–(6.47) into (6.44)–(6.45) leads to

$$\frac{\mathrm{d}U_0}{\mathrm{d}\bar{z}} + U_0(1 - U_0 - V_0) = 0, \quad (6.48)$$

$$\frac{\mathrm{d}V_0}{\mathrm{d}\bar{z}} - \gamma U_0 V_0 = 0, \quad (6.49)$$

with boundary conditions $U_0(\bar{z}) \to 1$ and $V_0(\bar{z}) \to 0$ as $\bar{z} \to -\infty$, $U_0(\bar{z}) \to 0$ and $V_0(\bar{z}) \to \mathcal{V}$ as $\bar{z} \to \infty$. Unlike Canosa [Canosa 1973], these differential equations for the $\mathcal{O}(1)$ terms in the perturbation solution do not have a closed-form solution. Nevertheless, we make progress by re-writing Equations (6.48)–(6.49) as

$$\frac{\mathrm{d}U_0}{\mathrm{d}V_0} = -\frac{1 - U_0 - V_0}{\gamma V_0}, \quad (6.50)$$

with $U_0(\mathcal{V}) = 0$. The solution of this problem is given by

$$U_0(V_0) = \frac{1}{(\gamma - 1)}\left[(V_0 + \gamma - 1) - (\mathcal{V} + \gamma - 1)\left(\frac{V_0}{\mathcal{V}}\right)^{\left(\frac{1}{\gamma}\right)}\right]. \quad (6.51)$$

For the special case $\gamma = 1$, this solution can be written as

$$U_0(V_0) = 1 + \left(\frac{V_0}{\mathcal{V}}\right)\left(\mathcal{V}\log\left[\frac{V_0}{\mathcal{V}}\right] - 1\right). \tag{6.52}$$
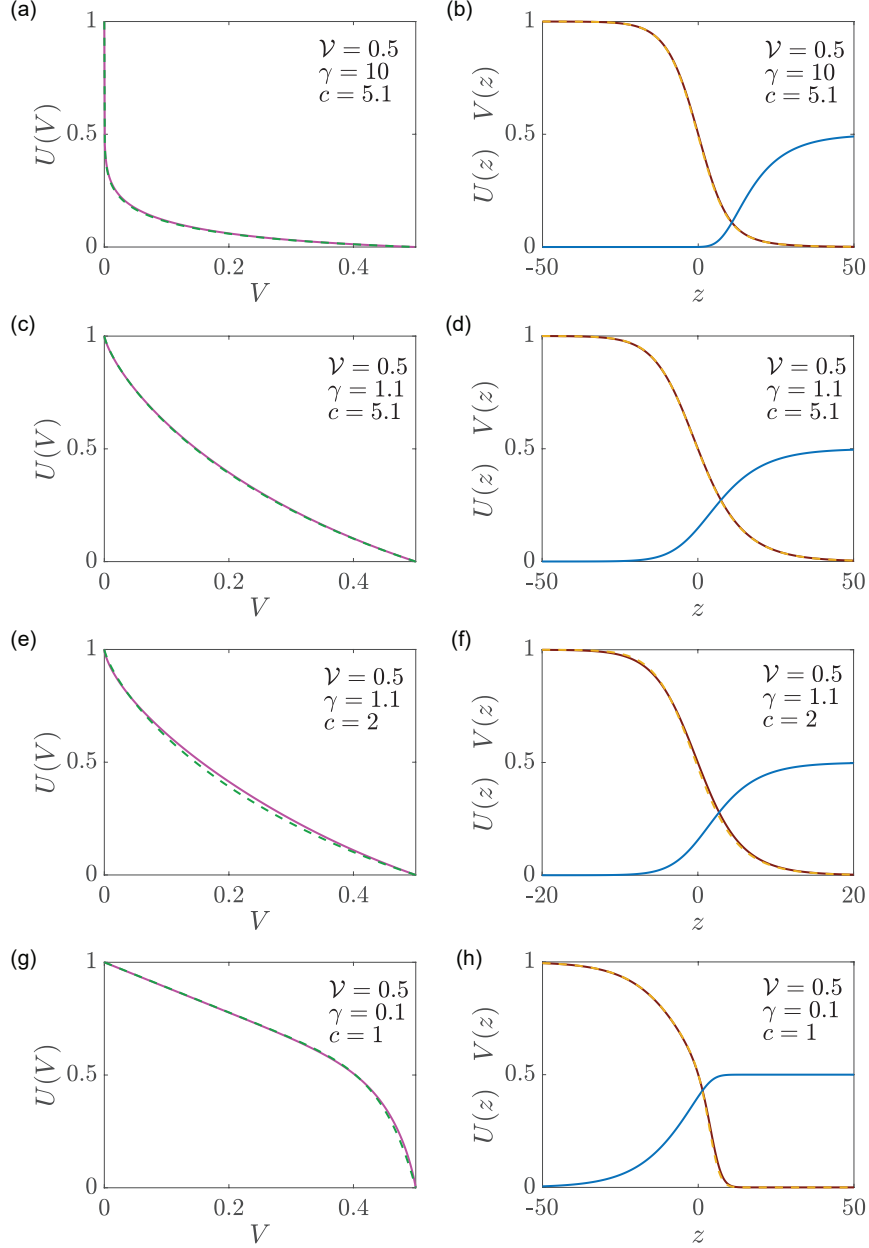
Figure 6.8: Comparison of numerical and perturbation solutions for $c \geq c_{\mathbf{cmin}}$. The $\mathcal{O}(1)$ perturbation solution shown in dashed green is compared to solution $U(V)$ from PDE shown in solid pink, in (a), (c), (e) and (g). Solutions $U(z)$ and $V(z)$ from PDE are shown in solid brown and in solid blue respectively in (b), (d), (f) and (h). Perturbation solution is shown in dashed yellow as $U(z)$ by using $V_0 = V(z)$ from PDE solution. The initial conditions (6.7)–(6.8) with $\beta = 10$ are used in (a)–(d), where $a = 0.1$, and in (e)–(f) where $a = 0.27$. The initial conditions with compact support are used in (g)–(h).

Results in Figure 6.8 compare travelling wave solutions with various c with

205

the $\mathcal{O}(1)$ perturbation solution (6.51). Results in the left column of Figure 6.8 show U as a function of V, as explicitly defined by Equation (6.51) superimposed on curves obtained from long-time numerical solutions of Equations (6.3)–(6.4) that are plotted in the same format. Results in the right column of Figure 6.8 show the late time solutions of Equations (6.3)–(6.4) plotted in the travelling wave coordinate, z, superimposed with the perturbation solution. Results in Figure 6.8(a)–(d) show perturbation results for $c = 5.1$ and different choices of γ. At this scale the perturbation solution is visually indistinguishable from the numerical solutions. Results in Figure 6.8(e)–(f) show that the perturbation solution performs well for $c = 2$, but that we can begin to see some discrepancy between the perturbation and numerical results. Interestingly, the perturbation solution in Figure 6.8(g)–(h) leads to reasonably accurate solutions for $c = 1$, despite the fact that Equation (6.51) is valid in the limit $c \to \infty$.

6.7 Conclusion and Outlook

In this work we study travelling wave solutions of a model of cellular invasion, (6.3)–(6.4), where the migration and proliferation of the invasive population is coupled to the degradation of surrounding skin tissues [Browning et al. 2019]. Time-dependent numerical solutions of the governing PDEs show that there is a complicated relationship between the travelling wave speed c and: (i) γ, the rate at which the invasive population degrades the surrounding skin tissues; and, (ii) $\mathcal{V}$, the far field density of surrounding tissues. Numerical exploration shows that long-time travelling wave solutions are smooth without compact support for $\mathcal{V} < 1$, or sharp-fronted with compact support with $\mathcal{V} = 1$. The relationship between c and the parameters in the model are partially established in this work. Numerical simulations and phase space analysis show that for initial conditions with compact support, we have $c = 2(1 - \mathcal{V})$, which is independent of γ for $\gamma < \gamma_c$. Further numerical simulations show that c increases with γ for $\gamma > \gamma_c$, with $c \to 2^-$ as $\gamma \to \infty$, but the precise details of this relationship are not revealed through standard phase space analysis. Of great interest is the fact that we always have $c < 2$ for the invasion model for initial conditions with compact support; this is very different to the standard Fisher-KPP model where $c \geq 2$. We also show that time-dependent PDE

solutions for initial conditions without compact support lead to travelling wave solutions with larger wave speed.

Analysis of the invasion model for fast decay, $\gamma \gg 1$, indicates that the width of the overlap region decreases with γ. This means that the density of the invading population becomes uncoupled from the density of the surrounding skin tissues, and suggests that the shape of the invading density profile is related to the shape of the travelling wave solution of the Fisher-KPP model. This is intriguing since the invasion model is associated with travelling waves with $c < 2$ whereas the Fisher-KPP model is associated with $c \geq 2$. Indeed, our results show that the well-known phase plane associated with travelling wave solutions of the Fisher-KPP model provides a novel approximation to the shape of the travelling wave solution of the invasion model for fast decay. This observation is mathematically interesting because standard analysis of the Fisher-KPP model disregards the phase plane for $c < 2$ [Murray 2002], whereas here we find that this previously disregarded phase plane is closely related to our model of invasion.

Overall, our analysis and numerical exploration shows how a simple mathematical model of invasion can generate biological hypotheses that can be further studied experimentally or clinically. For example, our model predicts that when the cancer population shares the exact same carrying capacity that the normal tissue and $\mathcal{V}{=}1$, the resulting invasion front is sharp and has compact support. Conversely, when the cancer population has a different carrying capacity and can grow to a larger density than the surrounding tissues the resulting invasion is smooth and without compact support. The differences between invasion fronts having compact support or being smooth is very important when considering surgical intervention, since it is always possible to completely remove an invasive population with compact support by excising tissue ahead of the invading front. In contrast, it is theoretically impossible to completely remove an invasive population by excising tissue when the front is smooth and without compact support.

Our observation that the normally-disregarded phase plane associated with travelling wave solutions of the Fisher-KPP model for $c < 2$ can be used to approximate the shape of the travelling wave solutions of the invasion model leads us to an interesting and previously unnoticed link with a very different

207

type of mathematical model of invasion, the Fisher-Stefan model [Du and Lin 2010, Du and Guo 2011, Du and Guo 2012, Du et al. 2014b, El-Hachem et al. 2019, El-Hachem et al. 2020, El-Hachem et al. 2021a, El-Hachem et al. 2021c]. The Fisher-Stefan model involves studying the Fisher-KPP model on a moving boundary, $0 < x < L(t)$. In this model the density vanishes on the moving boundary, $u(x, L(t)) = 0$, and the speed of the moving boundary is driven by a one-phase Stefan condition, $\mathrm{d}L(t)/\mathrm{d}t = -\kappa \partial u(L(t), t)/\partial x$. Here, $\kappa > 0$ is a constant that relates the speed of the moving boundary to the spatial gradient of density at the moving boundary. For both the invasion model and the Fisher-Stefan model it has been shown that time-dependent PDE solutions eventually evolve to travelling wave solutions with $c < 2$ [Du and Lin 2010, Du and Guo 2011, Du and Guo 2012, Du et al. 2014b, El-Hachem et al. 2019, El-Hachem et al. 2020, El-Hachem et al. 2021a, El-Hachem et al. 2021c] and the shape of the invading profiles in both cases is given by the normally-disregarded phase plane of the well-known Fisher-KPP model. This is very interesting because the normally-disregarded phase plane trajectories imply $U(z) < 0$ for certain intervals in z. However, here and in the Fisher-Stefan model, the profile of interest is given by a truncated trajectory in the phase plane where $U(z) > 0$.

There are many opportunities to extend the work presented in this study. There are several assumptions in the mathematical model (6.3)–(6.4), that could be relaxed or varied. Such extensions could involve working with different nonlinear diffusivity functions in (6.3), such as a power law [McCue et al. 2019]. Another extension of interest would be to explore the impact of using a different nonlinear source term in (6.3) to model the proliferation of cells [Sánchez Garduño and Maini 1994]. One of the limitations of our study is that we have not been able to arrive at a mathematical expression for γ_{c}, and it would be of great interest to arrive at some approximate expression for this critical decay rate, or to place some bound on that value. Further extensions could involve working in a different geometry since models of melanoma invasion in both two and three-dimensions with radial symmetry are of great interest for studying malignant invasion, e.g [Ward and King 1997, Ward and King 1999, Jin et al. 2021]. Finally, we acknowledge that all analysis here is limited to dealing with a continuum mathematical model only. One of the

limitations of working within a continuum framework is that it ignores the role of stochasticity. An alternative approach to study invasion is to consider individual based stochastic models, e.g. [Deutsch and Dormann 2005, Haridas et al. 2018], which explicitly describe variations between individual cells in the population.

6.8 Additional material

6.8.1 Numerical methods

We solve Equations (6.3)–(6.4) on $0 < x < L$ by uniformly discretising the domain with N mesh points, with spacing Δx. We approximate the spatial derivatives in Equations (6.3)–(6.4) using a central difference approximation, and solve the resulting system of coupled ordinary differential equation through time using an implicit Euler approximation, giving

$$\frac{u_i^{j+1} - u_i^j}{\Delta t} = \frac{1}{2\Delta x^2} \left(\left[2 - \left(v_{i+1}^{j+1} + v_i^{j+1} \right) \right] \left(u_{i+1}^{j+1} - u_i^{j+1} \right) \right.$$
$$\left. - \left[2 - \left(v_i^{j+1} + v_{i-1}^{j+1} \right) \right] \left(u_i^{j+1} - u_{i-1}^{j+1} \right) \right)$$
$$+ u_i^{j+1} \left(1 - u_i^{j+1} - v_i^{j+1} \right), \tag{6.53}$$

$$\frac{v_i^{j+1} - v_i^j}{\Delta t} = -\gamma u_i^{j+1} v_i^{j+1}, \tag{6.54}$$

where Δt is the time step, i is the spatial finite difference mesh index and j is the temporal index so that $u_i^j \approx u(x = (i-1)\Delta x, j\Delta t)$. Discretising the boundary conditions for $u(x, t)$ leads to

$$u_2^{j+1} - u_1^{j+1} = 0, \quad u_N^{j+1} - u_{N-1}^{j+1} = 0. \tag{6.55}$$

Note that there are no boundary conditions for v, so the spatial index on the discretisation for v is $i = 1, 2, \ldots, N$. This discretisation leads to a coupled system of nonlinear algebraic equations for u_i^{j+1} and v_i^{j+1}, which are solved sequentially to take advantage of the tridiagonal structure of the discretised equations. The nonlinear equations are solved using Newton-Raphson iterations that continue until the maximum change in the dependent variables falls below some tolerance ϵ in each time step. For all problems considered we always check that our choices of Δx, Δt and ϵ lead to grid-independent results. Matlab software to implement these numerical solutions is available on GitHub.

To estimate the travelling wave speed from our time-dependent PDE solutions we specify a contour value, $u(x, t) = U$. At the end of each time step in we use linear interpolation to find the value of X such that $u(X, t) = U$. At the end of each time step we have estimates of both $X(t + \Delta t)$ and $X(t)$,

allowing us to estimate the speed at which the contour moves

$$c = \frac{X(t + \Delta t) - X(t)}{\Delta t}.$$ (6.56)

Evaluating Equation (6.56) at each time step leads to a time series of estimates of c, and we find that these estimates asymptote to some positive constant value as t becomes sufficiently large. For all results presented we set $U = 0.5$, but we find that our estimates of c are independent of this choice of density contour.

To construct phase planes for Fisher-KPP equation, we solve Equation (6.21) numerically using Heun's method with a constant step size dz. Since we are interested in examining trajectories that leave the saddle $(1, 0)$ along the unstable manifold we choose the initial location on the trajectory to be on the appropriate unstable manifold and sufficiently close to $(1, 0)$. Matlab software to generate these phase planes and associated trajectories are available on GitHub.

Chapter 7

A continuum mathematical model of substrate-mediated tissue growth

Statement of Contribution of Co-Authors for
Thesis by Published Paper

The following is the suggested format for the required declaration provided at the start of any thesis chapter which includes a co-authored publication.

The authors listed below have certified that:

1. they meet the criteria for authorship and that they have participated in the conception, execution, or interpretation, of at least that part of the publication in their field of expertise;
2. they take public responsibility for their part of the publication, except for the responsible author who accepts overall responsibility for the publication;
3. there are no other authors of the publication according to these criteria;
4. potential conflicts of interest have been disclosed to (a) granting bodies, (b) the editor or publisher of journals or other publications, and (c) the head of the responsible academic unit, and
5. they agree to the use of the publication in the student's thesis and its publication on the QUT's ePrints site consistent with any limitations set by publisher requirements.

In the case of this chapter 7:

Please state the publication title and date of publication or status:
El-Hachem M, McCue SW, Simpson MJ, 2021. A continuum mathematical model of substrate-mediated tissue growth. Submitted on 15 November 2021.

Contributor	Statement of contribution*
Maud El-Hachem *Maud Elh* 15/11/2021	Conceived and designed the study, performed the mathematical analysis, performed all numerical and symbolic calculations except the 2D model, drafted the article, and gave final approval for publication.
Scott W McCue	Conceived and designed the study, performed the mathematical analysis, drafted the article, and gave final approval for publication.
Matthew J Simpson	Conceived and designed the study, performed the mathematical analysis, performed numerical calculations for the 2D model, drafted the article and gave final approval for publication.

Principal Supervisor Confirmation

7.1 Abstract

We consider a continuum mathematical model of biological tissue formation inspired by recent experiments describing thin tissue growth in 3D–printed bioscaffolds. The continuum model involves a partial differential equation describing the density of tissue, $\hat{u}(\hat{\mathbf{x}}, \hat{t})$, that is coupled to the concentration of an immobile extracellular substrate, $\hat{s}(\hat{\mathbf{x}}, \hat{t})$. Cell migration is modelled with a nonlinear diffusion term, where the diffusive flux is proportional to $\hat{s}$, while a logistic growth term models cell proliferation. The extracellular substrate $\hat{s}$ is produced by cells, and undergoes linear decay. Preliminary numerical simulations show that this mathematical model, which we call the *substrate model*, is able to reconstitute key features of recent tissue growth experiments, including the formation of sharp fronts. To provide a deeper understanding of the model we then analyse travelling wave solutions of the substrate model, showing that the model supports both sharp–fronted travelling wave solutions that move with a minimum wave speed, $c = c_{\min}$, as well as smooth–fronted travelling wave solutions that move with a faster travelling wave speed, $c > c_{\min}$. We provide a geometric interpretation that explains the difference between smooth– and sharp–fronted travelling wave solutions that is based on a slow manifold reduction of the desingularised three–dimensional phase space. In addition to exploring the nature of the smooth– and sharp–fronted travelling waves, we also develop and test a series of useful approximations that describe the shape of the travelling wave solutions in various limits. These approximations apply to both the sharp–fronted travelling wave solutions, and the smooth–fronted travelling wave solutions. Software to implement all calculations is available at GitHub.

7.2 Introduction

Over the last decade, tissue engineering has been revolutionised through the use of 3D printing technologies that produce 3D bioscaffolds upon which *in vitro* tissues can be grown in biologically realistic geometries [Ambrosi et al. 2019, Dzobo et al. 2018]. *In vitro* tissues grown on 3D scaffolds are more reproducible and more biologically realistic than tissues grown in traditional two–dimensional tissue culture [Lanaro et al. 2021]. The experimental images in Figure 7.1(a) show the evolution of thin 3D tissues that are produced by seeding a 3D–printed scaffold with osteoblast precursor cells [Buenzli et al. 2020, Browning et al. 2021]. In this experiment, cells are seeded onto the perimeter of 3D–printed square shaped pores, where each pore has sides of approximately 300 μm in length. Each subfigure in Figure 7.1(a) shows four adjacent pores. As the experiment proceeds, individual cells migrate off the scaffold into the pore, and then combined cell migration and cell proliferation leads to the formation of a sharp-fronted tissue profile that invades into the pore. This process eventually forms a thin tissue that closes or *bridges* the pore after approximately 14 days [Buenzli et al. 2020, Browning et al. 2021]. A notable feature of these experiments is the fact that tissue formation involves a well–defined moving front that is very obvious in Figure 7.1(a). Closer inspection of these experimental images shows that cells not only migrate and proliferate during the pore bridging process, but cells also produce an extracellular medium that is laid down onto the surface of the pore [Lanaro et al. 2021].
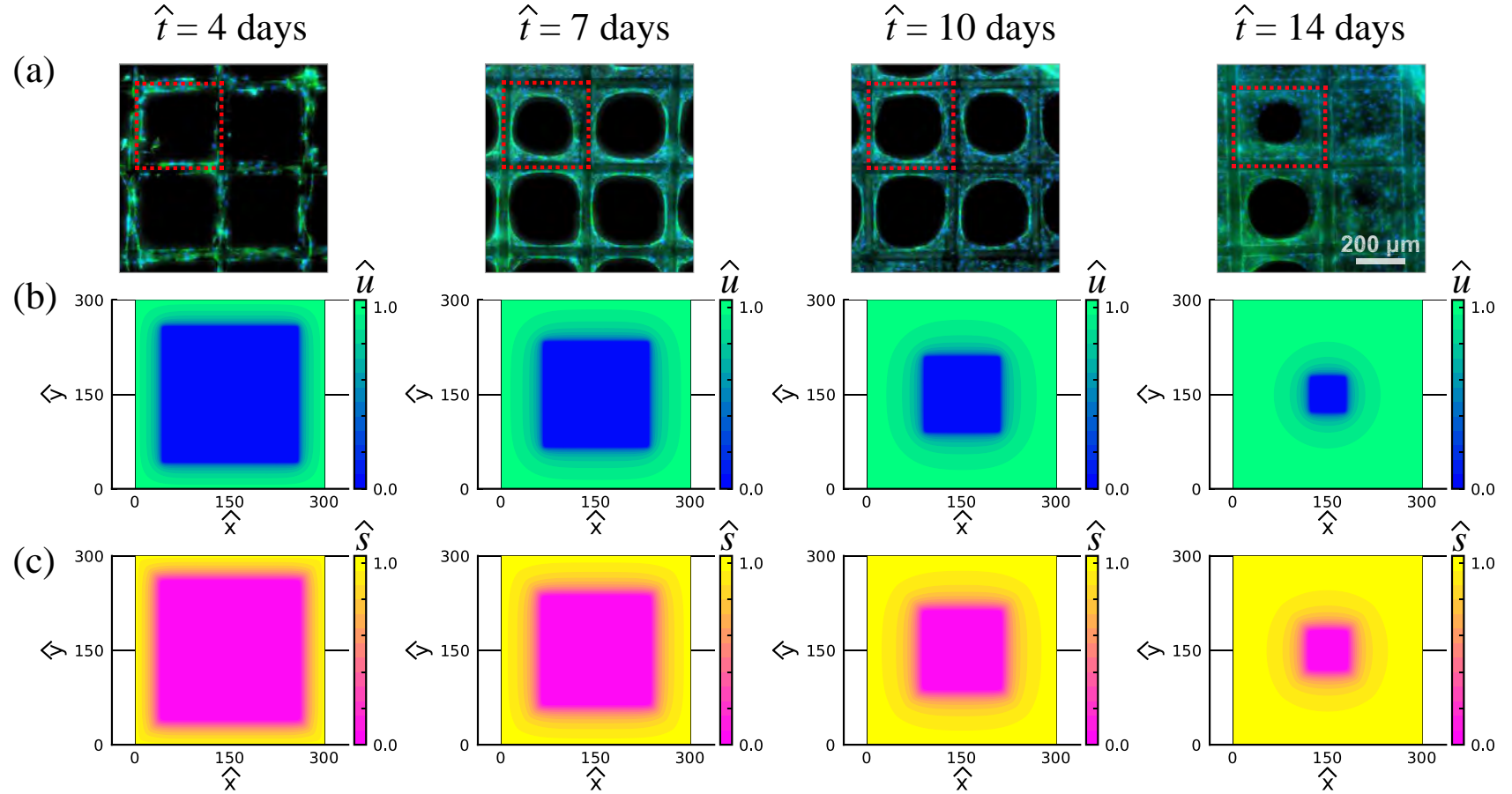
Figure 7.1: Experimental and simulated osteoblast tissue formation within a square–shaped 3D–printed pore. (a) Composite fluorescence microscopy images of pore bridging experiments [Buenzli et al. 2020, Browning et al. 2021]. Cell nuclei are shown in blue, tissue and cytoskeleton are shown in green. Each subfigure shows four adjacent square pores, each with side length of $\hat{L} = 300$ μm, and images are shown at various times, $\hat{t} = 4, 7, 10$ and 14 days, as indicated. For clarity, in each subfigure we outline the border of the upper–left pore (red dashed). Experimental images are reproduced from [Buenzli et al. 2020] with permission. (b)–(c) Numerical solution of Equations (7.1)–(7.2) on a square domain with side length $\hat{L} = 300$ μm. (b) Evolution of $\hat{u}$. (c) Evolution of $\hat{s}$. Each column of the figure corresponds to $\hat{t} = 4, 7, 10$ and 14 days, as indicated. Parameter values for the mathematical model are $\hat{D} = 300$ μm^2/day, $\hat{\lambda} = 0.6$ /day, $\hat{K}_u = 1$ cells/μm^2, $\hat{K}_s = 1$ mol/μm^2, $\hat{r}_1 = 1$ mol/(cells day), $\hat{r}_2 = 1$ /day. The numerical solution of (7.1)–(7.2) is obtained on a 101×101 mesh, and temporal integration is performed with uniform time steps of duration $\Delta\hat{t} = 1 \times 10^{-2}$ day.

Continuum mathematical models of tissue formation have a long history, with many early models based on the classical Fisher–KPP model [Ablowitz and Zeppetella 1979, Canosa 1973, Fisher 1937, Kolmogorov et al. 1937]. The Fisher–KPP model describes cell migration using a one dimensional linear diffusion term, and cell proliferation is modelled using a logistic source term. Many different types tissue formation experiments have been successfully modelled using the Fisher–KPP model [Maini et al. 2004a, Jin et al. 2016, Warne et al. 2019] or two–dimensional extensions of the Fisher–KPP model [Sherratt and Murray 1990, Swanson et al. 2003]. While these studies show that simple mathematical models based on the Fisher-KPP framework successfully capture certain features of tissue formation, there are several well–known limitations of the Fisher–KPP model that can be addressed by considering extensions of that model [Murray 2002]. One such criticism is that the linear diffusion term in the Fisher–KPP model leads to smooth density profiles that do not represent well–defined fronts, such as those we see in Figure 7.1(a).

One way to overcome this limitation is to work with the Porous–Fisher model where the linear diffusion term is generalised to a degenerate nonlinear diffusion term with a power law diffusivity [Fadai and Simpson 2020a, Sánchez Garduño and Maini 1994, Sengers et al. 2007, Witelski 1994, Witelski 1995]. While the Porous–Fisher model leads to sharp–fronted density profiles, this approach introduces a separate complication of having to justify the choice of the exponent in the power law diffusivity [Jin et al. 2016, McCue et al. 2019, Sherratt and Murray 1990, Simpson et al. 2011, Warne et al. 2019]. A further weakness of both the Fisher–KPP and Porous–Fisher models is that they deal with a single species, such as a density of cells, and do not explicitly describe how the population of cells invades into surrounding cells, or interacts with the surrounding environment. This second limitation has been addressed by introducing more complicated mathematical models, such as the celebrated Gatenby–Gawlinski model of tumour invasion [Gatenby and Gawlinski 1996], that explicitly describes how a population of tumour cells degrades and invades into a population of surrounding healthy tissue by explicitly modelling both populations and their interactions. Since the Gatenby–Gawlinski framework was proposed in 1996, subsequent studies have since analyzed the relationship between individual–level mechanisms and the resulting population–

level continuum descriptions [Painter and Sherratt 2003], calibrating these mathematical models to match experimental measurements of melanoma invasion [Browning et al. 2019], as well as analysing travelling wave solutions of these types of multi–species mathematical models [Colson et al. 2021, El-Hachem et al. 2021b, Gallay and Mascia 2021].

In this work we study a continuum mathematical model of cell invasion that is motivated by the experimental images in Figure 7.1(a). The mathematical model explicitly describes the evolution of the cell density, $\hat{u}(\hat{\mathbf{x}}, \hat{t})$, and the density of substrate produced by the cells, $\hat{s}(\hat{\mathbf{x}}, \hat{t})$, giving rise to a coupled system of nonlinear partial differential equations (PDE). We first explore numerical solutions of the mathematical model in two spatial dimensions to mimic the same patterns of tissue development that we see in the experimental images in Figure 7.1(a).

Within this modelling framework, it is natural for us to ask how the duration of time required for the pore to close is affected by the dynamics of substrate deposition and decay. We address this question by nondimensionalising the mathematical model, and numerically exploring travelling wave solutions in one dimension. Not only does travelling wave analysis of the mathematical model have a direct link to the application in question, we note that travelling wave analysis provides mathematical insight into various models of invasion with applications including tissue engineering [Landman and Cai 2007], directed migration [Krause and Van Gorder 2020], disease progression [Strobl et al. 2020] and various applications in ecology [Hogan and Myerscough 2017, El-Hachem et al. 2021a]. Our preliminary numerical explorations suggest that, similar to the well–known Porous–Fisher model, the substrate model supports both sharp–fronted and smooth travelling wave solutions. Working in three–dimensional phase space, we show that travelling wave solutions exist for all wave speeds $c \geq c_{\min}$, where $c_{\min} > 0$ is some minimum wave speed, and we provide a geometric argument based on a slow manifold reduction to distinguish between sharp–fronted travelling wave solutions that move with the minimum speed $c_{\min}$, from smooth travelling wave solutions that move faster than the minimum speed, $c > c_{\min}$. The three–dimensional phase space arguments are supported by some analysis of the time–dependent PDE problem where we show how the long–time travelling

219

wave speed relates to the initial decay rate of the cell density. All phase–space and time–dependent PDE analysis throughout this work are supported by detailed numerical simulations of the full time–dependent PDE model. For completeness we also present various perturbation solutions that give accurate mathematical expressions describing the shape of the travelling waves profiles in various limits.

Overall, we show that the substrate invasion model can be viewed as bridge between the relatively simple Porous–Fisher model and more detailed mathematical models of biological invasion. The substrate model supports various types of travelling wave solutions that are reminiscent of travelling wave solutions of the Porous–Fisher model, but the analysis of these travelling wave solutions is quite different, as we shall now explore.

7.3 Results and Discussion

In this work all dimensional variables and parameters are denoted with a circumflex, and nondimensional quantities are denoted using regular symbols.

7.3.1 Biological motivation

Following Buenzli et al. [Buenzli et al. 2020], we consider the following minimal model of cell invasion

$$
\frac{\partial \hat{u}}{\partial \hat{t}} = \hat{D} \boldsymbol{\nabla} \cdot \left(\frac{\hat{s}}{\hat{K}_s} \boldsymbol{\nabla} \hat{u} \right) + \hat{\lambda} \hat{u} \left(1 - \frac{\hat{u}}{\hat{K}_u} \right), \qquad \hat{\mathbf{x}} \in \Omega, \qquad (7.1)
$$

$$
\frac{\partial \hat{s}}{\partial \hat{t}} = \hat{r}_1 \hat{u} - \hat{r}_2 \hat{s}, \qquad \hat{\mathbf{x}} \in \Omega, \qquad (7.2)
$$

where $\hat{u}(\hat{\mathbf{x}}, \hat{t}) \geq 0$ is the density of cells, $\hat{s}(\hat{\mathbf{x}}, \hat{t}) \geq 0$ is the substrate concentration, $\hat{D} > 0$ is the cell diffusivity and $\hat{\lambda} > 0$ is the cell proliferation rate. This model assumes that cells produce an adhesive and immobile substrate at rate $\hat{r}_1 > 0$, and that the substrate decays at a rate $\hat{r}_2 > 0$. We assume that the carrying capacity density of cells is $\hat{K}_u > 0$, and that a typical maximum substrate density is $\hat{K}_s > 0$. The key feature of this mathematical model is that the diffusive flux of cells is proportional to the substrate density, $\hat{s}$. This assumption couples the cell density to the substrate concentration in a way that the diffusive flux vanishes when $\hat{s} = 0$. In this model the evolution of the cell density is affected by the substrate through the cell migration term,

without any direct coupling in the cell proliferation term. This assumption is consistent with recent two–dimensional studies that explored how different surface coatings affect combined cell migration and cell proliferation in wound healing assays [Jin et al. 2020]. This work showed that different surface coatings have a dramatic impact on cell migration, whereas cell proliferation is less sensitive.

In this modelling framework we make use of the fact that the tissues produced in the experiments in Figure 7.1(a) are thin; the horizontal length scale is approximately 300 μm whereas the depth of tissue is approximately one cell diameter only, which is around $10-20$ μm. In this setting it is appropriate and accurate to use a depth–averaged modelling framework where variations in the vertical direction are implicit, rather than being explicitly described [Simpson 2009].

We begin by considering Equations (7.1)–(7.2) on a two–dimensional square–shaped domain, $\Omega = \{(\hat{x}, \hat{y}) : 0 \leq \hat{x} \leq \hat{L}, 0 \leq \hat{y} \leq \hat{L}\}$ to match the geometry of the experiments in Figure 7.1(a). For simplicity we work with Dirichlet boundary conditions by setting $\hat{u} = \hat{K}_u$ and $\hat{s} = \hat{r}_1 \hat{K}_u / \hat{r}_2$ along all boundaries, with spatially uniform initial conditions $\hat{u} = \hat{s} = 0$, at $\hat{t} = 0$. A numerical solution of Equation (7.1)–(7.2) in Figure 7.1(b)–(c) shows the evolution of $\hat{u}$ and $\hat{s}$, respectively. Full details of the numerical methods used to solve Equations (7.1)–(7.2) are given in the Supplementary Material. The evolution of $\hat{u}$ in Figure 7.1(b) shows that the model predicts the sharp–fronted tissue growth that qualitatively matches the spatial and temporal patterns observed in the experiment. The evolution of $\hat{s}$ in Figure 7.1(c) shows that the invading cell density profile is associated with an invading substrate profile. The coupling between the spatial and temporal distribution of the tissue and the underlying substrate is similar to that observed in the experiments [Lanaro et al. 2021]. Given this experimental motivation we will now set about analysing the mathematical model to provide insight into how the substrate dynamics affect the speed of invasion.

7.3.2 One-dimensional numerical exploration

For the purpose of studying travelling wave solutions of the substrate model we re–write Equations (7.1)–(7.2) in the one–dimensional Cartesian coordinate

system. Introducing the following dimensionless quantities: $u = \hat{u}/\hat{K}_u$, $s = \hat{s}/\hat{K}_s$, $x = \hat{x}\sqrt{\hat{\lambda}/\hat{D}}$, $t = \hat{\lambda}\hat{t}$, $r_1 = \hat{r}_1\hat{K}_u/(\hat{\lambda}\hat{K}_s)$ and $r_2 = \hat{r}_2/\hat{\lambda}$, gives the following non–dimensional model

$$\frac{\partial u}{\partial t} = \frac{\partial}{\partial x}\left(s\frac{\partial u}{\partial x}\right) + u(1-u), \qquad\qquad 0 < x < \infty \qquad (7.3)$$

$$\frac{\partial s}{\partial t} = r_1 u - r_2 s, \qquad\qquad 0 < x < \infty, \qquad (7.4)$$

$$\frac{\partial u(0,t)}{\partial x} = 0, \qquad \text{and} \qquad u(x,t) \to 0, \ x \to \infty. \qquad (7.5)$$

This dimensionless model involves just two free parameters that relate to the rate of substrate production and the rate of substrate decay, r_1 and r_2, respectively. Note that Equation (7.4) does not involve any spatial derivatives so there is no need to specify any boundary conditions for s.

In this study we will consider two different types of initial conditions: (i) a biologically–realistic initial condition describing the situation where the initial cell population occupies a particular region, and the cell density vanishes outside of this region [Maini et al. 2004a, Sengers et al. 2007]; and, (ii) a mathematically insightful, but less biologically–realistic initial condition where the initial cell density decays exponentially as $x \to \infty$. For the biologically–realistic initial conditions we always consider

$$u(x,0) = 1 - H(\beta), \qquad\qquad (7.6)$$

$$s(x,0) = 0, \qquad\qquad (7.7)$$

on $0 < x < \infty$, where $H(x)$ is the usual Heaviside function and $\beta > 0$ is a constant describing the initial length of the domain that is occupied at $t = 0$. For the mathematically interesting initial condition we always consider

$$u(x,0) = \begin{cases} 1, & x < \beta, \\ \exp[-a(x-\beta)], & x > \beta, \end{cases} \qquad (7.8)$$

$$s(x,0) = 0, \qquad\qquad (7.9)$$

on $0 < x < \infty$, where $a > 0$ is the decay rate. For all results, we set $\beta = 10$.

We focus on long–time numerical solutions of Equations (7.3)– (7.4) in order to explore travelling wave solutions. Details of the numerical method we

use to solve the governing equations are given in the Supplementary Material. Of course, the travelling wave analysis of this model is relevant on the infinite domain, $0 < x < \infty$, but numerically we must always work with a truncated domain $0 < x < X$, where X is chosen to be sufficiently large that the late–time numerical solutions are unaffected by the choices of X. All algorithms required to re–create the results in this work are available on GitHub.

Before we present and discuss particular travelling wave solutions, it is convenient to state at the outset that we find the substrate invasion model leads to two types of travelling wave solutions, shown schematically in Figure 7.2. The travelling wave solution in Figure 7.2(a) arises from the biologically–relevant initial conditions (7.6)–(7.7), where we see that there is a well–defined sharp front with $u = s = 0$ ahead of the front, and $u \to 1^-$ and $s \to R^-$ well–behind the travelling wave front as $x \to 0^-$. In this case, as we will show, the travelling wave solution corresponds to the minimum wave speed, $c = c_{\min}$, that depends on the value of r_1 and r_2. In contrast, the travelling wave solution in Figure 7.2(b) arises from the mathematically interesting initial conditions (7.8)–(7.9). In this second type of travelling wave we have the same behaviour well–behind the wave front as in Figure 7.2(a), since $u \to 1^-$ and $s \to R^-$ as $x \to 0^-$. However, in this case we have a smooth travelling wave with $u \to 0^+$ and $s \to 0^+$ as $x \to \infty$. Further, as we will show, these smooth–fronted travelling wave solutions move with a faster travelling wave speed, $c > c_{\min}$.
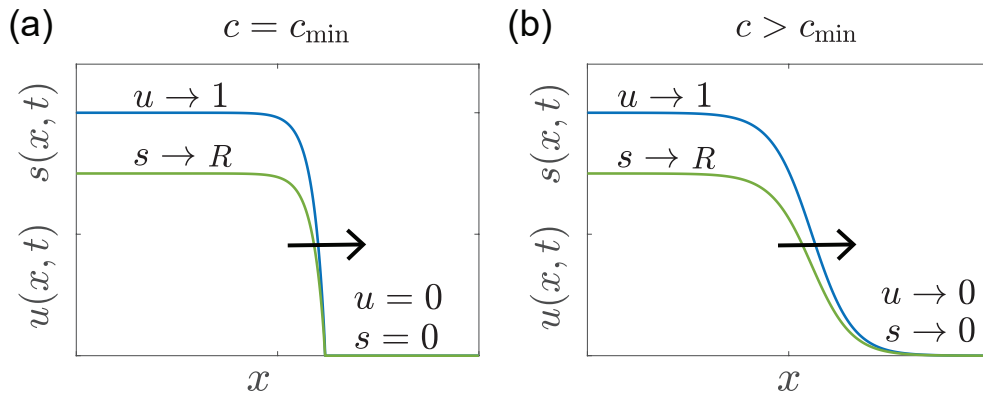
Figure 7.2: Schematic showing sharp and smooth–fronted travelling wave solutions. (a) Schematic showing a sharp-fronted travelling wave. (b) Schematic showing a smooth-fronted travelling wave. Arrows show the direction of movement.

The fact that the substrate model gives rise to both smooth and sharp–fronted travelling wave solutions is very interesting and worthy of exploration. Throughout this work we will explore parallels between the substrate model

and the Porous–Fisher model, and an obvious point of similarity is that both these models support smooth and sharp–fronted travelling wave solutions [Murray 2002, Sánchez Garduño and Maini 1994, Sherratt and Marchant 1996]. As we will explore in this work, however, the differences between the smooth and sharp–fronted travelling waves in the substrate model are more subtle than the Porous–Fisher model, and we must use different methods of analysis to understand these differences.

In addition to the schematic solutions in Figure 7.2, we present a range of time–dependent PDE solutions in Figure 7.3 where we explore the role of varying the substrate dynamics by choosing different values of r_1 and r_2.

Results in Figure 7.3(a)–(c) for the sharp–fronted travelling wave solutions show that the long–time minimum travelling wave speed, $c_{\min}$, depends on r_1 and r_2. In particular, comparing the results in (a)–(d) show that $c_{\min}$ appears to increase with r_1. In contrast, the smooth–fronted travelling wave solutions in Figure 7.3(e)–(h) lead to travelling wave solutions where the wave speed $c > c_{\min}$ appears to be independent of r_1 and r_2. These numerical solutions show that the value of s well–behind the travelling wave front depends on the choice of r_1 and r_2, and motivates us to define

$$R = \frac{r_1}{r_2}, \tag{7.10}$$

so that we have $s \to R^-$ as $x \to 0^-$, which is consistent with the schematics in Figure 7.2.
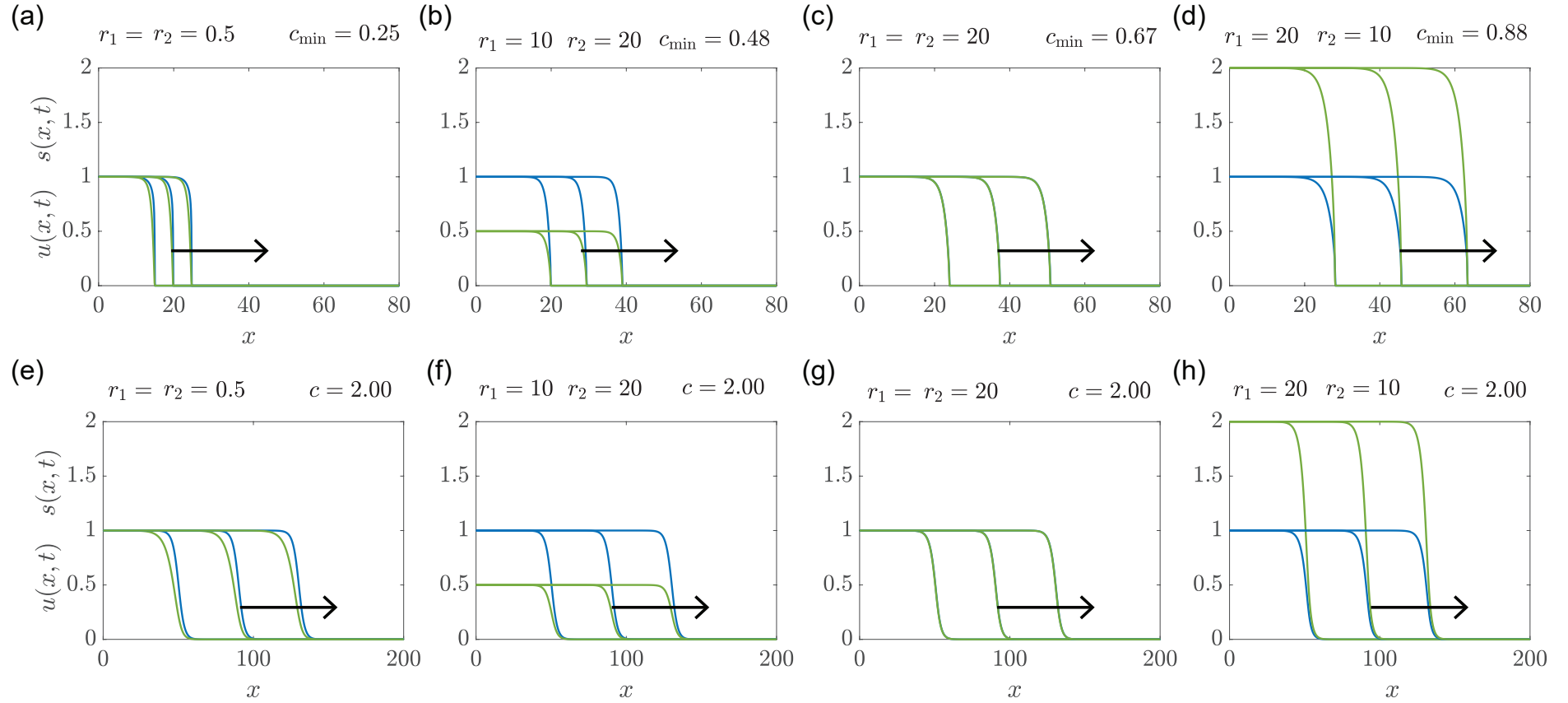
Figure 7.3: Time-dependant PDE solutions showing smooth and sharp–fronted travelling wave solutions. Sharp-fronted travelling wave solutions in (a)–(d) are obtained by solving Equations (7.3)–(7.5) with (7.6)–(7.7). Smooth–fronted travelling wave solutions in (e)–(h) are obtained by solving Equations (7.3)–(7.5) with (7.8)–(7.9) and $a = 1/2$. Values of r_1 and r_2 are indicated on each subfigure, and the long-time estimate of the travelling wave speed c is also given to two decimal places. Each subfigure shows profiles for $u(x,t)$ (blue) and $s(x,t)$ (green) at $t = 20, 40$ and 60, with the arrow showing the direction of increasing t. All numerical solutions correspond to $\Delta x = 1 \times 10^{-2}$, $\Delta t = 1 \times 10^{-3}$ and $\epsilon = 1 \times 10^{-10}$.

Now we have established that the long–time travelling wave speed for the sharp–fronted travelling wave solutions depends upon r_1 and r_2, we generate a suite of sharp–fronted travelling wave solutions numerically, and estimate $c_{\min}$ as a function of r_1 and r_2, as reported in Figure 7.4(a). This heat map suggests that holding r_2 constant and increasing r_1 leads to an increase in $c_{\min}$. In contrast, holding r_1 constant and increasing r_2 reduces $c_{\min}$. To further explore this relationship we superimpose three straight lines on the heat map in Figure 7.4(a). These straight lines correspond to $R = 0.5$ (yellow), $R = 1$ (red) and $R = 2$ (blue). Plotting $c_{\min}$ as a function of r_1 for these three fixed values of R in Figure 7.4(b) suggest that $c_{\min} \to \sqrt{R/2}^{\,-}$ for fixed R, as $r_1 \to \infty$. As we will explain later in Section 7.3.6, this numerical observation is related to the fact that the substrate model simplifies to the Porous–Fisher model when r_1 and r_2 are sufficiently large [Buenzli et al. 2020].
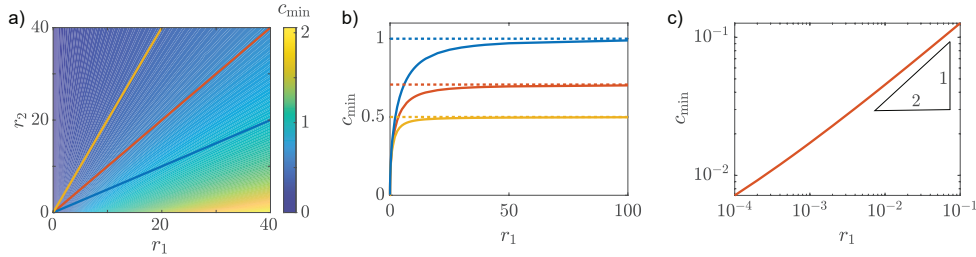
Figure 7.4: Numerical exploration of the relationship between $c_{\min}$, r_1 and r_2. (a) heat map of $c_{\min}$ as a function of r_1 and r_2 obtained by solving (7.3)–(7.5) with (7.6)–(7.7). The three straight lines superimposed on (a) correspond to $R = 0.5$ (yellow), $R = 1$ (red) and $R = 2$ (blue), and the relationship between $c_{\min}$ and r_1 for these fixed values of R is given in (b), showing that $c_{\min} \to \sqrt{R/2}^{\,-}$ as $r_1 \to \infty$. (c) shows $c_{\min}$ as a function of r_1 for $R = 0.5, 1$ and 2, suggesting that $c_{\min} \sim A\sqrt{r_1}$ as $r_1 \to 0$, for some constant $A > 0$. All numerical solutions correspond to $\Delta x = 1 \times 10^{-2}$, $\Delta t = 1 \times 10^{-2}$ and $\epsilon = 1 \times 10^{-10}$.

Results in Figure 7.4(b) explore the fast substrate production limit, $r_1 \to \infty$ for fixed R, whereas results in Figure 7.4(c) explore the small substrate production limit, $r_1 \to 0$. In this case we plot $c_{\min}$ as a function for r_1, for $R = 0.5, 1$ and 2, and we see that the results for different values of R are identical, suggesting that $c_{\min}$ is independent of r_2 as $r_1 \to 0$. Furthermore, the straight line relationship on the log–log plot in Figure 7.4(c) suggests that we have $c_{\min} \sim A\sqrt{r_1}$ as $r_1 \to 0$ for some constant $A > 0$.

In summary, results in Figure 7.4 summarise the numerically–determined relationship between $c_{\min}$, r_1, and r_2 for sharp–fronted travelling wave solutions of the substrate model. These numerical results are of interest because

some results are consistent with well–known results for the Porous–Fisher model as we further explore in Section 7.3.6. In contrast, we also observe different behaviour that is inconsistent with the Porous–Fisher model. For example, the non-dimensional Porous-Fisher model has a positive minimum wavespeed $c_{\min} = 1/\sqrt{2} \cong 0.71$, whereas the substrate–mediated invasion model supports sharp–fronted travelling wave solutions with vanishingly small minimum wave speed, $c_{\min} \to 0$ as $r_1 \to 0$. Table (7.1) summarises the differences and similarities between travelling wave solutions of the Porous–Fisher model and the substrate model. While some of these results have only been numerically explored so far, in later sections we will provide more thorough evidence to support these numerically–based observations.

Table 7.1: Key features of travelling wave solutions of the substrate–mediated invasion model with travelling wave solutions of the Porous–Fisher model.

Porous-Fisher		Substrate–mediated model	
Smooth front	Sharp front	Smooth front	Sharp front
$c = \begin{cases} \dfrac{1}{a} & a < \sqrt{2} \\ \dfrac{1}{\sqrt{2}} & a \geq \sqrt{2} \end{cases}$	$c_{\min} = \dfrac{1}{\sqrt{2}}$	$c = \dfrac{1}{a}$ $\displaystyle\lim_{\substack{r_1 \to \infty \\ r_2 \to \infty}} c = \sqrt{\dfrac{R}{2}}^{\,-}$	$\displaystyle\lim_{r_1 \to 0^+} c_{\min} = 0^+$ $\displaystyle\lim_{\substack{r_1 \to \infty \\ r_2 \to \infty}} c_{\min} = \sqrt{\dfrac{R}{2}}^{\,-}$

Given the numerical evidence developed in this section, we will now use phase space techniques to understand the differences between the sharp–fronted and smooth–fronted travelling wave solutions of the substrate model.

7.3.3 Phase space analysis for smooth travelling wave solutions

In the usual way, we seek to study travelling wave solutions of Equations (7.3)–(7.4) by writing $u(x,t) = U(z)$ and $S(x,t) = S(z)$, where z is the travelling wave variable, $z = x - ct$ [Murray 2002] to give

$$\frac{\mathrm{d}}{\mathrm{d}z}\left(S\frac{\mathrm{d}U}{\mathrm{d}z}\right) + c\frac{\mathrm{d}U}{\mathrm{d}z} + U(1-U) = 0, \qquad -\infty < z < \infty, \qquad (7.11)$$

$$c\frac{\mathrm{d}S}{\mathrm{d}z} + r_1 U - r_2 S = 0, \qquad -\infty < z < \infty. \qquad (7.12)$$

Boundary conditions for the smooth travelling wave solutions are $U(z) \to 1$ and $S(z) \to R$ as $z \to -\infty$, and $U(z) \to 0$ and $S(z) \to 0$ as $z \to \infty$. Given such a smooth–fronted travelling wave solution for $U(z)$, we can solve Equation

(7.12) to give

$$S(z) = \frac{r_1}{c} \exp\left[\frac{r_2 z}{c}\right] \int_z^\infty \exp\left[\frac{-r_2 y}{c}\right] U(y)\, \mathrm{d}y. \tag{7.13}$$

We will make use of this result later.

Following the usual approach to studying smooth travelling wave solutions, we re–write Equations (7.11)–(7.12) as a first order system

$$\frac{\mathrm{d}U}{\mathrm{d}z} = W, \tag{7.14}$$

$$\frac{\mathrm{d}S}{\mathrm{d}z} = -\left(\frac{r_1 U - r_2 S}{c}\right), \tag{7.15}$$

$$\frac{\mathrm{d}W}{\mathrm{d}z} = W\left(\frac{r_1 U - r_2 S - c^2}{cS}\right) - \frac{U(1-U)}{S}. \tag{7.16}$$

There are two equilibrium points of the phase space: (i) $(\bar{U}, \bar{S}, \bar{W}) = (1, R, 0)$ as $z \to -\infty$, which corresponds to the invaded boundary; and, (ii) $(\bar{U}, \bar{S}, \bar{W}) = (0, 0, 0)$ as $z \to \infty$, which corresponds to the uninvaded boundary.

To explore the possibility of a heteroclinic orbit connecting the two equilibrium points in the three–dimensional phase space, the Jacobian of this system is

$$\begin{bmatrix} 0 & 0 & 1 \\ -\dfrac{r_1}{c} & \dfrac{r_2}{c} & 0 \\ \dfrac{r_1 \bar{W} - c(1 - 2\bar{U})}{c\bar{S}} & \dfrac{(-r_1 \bar{U} + c^2)\bar{W} + c\bar{U}(1 - \bar{U})}{c\bar{S}^2} & \dfrac{-r_2 \bar{S} + r_1 \bar{U} - c^2}{c\bar{S}} \end{bmatrix}. \tag{7.17}$$

We see immediately that we cannot follow the usual practice of evaluating the Jacobian at the uninvaded equilibrium point since it is not defined at $(\bar{U}, \bar{S}, \bar{W}) = (0, 0, 0)$ and so linearisation is not useful here. In contrast, the Jacobian at the invaded equilibrium point $(\bar{U}, \bar{S}, \bar{W}) = (1, R, 0)$ is

$$\begin{bmatrix} 0 & 0 & 1 \\ -\dfrac{r_1}{c} & \dfrac{r_2}{c} & 0 \\ \dfrac{r_2}{r_1} & 0 & -\dfrac{cr_2}{r_1} \end{bmatrix}. \tag{7.18}$$

The eigenvalues of this Jacobian are $\lambda_1 = r_2/c$ and $\lambda_{2,3} = (-c \pm \sqrt{c^2 + 4R})/(2R)$. Since these eigenvalues are all real valued, with $\lambda_{1,2} > 0$ and $\lambda_3 < 0$, the in-

vaded equilibrium point is a three–dimensional saddle point.

As just mentioned, linearisation about the uninvaded equilibrium point is not possible, and so we revisit the dynamical system (7.14)–(7.16) as $z \to \infty$ in more detail in Section 7.3.5 below. For now, we suppose that a smooth travelling wave $U(z)$ decays exponentially, say

$$U(z) \sim C \exp(-bz) \quad z \to \infty, \tag{7.19}$$

where $b > 0$. Under this assumption it follows from (7.13) that

$$S(z) \sim \frac{r_1}{bc + r_2} U(z), \tag{7.20}$$

$$W(z) \sim -bU(z), \tag{7.21}$$

suggesting that $S(z)$ and $W(z)$ both decay to zero exponentially, at the same rate as $U(z)$, as $z \to \infty$. Further, to leading order as $z \to \infty$, (7.16) gives

$$\frac{\mathrm{d}W}{\mathrm{d}z} \sim (bc - 1)\left(\frac{bc + r_2}{r_1}\right) \quad \text{as} \quad z \to \infty. \tag{7.22}$$

At first glance this results appears inconsistent with our arguments so far, since for smooth travelling wave solutions we expect $\mathrm{d}W/\mathrm{d}z \to 0$ as $z \to \infty$, but here we have $\mathrm{d}W/\mathrm{d}z$ approaching a constant. However, by choosing $c = 1/b$ we avoid this inconsistency. This choice implies that the speed of the smooth–fronted travelling wave is related to the far–field decay rate of $U(z)$. We have tested this hypothesis numerically and found and excellent match between (7.19)–(7.21) and the shape of the smooth–fronted travelling waves for different choices of r_1, r_2 and c, with one example discussed in the Supplementary Material. In addition, we provide further evidence for this far–field behaviour in Section 7.3.5.

7.3.4 Dispersion relationship

We now explore how the decay rate of the initial condition, a in Equation (7.8), affects the long–time travelling wave speed for smooth–fronted travelling wave solutions. To be consistent with our observations in Section 7.3.3, we assume that smooth–fronted travelling wave solutions for $U(z)$ and $S(z)$ decaying at the same rate, and we seek solutions of the form $\tilde{u}(x,t) \sim C \exp[a(x - ct)]$

and $\tilde{s}(x,t) \sim D \exp\left[a(x - ct)\right]$ as $x \to \infty$. Substituting these solutions into Equation (7.3), and focusing on the leading edge of these solutions where $\tilde{u}(x,t) \ll 1$, we obtain

$$c = \frac{1}{a},\qquad(7.23)$$

which relates the long–time speed of the travelling wave solution to the decay rate of the initial condition, $u(x,0)$.
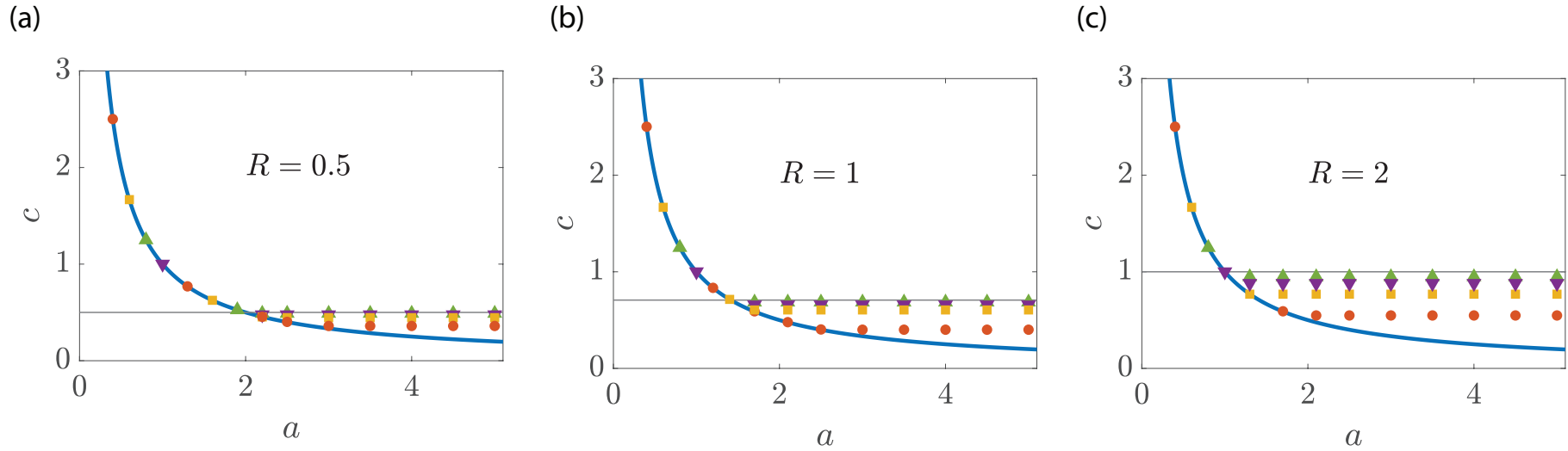
Figure 7.5: Dispersion relationship. (a)–(c) shows c as a function of the initial decay rate, a, for $R = 0.5, 1$ and 2, respectively. Numerical travelling wave speeds are estimated from long–time numerical solutions of Equations (7.3)–(7.5) with the initial condition given by Equations (7.8)–(7.9) with various values of a. The dispersion relationship, Equation (7.23), is plotted (solid blue) and results for $r_1 = 1, 5, 10$ and 20 are shown in orange discs, yellow squares, purple triangles and green triangles, respectively. Each plot shows a horizontal line at $\sqrt{R/2}$, which is an upper bound for the wavespeed for large a. All numerical PDE solutions correspond to $\Delta x = 1 \times 10^{-2}$, $\Delta t = 1 \times 10^{-3}$ and $\epsilon = 1 \times 10^{-10}$.

Results in Figure 7.5 explore the validity of Equation (7.23) by taking time–dependent PDE solutions with initial conditions (7.8)–(7.9) and varying the decay rate of $u(x, 0)$ for various values of r_1 and r_2. In particular, we generate travelling wave solutions for $r_1 = 1, 5, 10$ and 20, for fixed $R = 0.5, 1$ and 2. Results in Figure 7.5(a)–(c) corresponding to $R = 0.5, 1$ and 2, respectively, show that for sufficiently small a, we see that the long–time travelling wave speed matches Equation (7.23) regardless of r_1 and r_2. These results are consistent with the initial explorations in Figure 7.3(e)–(h) where we saw that the wave speed of certain smooth–fronted travelling wave solutions was independent of r_1 and r_2. As a increases, however, we see that c behaves differently. For large $a > a_{\text{crit}}$ we see that c approaches a constant value c_{min} that is independent of a. Our numerical evidence suggests that this limiting constant value depends on r_1 and r_2. For completeness, on each subfigure we plot a horizontal line at $c = \sqrt{R/2}$, and we note that this value appears to be an upper–bound for c as a becomes large.
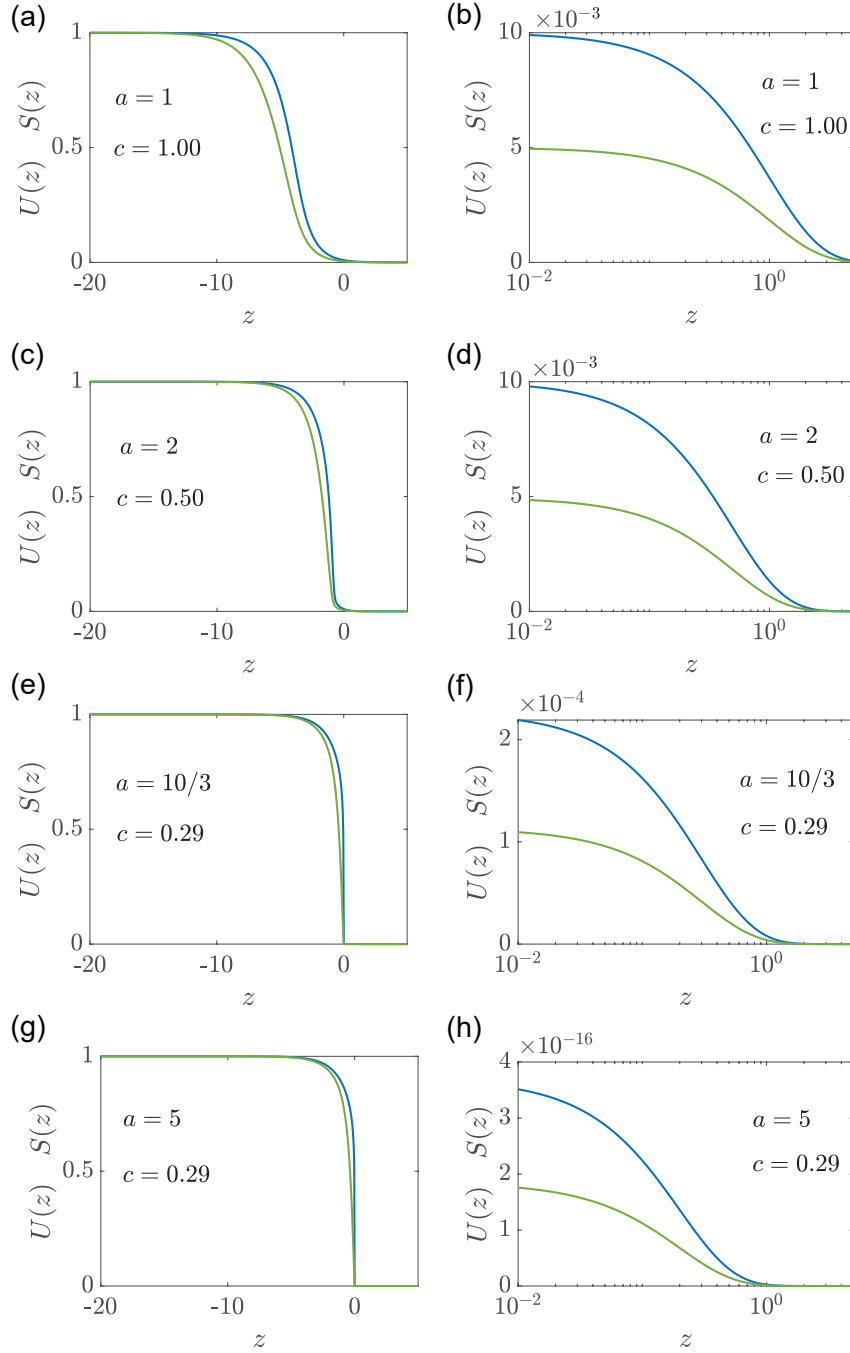
Figure 7.6: Smooth-fronted travelling wave solutions. Travelling wave solutions $U(z)$ and $S(z)$ are obtained by considering long–time numerical solutions of Equations (7.3)–(7.5) with initial conditions given by Equations (7.8)–(7.9) with variable decay rate, a. All results correspond to $r_1 = r_2 = 1$, and results in (a)–(b), (c)–(d), (e)–(f) and (g)–(h) correspond to $a = 1, 2, 10/3$ and 5, respectively, as indicated. Results in the left–most column show the various travelling wave solutions plotted on the usual scale with $0 \leq U(z), S(z) \leq 1$. Results in the right–most column show a magnification of the leading edge of the travelling waves.

The transition from $c = 1/a$ for $a < a_{\text{crit}}$ to constant c for $a > a_{\text{crit}}$ in Figure 7.5 is further explored in Figure 7.6 for $r_1 = r_2 = 1$. The long–time travelling wave solution in Figure 7.6(a)–(b) evolves from an initial condition

with decay rate $a = 1$. This solution evolves into a smooth travelling wave with $c = 1.00$, which is consistent with the dispersion relationship, Equation (7.23). Although it is clear that the travelling wave solution in Figure 7.6(a) is smooth at this scale, we also plot a magnification of the leading edge of that travelling wave in Figure 7.6(b). We now explore a series of travelling wave solutions as a increases to visualise the transition reported in Figure 7.5. The long–time travelling wave solution in Figure 7.6(c)–(d) evolves from an initial condition with a faster decay rate, $a = 2$, leading to a smooth–fronted travelling wave with $c = 0.50$. Again, this result is consistent with the dispersion relationship, and the magnification of the density profiles near the leading edge in Figure 7.6(d) confirms that the travelling wave solution is smooth. The travelling wave solution in Figure 7.6(e) for $a = 10/3$ leads to a travelling wave solution with $c = 0.29$. This estimate from the long–time numerical solution of the PDE is close to the travelling wave speed predicted by the dispersion relationship. At the scale shown in Figure 7.6(e) it might seem, at first glance, that the travelling wave is sharp, but the magnification in Figure 7.6(f) confirms that this travelling wave is indeed smooth–fronted. Finally, the travelling wave solution in Figure 7.6(g) for $a = 5$ evolves to a travelling wave solution with $c = 0.29$, which is much larger than the speed predicted by the dispersion relationship that would give $c = 1/5 = 0.2$. Again, while the travelling wave solution in Figure 7.6(g) appears to be sharp at this scale, the magnification of the solution in Figure 7.6(h) confirms that this solution is indeed smooth–fronted.

In summary, the dispersion relationship suggests that long–time speed of smooth–fronted travelling wave solutions is given by $c = 1/a$, where a is far-field the decay rate of $u(x, 0)$. Our numerical explorations in Figures 7.5–7.6 confirms that this result holds for sufficiently small decay rates, $a < a_{\text{crit}}$. As the decay rate increases, $a > a_{\text{crit}}$, we observe an interesting transition for smooth–fronted travelling waves where c becomes independent of a, and greater than the speed predicted by the dispersion relationship. While these travelling wave solutions remain smooth–fronted as a increases, it becomes increasingly difficult to draw a visual distinction between these smooth–fronted travelling wave solutions and sharp–fronted travelling wave solutions that evolve from initial conditions with compact support, such as those travelling

waves in Figure 7.3(a)–(d). We now seek to provide a geometric interpretation of the differences between these two classes of travelling wave solutions by returning to the phase space.

7.3.5 Desingularised phase space and slow manifold reduction

We now return to the phase space for travelling wave solutions and introduce a change of variables

$$\zeta(z) = \int_0^z \frac{\mathrm{d}y}{S(y)}, \tag{7.24}$$

which removes the singularity in Equation (7.16) when $S(z) = 0$. A similar transformation to desingularise the phase plane is often used in the analysis of sharp–fronted travelling wave solutions of the Porous–Fisher model [Murray 2002]. The desingularised system is given by

$$\frac{\mathrm{d}U}{\mathrm{d}\zeta} = SW, \tag{7.25}$$

$$\frac{\mathrm{d}S}{\mathrm{d}\zeta} = -S\left(\frac{r_1 U - r_2 S}{c}\right), \tag{7.26}$$

$$\frac{\mathrm{d}W}{\mathrm{d}\zeta} = W\left(\frac{r_1 U - r_2 S - c^2}{c}\right) - U(1 - U). \tag{7.27}$$

There are two equilibrium points of the desingularised phase space: (i) $(\bar{U}, \bar{S}, \bar{W}) = (1, R, 0)$ as $\zeta \to -\infty$, corresponding to the invaded boundary; and, (ii) $(\bar{U}, \bar{S}, \bar{W}) = (0, 0, 0)$ as $\zeta \to \infty$, corresponding to the uninvaded boundary. It is important to point out that the phase space analysis in Section 7.3.3 was relevant only for smooth–fronted travelling wave solutions, whereas the desingularised phase space is appropriate for both the sharp–fronted and smooth–fronted travelling wave solutions. The Jacobian of this system is

$$\begin{bmatrix} 0 & \bar{W} & \bar{S} \\ -\dfrac{r_1 \bar{S}}{c} & \dfrac{-r_1 \bar{U} + 2r_2 \bar{S}}{c} & 0 \\ \dfrac{r_1 \bar{W} - c(1 - 2\bar{U})}{c} & -\dfrac{r_2 \bar{W}}{c} & \dfrac{-r_2 \bar{S} + r_1 \bar{U} - c^2}{c} \end{bmatrix}. \tag{7.28}$$

We can now consider both equilibrium points $(\bar{U}, \bar{S}, \bar{W}) = (1, R, 0)$ and $(\bar{U}, \bar{S}, \bar{W}) = (1, 0, 0)$.

The Jacobian at the invaded equilibrium point, $(\bar{U}, \bar{S}, \bar{W}) = (1, R, 0)$, is

$$
\begin{bmatrix}
0 & 0 & \dfrac{r_1}{r_2} \\[2ex]
-\dfrac{r_1^2}{r_2} & \dfrac{r_1}{c} & 0 \\[2ex]
1 & 0 & -c
\end{bmatrix}.
\tag{7.29}
$$

The eigenvalues of this Jacobian are $\lambda_1 = r_1/c$ and $\lambda_{2,3} = (-c \pm \sqrt{c^2 + 4R})/2$. Since $\lambda_{1,2} > 0$ and $\lambda_3 < 0$, the uninvaded equilibrium point is a three–dimensional saddle. These expressions are identical to the corresponding expressions in Section (7.3.3), which is not surprising since $\zeta = z$ near the invaded equilibrium point, $z \to -\infty$.

The Jacobian at the uninvaded equilibrium point, $(\bar{U}, \bar{S}, \bar{W}) = (0, 0, 0)$, is

$$
\begin{bmatrix}
0 & 0 & 0 \\
0 & 0 & 0 \\
-1 & 0 & -c
\end{bmatrix}.
\tag{7.30}
$$

The eigenvalues are $\lambda_1 = -c$ and $\lambda_2 = \lambda_3 = 0$, which means that $(\bar{U}, \bar{S}, \bar{W}) = (0, 0, 0)$ is a non-hyperbolic equilibrium point suggesting that the dynamics near this point take place on a slow manifold [Wiggins 2003]. To explore these local dynamics near $(\bar{U}, \bar{S}, \bar{W}) = (0, 0, 0)$ we apply the centre manifold theory to identify the slow manifold. To proceed we rotate the coordinate system using a transformation defined by the eigenvectors $[-c, 0, 1]^\top$, $[0, 1, 0]^\top$ and $[0, 0, 1]^\top$ that are associated with λ_1, λ_2 and λ_3, respectively. The relationship between the original unrotated coordinate system (U, S, W) and the rotated coordinate system $(\mathscr{U}, \mathscr{S}, \mathscr{W})$ is given by the transformation [Maclaren 2020],

$$
\begin{bmatrix}
U \\
S \\
W
\end{bmatrix}
=
\begin{bmatrix}
-c & 0 & 0 \\
0 & 1 & 0 \\
1 & 0 & 1
\end{bmatrix}
\begin{bmatrix}
\mathscr{U} \\
\mathscr{S} \\
\mathscr{W}
\end{bmatrix},
\tag{7.31}
$$

and the associated inverse transformation

$$
\begin{bmatrix}
\mathscr{U} \\
\mathscr{S} \\
\mathscr{W}
\end{bmatrix}
=
\frac{1}{c}
\begin{bmatrix}
-1 & 0 & 0 \\
0 & c & 0 \\
1 & 0 & c
\end{bmatrix}
\begin{bmatrix}
U \\
S \\
W
\end{bmatrix}.
\tag{7.32}
$$

These transformations allow us to re-write the dynamical system in the following format

$$
\begin{bmatrix} \dfrac{\mathrm{d}\mathscr{U}}{\mathrm{d}\zeta} \\[2mm] \dfrac{\mathrm{d}\mathscr{S}}{\mathrm{d}\zeta} \\[2mm] \dfrac{\mathrm{d}\mathscr{W}}{\mathrm{d}\zeta} \end{bmatrix}
= \begin{bmatrix} 0 & 0 & 0 \\ 0 & 0 & 0 \\ 0 & 0 & -c \end{bmatrix} \begin{bmatrix} \mathscr{U} \\ \mathscr{S} \\ \mathscr{W} \end{bmatrix}
$$

$$
+ \frac{1}{c} \begin{bmatrix} -\left[\mathscr{S}(\mathscr{U} + \mathscr{W})\right] \\[2mm] \left[\mathscr{S}(r_1 c\mathscr{U} + r_2\mathscr{S})\right] \\[2mm] \left[(\mathscr{U} + \mathscr{W})\left[-r_1 c\mathscr{U} + (1 - r_2)\mathscr{S}\right] + c^2\mathscr{U}(1 + c\mathscr{U})\right] \end{bmatrix} . \quad (7.33)
$$

To find the slow manifold we take the usual approach of writing the fast dynamics associated with λ_1 as a function of the slow dynamics that are associated with the zero eigenvalues by assuming that slow manifold can be locally expressed as a quadratic in $\mathscr{U}$ and $\mathscr{V}$. Equating coefficients with the tangency condition [Wiggins 2003] gives the slow manifold,

$$
\mathscr{W}(\mathscr{U}, \mathscr{S}) = \frac{1}{c^2} \left[c(c^2 - r_1)\mathscr{U}^2 + (1 - r_2)\mathscr{U}\mathscr{S}\right], \quad (7.34)
$$

and the dynamics on the slow manifold are given by

$$
\frac{\mathrm{d}\mathscr{U}}{\mathrm{d}\zeta} = -\frac{1}{c^3} \left[c(c^2 - r_1)\mathscr{U}^2\mathscr{S} + (1 - r_2)\mathscr{U}\mathscr{S}^2 + c^2\mathscr{S}\mathscr{U}\right], \quad (7.35)
$$

$$
\frac{\mathrm{d}\mathscr{S}}{\mathrm{d}\zeta} = \frac{1}{c} \left[r_2\mathscr{S}^2 + r_1 c\mathscr{U}\mathscr{S}\right]. \quad (7.36)
$$

We can now re–write the slow manifold and the dynamics on the slow manifold in the original, unrotated coordinate system, giving

$$
W(U, S) = \frac{1}{c^3} \left[(c^2 - r_1)U^2 - (1 - r_2)US - c^2U\right], \quad (7.37)
$$

and

$$
\frac{\mathrm{d}U}{\mathrm{d}\zeta} = \frac{1}{c^3} \left[(c^2 - r_1)SU^2 - (1 - r_2)US^2 - c^2SU\right], \quad (7.38)
$$

$$
\frac{\mathrm{d}S}{\mathrm{d}\zeta} = \frac{1}{c} \left[r_2S^2 - r_1US\right]. \quad (7.39)
$$

With these tools we may now plot the phase space including the two equilib-

rium points, and superimpose the slow manifold and the heteroclinic orbit obtained be re-writing the long–time PDE solution in terms of the $(U(\zeta), S(\zeta), W(\zeta))$ coordinates. This information is summarised in Figure 7.7 for two smooth–fronted travelling waves and one sharp–fronted travelling wave, each with $r_1 = r_2 = 1$. Before considering Figure 7.7 in detail, note that a small S and U analysis of (7.38)–(7.39) shows that the heteroclinic orbit must have $U \sim (r_2 + 1)S/r_1$ as $S \to 0^+$, meaning that the slope of the heteroclinic orbit is $r_1/(r_2 + 1)$ in the US–plane near the origin, and $U \sim A\exp(-z/c)$ and $S \sim B\exp(-z/c)$, for some constants $A > 0$, $B > 0$, as $z \to \infty$ for smooth–fronted travelling wave solutions. These results for the flow on the slow manifold confirm (7.19)–(7.20) with $c = 1/b$.
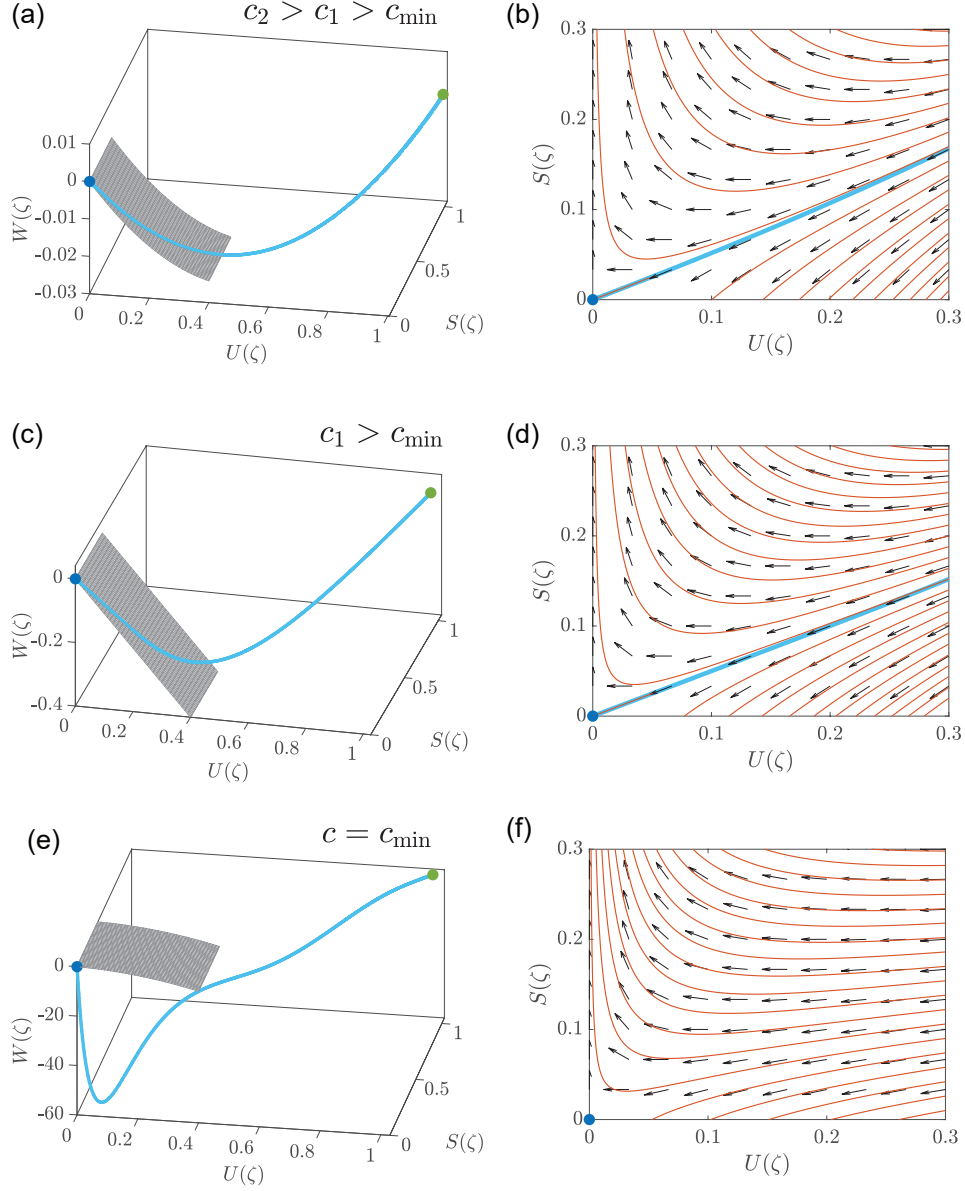
Figure 7.7: Desingularised phase space and slow manifold reduction. All results correspond to $r_1 = r_2 = 1$. Results in: (a)–(b) correspond to a smooth–fronted travelling wave with $c_2 = 10$; (c)–(d) correspond to a smooth–fronted travelling wave with $c_1 = 1$; and, (e)–(f) correspond to a sharp–fronted travelling wave with $c_{\min} = 0.29$. Results in the left–most column show the three–dimensional desingularised phase space with the invaded equilibrium point (green dot), the uninvaded equilibrium point (blue dot) and the slow manifold (grey surface). Results in the right–most column show the vector field on the slow manifold, superimposed with several solution trajectories, including the heteroclinic orbit (blue) and several unphysical trajectories (red). The heteroclinic orbit is obtained by solving Equations (7.3)–(7.5) numerically with appropriate initial conditions. For (a)–(b) and (c)–(d) the initial conditions are given by Equations (7.8)–(7.9) with $a = 1/10$ and $a = 1$, respectively. For (e)–(f) the initial conditions are given by Equations (7.6)–(7.7). All numerical PDE solutions correspond to $\Delta x = 1 \times 10^{-4}$, $\Delta t = 1 \times 10^{-3}$ and $\epsilon = 1 \times 10^{-4}$.

Figure 7.7(a) shows the three–dimensional desingularised phase space together with the invaded equilibrium point in green, the uninvaded equilibrium point in blue, the heteroclinic orbit in solid blue and the slow manifold in grey. In this case we have $c_2 = 10$ and we see that, as expected, the heteroclinic orbit enters the uninvaded equilibrium point after moving along the slow manifold. In Figure 7.7(b) we plot the slow manifold locally around the uninvaded equilibrium point together with the vector field defined by Equations (7.38)–(7.39). The heteroclinic orbit from the long–time PDE solution is shown in blue. We see that the heteroclinic orbit is tangential to the vector field and enters the uninvaded equilibrium point. For completeness we also solve Equations (7.38)–(7.39) numerically to show a number of other solution trajectories on the slow manifold in red. While these other solution curves are valid solutions of Equations (7.38)–(7.39), they are unphysical in the sense that they are not associated with the travelling wave solution since they do not form a heteroclinic orbit joining the invaded and uninvaded equilibrium points. Figure 7.7(b)–(c) shows a similar set of results to those in Figure 7.7(a)–(b) for a different smooth–fronted travelling wave, this time with $c_1 = 1$. Again we see that the heteroclinic orbit moves into the uninvaded equilibrium point along the slow manifold in Figure 7.7(c), with additional details shown on the slow manifold in Figure 7.7(d). Interestingly, results in Figure 7.7(e)–(f), for a sharp–fronted travelling wave with $c_{\min} = 0.29$ are quite different to the smooth–fronted travelling waves in Figure 7.7(a)–(d). Here the heteroclinic orbit joining the invaded and uninvaded equilibrium points enters the uninvaded equilibrium point directly, without moving along the slow manifold. This difference is highlighted in Figure 7.7(d) where we see that there is no component of the heteroclinic orbit on the slow manifold. These results in Figure 7.7 are for one particular choice of $r_1 = r_2 = 1$, and similar results for different choices of r_1 and r_2 show the same qualitative behaviour (Supplementary Material).

In summary, these results show us that we can make a simple geometric distinction between smooth–fronted travelling waves and sharp–fronted travelling waves using the slow manifold reduction. Smooth–fronted travelling waves involve a heteroclinic orbit joining $(\bar{U}, \bar{S}, \bar{W}) = (1, R, 0)$ and $(\bar{U}, \bar{S}, \bar{W}) = (0, 0, 0)$, such that the heteroclinic orbit enters $(0, 0, 0)$ along the slow manifold, given by Equation (7.37). In contrast, sharp–fronted travelling

240

waves involve a heteroclinic orbit joining the same two equilibrium points, with the difference being that the heteroclinic orbit enters $(0,0,0)$ directly, without moving along the slow manifold. These differences are summarised schematically in Figure 7.8.
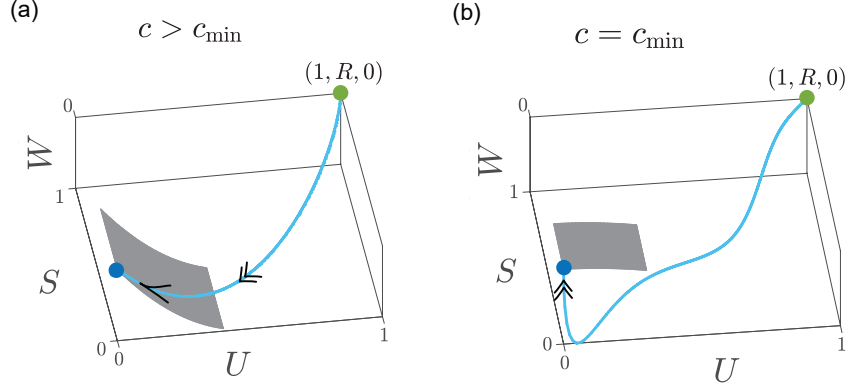
Figure 7.8: Schematic distinction between smooth–fronted and sharp–fronted travelling wave solutions. The schematic in (a) corresponds to a smooth–fronted travelling wave solution with $c > c_{\min}$, where the heteroclinic orbit (blue) in the desingularised phase space moves into the $(0,0,0)$ along the slow manifold (grey surface). The schematic in (b) corresponds to a sharp–fronted travelling wave solution with $c = c_{\min}$, where the heteroclinic orbit (blue) enters the uninvaded equilibrium point, $(0,0,0)$, without moving along the slow manifold (grey surface).

It is worth noting that the computational phase space tools in Figure 7.7(a),(c) and (e) provide physical insight into the interpretation of the minimum wave speed, $c_{\min}$, for the substrate model. While it is not possible to compute a long–time PDE solution with $c < c_{\min}$, it is straightforward to plot the three–dimensional phase space and integrate Equations (7.25)–(7.27) numerically to explore various trajectories in the relevant octant where $U \geq 0$, $S \geq 0$ and $W \leq 0$. These explorations show that we can identity a unique trajectory that enters the origin just like we did for $c \geq c_{\min}$, however part of this trajectory has $U < 0$ which is why it can never be associated with a physically relevant travelling wave solutions (Supplementary Material). This observation shares similarities and differences with the phase plane analysis of the classical Fisher-KPP model, where the exact result $c_{\min} = 2$ is found by ensuring that $U > 0$ near the origin [Murray 2002]. In the simpler Fisher-KPP model, the origin is an equilibrium point and so linearisation gives us the local properties of the phase plane, leading to this result. Similar methodology applies for more complicated generalisations of the Fisher-KPP model [Vittadello et al. 2018]. In the case of our substrate model, it appears that $c_{\min}$ is also defined by requiring that $U > 0$ along the heteroclinic orbit (Supplementary Mate-

rial). Conversely, numerical explorations show that when $c < c_{min}$ we observe that $U < 0$ for portions of the orbit that do not pass through a neighbourhood of the equilibrium point. This observation suggests that linearisation cannot be used to find a mathematical expression for c_{min}.

For the next part of this work we attempt to understand how the shape of the travelling wave profiles depends upon the parameters in the mathematical model. We will derive two such approximations; one for sharp–fronted travelling wave solutions, and the other for smooth–fronted travelling wave solutions. In both cases we test our approximations using full time–dependent PDE solutions.

7.3.6 Approximate solution for sharp–fronted travelling waves

Numerical results in Section 7.3.2 imply a relationship between the substrate model and the Porous–Fisher model, which we now explore further. For fast substrate production and decay, $r_1 \gg 1$ and $r_2 \gg 1$, respectively, we anticipate that Equation (7.4) gives approximately $s = Ru$, and that Equation (7.3) is approximately

$$\frac{\partial u}{\partial t} = R\frac{\partial}{\partial x}\left(u\frac{\partial u}{\partial x}\right) + u(1 - u), \quad 0 < x < \infty, \tag{7.40}$$

which is the non–dimensional Porous–Fisher model with the diffusion term scaled by the constant R. Therefore, we can make use of known results for the Porous–Fisher model in this limit. In particular, sharp–fronted travelling wave solutions of the Porous–Fisher model are known to have the closed–form solution [Murray 2002, Sherratt and Marchant 1996]

$$U(z) = \begin{cases} 1 - \exp\left(\dfrac{z - z_c}{2c}\right), & z < z_c, \\ 0, & z > z_c, \end{cases} \tag{7.41}$$

$$S(z) = RU(z) \qquad -\infty < z < \infty, \tag{7.42}$$

where $c = c_{min} = \sqrt{R/2}$ and z_c is the location of the sharp front [Murray 2002]. Note that Equation (7.42) is equivalent to substituting Equation (7.41) into Equation (7.13) and evaluating the resulting expression in the limit that $r_1 \to \infty$ and $r_2 \to \infty$.

Results in Figure 7.9 examine how late–time numerical PDE solutions can be approximated by Equations (7.41)–(7.42). Results in (a)–(c), (d)–(f) and (g)–(i) correspond to $R = 0.5, 1$ and 2, respectively, and in each case we see that Equations (7.41)–(7.42) provide a good match with the shape of the travelling wave solution of the substrate model as r_1 and r_2 increase.
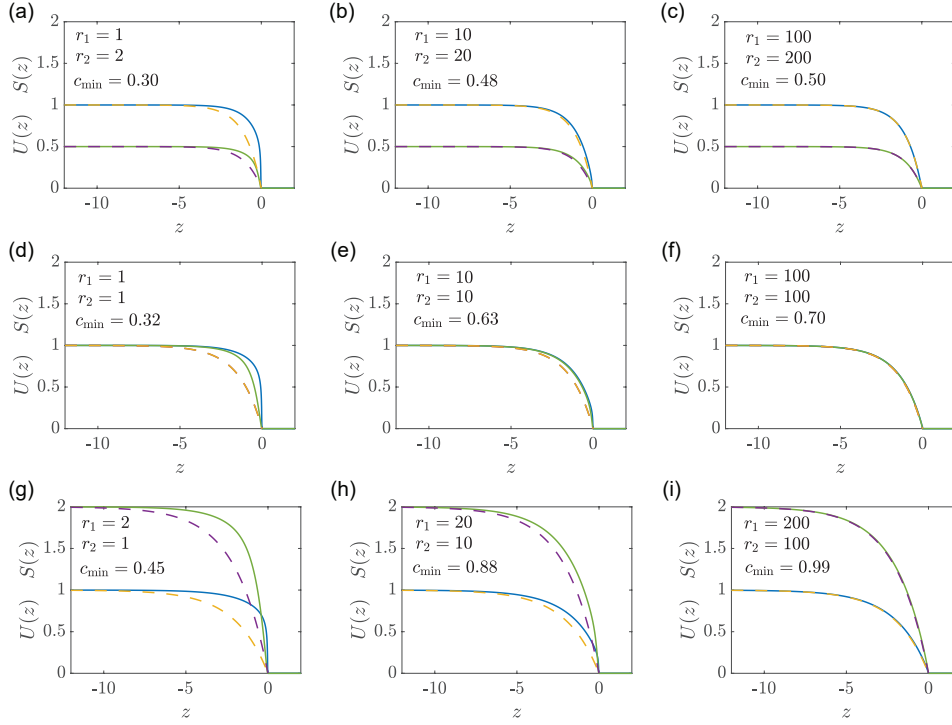
Figure 7.9: Approximate shape of sharp–fronted travelling wave solutions. Various numerical travelling wave solutions, $U(z)$ and $S(z)$, obtained by solving Equations (7.3)–(7.7) are compared with the approximation given by Equations (7.41)–(7.42), where z is shifted so that $z_c = 0$. Results in (a)–(c), (d)–(f) and (g)–(i) correspond to $R = 0.5, 1$ and 2, respectively. Each subfigure shows the appropriate value of r_1, r_2 and $c_{\min}$. All numerical PDE solutions correspond to $\Delta x = 1 \times 10^{-2}$, $\Delta t = 1 \times 10^{-3}$ and $\epsilon = 1 \times 10^{-10}$.

7.3.7 Approximation solution for smooth–fronted travelling waves

Previous results in Figure 7.8 suggest that smooth–fronted travelling waves become less steep as c increases, implying that $W(z) = \mathrm{d}U/\mathrm{d}z \to 0$ as $c \to \infty$. Following the work of Canosa we make use of this observation to develop a perturbation solution by re-scaling the independent variable, $\hat{z} = z/c$ to give [Canosa 1973],

$$\frac{1}{c^2}\frac{\mathrm{d}}{\mathrm{d}\hat{z}}\left(S\frac{\mathrm{d}U}{\mathrm{d}\hat{z}}\right) + \frac{\mathrm{d}U}{\mathrm{d}\hat{z}} + U(1-U) = 0, \qquad -\infty < \hat{z} < \infty, \tag{7.43}$$

$$\frac{\mathrm{d}S}{\mathrm{d}\hat{z}} + r_1 U - r_2 S = 0, \qquad -\infty < \hat{z} < \infty. \tag{7.44}$$

To proceed, we seek a perturbation solution in terms of the small parameter $1/c^2$ by expanding the dependent variables in a power series [Murray 1984],

$$U(\hat{z}) = \sum_{n=0}^{\infty} c^{-2n} U_n(\hat{z}), \quad S(\hat{z}) = \sum_{n=0}^{\infty} c^{-2n} S_n(\hat{z}). \tag{7.45}$$

Substituting these power series into Equations (7.43)–(7.44) and truncating after the first few terms gives

$$\frac{\mathrm{d}U_0}{\mathrm{d}\hat{z}} + U_0(1-U_0) = 0, \tag{7.46}$$

$$\frac{\mathrm{d}S_0}{\mathrm{d}\hat{z}} + r_1 U_0 - r_2 S_0 = 0, \tag{7.47}$$

$$\frac{\mathrm{d}}{\mathrm{d}\hat{z}}\left(S_0\frac{\mathrm{d}U_0}{\mathrm{d}\hat{z}}\right) + \frac{\mathrm{d}U_1}{\mathrm{d}\hat{z}} + U_1(1-2U_0) = 0, \tag{7.48}$$

with boundary conditions $U_0 \to 1$, $U_1 \to 0$ and $S_0 \to R$ as $\hat{z} \to -\infty$, and $U_0 \to 0$, $U_1 \to 0$ and $S_0 \to 0$ as $\hat{z} \to \infty$. It is straightforward to solve these differential equations for $U_0(\hat{z})$, $U_1(\hat{z})$ and $S_0(\hat{z})$, however additional terms in the perturbation solution are governed by differential equations that do not have closed–form solutions. Regardless, as we shall now show, these first few terms in the perturbation solution provide accurate approximations, even for relatively small values of c.

The solution of Equation (7.46) is

$$U_0(z) = \frac{1}{1+\exp\left(\hat{z}\right)}, \tag{7.49}$$

where we have arbitrarily chosen the integration constant so that $U_0(0) = 1/2$. Given $U_0(z)$, we solve (7.47) using an integrating factor to give

$$S_0(\hat{z}) = -r_1 \exp(r_2 \hat{z}) \int_{\hat{z}}^{\infty} \frac{\exp(-r_2 \hat{z})}{1 + \exp(\hat{z})} \, \mathrm{d}\hat{z}. \qquad (7.50)$$

If r_2 is an integer we obtain

$$S_0(\hat{z}) = (-1)^{r_2} \exp(r_2 \hat{z}) \, r_1 \left[\ln\left(\exp[-\hat{z}] + 1\right) + \sum_{n=1}^{r_2} \frac{\exp(-n\hat{z})}{n(-1)^n} \right]. \qquad (7.51)$$

If r_2 is not an integer there is no closed–form expression for $S_0(\hat{z})$ that we could find. For particular integer choices of r_1 the expression for $S_0(\hat{z})$ is quite simple. For example, with $r_2 = 1$ we have $S_0(\hat{z}) = r_1 \left[1 - \exp(\hat{z})\ln(\exp[-\hat{z}] + 1)\right]$, whereas for $r_2 = 2$ we have $S_0(\hat{z}) = r_1 \left[1/2 - \exp(\hat{z}) + \exp(2\hat{z})\ln(\exp[-\hat{z}] + 1)\right]$. The solution for $U_1(\hat{z})$ is obtained by integrating Equation (7.48) using an integrating factor to give

$$U_1(\hat{z}) = \frac{\exp(\hat{z})}{(1 + \exp[\hat{z}])^2} \int_{\hat{z}}^{\infty} \frac{\mathrm{d}}{\mathrm{d}\hat{z}} \left[S_0 \frac{\exp(\hat{z})}{(1 + \exp[\hat{z}])^2} \right] \left[\frac{(1 + \exp[\hat{z}])^2}{\exp(\hat{z})} \right] \mathrm{d}\hat{z}. \qquad (7.52)$$
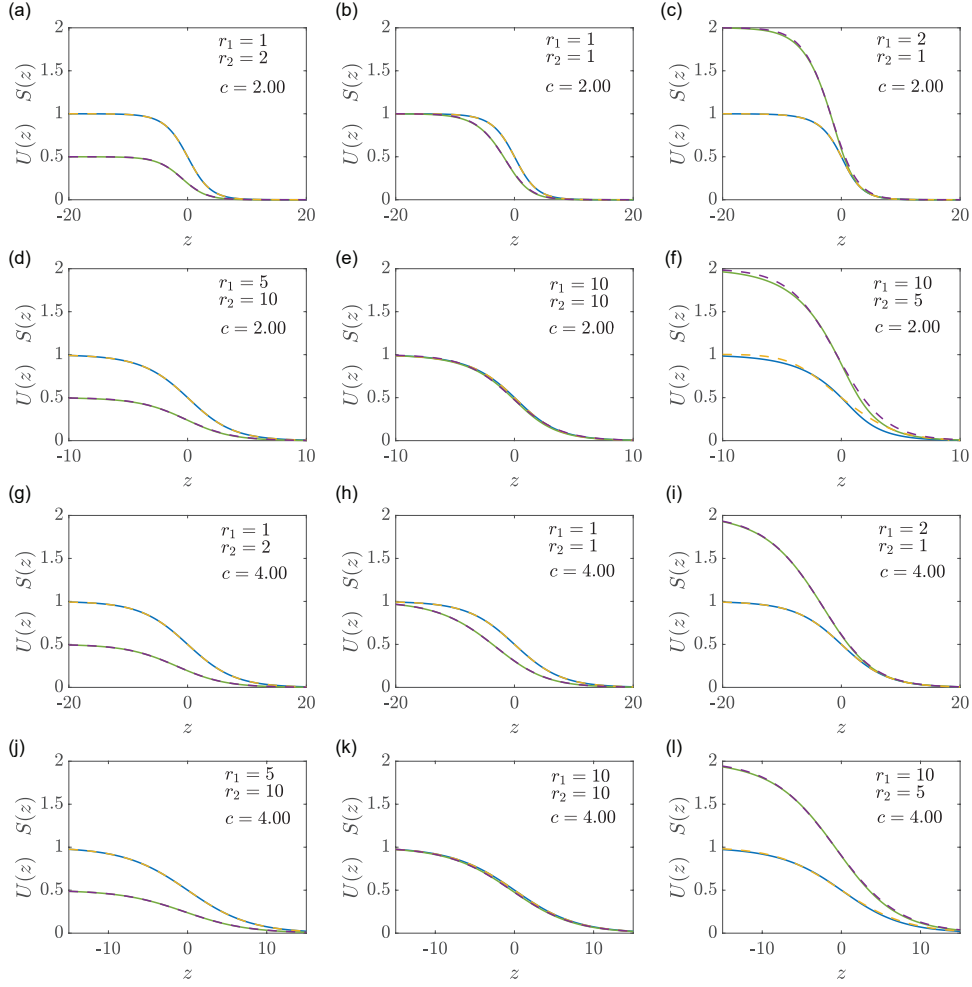
Figure 7.10: Approximate shape of smooth–fronted travelling wave solutions. Results in (a)–(f) and (g)–(l) compare the numerical and perturbation solutions for $c = 2.00$ and $c = 4.00$, respectively. Results in the left–most column correspond to $R = 0.5$, those in the central column correspond to $R = 1$, and those in the right–most column correspond to $R = 2$. Numerical solutions correspond to late–time numerical solutions of Equations (7.3)–(7.5), with initial conditions given by Equations (7.8)–(7.9) with appropriate values of a. Numerical solutions of $U(z)$ and $S(z)$ are shown in blue and green, respectively. Each numerical solution is superimposed with an $\mathcal{O}(1)$ perturbation solution for $S(z)$ and an $\mathcal{O}(1/c^2)$ for $U(z)$, and these perturbation solutions are shown in yellow and purple dashed curves, respectively.

Since this expression for $U_1(\hat{z})$ depends upon the expression for $S_0(\hat{z})$, we can only obtain closed–form expressions for $U_1(\hat{z})$ for integer values of r_2. In these cases, expressions for $U_1(\hat{z})$ are relatively complicated and so we include these expressions in the Supplementary Material. We note that care is required when evaluating $U_1(\hat{z})$ since the expression is indeterminate for large $\hat{z}$. We address this simply by expanding $U_1(\hat{z})$ in a Taylor series as $\hat{z} \to \infty$ and plotting the series expansion for large $\hat{z}$.

Results in Figure 7.10 compare the shapes of various smooth–fronted trav-

246

elling wave solutions, for $c = 2$ and $c = 4$, with the $\mathcal{O}(1)$ perturbation solution for $S(z)$ and the $\mathcal{O}(c^{-2})$ perturbation solution for $U(z)$. These comparisons are made across a range of values of r_1 and r_2, and for $c = 4$ the perturbation solutions are indistinguishable from the late–time numerical solutions. In cases where $c = 2$ we begin to see a small departure between the numerical and perturbation approximations. Given that the perturbation solutions are valid in the limit $c \to \infty$, the quality of match in Figure 7.10 for $c = 2$ and $c = 4$ is quite good.

7.4 Conclusion and Future Work

In this study we investigate a minimal model of cell invasion that couples cell migration, cell proliferation and cell substrate production and decay. A key feature of the mathematical model is that the diffusive flux is proportional to the substrate density so that the flux vanishes when the substrate is absent. This feature leads to predictions of tissue formation involving the propagation of well–defined sharp fronts, and two–dimensional numerical simulations of the mathematical model reconstitute key features of recent experiments that involved the formation of thin tissues grown on 3D–printed scaffolds [Lanaro et al. 2021]. To gain a deeper understanding of how the rate of substrate production and decay affects the rate of tissue production, the focus of this work is to study solutions of the substrate model in a one–dimensional geometry.

Preliminary numerical simulations of the substrate model in one dimension indicate that the mathematical model supports two types of travelling wave solutions. As we show, sharp–fronted travelling waves that propagate with a minimum wave speed, c_{min}, evolve from initial conditions with compact support, whereas smooth–fronted travelling waves that move with a faster wave speeds, $c > c_{\text{min}}$, evolve from initial conditions where the density decays exponentially with position. These numerical features are reminiscent of established features of travelling wave solutions of the well–known Porous–Fisher model.

Much of our analysis focuses on exploring the relationships between smooth–fronted and sharp–fronted travelling wave solutions, and here key features of the analysis of the substrate model are very different to the analysis of the Porous–Fisher model. For example, there are three equilibrium points in

the desingularised phase plane for the Porous–Fisher model whereby smooth–fronted travelling wave solutions are characterised by a heteroclinic orbit that enters $(\bar{U}, \bar{V}) = (0, 0)$, whereas sharp–fronted travelling wave solutions involves a heteroclinic orbit that enters $(\bar{U}, \bar{V}) = (0, -c)$. In contrast, the desingularised phase space for the substrate model involves two equilibrium points only. This means that both smooth–fronted and sharp–fronted travelling waves correspond to heteroclinic orbits that enter $(\bar{U}, \bar{S}, \bar{W}) = (0, 0, 0)$, which is fundamentally different to the Porous–Fisher model. We provide a geometric interpretation that explains the difference between sharp–fronted and smooth–fronted travelling wave solutions since smooth–fronted travelling wave solutions are associated with a heteroclinic orbit that enters the origin in the desingularised phase space by moving along a slow manifold. In contrast, sharp–fronted travelling wave solutions are associated with a heteroclinic orbit that enters the origin of the desingularised phase space directly, without moving along the slow manifold. Additionally, we also develop and test useful closed–form expressions that describe the shape of the travelling wave solutions in various limits. In particular, we provide accurate approximations for the shape of sharp–fronted travelling waves for sufficiently large r_1 and r_2, as well as accurate approximation of the shape of the smooth–fronted travelling wave solutions relevant for large c.

There are many avenues for extending the current work, and these options include further analysis of the current model as well as conducting parallel analysis for related mathematical models. In terms of the current model, our analysis has not provided any relationship between c_{min} and the two parameters in the nondimensional model, r_1 and r_2. For simpler mathematical models, such as the Fisher-KPP model, the relationship between the minimum wave speed and the parameters in the model arises by linearising about the leading edge of the travelling wave [Murray 2002]. As we have shown, an interesting feature of the substrate model is that standard techniques to linearise about the leading edge do not apply. Another possibility for extending the analysis of this model would be to consider the mathematical model in two-dimensions, such as describing the late–time dynamics of hole–closing phenomena [McCue et al. 2019].

A different class of extensions of this work would be to consider generalising

the nonlinear diffusion term in the substrate model, such as

$$\frac{\partial u}{\partial t} = \frac{\partial}{\partial x}\left(\mathcal{D}(s)\frac{\partial u}{\partial x}\right) + u(1-u), \qquad 0 < x < \infty \qquad (7.53)$$

$$\frac{\partial s}{\partial t} = r_1 u - r_2 s, \qquad 0 < x < \infty. \qquad (7.54)$$

This generalised substrate model involves a nonlinear diffusivity function, $\mathcal{D}(s)$. We anticipate that nonlinear diffusivity functions with the property $\mathcal{D}(0) = 0$ will support sharp–fronted travelling wave solutions, and there are many such candidate functions. One option of interest is a power–law diffusivity $\mathcal{D}(s) = s^n$, where n is some exponent. It would be interesting to explore how different choices of n affect various qualitative and quantitative features of the travelling wave solutions that have been established in the present study for $n = 1$. We hope to return to address these open questions in future research.

7.5 Additional material

7.5.1 Numerical methods

7.5.1.1 Two–Dimensional partial differential equations

Numerical solutions of the substrate model in two–dimensions are obtained by re-writing Equations (1)–(2) as

$$\frac{\partial u}{\partial t} = \frac{\partial}{\partial x}\left[\mathcal{D}(s)\frac{\partial u}{\partial x}\right] + \frac{\partial}{\partial y}\left[\mathcal{D}(s)\frac{\partial u}{\partial y}\right] + f(u), \tag{7.55}$$

$$\frac{\partial s}{\partial t} = g(u, s), \tag{7.56}$$

where we have written the mathematical model in terms of a general nonlinear diffusivity function $\mathcal{D}(s)$, and general source terms, $f(u)$ and $g(u, s)$. To be consistent with our dimensional model we have $\mathcal{D}(s) = Ds/K_s$, $f(u) = \lambda u(1 - u/K_u)$ and $g(u, s) = r_1 u - r_2 s$, but our numerical method can deal with other functional forms if required. Our aim is to obtain numerical solutions of Equations (7.55)–(7.56) on the square domain $\Omega = \{(x, y), 0 < x < L, 0 < y < L\}$. For convenience we assume that the origin is at the lower left corner of the domain and we discretise Ω on a spatially uniform finite difference mesh with mesh spacing $\Delta x = \Delta y > 0$. We index the mesh in the usual way so that the coordinates of each mesh point are (x_i, y_j), with $i = 0, 1, 2, \ldots, I$ and $j = 0, 1, 2, \ldots, J$. Since we always consider a square mesh we have $I = J$. All numerical results correspond to a 101×101 mesh which, with $L = 300$ μm, gives $\Delta x = 3$ μm. We found that solutions obtained on a finer mesh gave visually indistinguishable results for the parameter values that we considered.

We solve Equations (7.55)–(7.56) using a standard method of lines approach so that at each internal mesh point we have

$$\begin{aligned}
\frac{\mathrm{d}u_{i,j}}{\mathrm{d}t} &= \frac{1}{2\Delta x^2}\left[(\mathcal{D}(s_{i,j}) + \mathcal{D}(s_{i+1,j}))\,(u_{i+1,j} - u_{i,j})\right. \\
&\quad \left. - (\mathcal{D}(s_{i,j}) + \mathcal{D}(s_{i-1,j}))\,(u_{i,j} - u_{i-1,j})\right] \\
&\quad + \frac{1}{2\Delta x^2}\left[(\mathcal{D}(s_{i,j}) + \mathcal{D}(s_{i,j+1}))\,(u_{i,j+1} - u_{i,j})\right. \\
&\quad \left. - (\mathcal{D}(s_{i,j}) + \mathcal{D}(s_{i,j-1}))\,(u_{i,j} - u_{i,j-1})\right] + f(u_{i,j}), \tag{7.57}
\end{aligned}$$

$$\frac{\mathrm{d}s_{i,j}}{\mathrm{d}t} = g(u_{i,j}, s_{i,j}), \tag{7.58}$$

where we have approximated the internode diffusivity with an arithmetic av-

erage. These discretised equations are valid at central nodes, $i = 1, 2, \ldots, I-1$ and $j = 1, 2, \ldots, I - 1$, and we implement Dirichlet boundary conditions for both dependent variables along all boundaries. We explored various temporal integration methods and found that all standard approaches led to grid–independent results when Δx and the temporal step size are sufficiently small. For simplicity all results in the main document correspond to the simplest forward Euler temporal integration with constant time steps of duration Δt.

7.5.1.2 One–dimensional partial differential equations

To solve Equations (7.3)–(7.5) we consider a domain $0 < x < L$ that we discretise into m equally–sized intervals with spacing Δx. We approximate Equations (7.3)–(7.4) using a central difference approximation for the spatial derivative. Since we use this algorithm to study long–time travelling wave solutions we approximate the temporal derivative with an implicit Euler approximation, giving

$$\frac{u_i^{j+1} - u_i^j}{\Delta t} = \frac{1}{2\Delta x^2} \left[(s_{i+1}^{j+1} + s_i^{j+1})(u_{i+1}^{j+1} - u_i^{j+1}) - (s_i^{j+1} + s_{i-1}^{j+1})(u_i^{j+1} - u_{i-1}^{j+1}) \right]$$
$$+ u_i^{j+1} \left(1 - u_i^{j+1} \right), \tag{7.59}$$

$$\frac{s_i^{j+1} - s_i^j}{\Delta t} = r_1 u_i^{j+1} - r_2 s_i^{j+1}, \tag{7.60}$$

for $i = 2, \ldots, m-1$, where $m = 1/h + 1$ is the total number of spatial nodes on the finite difference mesh, and the index j represents the time index so that $u_i^j \approx u(x, t)$ and $s_i^j \approx s(x, t)$, where $x = (i-1)\Delta x$ and $t = j\Delta t$. The boundary conditions for u are discretized to give

$$u_2^{j+1} - u_1^{j+1} = 0, \quad u_m^{j+1} = 0. \tag{7.61}$$

We solve the resulting system of nonlinear algebraic equations for u using Newton-Raphson algorithm with convergence tolerance ϵ. Once we have the updated solutions for u_i^{j+1}, updated estimates of s_i^{j+1} are given by Equation (7.60).

7.5.2 Numerical estimate of the travelling wave speed c

We estimate the travelling wave speed by specifying a particular contour value, $u(x,t) = u^*$ and use linear interpolation to estimate x^* such that $u(x^*,t) = u^*$ at each time step. With this data we then calculate

$$c = \frac{x^*(t + \Delta t) - x^*(t)}{\Delta t}, \tag{7.62}$$

at each time step, which we find settles to a constant value for sufficiently large t. Given this time series of estimates for c we fit a straight line to the late–time data to provide an estimate of c. All results in this work correspond to $u^* = 0.5$, but we find that our results are insensitive to this choice and other values of $u^* \in (0,1)$ give the same results provided that δt and h are chosen to be sufficiently small.

7.5.2.1 Phase plane on the slow manifold

We solve Equations (7.38)–(7.39) numerically to estimate trajectories on the slow manifold using Heun's method with a constant step size $d\zeta$. The vector field of the dynamical system is plotted on the phase planes using the MATLAB *quiver* function [Mathworks 2021].

7.5.3 Additional results and discussion

7.5.3.1 Far–field behaviour of smooth–fronted travelling waves

Here we provide numerical evidence to test the hypothesis that the shape of smooth–fronted travelling waves are given by Equations (7.19)–(7.21). Results in Figure 7.11(a) show a smooth–fronted travelling wave with $c = 2.00$ for $r_1 = r_2 = 1$. Using our long–time numerical PDE solution we plot $U(z)$, $S(z)$ and $W(z)$ at the leading edge of the travelling wave in Figure 7.11(b). The profiles in Figure 7.11(b) are a magnified view of the region contained within the purple rectangle in Figure 7.11(a). At the scale shown in Figure 7.11(b) we clearly see $U(z)$, $S(z)$ and $W(z)$ decaying to zero with z, and each numerical profile is superimposed with the expressions given by Equations (7.19)–(7.21) which match the numerical results extremely well. To further illustrate this point we show an inset in Figure 7.11(b) comparing the shape of $U(z)$, $S(z)$ and $W(z)$ from the late–time PDE solutions with our proposed

asymptotic expressions (7.19)–(7.21) for even larger values of z, and again we see an excellent match. While the comparison in Figure 7.11 is made for one particular choices of r_1, r_2 and c, we also made similar comparisons for different choice of r_1, r_2 and c, and in each case we found an excellent match between Equations (7.19)–(7.21) and the shape of the smooth–fronted travelling waves as $z \to \infty$ (not shown).
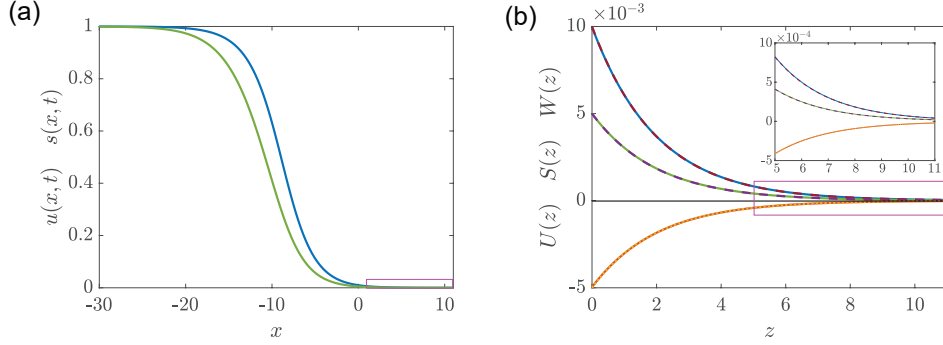
Figure 7.11: Shape of the leading edge for smooth–fronted travelling waves as $z \to \infty$. (a) late time numerical solutions of (7.3)–(7.5), with initial conditions (7.8)–(7.9) and $a = 1/2$. The profile for $u(x, t)$ is shown in blue, and the profile for $s(x, t)$ is shown in green. Parameters in the PDE model are $r_1 = r_2 = 1$ and the long–time speed of the smooth–fronted travelling wave is $c = 2.00$. (b) shows the far-field behaviour of $U(z)$ (blue), $S(z)$ (green) and $W(z)$ (yellow) estimated from the late–time PDE solution superimposed with the solutions given by Equations (7.19)–(7.21) in dashed red, dashed purple and dotted red, respectively, for $0 \le z \le 11$. The constant C in Equation (7.19) is obtained by matching the PDE solution with the exponentially decaying solution at $U = 1 \times 10^{-2}$. The solutions in (b) correspond to that part of the solution in (a) contained in the purple rectangle. Similarly, the solution contained in the purple rectangle in (b) is shown as an inset in (b) where the PDE solutions compare very well with the approximate far–field solutions. All numerical PDE solutions correspond to $\Delta x = 1 \times 10^{-2}$, $\Delta t = 1 \times 10^{-3}$ and $\epsilon = 1 \times 10^{-10}$.

7.5.3.2 Phase space and slow manifold

Results in Figure 7 show the phase space and slow manifold for $R = 1$. Analogous results for $R = 0.5$ and $R = 2$ are given here in Figures (7.11) and (7.12) where we see that the same trends persist for different values of R.

7.5.3.3 Phase space
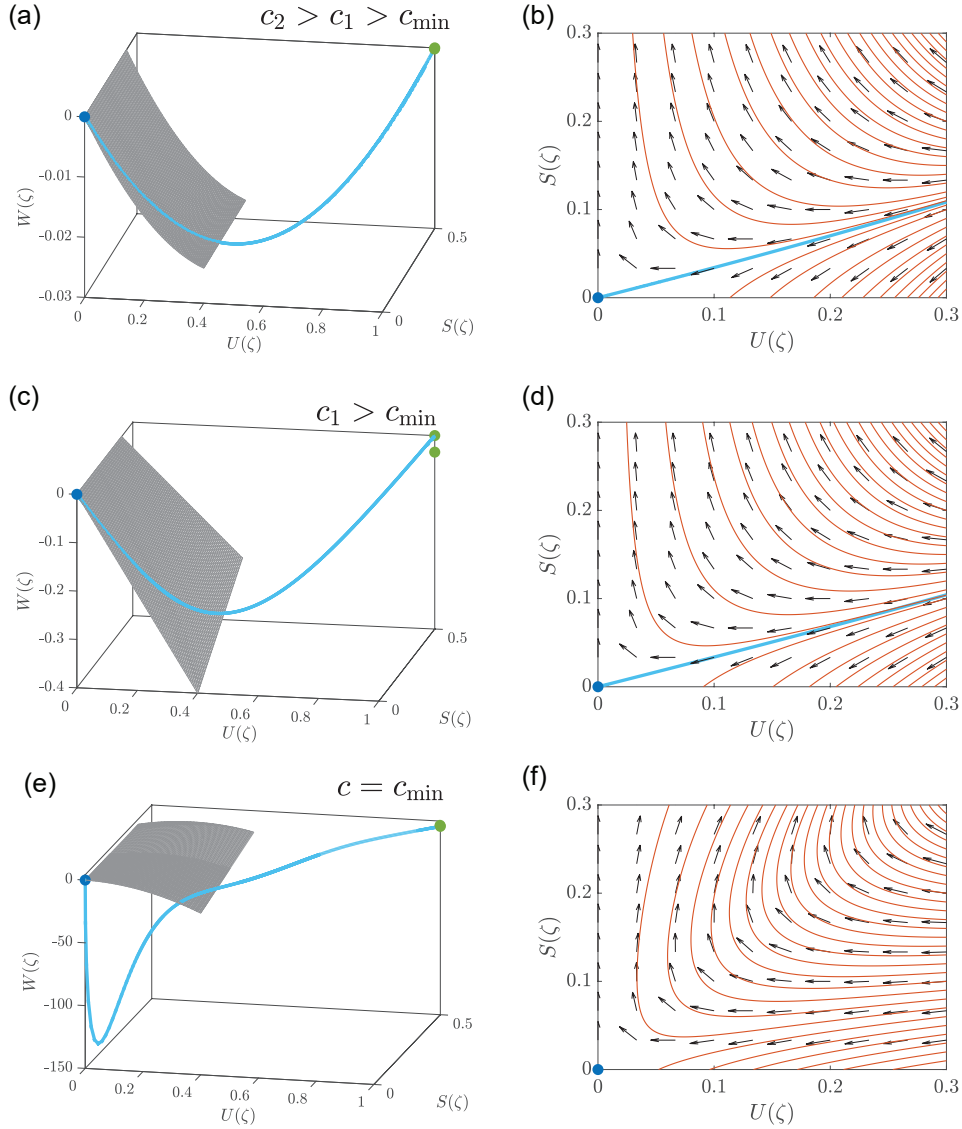
Figure 7.12: Desingularised phase space and slow manifold reduction. All results correspond to $R = 0.5$ ($r_1 = 1$, $r_2 = 2$). Results in: (a)–(b) correspond to a smooth–fronted travelling wave with $c_2 = 10$; (c)–(d) correspond to a smooth–fronted travelling wave with $c_1 = 1$; and, (e)–(f) correspond to a sharp–fronted travelling wave with $c_{\min} = 0.27$. Results in the left–most column show the three–dimensional desingularised phase space with the invaded equilibrium point (green dot), the un-invaded equilibrium point (blue dot) and the slow manifold (grey surface). Results in the right–most column show the vector field on the slow manifold, superimposed with several solution trajectories, including the heteroclinic orbit (blue) and several unphysical trajectories (red). The heteroclinic orbit is obtained by solving Equations (7.3)–(7.5) numerically with appropriate initial conditions. For (a)–(b) and (c)–(d) the initial conditions are given by Equations (7.8)–(7.9) with $a = 1/10$ and $a = 1$, respectively. For (e)–(f) the initial conditions are given by Equations (7.6)–(7.7). All numerical PDE solutions correspond to $\Delta x = 1 \times 10^{-4}$, $\Delta t = 1 \times 10^{-3}$ and $\epsilon = 1 \times 10^{-4}$.

Figure 7.13: Desingularised phase space and slow manifold reduction. All results correspond to $R = 2$ ($r_1 = 1$, $r_2 = 0.5$). Results in: (a)–(b) correspond to a smooth–fronted travelling wave with $c_2 = 10$; (c)–(d) correspond to a smooth–fronted travelling wave with $c_1 = 1$; and, (e)–(f) correspond to a sharp–fronted travelling wave with $c_{\min} = 0.30$. Results in the left–most column show the three–dimensional desingularised phase space with the invaded equilibrium point (green dot), the un-invaded equilibrium point (blue dot) and the slow manifold (grey surface). Results in the right–most column show the vector field on the slow manifold, superimposed with several solution trajectories, including the heteroclinic orbit (blue) and several unphysical trajectories (red). The heteroclinic orbit is obtained by solving Equations (7.3)–(7.5) numerically with appropriate initial conditions. For (a)–(b) and (c)–(d) the initial conditions are given by Equations (7.8)–(7.9) with $a = 1/10$ and $a = 1$, respectively. For (e)–(f) the initial conditions are given by Equations (7.6)–(7.7). All numerical PDE solutions correspond to $\Delta x = 1 \times 10^{-4}$, $\Delta t = 1 \times 10^{-3}$ and $\epsilon = 1 \times 10^{-4}$.

7.5.3.4 Phase space for $c < c_{\mathbf{min}}$

In this section we explore the consequences of setting $c < c_{\min}$ in the phase space. Results in Figure 7.14 show the desingularised phase spaces for $r_1 = r_2 = 1$, where as have previously demonstrated in Figure 7 that late–time numerical solutions of the time–dependent PDE model gives $c_{\min} = 0.29$. Results in Figure 7.14(a) shows the three–dimensional phase space with $c = 0.40 > c_{\min}$. The yellow trajectory is obtained by integrating (7.25)–(7.27) and carefully choosing an initial point to give a heteroclinic orbit that joins the invaded and uninvaded equilibrium points. Figure 7.14(b) shows a two–dimensional projection of this trajectory in the US plane. Results in Figure 7.14(c)–(d) show analogous results for $c = 0.29 = c_{\min}$. The most interesting results here are in Figure 7.14 for $c = 0.25 < c_{\min}$ where we see that the trajectory enters the uninvaded equilibrium point at the origin, but that this trajectory is non-physical since it involves $U < 0$ along that trajectory. This transition is clear in Figure 7.14(f) where we show the projection of the trajectory in the US plane. This transition from having $U > 0$ for $c > c_{\min}$ to $U < 0$ for $c < c_{\min}$ also holds for other choices of r_1 and r_2 (not shown).
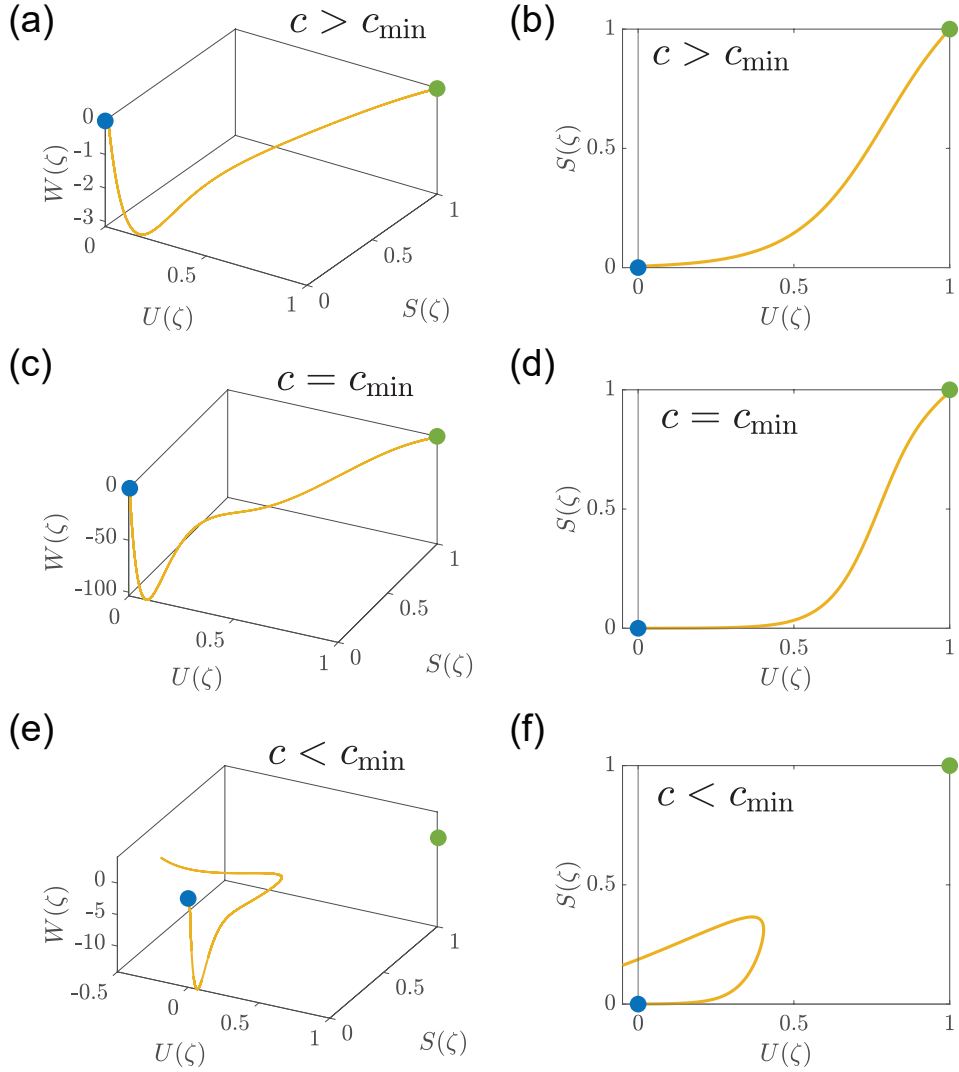
Figure 7.14: Phase space for $c < c_{\mathbf{min}}$. All results correspond to $r_1 = 1$ and $r_2 = 2$. Results in: (a)–(b) correspond to a smooth–fronted travelling wave with $c = 0.4 > c_{\min}$; (c)–(d) correspond to a sharp–fronted travelling wave with $c = 0.29 = c_{\min}$; and, (e)–(f) does not correspond to a travelling wave since $c = 0.25 < c_{\min}$. Results in (a), (c) and (e) are obtained by integrating (7.25)–(7.27) numerically, with a careful choice of initial condition so that we find the unique trajectory that enters the origin. Results in (b), (d) and (f) are obtained by projecting the three–dimensional trajectory in (a), (c) and (e), respectively, onto the US plane. In each panel the invaded equilibrium point, $(\bar{U}, \bar{S}, \bar{W}) = (1, R, 0)$, is shown with a green disc. The uninvaded equilibrium point, $(\bar{U}, \bar{S}, \bar{W}) = (0, 0, 0)$, is shown with a blue disc. All trajectories are obtained by integrating (7.25)–(7.27) using Heun's method with $d\zeta = 1 \times 10^{-2}$.

7.5.3.5 Perturbation solution for $c \to \infty$

In Equation (52) we left the expression for $U_1(\hat{z})$ as an integral. Here, we give present a solution for $U_1(\hat{z})$ for some special choices. For $r_2 = 1$ we obtain

$$
\begin{aligned}
U_1(\hat{z}) = \left(\frac{r_1 \exp(\hat{z})}{[1 + \exp(\hat{z})]^2} \right) \big(&-\ln[1 + \exp(\hat{z})]^2 + 2\hat{z}\ln[1 + \exp(\hat{z})] \\
&+ 2\mathrm{Li}_2[1 + \exp(\hat{z})] - \ln[\exp(-\hat{z}) + 1] \big),
\end{aligned}
\tag{7.63}
$$

257

and when $r_2 = 2$ we obtain

$$U_1(\hat{z}) = \left(\frac{r_1 \exp(\hat{z})}{2[1 + \exp(\hat{z})]^2} \right) \left(-2 \ln[1 + \exp(\hat{z})]^2 + 4\hat{z} \ln[1 + \exp(\hat{z})] \right.$$

$$\left. + 4\mathrm{Li}_2[1 + \exp(\hat{z})] + [\exp(2\hat{z}) + 4\exp(\hat{z}) - 1] \ln[\exp(-\hat{z}) + 1] - \exp(\hat{z}) \right),$$

$$(7.64)$$

where $\mathrm{Li}_2(x)$ is a special function called the dilogarithm function that is given by [Maple 2021]

$$\mathrm{Li}_2(x) = \int_1^x \frac{\ln(t)}{1 - t} \, \mathrm{d}t. \tag{7.65}$$

Additional results in Figure (7.15) compare the $\mathcal{O}(1/c^2)$ perturbation solution for $U(z)$ with numerical estimates from the long–time numerical PDE solution, together with the $\mathcal{O}(1)$ perturbation solution for $S(z)$ with numerical estimates from the long–time numerical PDE solution. In this case we focus on $c = 1$ for various values of r_1 and r_2, as indicated. Here, despite the fact we are working with a relatively small value of c and the perturbation solutions are valid in the limit $c \to \infty$, the accuracy of the perturbation solutions is remarkable.
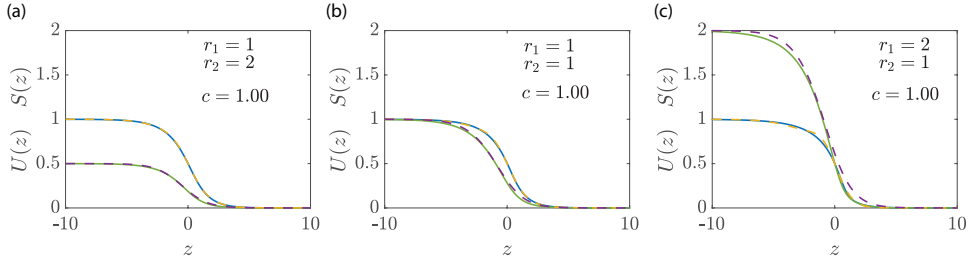
Figure 7.15: Perturbation solution for smooth–fronted travelling wave solutions. Travelling wave solutions $U(z)$ and $S(z)$ are obtained from solving Equations (7.3)–(7.5) with initial conditions (7.8)–(7.9), where $a = 1$ such as the obtained wave speed is $c = 1.00$, with $R = 0.5, 1$ and 2 in (a)–(c), respectively. Numerical solutions $U(z)$ and $S(z)$ are shown in blue and green, respectively, and perturbation solutions for $U(z)$ and $S(z)$ are shown in dashed yellow and purple, respectively.

Chapter 8

Conclusion

8.1 Summary of the research

We started this work by explaining some limitations of the Fisher-KPP model, such as the inability to mimic an invading sharp front of cell population. The model does not support the extinction and the recession of a population. The Fisher-KPP model consists of a single-species equation that does not describe explicitly the interaction of the population with its environment. In our research objectives, we aimed at removing those limitations.

In Chapter 2, we posed the Fisher-Stefan model and studied the solutions of the model. We compared the features of the travelling wave solutions of the Fisher-KPP and the Fisher-Stefan models. The differences between the two models are due to different boundary conditions. The Fisher-KPP equation is defined on an infinite domain where the population vanishes only at infinity. The Fisher-Stefan model is characterised by a moving boundary, governed by a Stefan condition. The first major difference between both models appears in the shape and the speed of the travelling wave solutions: the Fisher-KPP solution is smooth without compact support while the Fisher-Stefan travelling wave solution has a sharp-front with compact support. This difference can also be seen in the phase plane: the physical solutions of the Fisher-KPP model correspond to minimum speed $c_{\min} = 2$ and Fisher-Stefan travelling solutions correspond to wave speeds $0 < c < 2$, that are usually discarded in the Fisher-KPP model. The Stefan condition in the phase plane removes the non-physical part of the trajectory, where the density falls below zero. The second major difference between both models is that the initial population

of Fisher-KPP model always evolve to a travelling solution while some initial conditions in the Fisher-Stefan model lead to extinction. For $\kappa < \kappa_{\text{crit}}$, the solution eventually goes extinct depending if the initial population occupies a domain smaller than the critical length, $L_{\text{crit}} = \pi/2$. Using phase plane and perturbation analysis, we provided a practical relationship between the wave speed of the Fisher-Stefan model and the parameter κ of the Stefan condition.

In Chapter 3, we extended the Fisher-Stefan model to support travelling solutions representing invasion and recession. The model gives rise to invading travelling wave solution with $c \to 2^-$ when $\kappa \to \infty$ and to receding travelling wave solutions with $c \to -\infty$ when $\kappa \to -1$. Using perturbation analysis, we showed that slowly invading or receding travelling wave solutions of the Fisher-Stefan model move with speed $c \sim \kappa/\sqrt{3}$ as $\kappa \to 0$, whereas rapidly receding travelling wave solutions of the Fisher-Stefan model move with speed $c \sim 2^{-1}(\kappa + 1)^{-1/2}$ as $\kappa \to -1^+$.

In Chapter 4, we proposed a generalisation of the Fisher-Stefan model that enables us to study travelling wave solutions with any wave speed, $-\infty < c < \infty$. We modified the Stefan condition in the Fisher-Stefan model to set the density of population $u_{\text{f}} \in [0, 1)$, at the moving boundary. With the previous Fisher-Stefan model, where $u_{\text{f}} = 0$, the wave speeds were restricted to $c < 2$. In the generalised Fisher-Stefan model with $u_{\text{f}} \in [0, 1)$, the speed $c = 2$ does not represent any special limit. We used phase plane and perturbation analysis to give a practical relationship of the wave speed c, in function of κ and u_{f}, for slow ($|c| \ll 1$) invading and receding travelling waves solutions, fast invading ($c \to \infty$) and fast receding ($c \to -\infty$) travelling waves solutions.

In Chapter 5, we extended the Fisher-Stefan model to a two-phase moving boundary model. The two-phase model describes two populations of cells migrating and proliferating, as when cancer cells invade into surrounding skin cells. The moving boundary model gives rise to travelling wave solutions that move in either the positive or negative direction, meaning that the model can simulate malignant invasion or recession. We used numerical simulations and perturbation methods to show that the travelling wave solution for each population is associated with a different trajectory in the phase plane, that is normally disregarded as being non physical in the classical Fisher-KPP model. We presented the steady states behind and ahead of the moving front, for each

population, in either the positive or negative direction, and we showed how the invasion of cancer into skin is symmetrical to the invasion of the skin into cancer. Finally, we explored qualitatively other possible solutions, such as stalling or extinction.

In Chapter 6, we studied two coupled differential equations that describe the dynamics of acid-mediated invasion of cancer into surrounding skin tissues. We used time-dependent numerical solutions of the governing partial differential equations to illustrate how the travelling wave speed c depends on γ, the rate of degradation of skin by cancer cells, and on $\mathcal{V}$, the far field density of surrounding tissues. We obtained smooth-fronted travelling wave solutions when $\mathcal{V} < 1$ and sharp-fronted travelling wave solutions when $\mathcal{V} = 1$. Numerical simulations were useful to establish that the minimal speed $c_{\min} = 2(1-\mathcal{V})$ was independent of γ for $\gamma < \gamma_c$ and that the invading speed c increases with γ for $\gamma > \gamma_c$, with $c \to 2^-$ as $\gamma \to \infty$. We also deduced the dispersion relationship using linearisation and numerical results from initial conditions where the density decays exponentially with position. We studied the role of γ, the decay rate of the skin. Analysis of the invasion model for $\gamma \gg 1$ indicates that the width of the overlap region decreases while γ is increasing, implying that both densities of population become decoupled. Comparison of travelling wave solution when $\gamma \gg 1$ to the disregarded trajectory of Fisher-KPP model in the phase plane showed an interesting similarity.

In Chapter 7, we studied two coupled differential equations that describe the dynamics of substrate-mediated invasion. Time-dependent numerical solutions of the governing partial differential equations from the substrate model evolves to two types of travelling wave solutions, depending of the initial conditions. Sharp-fronted travelling waves solutions with $c = c_{\min}$ evolve from initial conditions with compact support while smooth-fronted travelling waves solutions with $c > c_{\min}$ evolve from initial conditions with exponential decay. We compared the features of travelling wave solutions of the substrate model to travelling wave solutions of the Porous-Fisher model in the limit where $r_1 \gg 1$ and $r_2 \gg 1$. We used a desingularised phase space and the slow manifold reduction to show the differences between travelling waves with minimum speed and fast travelling waves. We provided accurate approximations for the shape of sharp-fronted travelling waves when $r_1 \gg 1$ and $r_2 \gg 1$, and for the

261

shape of smooth-fronted travelling wave solutions when $c \gg 1$.

8.2 Future work

8.2.1 Fisher-Stefan model

In Chapters 2 to 4, we generalised the Fisher-Stefan model to support receding and invading travelling wave solutions, with wave speed $-\infty < c < \infty$. In chapter 4, we studied the two-phase moving boundary problem where the population dynamics are described by the Fisher-KPP model. The Fisher-Stefan model has been studied only for one dimension, regardless of the number of populations. Realistic biological models requires simulations in two or three dimensions, to represent the shape of tumours for example [Byrne and Chaplain 1997, Swanson et al. 2003]. The extension of the one and two-phase Fisher-Stefan model for two or three dimensions is an important future work, if the model is to be applied to real biological systems.

We have shown that we can estimate the travelling wave speed c from the parameter κ, and inversely we can obtain the parameter κ from the wave speed c. We have not provided a sufficient exhaustive biological interpretation of the parameter κ in the Stefan condition. Typical values of diffusivity, proliferation rate and carrying capacity density are obtained from experiments [Johnston et al. 2015, Johnston et al. 2016, Jin et al. 2016] and are used to confirm the relationship $c = 2\sqrt{\lambda D}$. In the same way, there is a crucial work to be done to confirm experimentally the relationship between κ and wave speed c, either by calculating the wave speed from the relationship $c = 2\sqrt{\lambda D}$ and then deducing the typical range for κ, or by setting an experiment to measure the loss of population at the boundary.

The Fisher-Stefan model that we studied was built on the Fisher-KPP model that describes the proliferation of cells using a logistic growth function. It would be interesting to include a general source term [Tsoularis and Wallace 2002] in the Fisher-Stefan model. For example, including a source term that describes a strong Allee effect [Fadai and Simpson 2020b] can lead to the extinction of the population, without the need to define a moving boundary. It would be interesting to see what modifications would be brought to the outcomes of the model with an Allee effect by adding a moving boundary.

8.2.2 Models of invasion with coupled differential equations

Finally in chapter 5, we added a second population to the moving boundary model. We used a single-species equation for each population, thereby we limited the interaction between both populations to the interface governed by a two-phase Stefan condition. The speed of the moving boundary is related to the flux of density of each population at the boundary. Measuring the loss or the gain of density for each population at the boundary is not an easy task in the context of a biological experiment. The Stefan condition is coupled to a system of differential equations that yields a travelling wave. Therefore, the loss or the gain of population at the moving boundary described by the Stefan condition is related to the shape and the speed of the travelling wave. Each term in the Stefan condition may not be explicitly related to a measurement in a laboratory experiment. We suggest to parametrise the model by measuring the speed of the moving front. In the same manner as for one population, the parameter κ can deduced from the speed of the invading or retreating front. The observation that we have two parameters κ to estimate does not cause any supplementary challenge, as one parameter could be estimated relatively to the other parameter, set to be one.

The cancer and the skin population are not coupled in the two-phase boundary model that we studied. As shown Figure 8.1(a), the populations are separated by an interface at the moving boundary. A model that describes the interactions between the two populations would require two coupled differential equations, where each population occupies a domain well-defined with a moving boundary as in Figure 8.1(b). Each moving boundary would evolve following a Stefan condition and the domain occupied by one population could overlap on the domain occupied by the other population.

Chapter 6 studied a model of cancer cells invading into surrounding skin tissues. The model uses two coupled differential equations where the proliferation of cancer follows a logistic growth. A obvious extension is to study other types of function for the proliferation term [Tsoularis and Wallace 2002]. It would be interesting to find a mathematical expression for the critical value γ_c beyond which the minimal speed depends on γ.

Chapter 7 studied a continuum model of coupled partial differential equations to simulate the growth of tissues on bioscaffolds, where the cells produced
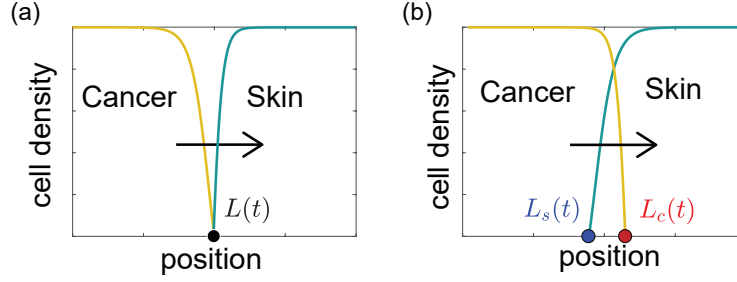
Figure 8.1: Adding another moving boundary to the two-phase model. (a) Populations of skin and cancer are separated by a moving boundary at $x = L(t)$, represented by a black disc. (b) Each population has a domain defined by a moving boundary. $L_c(t)$ and $L_s(t)$ correspond to the moving boundaries of the domain of the populations of cancer and skin, respectively, and are represented by red and blue discs.

a substrate composed of an extracellular matrix of macromolecules. The decay due to the natural process of degradation of the substrate is a linear term in the differential equation that describes the rate of change of the substrate. The advantage of keeping a linear term is to simplify the work to be done when estimating the parameter of the decay rate. A future work could consider a quadratic decay or a more complicated term. The diffusion of the tissue cells was described by a nonlinear term, where the diffusion of cells would increase with the density of the substrate. It would be pertinent to study different power law functions to describe the nonlinear diffusion. Finally, the growth of tissue on bioscaffolds is replicated in experiments in two or three dimensions. It is natural to verify if the travelling wave analysis that we effectuated for the model in one dimension still holds in two or three dimensions.

Bibliography

Ablowitz MJ, Zeppetella A (1979) Explicit solutions of Fisher's equation for a special wave speed. *Bulletin of Mathematical Biology* **41**, 835–840. (doi:10.1007/BF02462380)

Ambrosi D, Ben Amar M, Cyron CJ, DeSimone A, Goriely A, Humphrey JD, Kuhl E (2019) Growth and remodelling of living tissues: perspectives, challenges and opportunities. *Journal of the Royal Society Interface* **16**, 20190233. (doi:10.1098/rsif.2019.0233)

Amor DR, Fort J (2010) Virus infection speeds: theory versus experiment. *Physical Review E* **82**, 061905. (doi:10.1103/PhysRevE.82.061905)

Amor DR, Montañez R, Duran-Nebreda S, Solé R (2017) Spatial dynamics of synthetic microbial mutualists and their parasites. *PLoS Computational Biology* **13**, e1005689. (doi:10.1371/journal.pcbi.1005689)

Anderson ARA, Quaranta V (2008) Integrative mathematical oncology. *Nature Reviews Cancer* **8**, 227–234. (doi:10.1038/nrc2329)

Aronson DG, Weinberger HF (1978) Multidimensional nonlinear diffusion arising in population genetics. *Advances in Mathematics* **30**, 33–76. (doi:10.1016/0001-8708(78)90130-5)

Astanin S, Preziosi L (2009) Mathematical modelling of the Warburg effect in tumour cords. *Journal of Theoretical Biology* **258**, 578–590. (doi:10.1016/j.jtbi.2009.01.034)

Bate AM, Hilker FM (2019) Preytaxis and travelling waves in an eco-epidemiological model. *Bulletin of Mathematical Biology* **81**, 995–1030. doi:10.1007/s11538-018-00546-0

Bitsouni V, Trucu D, Chaplain MAJ, Eftimie R (2018) Aggregation and travelling wave dynamics in a two-population model of cancer cell growth and invasion. *Mathematical Medicine and Biology* **35**, 541–577. (doi:10.1093/imammb/dqx019)

Bradshaw-Hajek BH, Broadbridge P (2004) A robust cubic reaction-diffusion system for gene propagation. *Mathematical and Computer Modelling* **39**, 1151–1163. (doi:10.1016/S0895-7177(04)90537-7)

Breward CJ, Byrne HM, Lewis CE (2002) The role of cell-cell interactions in two-phase model for avascular tumour growth. *Journal of Mathematical Biology* **45**, 125–152. (doi:10.1007/s002850200149)

Broadbridge P, Bradshaw BH, Fulford GR, Aldis GK (2002) Huxley and Fisher equations for gene propagation: An exact solution. *ANZIAM Journal* **44**, 11–20. (doi:10.1017/S1446181100007860)

Brosa Planella F, Please CP, Van Gorder (2019) Extended Stefan problem for solidification of binary alloys in a finite planar domain. *SIAM Journal on Applied Mathematics* **79**, 876-913. (10.1137/18M118699X).

Brosa Planella F, Please CP, Van Gorder (2021) Extended Stefan problem for the solidification of binary alloys in a sphere. (*European Journal of Applied Mathematics* **32**, 242-279. doi.org/10.1017/S095679252000011X)

Browning AP, McCue SW, Simpson MJ (2017) A Bayesian computational approach to explore the optimal the duration of a cell proliferation assay. *Bulletin of Mathematical Biology* **79**, 188–1906. (10.1007/s11538-017-0311-4)

Browning AP, Haridas P, Simpson MJ (2019) A Bayesian sequential learning framework to parameterise continuum models of melanoma invasion into human skin. *Bulletin of Mathematical Biology* **81**, 676–698. (doi:10.1007/s11538-018-0532-1)

Browning AP, Maclaren OJ, Buenzli PR, Lanaro M, Allenby MC, Woodruff MA, Simpson MJ (2021) Model-based data analysis of tissue growth in thin 3D printed scaffolds. *Journal of Theoretical Biology* **528**, 110852. (doi:10.1016/j.jtbi.2021.110852)

Buenzli PR, Lanaro M, Wong C, McLaughlin MP, Allenby MC, Woodruff MA, Simpson MJ (2020) Cell proliferation and migration explain pore bridging dynamics in 3D printed scaffolds of different pore size. *Acta Biomaterialia* **114**, 285–295. (doi:10.1016/j.actbio.2020.07.010)

G Bunting, Y Du, K Krakowski (2012) Spreading speed revisited: Analysis of a free boundary model. *Networks & Heterogeneous Media* **7**, 583–603. (doi:10.3934/nhm.2012.7.583)

Burden RL, Faires JD (2011) Numerical analysis. Ninth edition, Brooks/-Coles, Boston.

Byrne HM, Chaplain MAJ (1997) Free boundary value problems associated with the growth and development of multicellular spheroids. *European Journal of Applied Mathematics* **8**, 639–658. (doi:10.1017/S0956792597003264)

Byrne H, Preziosi L (2003) Modelling solid tumour growth using the theory of mixtures. *Mathematical Medicine and Biology: A Journal of the IMA* **20**, 341–366. (doi:10.1093/imammb20.4.341)

Byrne HM, King JR, McElwain DLS, Preziosi L (2003) A two-phase model of solid tumour growth. *Applied Mathematics Letters* **16**, 567–573. (doi:10.1016/S0893-9659(03)00038-7)

Byrne HM (2010) Dissecting cancer through mathematics: from the cell to the animal model. *Nature Reviews Cancer* **10**, 221–230. (doi:10.1038/nrc2808)

Cai AQ, Landman KA, Hughes BD (2007) Multi-scale modeling of a wound-healing cell migration assay. *Journal of Theoretical Biology* **245**, 576–594. (doi:/10.1016/j.jtbi.2006.10.024)

Canosa J (1973) On a nonlinear diffusion equation describing population growth. *IBM Journal of Research and Development* **17**, 307–313. (doi:10.1147/rd.174.0307)

Chang C-H, Chen C-C (2013) Travelling wave solutions of a free boundary problem for a two-species competitive model. *Communications on Pure and Applied Analysis* **12**, 1065–1074.(doi:10.3934/cpaa.2013.12.1065)

Chaplain MAJ, Lorenzi T, Mcfarlane FR (2020) Bridging the gap between individual-based and continuum models of growing cell populations. *Journal of Mathematical Biology* **80**, 343–371. (doi:10.1007/s00285-019-01391-y)

Colson C, Sánchez Garduno F, Byrne HM, Maini PK, Lorenzi T (2021) Travelling-wave analysis of a model of tumour invasion with degenerate, cross-dependent diffusion. arXiv. 2021: 2107.11106. (doi:arxiv.org/abs/2107.11106v1)

Courchamp F, Berec L, Gascoigne J (2008) Allee effects in ecology and conservation. Oxford University Press, Oxford.

Crank J (1979) The mathematics of diffusion. Oxford University Press, Oxford.

Crank J (1987) Free and moving boundary problems. Oxford University Press, Oxford.

Curtin L, Hawkins-Daarud A, van der Zee KG, Swanson KR, Owen MR (2020) Speed switch in glioblastoma growth rate due to enhanced hypoxia-induced migration. *Bulletin of Mathematical Biology* **82**, 43. (10.1007/s11538-020-00718-x)

Dalwadi MP, Waters SL, Byrne HM, Hewitt IJ (2020). A Mathematical framework for developing freezing protocols in the cryopreservation of cells. *SIAM Journal on Applied Mathematics* **80**, 657–689. (doi:10.1137/19M1275875)

Deutsch A, Dormann S (2005) Mathematical modeling of biological pattern formation. In: Cellular Automaton Modeling of Biological Pattern Formation. Modeling and Simulation in Science, Engineering and Technology. Birkhäuser, Boston. (doi:/10.1007/0-8176-4415-6_3)

Du Y, Lin Z (2010) Spreading-vanishing dichotomy in the diffusive logistic model with a free boundary. *SIAM Journal on Mathematical Analysis* **42**, 377–405. (doi:10.1137/090771089)

Du Y, Guo Z (2011) Spreading-vanishing dichotomy in a diffusive logistic model with a free boundary, II. *Journal of Differential Equations* **250**, 4336–4366. (doi:10.1016/j.jde.2011.02.011)

Du Y, Guo Z. 2012. The Stefan problem for the Fisher-KPP equation. *Journal of Differential Equations* **253**, 996–1035.

Du Y, Lou B (2015) Spreading and vanishing in nonlinear diffusion problems with free boundaries. *Journal of the European Mathematical Society* **17**, 2673–2724. (doi:10.4171/JEMS/568)

Du Y, Matano H, Wang K (2014) Regularity and asymptotic behavior of nonlinear Stefan problems. *Archive for Rational Mechanics and Analysis* **212**, 957–1010. (doi:10.1007/s00205-013-0710-0)

Du Y, Matsuzawa H, Zhou M (2014) Sharp estimate of the spreading speed determined by nonlinear free boundary problems. *SIAM Journal on Mathematical Analysis* **46**, 375–396. (doi:10.1137/130908063)

Dzobo K, Thomford NE, Senthebane DA, Shipanga H, Rowe A, Dandara C, Pillay M, Motaung KSCM (2018) Advances in regenerative medicine and tissue engineering: Innovation and transformation of medicine. *Stem Cells International* **2018**, 2495848. (doi:10.1155/2018/2495848)

Edelstein-Keshet L (2005) Mathematical models in biology. SIAM, Philadelphia. (doi:10.1137/1.9780898719147).

El-Hachem M, McCue SW, Jin W, Du Y, Simpson MJ (2019) Revisiting the Fisher-Kolmogorov-Petrovsky-Piskunov equation to interpret the spreading-extinction dichotomy. *Proceedings of the Royal Society A : Mathematical, Physical and Engineering Sciences* **475**, 20190378. (10.1098/rspa.2019.0378)

El-Hachem M, McCue SW, Simpson MJ (2020) A sharp-front moving boundary model for malignant invasion. *Physica D: Nonlinear Phenomena* **412**, 132639. (doi:10.1016/j.physd.2020.132639)

El-Hachem M, McCue SW, Simpson MJ (2021) Invading and receding sharp-fronted travelling waves. *Bulletin Mathematical Biology* **83**, 35. (doi:10.1007/s11538-021-00862-y)

El-Hachem M, McCue SW, Simpson MJ (2021) Travelling wave analysis of cellular invasion into surrounding tissues. *Physica D: Nonlinear Phenomena* **428**, 133026. (doi:10.1016/j.physd.2021.133026)

El-Hachem M, McCue SW, Simpson MJ (2021) Non-vanishing sharp-fronted travelling wave solutions of the Fisher-Kolmogorov model. Accepted for publication in *Mathematical Medecine and Biology.* (arXiv:2107.05210v2)

Fadai NT, Simpson MJ (2020) Population dynamics with threshold effects give rise to a diverse family of Allee effects. *Bulletin of Mathematical Biology* **82**, 74. (doi:10.1007/s11538-020-00756-5)

Fadai NT, Simpson MJ (2020) New travelling wave solutions of the Porous-Fisher model with a moving boundary. *Journal of Physics A: Mathematical and Theoretical* **53**, 095601. (10.1088/1751-8121/ab6d3c).

Fasano A, Herrero MA, Rodrigo MR (2009) Slow and fast invasion waves in a model of acid-mediated tumour growth. *Mathematical Biosciences* **220**, 45–56. (doi:10.1016/j.mbs.2009.04.001)

Fife PC (1979) Long time behavior of solutions of bistable nonlinear diffusion equations. *Archive for Rational Mechanics and Analysis* **70**, 31–36. (doi:10.1007/BF00276380)

Fisher RA. 1937. The wave of advance of advantageous genes. *Annals of Eugenics* **7**, 355–369. (doi:10.1111/j.1469-1809.1937.tb02153.x)

Flegg JA, Menon SN, Byrne HM, McElwain DLS (2020) A current perspective on wound healing and tumour-induced angiogenesis. *Bulletin of Mathematical Biology* **82**, 43. (doi:10.1007/s11538-020-00696-0)

Font F, Mitchell SL, Myers TG (2013) One-dimensional solidification of supercooled melts. *International Journal of Heat and Mass Transfer* **62**, 411–421. (doi:10.1016/j.ijheatmasstransfer.2013.02.070)

Forbes L. 1997. A two-dimensional model for large-scale bushfire spread. *Journal of the Australian Mathematical Society. Series B, Applied mathematics.* **39**, 171–194. (doi:10.1017/S0334270000008791)

Fort J (2012) Synthesis between demic and cultural diffusion in the Neolithic transition in Europe. *Proceedings of the National Academy of Sciences* **109**, 18669–18673. (doi:10.1073/pnas.1200662109)

Friedman A (2008) A multiscale tumour model. *Interfaces and Free Boundaries* **10**, 245–262. (doi:10.4171/ifb/188)

Friedman A (2014) Free boundary problems in biology. *Proceedings of the Royal Society A: Mathematical, Physical and Engineering Sciences* **373**, 20140368. (doi:10.1098/rsta.2014.0368)

Gaffney EA, Maini PK (1999) Modelling corneal epithelial wound closure in the presence of physiological electric fields via a moving boundary formalism. *IMA Journal of Mathematics Applied in Medicine and Biology* **16**, 369–393. (doi:10.1093/imammb/16.4.369)

Gallay T, Mascia C (2021). Propagation fronts in a simplified model of tumor growth with degenerate cross-dependent self-diffusivity. *Nonlinear Analysis: Real World Applications* **63**, 103387. (doi:10.1016/j.nonrwa.2021.103387)

Gatenby RA, Gawlinski ET (1996) A reaction-diffusion model of cancer invasion. *Cancer Research* **56**, 5745–5753. (doi:10.1007/s00285-013-0665-7)

Gerlee P, Nerlander S (2012) The impact of phenotypic switching on glioblastoma growth and invasion. *PLoS Computational Biology* **8**, e1002556. (doi:0.1371/journal.pcbi.1002556)

Griffith B, Michael Scott J, Carpenter JW, Reed C (1989) Translocation as a species conservation tool: status and strategy. *Science* **245**, 477–480. (doi:10.1126/science.245.4917.477)

Grindrod P (2007) Patterns and waves. Oxford: Oxford University Press.

Gupta SC (2017) The classical Stefan problem. Basic concepts, modelling and analysis with quasi-analytical solutions and methods. Second edition. Elsevier, Amsterdam.

Hanahan D, Weinberg RA (2000) The hallmarks of cancer. *Cell* **100**, 57–70. (doi:10.1016/j.cell.2011.02.013)

Haridas P, McGovern JA, McElwain DLS, Simpson MJ (2017) Quantitative comparison of the spreading and invasion of radial growth phase and metastatic melanoma cells in a three-dimensional human skin equivalent model. *PeerJ* **5**, e3754. (doi:10.7717/peerj.3754)

Haridas P, Browning AP, McGovern JA, McElwain DLS, Simpson MJ (2018) Three-dimensional experiments and individual based simulations show that

cell proliferation drives melanoma nest formation in human skin tissue. *BMC Systems Biology* **12**, 34. (doi:10.1186/s12918-018-0559-9)

Harley K, van Heijster P, Marangell R, Pettet GJ, Wechselberger M (2015) Numerical computation of an Evans function for travelling waves. *Mathematical Biosciences* **266**, 36–51. (doi:10.1016/j.mbs.2015.05.009)

Harris S (2004) Fisher equation with density-dependent diffusion: special solutions. *Journal of Physics A: Mathematical and Theoretical* **37**, 6267. (10.1088/0305-4470/37/24/005)

Hill JM (1987) One-dimensional Stefan problems: an introduction. First Edition, Longman Scientific & Technical, Harlow.

Hogan AB, Myerscough MR (2017) A model for the spread of an invasive weed *Tradescantia fluminensis*. *Bulletin of Mathematical Biology* **79**, 1201–1217. (doi:10.1007/s11538-017-0280-7)

Holder AB, Rodrigo MR (2015) Model for acid-mediated tumour invasion with chemotherapy intervention II: Spatially heterogeneous populations. *Mathematical Biosciences* **270**, 10–29. (doi:10.1016/j.mbs.2015.09.007)

Holder AB, Rodrigo MR, Herrero MA (2014) A model for acid-mediated tumour growth with nonlinear acid production term. *Applied Mathematics and Computation* **227**, 176–198. (doi:10.1016/j.amc.2013.11.018)

Holmes EE, Lewis MA, Banks JE, Veit RR (1994) Partial differential equations in ecology: spatial interactions and population dynamics. *Ecology* **74**, 17–29. (doi:10.2307/1939378)

Horgan FG (2009) Invasion and retreat: shifting assemblages of dung beetles amidst changing agricultural landscapes in central Peru. *Biodiversity and Conservation* **18**, 3519. (doi:10.1007/s10531-009-9658-7)

Ibrahim K, Sourrouille P, Hewitt GM (2000) Are recession populations of the desert locust (Schistocerca gregaria) remnants of past swarms? *Molecular Ecology* **9**, 783–791. (doi:10.1046/j.1365-294x.2000.00932.x)

Jin W, Shah ET, Penington CJ, McCue SW, Chopin LK, Simpson MJ (2016) Reproducibility of scratch assays is affected by the initial degree of confluence:

experiments, modelling and model selection. *Journal of Theoretical Biology* **390**, 136–145. (doi:10.1016/j.jtbi.2015.10.040)

Jin W, Shah ET, Penington CJ, McCue SW, Maini PK, Simpson MJ (2017) Logistic proliferation of cells in scratch assays is delayed. *Bulletin of Mathematical Biology* **79**, 1028–1050. (doi:10.1007/s11538-017-0267-4)

Jin W, Lo K-Y, Chou S-E, McCue SW, Simpson MJ (2018) The role of initial geometry in experimental models of wound closing. *Chemical Engineering Science* **179**, 221–226. (doi:10.1016/j.ces.2018.01.004)

Jin W, Lo K-Y, Sun Y-S, Ting Y-H, Simpson MJ (2020) Quantifying the role of different surface coatings in experimental models of wound healing. *Chemical Engineering Science* **220**, 115609. (doi:10.1016/j.ces.2020.115609)

Jin W, Spoerri L, Haass NK, Simpson MJ (2021) Mathematical model of tumour spheroid experiments with real-time cell cycle imaging. *Bulletin of Mathematical Biology* **83**, 44. (10.1007/s11538-021-00878-4).

Johnston ST, Shah ET, Chopin LK, McElwain DLS, Simpson MJ (2015) Estimating cell diffusivity and cell proliferation rate by interpreting IncuCyte ZOOM$^{\mathrm{TM}}$ assay data using the Fisher-Kolmogorov model. *BMC Systems Biology* **9**, 38. (doi:10.1186/s12918-015-0182-y)

Johnston ST, Ross JV, Biner BJ, McElwain DLS, Haridas P, Simpson MJ (2016) Quantifying the effect of experimental design choices for in vitro scratch assays. *Journal of Theoretical Biology* **400**, 19–31. (doi:10.1016/j.jtbi.2016.04.012) (doi:10.1016/j.jtbi.2006.06.021)

Johnston ST, Baker RE, McElwain DLS, Simpson MJ (2017) Co–operation, competition and crowding: a discrete framework linking allee kinetics, nonlinear diffusion, shocks and sharp–fronted travelling waves. *Scientific Reports* **7**, 42134. (doi:10.1038/srep42134)

Kaliappan P (1983) An exact solution for travelling waves of $u_t = Du_{xx} + u - u^k$. *Physica D: Nonlinear Phenomena* **11**, 368-374. (doi:10.1016/0167-2789(84)90018-6)

Keller EF, Segel LA (1971) Model for chemotaxis. *Journal of Theoretical Biology* **30**, 225–234. (doi:https://doi.org/10.1016/0022-5193(71)90050-6)

Killengreen ST, Ims RA, Yoccoz NG, Bråthen KA and Henden J–A, Schott T (2007) Structural characteristics of a low Arctic tundra ecosystem and the retreat of the Arctic fox. *Biological Conservation* **135**, 459–472. (doi:10.1016/j.biocon.2006.10.039)

Kimpton LS, Whiteley JP, Waters SL, King JR, Oliver JM (2013) Multiple travelling-wave solutions in a minimal model for cell motility. *Mathematical Medicine and Biology* **30**, 241-272. (doi:10.1093/imammb/dqs023)

King JR, McCabe PM (2003) On the Fisher-KPP equation with fast non-linear diffusion. *Proceedings of the Royal Society A: Mathematical, Physical and Engineering Sciences* **459**, 2529–2546. (doi:/10.1098/rspa.2003.1134)

King JR, Riley DS (2000) Asymptotic solutions to the Stefan problem with a constant heat source at the moving boundary. *Proceedings of the Royal Society A: Mathematical, Physical and Engineering Sciences* **456**, 1163–1174. (doi:10.1098/rspa.2000.0556)

King JR, Riley DS, Wallman AM (1999) Two-dimensional solidification in a corner. *Proceedings of the Royal Society A: Mathematical, Physical and Engineering Sciences* **455**, 3449–3470. (doi:10.1098/rspa.1999.0460)

Kolmogorov AN, Petrovskii PG, Piskunov NS (1937) A study of the diffusion equation with increase in the amount of substance, and its application to a biological problem. *Moscow University Mathematics Bulletin* **1**, 1–26.

Kot M (2003) Elements of Mathematical Ecology. Cambridge University Press, Cambridge.

Krause AL, Van Gorder RA (2020) A non-local cross-diffusion model of population dynamics II: Exact, approximate and numerical traveling waves in single- and multi-species populations. *Bulletin of Mathematical Biology* **82**, 113. (doi:10.1007/s11538-020-00787-y)

Kutluay S, Bahadir AR, Özdeş A (1997) The numerical solution of one-phase classical Stefan problem. *Journal of Computational and Applied Mathematics* **81**, 135-144. (doi:10.1016/S0377-0427(97)00034-4)

Lagergren JH, Nardini JT, Lavigne GM, Rutter EM, Flores KB (2021) Learning partial differential equations for biological transport mod-

els from noisy spatio-temporal data. *Proceedings of the Royal Society A: Mathematical, Physical and Engineering Sciences* **476**, 20190800. (doi:10.1098/rspa.2019.0800)

Largergren JH, Nardini JT, Baker RE, Simpson MJ, Flores KB. Biologically-informed neural networks guide mechanistic modelling from sparse experimental data. *PLOS Computational Biology* **16**, e1008462. (doi:0.1371/journal.pcbi.1008462)

Lanaro M, Mclaughlin M, Maximilion P, Simpson MJ, Buenzli PR, Wong CS, Allenby MC, Woodruff MA (2021) A quantitative analysis of cell bridging kinetics on a scaffold using computer vision algorithms. *Acta Biomaterialia.* (doi:10.1016/j.actbio.2021.09.042)

Landman KA, Cai A (2007) Cell proliferation and oxygen diffusion in a vascularising scaffold. *Bulletin of Mathematical Biology* **69**, 2405–2428. (doi:10.1007/s11538-007-9225-x)

Landman KA, Pettet GJ (1998) Modelling the action of proteinase and inhibitor in tissue invasion. *Mathematical Biosciences* **154**, 23–37. (doi:10.1016/s0025-5564(98)10038-x)

Landman KA, Simpson MJ, Slater JA, Newgreen DF (2005) Diffusive and chemotactic cellular migration: smooth and discontinuous travelling wave solutions. *SIAM Journal on Applied Mathematics* **65**, 1420–1442. (doi:10.1137/040604066)

Landman KA, Simpson MJ, Pettet GJ (2008) Tactically-driven nonmonotone travelling waves. *Physica D: Nonlinear Phenomena* **237**, 678–691. (doi:10.1016/j.physd.2007.10.003)

Lei C, Nie H, Dong W, Du Y. Spreading of two competing species governed by a free boundary model in a shifting environment. *Journal of Mathematical Analysis and Applications* **462**, 1254-1282. (doi:10.1016/j.jmaa.2018.02.042)

Levin SA, Muller-Landau HC, Nathan R, Chave J (2003) The ecology and evolution of seed dispersal: a theoretical perspective. *Annual Review of Ecology, Evolution, and Systematics* **34**, 575–604. (doi:10.1146/annurev.ecolsys.34.011802.132428)

Lewis MA, Kareiva P (1993) Allee dynamics and the spread of invading organisms. *Theoretical Population Biology* **43**, 141–158. (doi:10.1006/tpbi.1993.1007)

Maclaren OJ (2020) Qualitative analysis of differential equations. https://github.com/omaclaren.

Maini PK, McElwain DLS, Leavesley DI (2004) Traveling wave model to interpret a wound-healing cell migration assay for human peritoneal mesothelial cells. *Tissue Engineering* **10**, 475–482. (doi:10.1089/107632704323061834)

Maini PK, McElwain DLS, Leavesley D (2004) Traveling waves in a wound healing assay. *Applied Mathematics Letters* **17**, 575–580. (doi:10.1016/S0893-9659(04)90128-0)

Maplesoft, a division of Waterloo Maple Inc. (2021) *Maple User Manual: Dilog.* Retrieved December 2021 from https://www.maplesoft.com/support/help/Maple/view.aspx?path=dilog.

Marchant BP, Norbury J, Perumpanani AJ (2000) Travelling shock waves arising in a model of malignant invasion. *SIAM Journal on Applied Mathematics* **60**, 463–476. (doi:10.1137/S0036139998328034)

Marchant BP, Norbury J, Sherratt JA (2001) Travelling wave solutions to a haptotaxis-dominated model of malignant invasion. *Nonlinearity* **14**, 1653–1671. (doi:10.1088/0951-7715/14/6/313)

The MathWorks Inc. *eig.* Retrieved December 2021 from https://au.mathworks.com/help/matlab/ref/eig.html.

The MathWorks Inc. *fsolve.* Retrieved from https://www.mathworks.com/help/optim/ug/fsolve.html December 2021.

The MathWorks Inc. *ode45.* Retrieved from http://mathworks.com/help/matlab/ref/ode45.html in December 2021.

The MathWorks Inc. *quiver.* Retrieved from http://au.mathworks.com/help/matlab/ref/quiver.html in December 2021.

McCue SW, King JR, Riley DS (2003) Extinction behaviour for two-dimensional inward-solidification problems. *Proceedings of the Royal Society A: Mathematical, Physical and Engineering Sciences* **459**, 977–999. (doi:10.1098/rspa.2002.1059)

McCue SW, King JR, Riley DS (2005) The extinction problem for three-dimensional inward solidification. *Journal of Engineering Mathematics* **52**, 389–409. (doi:10.1007/s10665-005-3501-2)

McCue SW, Wu B, Hill JM (2008) Classical two-phase Stefan problem for spheres. *Proceedings of the Royal Society A: Mathematical, Physical and Engineering Sciences* **464**, 2055–2076. (doi:10.1098/rspa.2007.0315)

McCue SW, Jin W, Moroney TJ, Lo K-Y, Chou S-E, Simpson MJ (2019) Hole-closing model reveals exponents for nonlinear degenerate diffusivity functions in cell biology. *Physica D: Nonlinear Phenomena* **398**, 130–140. (doi:10.1016/j.physd.2019.06.005)

McCue SW, El-Hachem M, Simpson MJ (2021) Exact sharp-fronted travelling wave solutions of the Fisher-KPP equation. *Applied Mathematics Letters* **114**, 106918. doi:10.1016/j.aml.2020.106918.

McCue SW, El-Hachem M, Simpson MJ (2021) Travelling waves, blow-up and extinction in the Fisher-Stefan model. *Studies in Applied Mathematics*, 1–21. (doi:10.1111/sapm.12465)

Mercer GN, Weber RO (1995) Combustion wave speed. *Proc. R. Soc. A-Math. Phy.* **450**, 193–198. (doi:10.1098/rspa.1995.0079)

Mitchell SL (2015) Applying the combined integral method to two-phase Stefan problems with delayed onset of phase change. *Journal of Computational and Applied Mathematics* **281**, 58–73.

Mitchell SL, O'Brien SBG (2014) Asymptotic and numerical solutions of a free boundary problem for the sorption of a finite amount of solvent into a glassy polymer. *SIAM Journal on Applied Mathematics* **74**, 697–723. doi:10.1137/120899200

Mitchell SL, Vynnycky M (2014) On the numerical solution of two-phase Stefan problems with heat-flux boundary conditions. *Journal of Computational and Applied Mathematics* **264**, 49–64.

Mitchell SL, Vynnycky M (2016) On the accurate numerical solution of a two-phase Stefan problem with phase formation and depletion. *Journal of Computational and Applied Mathematics* **300**, 259–274. (doi:10.1016/j.cam.2015.12.021)

Mũller MJI, Beverly IN, Nelson DR, Murray AW (2014) Genetic drift opposes mutualism during spatial population expansion. *Proceedings of the National Academy of Sciences* **111**, 1037–1042. (doi:10.1073/pnas.1313285111)

Murray JD (1984) Asymptotic analysis. First Edition, Springer, New York.

Murray JD (2002) Mathematical Biology I: An Introduction. Third edition. Springer, New York.

Nardini JT, Chapnick DA, Liu X, Bortz DM (2016) Modeling keratinocyte wound healing dynamics: Cell–cell adhesion promotes sustained collective migration. *Journal of Theoretical Biology* **400**, 103–117. (doi:10.1016/j.jtbi.2016.04.015)

National Cancer Institute (1985) Melanoma. Retrieved December 2020 National Cancer Institute.

Otto G, Bewick S, Li B, Fagan WF (2018) How phenological variation affects species spreading speeds. *Bulletin of Mathematical Biology* **80**, 1476–1513. (doi:10.1007/s11538-018-0409-3)

Pérez-Beteta J, Martínez-González A, Pérez-García VM. 2018. A three-dimensional computational analysis of magnetic resonance images characterizes the biological aggressiveness in malignant brain tumours. *Journal of the Royal Society Interface* **15**, 20180503. (doi:10.1098/rsif.2018.0503)

Painter KJ, Hillen T (2013) Mathematical modelling of glioma growth: the use of diffusion tensor imaging (DTI) data to predict the anisotropic pathways of cancer invasion. *Journal of Theoretical Biology* **323**, 25–39. (doi:10.1016/j.jtbi.2013.01.014)

Painter KJ, Sherratt JA (2003) Modelling the movement of interacting cell populations. *Journal of Theoretical Biology* **225**, 327–339. (doi:10.1016/j.jtbi.2015.01.025)

Painter KJ, Bloomfield JM, Sherratt JA, Gerish A (2015) A nonlocal model for contact attraction and repulsion in heterogeneous cell populations. *Journal of Mathematical Biology* **77**, 1132–1165. (doi:10.1007/s11538-015-0080-x)

Perthame B, Tang M, Vauchelet N (2014) Traveling wave solution of the Hele–Shaw model of tumor growth with nutrient. *Mathematical Models and Methods in Applied Sciences* **24**, 2601–2626. (doi:10.1142/S0218202514500316)

Perthame B, Vauchelet N (2105) Incompressible limit of a mechanical model of tumour growth with viscosity. *Proceedings of the Royal Society A: Mathematical, Physical and Engineering Sciences* **373**, 20140283. (doi:10.1098/rsta.2014.0283)

Perumpanani AJ, Sherratt JA, Norbury J, Byrne H (1999) A two parameter family of travelling waves with a singular barrier arising from the modelling of matrix mediated malignant invasion. *Physica D: Nonlinear Phenomena* **126**, 145–159. (doi:10.1016/S0167-2789(98)00272-3)

Roose T, Chapman SJ, Maini PK (2007) Mathematical models of avascular tumor growth. *SIAM Review* **49**, 179–208. (doi:10.1137/S0036144504446291)

Sánchez Garduño F, Maini PK (1994) An approximation to a sharp type solution of a density-dependent reaction-diffusion equation. *Applied Mathematics Letters* **7**, 47–51. (doi:10.1016/0893-9659(94)90051-5)

Sánchez-Garduño F, Maini PK (1994) Existence and uniqueness of a sharp travelling wave in degenerate non-linear diffusion Fisher-KPP equations, *Journal of Mathematical Biology* **33**, 163–192. (doi:10.1007/BF00160178)

Sánchez Garduno F, Maini PK (1995) Traveling wave phenomena in some degenerate reaction–diffusion equations. *Journal of Differential Equations* **117**, 281–319. doi:https://doi.org/10.1006/jdeq.1995.1055

Sengers BG, Please CP, Oreffo ROC (2007) Experimental characterization and computational modelling of two-dimensional cell spreading for

skeletal regeneration. *Journal of the Royal Society Interface* **4**, 1107–1117. (doi:10.1098/rsif.2007.0233)

Sherratt, JA, Marchant BP. 1996. Non-sharp travelling wave fronts in the Fisher equation with degenerate nonlinear diffusion. *Applied Mathematics Letters* **9**, 33–38. (doi:10.1016/0893-9659(96)00069-9)

Sherratt JA, Murray JD (1990) Models of epidermal wound healing. *Proceedings of the Royal Society of London: Series B* **241**, 29–36. (doi:10.1098/rspb.1990.0061)

Shigesada N, Kawasaki K, Takeda Y (1995) Modeling stratified diffusion in biological invasions. *American Naturalist* **146**, 229–251. (doi:10.1086/285796)

Simpson MJ (2009) Depth-averaging errors in reactive transport modelling. *Water Resources Research* **45**, W02505. (doi:10.1029/2008WR007356).

Simpson MJ (2015) Exact solutions of linear reaction-diffusion processes on a uniformly growing domain: criteria for successful colonization. *PLoS One* **10**, e0117949. (doi:10.1371/journal.pone.0117949)

Simpson MJ (2020) Critical length for the spreading-vanishing dichotomy in higher dimensions. *ANZIAM J* **62**, 3–17. (doi:10.21914/anziamj.v62i0.15360)

Simpson MJ, Landman KA (2006) Characterizing and minimizing the operator split error for Fisher's equation. *Applied Mathematics Letters* **19**, 604–612. (doi:10.1016/j.aml.2005.08.011)

Simpson MJ, Landman KA, Clement TP (2005) Assessment of a non–traditional operator split algorithm for simulation of reactive transport. *Mathematics and Computers in Simulation* **70**, 44–60. (doi:https://doi.org/10.1016/j.matcom.2005.03.019)

Simpson MJ, Landman KA, Hughes BD, Newgreen DF (2006) Looking inside an invasion wave of cells using continuum models: proliferation is the key. *Journal of Theoretical Biology* **243**, 343–360. (doi:10.1016/j.jtbi.2006.06.021)

Simpson MJ, Zhang DC, Mariani M, Landman KA, Newgreen DF (2007) Cell proliferation drives neural crest cell invasion of the intestine. *Developmental Biology* **302**, 553–568. (doi:j.ydbio.2006.10.017)

Simpson MJ, Landman KA, Bhaganagarapu K (2007) Coalescence of interacting cell populations. *Journal of Theoretical Biology* **247**, 525–543. (doi:10.1016/j.jtbi.2007.02.020)

Simpson MJ, Landman KA, Hughes BD (2010) Cell invasion with proliferation mechanisms motivated by time-lapse data. *Physica A: Statistical Mechanics and its Applications* **389**, 3779–3790. (doi:10.1016/j.physa.2010.05.020)

Simpson MJ, Baker RE, McCue SW (2011) Models of collective cell spreading with variable cell aspect ratio: A motivation for degenerate diffusion models. *Physical Review E* **83**, 021901. (doi:10.1103/physreve.83.021901)

Simpson MJ, Treloar KK, Binder BJ, Haridas P, Manton KJ, Leavesley DI, McElwain DLS, Baker RE (2013) Quantifying the roles of motility and proliferation in a circular barrier assay. *Journal of the Royal Society Interface* **10**, 20130007. (doi:10.1098/rsif.2013.0007)

Sinkins PA, Otfinowski R (2012) Invasion or retreat? The fate of exotic invaders on the northern prairies, 40 years after cattle grazing. *Plant Ecology* **213**, 1251–1262. (doi:10.1007/s11258-012-0083-8)

Skellam JG (1951) Random dispersal in theoretical populations. *Biometrika* **38**, 196–218. (doi:10.1093/biomet/38.1-2.196)

Smallbone K, Gavaghan DJ, Gatenby RA, Maini PK (2005) The role of acidity in solid tumour growth and invasion. *Journal of Theoretical Biology* **235**, 476–484. (doi:10.1016/j.jtbi.2005.02.001)

Steele J, Adams J, Sluckin T (1998) Modelling paleoindian dispersals. *World Archaeology* **30**, 286–305. (doi:10.1080/00438243.1998.9980411)

Strobl MAR, Krause AL, Damaghi M, Gillies R, Anderson ARA, Maini PK (2020) Mix and match: Phenotypic coexistence as a key facilitator of cancer invasion. *Bulletin of Mathematical Biology* **82**, 15. (doi:10.1007/s11538-019-00675-0)

Swanson KR, Bridge C, Murray JD, Alvord EC Jr (2003) Virtual and real brain tumors: using mathematical modeling to quantify

glioma growth and invasion. *Journal of Neurological Sciences* **216**, 1–10. (doi:[/10.1016/j.jns.2003.06.001](/10.1016/j.jns.2003.06.001))

Swanson KR, Rostomily RC, Alvord EC Jr (2008) A mathematical modelling tool for predicting survival of individual patients following resection of glioblastoma: a proof of principle. *Brit. J. Cancer.* **98**, 113–119. (doi:[/10.1038/sj.bjc.6604125](/10.1038/sj.bjc.6604125))

Tang S, Qin S, Weber R. 1993. Numerical studies on 2–dimensional reaction–diffusion equations. *Journal of the Australian Mathematical Society. Series B, Applied mathematics.* **35**, 223–243. (doi:[10.1017/S0334270000009140](10.1017/S0334270000009140))

Taylor CM, Hastings A (2005) Allee effects in biological invasions. *Ecology Letters* **8**, 895–908. (doi:[10.1111/j.1461-0248.2005.00787.x](10.1111/j.1461-0248.2005.00787.x))

Tindall MJ, Dyson L, Smallbone K, Maini PK (2012) Modelling acidosis and the cell cycle in multicellular tumour spheroids. *Journal of Theoretical Biology* **298**, 107–115. (doi:10.1016/j.jtbi.2011.11.009)

Treloar KK, Simpson MJ, McElwain DLS, Baker RE (2014) Are *in vitro* estimates of cell diffusivity and cell proliferation rate sensitive to assay geometry? *Journal of Theoretical Biology* **356**, 71–84. (doi:10.1016/j.jtbi.2014.04.026)

Tremel A, Cai A, Tirtaatmadja N, Hughes BD, Stevens GW, Landman KA, O'Connor AJ (2009) Cell migration and proliferation during monolayer formation and wound healing. *Chemical Engineering Science* **64**, 247–253. (doi:[10.1016/j.ces.2008.10.008](10.1016/j.ces.2008.10.008))

Tsoularis A, Wallace J (2002) Analysis of logistic growth models. *Mathematical Biosciences* **179**, 21–55. (doi:[10.1016/S0025-5564(02)00096-2](10.1016/S0025-5564(02)00096-2))

Van Dyke M, 1975. *Perturbation methods in fluid mechanics.* The Parabolic Press, Stanford, USA.

Vittadello ST, McCue SW, Gunasingh G, Haass NK, Simpson MJ (2018) Mathematical models for cell migration with real-time cell cycle dynamics. *Biophysical Journal* **114**, 1241–1253. (doi:[10.1016/j.bpj.2017.12.041](10.1016/j.bpj.2017.12.041))

Vo BN, Drovandi CC, Pettitt AN, Simpson MJ (2015) Quantifying uncertainty in parameter estimates for stochastic models of collective cell spread-

ing using approximate Bayesian computation. *Math. Biosci.* **263**, 133–142. (doi:10.1016/j.mbs.2015.02.010)

Ward JP, King JR (1997) Mathematical modelling of avascular-tumour growth. *Mathematical Medicine and Biology* **14**, 39–69. (doi:10.1093/imammb/14.1.39)

Ward JP, King JR (1999) Mathematical modelling of avascular-tumour growth II: Modelling growth saturation. *Mathematical Medicine and Biology* **16**, 171–211. (doi:10.1093/imammb/16.2.171)

Warne DJ, Baker RE, Simpson MJ. 2019. Using experimental data and information criteria to guide model selection for reaction–diffusion problems in mathematical biology. *Bulletin of Mathematical Biology* **81**, 1760–1804. (doi:10.1007/s11538-019-00589-x)

Wiggins S (2003) Introduction to Applied Nonlinear Dynamical Systems and Chaos. Second edition, Springer, New York.

Wikipedia (2016) Wound healing assay. Retrieved from en.wikipedia.org/wiki/Wound_healing_assay in December 2021.

Witelski TP (1994) An asymptotic solution for traveling waves of a nonlinear-diffusion Fisher's equation. *Journal of Mathematical Biology* **33**, 1–16. (doi:10.1007/BF00160171)

Witelski TP (1995) Merging traveling waves for the porous-Fisher's equation. *Applied Mathematics Letters* **8**, 57–62. (doi:10.1016/0893-9659(95)00047-T)

Yang J (2015) Asymptotic behavior of solutions for competitive models with a free boundary. *Discrete and Continuous Dynamical Systems* **35**, 3253–3276. (doi:10.3934/dcds.2015.35.3253)